A portable diagnostic tool for the absolute determination of photon fluxes in low pressure plasmas down to the VUV region

Dissertation

zur Erlangung des akademischen Grades

Dr. rer. nat

eingereicht an der

Mathematisch-Naturwissenschaftlich-Technischen Fakultät

der Universität Augsburg

von

Caecilia Johanna Fröhler-Bachus

Augsburg, August 2022

Tag der mündlichen Prüfung: 14. November 2022

Erstprüfer: apl. Prof. Dr.-Ing. Ursel Fantz

Zweitprüfer: Prof. Dr. Wolfgang Brütting

Contents

1 Introduction

Plasmas allow a wide range of material modifications in order to optimize material properties for a specific purpose by applying different methods. For instance, plasma etching has enabled a technical revolution in the semiconductor industry [DK13], and plasma enhanced chemical vapour deposition provides the generation of functional layers, e.g. in solar cells [RRM$^+$02, CCC16]. During the COVID-19 pandemic, the need of sterilizing medical instruments or human skin has gained special attention. But already prior to that, plasma discharges have been investigated and applied for sterilization purposes [LWY01, MBC$^+$02].

These examples illustrate the great number of plasma treatment processes which all use the different plasma species. Heavy particles (i.e. atoms, molecules, ions or radicals), electrons as well as photons produce a collective flux onto the material. The resulting effect depends both on the particular absolute fluxes and the energy of the impinging particle species. Since ions can be guided directionally onto surfaces due to their charge, they are commonly used as main reactive species in low pressure plasmas. Photons cover a wide energy range from the infrared with energies below 1.8 eV to the vacuum ultraviolet region with a photon energy above 6.2 eV. Due to the high photon energy, VUV/UV photons may have a significant influence [SZDE12, TGYH11, LWY01] on the material.

While the supply gas roughly sets the photons' spectral distribution, the discharge's operating parameters (e.g. pressure, input power) have an influence on the absolute fluxes as well as on the photon-to-ion flux ratios. Depending on the specific application, the photon-to-ion flux ratio might affect the process performance beneficially or adversely and can serve as tuning knob to optimize or to taylor a specific plasma setup. For this purpose, an energy resolved quantification of VUV/UV photon fluxes with respect to external operating parameters is essential.

However, this claim implies great challenges regarding absolute in-situ wavelength resolved measurements down to the vacuum ultraviolet range. Commonly, large and expensive VUV spectrometers are used which require a direct vacuum connec-

tion to the plasma chamber. Due to their size, they cannot be easily transported or applied at different setups. Over and above, an absolute intensity calibration of the VUV diagnostic must be performed. Radiation produced by electron storage rings serves as typical primary standard source below 116 nm, but is associated with high efforts. Moreover, the solid angles both of the standard source's emission and the instrument's collection volume must be carefully considered in the calibration. As a consequence, quantitative measurements in the VUV region are limitedly performed [WRA+01, GBMB08, TGYH11, FHL+18].

To overcome these difficulties regarding VUV spectrometers, the recent years have shown a growing interest in transferrable VUV detectors, e.g. based on a VUV silicon diode [KTK+15] or on the conversion of VUV radiation by a sodium salicylate layer into visible light [BLC+14, IMF+17]. Wavelength resolution can be achieved by inserting spectral filters between the plasma and the detector.

Their absolute calibration depends on the complex calculation of solid angles corresponding to the plasma emission and the collecting volume of the device. Moreover, the procedures do not consider effects arising from spectral variations in different gases since the calibration is commonly performed only in one single gas. Besides, the results are exposed to several uncertainties due to underlying assumptions: Regarding the device based on a diode which is presented in [KTK+15], the calibration relies on wavelength-averaged values of the filter transmission and the diode's responsivity. Detectors based on a sodium salicylate layer must crucially consider the wavelength dependency of the quantum efficiency. It might be affected both by the manufacturing process and by degradation effects. These aspects might limit the accuracy of the absolute quantification of photon fluxes.

In this work, a portable diagnostic tool based on a VUV silicon diode and a set of bandpass and edge filters will is developed. In contrast to the above mentioned detectors, its unique feature is the direct absolute calibration against an absolutely intensity calibrated VUV spectrometer. This calibration is performed both individually for each filter and specifically for a variety of supply gases. It directly includes the wavelength dependency of the filter transmission and the diode's sensitivity as well as the viewing volume of the device.

The absolute intensity calibration of the VUV spectrometer is performed in-house by extending the standard method which is based on a deuterium arc lamp and using branching ratios in nitrogen [MZ71]. The corresponding relative calibration curve down to 116 nm from the standard procedure is continued down to 46 nm applying a high current hollow cathode [DGF+88, HKW94, HKHW02]. Absolute

scaling is achieved against an absolutely intensity calibrated optical spectrometer using a helium discharge.
The entire spectroscopic system at *PlanICE* which includes an optical emission spectrometer as well as the VUV spectrometer spectrometer equipped with two detectors — a photomultiplier tube and a channel electron multiplier — allows the investigation of photon fluxes in the range from 46 nm to 933 nm. In order to compile appropriate filter sets for the VUV diode system, emission ranges of gases that are typically applied for process plasmas are investigated in pressure and power scans. The gases include the pure gases argon, hydrogen, nitrogen and oxygen as well as mixtures thereof. Emission ranges with relevant photon fluxes are identified with respect to the ion flux. The latter is determined using Langmuir probe measurements and an energy resolved mass spectrometer.
Having selected appropriate filter sets, the diode system is absolutely calibrated in each gas and for each corresponding filter individually against the VUV spectrometer. Furthermore, a detailed characterization of the diode system is carried out regarding, inter alia, different performance aspects (e.g. reproducibility, linearity) and aging effects due to high energetic VUV radiation. It is complemented by extensive benchmark measurements at *PlanICE* using the VUV spectrometer and the optical spectrometer as reference.
The diode system's applicability as a portable, flexible and reliable VUV diagnostic tool will be demonstrated at three different plasma experiments — the in-house laboratory setup *ACCesS*, the low pressure sterilization reactor *PlasmaDecon* at the Ruhr-Universität Bochum and the ion source of the *Batman Upgrade* test stand at the Max-Planck-Institut für Plasmaphysik (IPP, Garching).

2 Atoms and molecules in low pressure plasmas

2.1 General properties of low pressure plasmas

The *plasma* state describes a partly or fully ionized gas which, therefore, contains neutral particles, positive as well as negative ions and electrons. In contrast to plasmas around or exceeding atmospheric pressure, the low pressure regime typically covers the range of several Pascal and below [CB11]. Their properties are summarized in the following, mainly based on the detailed description in [CB11, LL05].

Quasineutrality

The plasma is *quasineutral*. This term describes the balance between the sum of the positively charged particle densities and the sum of the negatively charged particle densities. Hence, no charge accumulation takes places. On a macroscopic scale, this leads to the equation

$$\sum_i Z_i n_i^+ = \sum_j Z_j n_j^- + n_\mathrm{e}, \tag{2.1}$$

where n_i^+ and n_j^- denote the density of positively charged ion species i and negatively charged ion species j, respectively, with the corresponding ionization levels Z_i and Z_j. The electron density is stated with n_e. Neglecting negative ions and assuming only single ionization, which serves as good approximation for common low pressure plasmas, the quasineutral property of a plasma can be expressed with

$$n_\mathrm{ion}^+ = n_\mathrm{e}, \tag{2.2}$$

where n_ion^+ characterizes the positive ion density.

Distribution function & particle temperature

Distribution functions $f(\mathbf{r},\ \mathbf{v}, t)$ describe a specific particle's probability of being located in a differential volume at the position $\mathbf{r}$ with a velocity $\mathbf{v}$ at a given point in time t.

The velocity distribution of an ensemble with a density n and a particle mass m gives the probability for one particle in the ensemble having a velocity in the range between $\mathbf{v}$ and $\mathbf{v} + \mathrm{d}\mathbf{v}$. Under thermodynamic equilibrium conditions, it follows the isotropic *Maxwell-Boltzmann distribution*

$$f_{\mathrm{M}}(v) = \left(\frac{m}{2\pi k_{\mathrm{B}} T}\right)^{3/2} 4\pi v^2 \exp\left(-\frac{m v^2}{2 k_{\mathrm{B}} T}\right) \tag{2.3}$$

with the characteristic thermodynamic temperature T and the normalization

$$\int_0^\infty f_{\mathrm{M}}(\mathbf{r}, v, t)\mathrm{d}v = 1. \tag{2.4}$$

Equation (2.3) can be transformed into the energy distribution

$$f_{\mathrm{M}}(E) = \frac{2}{\sqrt{\pi}}\left(\frac{1}{k_{\mathrm{B}} T}\right)^{3/2} E^{1/2} \exp\left(-\frac{E}{k_{\mathrm{B}} T}\right) \tag{2.5}$$

with the kinetic energy being in the range E and $E + \mathrm{d}E$. The mean velocity

$$< v >= \int_0^\infty v f_{\mathrm{M}}(v)\ \mathrm{d}v = \left(\frac{8 k_{\mathrm{B}} T}{\pi m}\right)^{1/2} \tag{2.6}$$

and the mean particle energy

$$< E >= \int_0^\infty E f_{\mathrm{M}}(E)\ \mathrm{d}E = \frac{3}{2} k_{\mathrm{B}} T \tag{2.7}$$

can be derived.

Plasma generation is commonly achieved via electric or electromagnetic fields transferring the external power predominantly to the electrons. They distribute their kinetic energy among each other via electron-electron collisions. Under the assumption of a sufficiently high collision frequency, a thermalized electron ensemble evolves. Its *electron energy distribution function* (EEDF) $f(E_{\mathrm{e}})$ follows

a Maxwell-Boltzmann distribution according to equation (2.5) with the electron temperature $T = T_e$ and the electron energy E_e. Nevertheless, one has to be aware that deviations from a Maxwellian distribution function can occur depending on the present energy exchange processes (e.g. excitation or ionization of heavy particles induced by electron impact or particular heating processes). Other possible distribution types for example are a *Bi-Maxwellian* or a *Druyvensteyn* distribution [GPA93].
The *electron energy probability function* (EEPF) $g(E_e)$ is defined as

$$g(E_e) = E_e^{-1/2} \cdot f(E_e). \tag{2.8}$$

The electron ensemble passes the energy to the neutrals and ions via elastic collisions. The difference in mass and the small collision probability at low pressure lead to an inefficient heating mechanism of the heavy particles and prevent a thermalization between the electrons and the neutral particles and ions. As a consequence, the three particle ensembles might be characterized by the electron temperature T_e and the temperatures $T_{neutral}$ and T_{ion} of the neutral particle and the ion ensemble, respectively. In low pressure plasmas, T_e is typically much higher than the temperatures of the ions and the neutrals with $T_{ion} \approx T_{neutral} = T_{gas}$. In the present work, the gas temperature T_{gas} is in the range of 0.04 - 0.13 eV ($\approx 500 - 1500\,\mathrm{K}$) while the typical electron temperature is in the order of several eV.

Plasma sheath

Due to necessary vacuum conditions, low pressure discharges are contained in plasma vessels. The interaction of the plasma with the walls is inevitable and forms a boundary layer between the bulk plasma and the surface. For a plasma which is on a certain *plasma potential* V_{pl} and which has a negligible portion of negative ions in vicinity of an insulated object, the flux of electrons leaving the plasma can be expressed via $\Gamma_e = n_e v_e$ with the electron density n_e and the electrons' velocity v_e. It exceeds the positive ion flux $\Gamma_{ion} = n_{ion}^+ v_{ion}$ characterized by the positive ion density n_{ion}^+ and the ions' velocity v_{ion}. As a result, the surface is charging negatively and evolves a potential difference with respect to the bulk plasma. Therefore, electrons are decelerated and positive ions are attracted towards the object such that $\Gamma_e = \Gamma_{ion}$ is valid. The creation of the so-called *plasma sheath* region is driven by the quasi-neutrality of the plasma which stays valid for the bulk plasma. Since the electrons are repelled, the electron density

decreases more rapidly towards the surface than the ion density within the sheath. This can be seen in the lower part of figure 2.1. In steady-state condition ($\Gamma_e = \Gamma_{ion}$) the potential of the surface has reached the *floating potential* V_{fl} with $V_{fl} < V_{pl}$. This situation is presented in the upper part of figure 2.1.

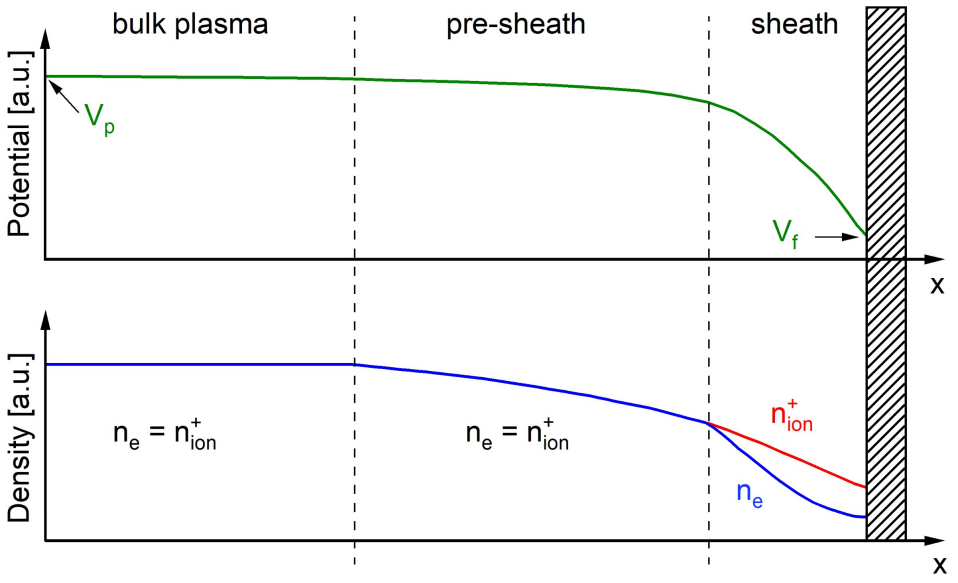

Figure 2.1: Schematic spatial profiles of the electrostatic potential, the positive ion density n_{ion}^{+} and electron density n_e for a plasma in contact with an insulated surface [LL05].

Neglecting collisional processes within the sheath region, the continuity of the positive ion flux and the ion energy conservation lead to the *Bohm criterion* [CB11]

$$v_{ion} \geq v_B := \sqrt{\frac{k_B T_e}{m_{ion}}} \tag{2.9}$$

for the ion speed v_{ion}. Accordingly, positive ions entering the plasma sheath must have a directed velocity greater than the *Bohm velocity* v_B in order to maintain the flux continuity across the sheath. On their way from the bulk to the surface, ions gain this necessary speed due to a small electric field in the quasi-neutral *pre-sheath*. Following [LL05], the typical dimension of the sheath region is below one mm in the plasmas investigated during this work.

2.2 Atomic and molecular energy levels

2.2.1 Atoms

General aspects given in the following overview are mainly taken from [Dem16, TLJ99]. Atoms exhibit discrete energy levels. The corresponding wave function of an electron in an atomic level is unambiguously characterized by the four quantum numbers n, l, m_l and m_s. While the main quantum number $n \in \mathbb{N}$ basically determines the energy of the atomic state, the orbital angular momentum number $l \leq n-1$ gives information about the spatial probability density — also referred to as *orbital* — of the electron. The projection m_l (with $-l \leq m_l \leq +l$) of the orbital angular momentum onto an arbitrary quantizing axis describes the annulment of the energy level's degeneracy within an external magnetic field. An electronic spin with quantum number $s = 1/2$ is associated with the electron and its analogous projection is referred to as $m_s = \pm 1/2$. The spin linked to the nucleus is not further considered.

Hydrogen with one electron in the atomic shell is the simplest representative of atoms. The electronic energy of the atomic hydrogen state n calculates with

$$E_n = \frac{m_\mathrm{e} e^4}{8\epsilon_0^2 h^2} \cdot \left(1 - \frac{1}{n^2}\right) \tag{2.10}$$

$$:= R_\mathrm{y} \cdot \left(1 - \frac{1}{n^2}\right) = 13.6\,\mathrm{eV} \cdot \left(1 - \frac{1}{n^2}\right) \tag{2.11}$$

including the electron mass m_e, the elementary charge e, the permittivity of free space ϵ_0, the Planck's constant h and the Rydberg constant R_y.

Apart from the one-electron system hydrogen, in the atomic shell of atoms several electrons are present with the individual orbital angular momenta $\boldsymbol{l}_i$ and electronic spins $\boldsymbol{s}_i$. Different coupling cases of the angular momenta occur such as *LS coupling, jj coupling* and *jl coupling.*

LS coupling

The case of *LS coupling* usually applies for light atoms with a low nuclear charge and describes the situation that both the coupling between the $\boldsymbol{l}_i$ as well as between the $\boldsymbol{s}_i$ of all electrons exceeds the interaction between orbital movement and spin for one individual electron. The resulting total orbital angular momentum $\boldsymbol{L}$ and electronic spin $\boldsymbol{S}$ together with the quantum numbers L and S are

defined as

$$\boldsymbol{L} = \sum_i \boldsymbol{l}_i \quad \text{with} \quad |\boldsymbol{L}| = \sqrt{L(L+1)}\hbar \quad \text{and} \tag{2.12}$$

$$\boldsymbol{S} = \sum_i \boldsymbol{s}_i \quad \text{with} \quad |\boldsymbol{S}| = \sqrt{S(S+1)}\hbar \tag{2.13}$$

with $\hbar = \frac{h}{2\pi}$. Further coupling of $\boldsymbol{L}$ with $\boldsymbol{S}$ leads to the total angular momentum $\boldsymbol{J}$ of the electronic shell:

$$\boldsymbol{J} = \boldsymbol{L} + \boldsymbol{S} \quad \text{with} \quad |\mathbf{J}| = \sqrt{J(J+1)}\hbar. \tag{2.14}$$

According to the principles of quantum mechanical angular momentum addition, the corresponding quantum number J takes the values $|L-S|, \ldots, |L+S|$. In this case, the degeneracy of an electronic level is given by

$$g_J = (2L+1) \cdot (2S+1). \tag{2.15}$$

The resulting energetic splitting according to J is referred to as *fine structure*. The spectroscopic notation of a state in the LS coupling case is

$$n^{2S+1}Z_J \tag{2.16}$$

and includes the main quantum number n of the state, the multiplicity $2S+1$ and the quantum number J and the capital latin letter $Z = S, P, D, \ldots$ corresponding to the quantum numbers $L = 0, 1, 2, \ldots$. The multiplicity allows the classification of atomic states to different spin systems. For example, atomic states with $2S+1 = 1$ belong to the *singlet system* while $2S+1 = 2$ refers to the *doublet system* and levels with $2S+1 = 3$ are called *triplet*. Based on quantum mechanical principles, the selection rules

$$\Delta L = 0, \pm 1 \quad \text{with} \quad L = 0 \nrightarrow L = 0, \tag{2.17}$$

$$\Delta S = 0, \quad \text{and} \tag{2.18}$$

$$\Delta J = 0, \pm 1 \quad \text{with} \quad J = 0 \nrightarrow J = 0 \tag{2.19}$$

apply for dipole transitions between two atomic levels (i.e. emission or absorption of a photon). For so-called *metastable states*, dipole transitions to energetic lower states (e.g. the ground state) are forbidden due to the quantum mechanical

selections rules. Such metastables occur in atoms as well as in molecules and are characterized by 'long' lifetimes. Therefore, transport mechanisms play an important role.
Energy schemes and corresponding prominent emission lines are examplarily shown for atomic hydrogen in figure 2.4 (b) and in the appendix for atomic nitrogen and oxygen (see figures A.2 and A.1).

jj coupling

The *jj coupling* case commonly occurs in heavy atoms (e.g. lead) where the coupling between the individual angular momenta and spins of the single electrons, $\boldsymbol{l}_i$ and $\boldsymbol{s}_i$, is stronger than among the momenta and among the spins. In this case, the total angular momentum of *one* electron is given by $\boldsymbol{j_i} = \boldsymbol{l_i} + \boldsymbol{s_i}$ and the total angular momentum of the shell results to

$$\boldsymbol{J} = \sum_i \boldsymbol{j_i} \quad \text{with} \quad |\boldsymbol{J}| = \sqrt{J(J+1)}\hbar. \tag{2.20}$$

$\boldsymbol{L}$ and $\boldsymbol{S}$ are no longer defined. According to [TLJ99] the notation

$$(j_1, j_2)_J \tag{2.21}$$

applies with the total angular momentum J of the shell. The quantum numbers j_1 and j_2 refer to the angular momentum of one electron or of a certain group of levels [MW02].

jl coupling in argon

The so-called *jl coupling* will be presented exemplarily in the following for argon based on [KD80]. The ground state is characterized by six electrons located in the $3p$ orbital. If one electron is excited (into a level with higher main quantum number n), the remaining five electrons and the excited electron are first considered independently. For the former, LS coupling applies leading to the total angular momentum $\boldsymbol{j_{\mathrm{core}}}$. The two possible configurations ${}^2P_{1/2}$ and ${}^2P_{3/2}$ result. Subsequently, $\boldsymbol{j_{\mathrm{core}}}$ couples with the orbital angular momentum $\boldsymbol{l}$ of the excited electron to

$$\boldsymbol{K} = \boldsymbol{j_{\mathrm{core}}} + \boldsymbol{l}. \tag{2.22}$$

The corresponding quantum number K takes the values $|K - l|, \ldots, |K + l|$.

Finally, the total angular momentum

$$\boldsymbol{J} = \boldsymbol{K} + \boldsymbol{s} \tag{2.23}$$

results from the interaction of $\boldsymbol{K}$ and the spin vector $\boldsymbol{s}$ of the excited electron. The corresponding quantum number is given by

$$J = K \pm \frac{1}{2} \tag{2.24}$$

with the spin quantum number $s = 1/2$ of the excited electron. An example of the spectroscopic notation for the jl coupling case, which is proposed in [Rac42], is given in the following for $j_{\text{core}} = 1/2$:

$$(^2P_{1/2})nl[K]_J. \tag{2.25}$$

It includes the term of the core in round brackets, the quantum numbers n and l of the excited electron, the quantum number K in square brackets and the quantum number J of the total angular momentum as index. An energy term scheme of argon for the ground state and several excited states is shown in figure 2.2. The resonant states are $^2P^{\text{o}}_{3/2}4s[3/2]_1$ and $^2P^{\text{o}}_{1/2}4s[1/2]_1$ which correspond to the states $1s_4$ and $1s_2$, respectively, in Paschen's notation. Metastable states are $^2P^{\text{o}}_{3/2}4s[3/2]_2$ and $^2P^{\text{o}}_{1/2}4s[1/2]_0$ which are $1s_5$ and $1s_3$ in Paschen's notation.

2.2.2 Molecules

Molecules consist of at least two atoms and have shared electrons in the shell. The following overview is mainly based on [Dem16, TLJ99, Ber02] and focuses on diatomic molecules such as hydrogen, nitrogen and oxygen which are investigated in the present work. Due to the vibration along and the rotation perpendicular to the internuclear axis, the molecular energy structure is much more complex than it is for atoms. In general, the total energy of a molecular state is denoted with G and is composed by the contributions from electronic excitation G_{e} corresponding to the minimum of the potential curve, the vibrational motion G_{vib} and the rotational G_{rot}, respectively. It follows

$$G = G_{\text{e}} + G_{\text{vib}} + G_{\text{rot}}. \tag{2.26}$$

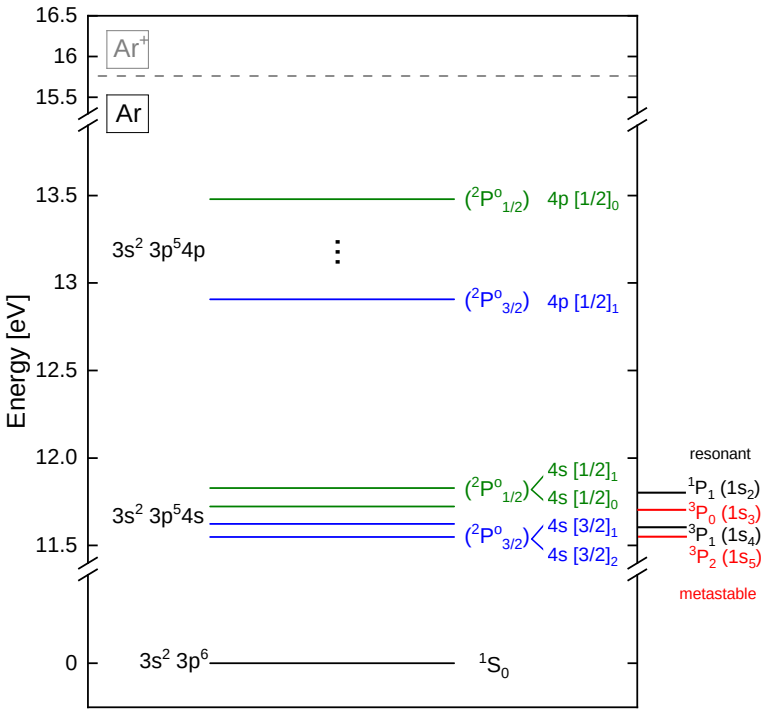

Figure 2.2: Energy diagram of the argon atom including ground state and first excited states [KYRa19a]. The Racah notation is used for the excited states and the ionization energy of 15.57 eV is taken from [VHU99]. Prominent metastable and resonant states are indicated in red and black, respectively, taken from [MMS12].

Due to the mass difference, the vibration and rotation of the nuclei are much slower than the electrons' motion. Therefore, the movement of the nuclei and the electrons can be considered separately following the so-called *Born-Oppenheimer approximation*. The wave function

$$\Psi(R_1, R_2, \{r_i\}) = \Psi_{\text{elec}}(R_1, R_2, \{r_i\})\chi_{\text{nuc}}(R_1, R_2) \tag{2.27}$$

of a diatomic molecule is the product of the electronic wave function Ψ_{elec} corresponding to the electrons and the wave function χ_{nuc} describing the vibrational and rotational motion of the nuclei. The latter solely depends on the spatial coordinates R_1 and R_2 of the atoms while the former additionally depends on the positions $\{r_i\}$ of the i electrons.

Following a separation approach, it is possible to split the wave function χ_{nuc} of the nuclear motion into a vibrational and a rotational part which can be considered individually.

Electronic states

The electronic *Schrödinger equation* gives the energy eigenvalues $E_n(R)$ which depend on the internuclear distance R including the potential energy and temporally averaged kinetic energy of the electrons. $E_n(R)$ are referred to as *potential curves* and indicate the potential in which the ro-vibrational motion of the molecule occurs. The potential curve of a stable state is characterized by a minimum whose corresponding energy is denoted with G_e while dissociative states are characterized by a minimum for $R \to \infty$. In accordance to atoms, the electronic states of molecules depend on the orbital angular momenta and the spins of the electrons. The individual $\boldsymbol{l}_i$ and $\boldsymbol{s}_i$ of the electrons couple to the total momenta of the electron shell $\boldsymbol{L} = \sum_i \boldsymbol{l}_i$ and $\boldsymbol{S} = \sum_i \boldsymbol{s}_i$ with $|\boldsymbol{S}| = \sqrt{S(S+1)}\hbar$. The projection of $\boldsymbol{L}$ onto the internuclear axis (which is arbitrarily denoted as z axis in the following) is quantized by the quantum number Λ with $|L_z| = \Lambda\hbar$. In this case, a molecular state can be specified in the spectroscopic notation

$$Z\ {}^{2S+1}\Lambda_{\mathrm{u/g}}^{(+/-)} \tag{2.28}$$

which is similar to the one for atoms. Analogously, the multiplicity $2S+1$ is stated while the quantum number Λ is denoted with the greek letters $\Sigma, \Pi, \Delta, \ldots$ for $\Lambda = 0, 1, 2, \ldots$. The capital letter Z gives the name of the electronic state with $Z = X$ indicating the ground state. Information about symmetry properties of the corresponding wave function can be added. In the case of a symmetry with respect to the center of the nuclear axis, the wave function is denoted with the German expressions *gerade* (g) which means even, otherwise *ungerade* (u) meaning odd. This characterization exclusively applies for homonuclear molecules. For all molecular states with $\Lambda = 0$, i.e. a Σ state, a classification based on the symmetry under a reflection on a plane containing the molecular axis leads to *symmetric* (+) or *antisymmetric* (-) wave functions. Furthermore, states with $\Lambda > 0$ exhibit a twofold degeneracy which is revoked by an interaction between the total electronic angular momenta and the rotation of the nuclei. This effect leads to the so-called Λ doubling which results in a splitting of the corresponding energy level according to $\pm\Lambda$ [Kov69].

In general, depending on the interaction strength of the electronic momenta $\boldsymbol{L}$ and $\boldsymbol{S}$ among each other and with the molecular axis and the molecular rotation, respectively, several different coupling schemes can be identified [NZ94] which are classified as *Hund's coupling cases a - e*. The following description is restricted

to *case a* and based on [Kov69] which is also recommended for further details on the variety of Hund's cases. A corresponding schematic is presented in figure 2.3. In *case a*, $\boldsymbol{L}$ is not conserved due to the strong coupling of the orbital angular momentum to the molecular axis, and is replaced by its projection $\boldsymbol{\Lambda}$ onto the axis. Resulting from the interaction between orbital angular momentum and electron spin, the vector $\boldsymbol{S}$ is in precission around the nuclear axis with a projection $\boldsymbol{\Sigma}$ onto the z axis. The quantum numbers of the components parallel to the internuclear axis are Λ and $\Sigma = -S, \ldots, S$. The resulting angular momentum of spin-orbital coupling is $\boldsymbol{\Omega} = \boldsymbol{\Lambda} + \boldsymbol{\Sigma}$ with the quantum number $\Omega = \Lambda + \Sigma$. $\boldsymbol{\Omega}$ and the vector $\boldsymbol{R}$ assigned to the molecular rotation form the total angular momentum $\boldsymbol{J} = \boldsymbol{\Omega} + \boldsymbol{R}$ of the molecule with $J = |\Omega|, |\Omega| + 1, \ldots$ being the corresponding quantum number. Sometimes, Ω is added in the spectroscopic notation (2.28) as index.

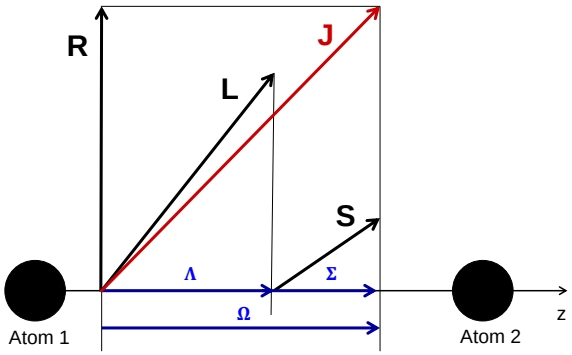

Figure 2.3: Coupling of the angular momenta in a diatomic molecule according to *Hund's case a* following [Kov69]. The orbital angular momentum $\boldsymbol{L}$ and the spin vector $\boldsymbol{S}$ of the electrons are coupled to the internuclear axis z. Their projections on this axis, $\boldsymbol{\Lambda}$ and $\boldsymbol{\Sigma}$, form the vector $\boldsymbol{\Omega}$ which couples with the angular momentum $\boldsymbol{R}$ of the molecular rotation resulting in the total angular momentum $\boldsymbol{J}$.

Vibrational levels

The vibration of a molecule's nuclei is significantly determined by the potential curves of the electronic states which are commonly approximated by a *Morse potential*. In this case, the vibrational Schrödinger equation provides discrete vibrational levels with quantum number $v \in \mathbb{N}_0$ and the corresponding energy

$$G_{\mathrm{vib}}(v) = \omega_{\mathrm{e}}\left(v + \frac{1}{2}\right) - \omega_{\mathrm{e}}x_{\mathrm{e}}\left(v + \frac{1}{2}\right)^2 \pm \ldots. \tag{2.29}$$

It is given in units of [cm^{-1}] whereas ω_e is the *vibrational constant* and x_e denotes the *anharmonicity constant*. Characteristic properties of the molecular vibration are the finite *zero-point energy* for $v = 0$ and a decreasing but finite distance between the vibrational levels with rising quantum number v. The number of vibrational levels in an electronic state is finite.

Rotational levels

Including the *centrifugal distortion* of the internuclear distance due to the molecular rotation, the energy of a rotational level with quantum number J is given by

$$G_\mathrm{rot}(v, J) = B_\mathrm{v} J(J+1) - D_\mathrm{v} J^2 (J+1)^2 \pm .... \tag{2.30}$$

The possible values of J are characterized by the specific electronic state. The *rotational constant* B_v and the *centrifugal distortion constant* D_v are dependent on the electronic and vibrational state and can be calculated with

$$B_\mathrm{v} = B_\mathrm{e} - \alpha_\mathrm{e}\left(v + \frac{1}{2}\right) \pm ..., \tag{2.31}$$

$$D_\mathrm{v} = D_\mathrm{e} + \beta_\mathrm{e}\left(v + \frac{1}{2}\right) \pm .... \tag{2.32}$$

The corresponding constants $\omega_\mathrm{e}, \omega_\mathrm{e}x_\mathrm{e}, B_\mathrm{e}$, D_e, α_e and β_e for diatomic molecules are summarized in [HH18].

Selection rules

Similar to atoms, a dipole transition between *different* molecular electronic states A' and A'' with (ν', J') and (ν'', J''), respectively, is subject to the following quantum mechanical selection rules [TLJ99]:

$$\Delta\nu = 0, \pm 1, \pm 2, \ldots, \tag{2.33}$$

$$\Delta\Lambda = 0, \pm 1, \tag{2.34}$$

$$\Delta S = 0 \quad \text{and} \tag{2.35}$$

$$\Delta J = 0, \pm 1 \quad \text{with} \qquad J = 0 \nrightarrow J = 0. \tag{2.36}$$

The upper state is denoted by a single prime ($'$), the lower state by the double prime ($''$). For states with $\Lambda = 0$, only the transitions $\Sigma^- \rightarrow \Sigma^-$ or $\Sigma^+ \rightarrow \Sigma^+$ are allowed. For homonuclear molecules, the further restriction u $\longleftrightarrow$ g ap-

plies. Equation (2.36) classifies the *rotational P-, Q-, R-branches* according to $\Delta J = J' - J'' = -1, 0, +1$. Rotational transitions assigned to a specific Δv are summarized to a *vibrational band*.

In the presented work, only the homonuclear molecular gases hydrogen, nitrogen and oxygen are investigated. In these cases, ro-vibrational transitions $A(v', J') \rightarrow A(v'', J'')$ within the *same* electronic state A are not allowed and, therefore, are not further discussed.

In figure 2.4 (a) the potential curves of several electronic states of molecular hydrogen are exemplarily depicted [Sha70, Sha71]. For the ground state also vibrational levels are indicated [FW06], rotational levels are neglected for the sake of clarity. Further energy diagrams for molecular nitrogen and oxygen are given in the figures B.1 and B.2 in the appendix. Typical energy distances between electronic states are in the range of several eV. For vibrational levels, the distance is around or below 0.5 eV while the energy gap between rotational states is in the order of few 10^{-3} eV [FK11].

2.3 Plasma processes

Due to the great variety of plasma particles (e.g. atomic and molecular neutrals, positive and negative ions, electrons) a big number of processes can occur between the individual species, e.g. particle collisions, photon emission and absorption. Due to the high electron temperature compared to the gas temperature in low pressure plasmas, electronic excitation processes of heavy particles predominantly take place via collisions with electrons. Therefore, in the following overview first a series of important electron-induced processes are highlighted. Subsequently, a selection of processes including photons will be discussed because they also contribute to the population density of atomic and molecular states. Since the plasma is contained in a vessel, the section will be completed with a short review of loss mechanisms to the walls which are important regarding positive ions and metastable states of neutrals.

For a more comprehensive description of plasma processes, the reader is referred to [FK11].

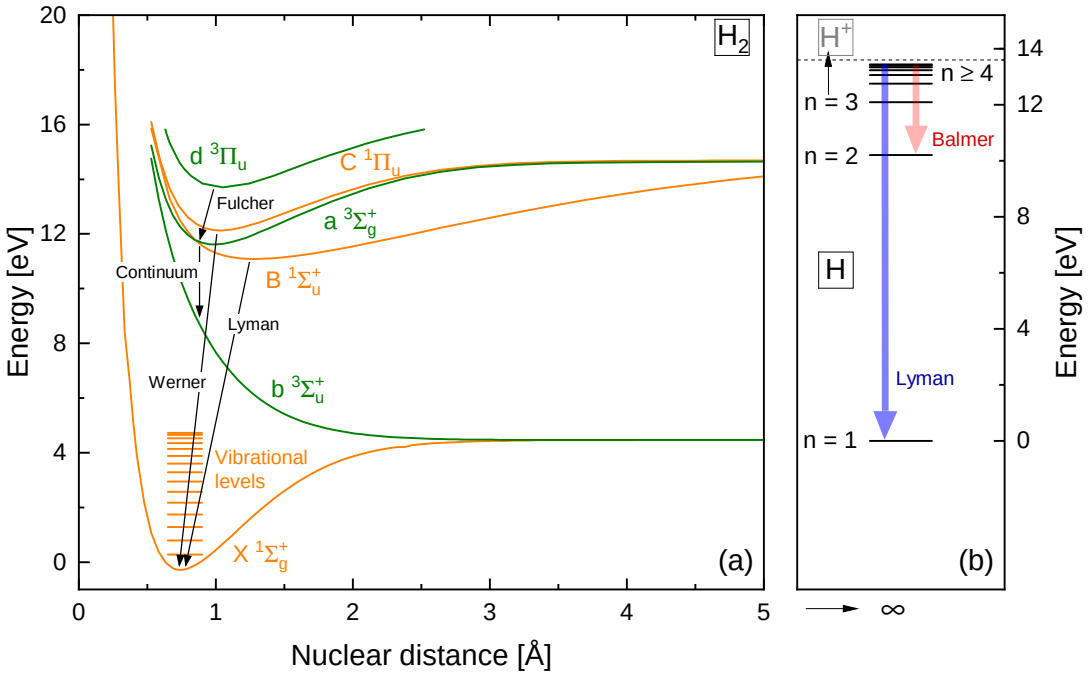

Figure 2.4: (a) Potential energy curves of several molecular hydrogen states [Sha70, Sha71] in the singlet (orange) and triplet system (green) with the vibrational levels indicated for the ground state [FW06]. (b) Atomic energy levels of hydrogen for the main quantum number n. The shift of the right energy axis gives an impression about the correlation between the molecule and its dissociation products. For the molecule as well as for the atom the most important emission characteristics are indicated.

2.3.1 Electron impact processes

Electron impact excitation

Excitation of an electronic state of a heavy particle A occurs following the scheme:

$$A(k) + e \longleftrightarrow A(i) + e. \tag{2.37}$$

The transfer of kinetic energy from the electron e to the heavy particle A in the initial state k leads to an excitation into the final state i and a deceleration of the electron. The initial state of the heavy particle can be the ground state or another energy level with $k < i$, e.g. metastable states. During this transition, the vibrational population of the initial molecular state is not necessarily conserved. However, the *Franck-Condon Principle* allows a description of how the population of the initial state is 'mapped' into the excited state. It is based on the fact that

the electronic transition is considerably faster than the molecular vibration cycle [FK11, TLJ99]. Therefore, electronic excitation occurs at a constant distance R of the nuclei in the diatomic molecule. The overlap integral [TLJ99]

$$q_{ik}^{v'v''} = \left| \int \Psi_i^{v'*}(R)\Psi_k^{v''}(R)\mathrm{d}R \right|^2 \tag{2.38}$$

between the wavefunctions $\Psi_i^{v'*}(R)$ of the vibrational level v' in the upper electronic state i and $\Psi_k^{v''}(R)$ of the vibrational level v'' in the lower electronic level k is referred to as *Franck-Condon factor*. It characterizes the probability that the electronic transition $k \rightarrow i$ is simultaneously accompanied by a vibrational transition $v'' \rightarrow v'$ and spans values between 0 and 1. Following the Franck-Condon factors the vibrational population of the ground state is 'mapped' into the excited state as Δv might be different in the excited state.

Excitation of rotational levels in electronically excited states also predominantly occur via electron impact. In the ground state, T_{rot} often equals the gas temperature T_{gas} since the rotational distribution is determined by heavy particle collisions. The cross sections for transitions between two rotational levels with quantum numbers J and $J + \Delta J$ belonging to two different electronic states steeply decrease with growing ΔJ [LOU79]. Therefore, the rotational number is either preserved or affected only slightly.

Electron impact ionization

The most important generation channel of positive ions in low pressure plasmas is given by electron impact ionization of a heavy particle A according to

$$A(k) + e \longleftrightarrow A^+(i) + 2e. \tag{2.39}$$

The kinetic energy transferred from a fast electron to the neutral particle exceeds the difference of the ionization threshold and the initial energy level of k. During this process the corresponding ion A^+ in the electronic state i as well as an additional electron are produced while the primary electron slows down. The inverse process of *three-body recombination* requires a concurrent collision of three particles and happen only at high electron densities in the plasma volume. Therefore, the dominant loss pathway of positive ions is via diffusion to the vessel walls which will be discussed in detail below.

Electron impact dissociation

Regarding molecules, electron impact might also induce the dissociation

$$AB(k) + e \longleftrightarrow A(i) + B(j) + e \tag{2.40}$$

of the molecule AB (in initial electronic state k) into the products A and B with the electron losing kinetic energy. The electronic states i and j of the fragments A and B can be the ground state as well as excited states. Besides this 'normal' dissociation, a multitude of further complex dissociation processes with simultaneous ionization, recombination or electron attachment are possible [LL05]. Nevertheless, recombination of atoms can occur via catalytic surface reactions at the vessel walls.

The presented electron-impact processes are inelastic 'using' a portion of the total kinetic energy for excitation, ionization or dissociation of the participating heavy particles. Since a certain amount of energy is required to overcome the corresponding energy potential differences between initial and final state, the shown reactions exhibit a threshold energy. The electron energy must exceed this crucial limit to induce the reaction. Besides, also elastic collisions between electrons and heavy particles occur conserving the total kinetic energy of the system. These scattering processes have no threshold energy. Hence, they are the dominant collisional process in low pressure plasmas and determine the mean free path of particles within the plasma volume.

2.3.2 Processes including photons

In general, the basic reactions including photons are *spontanous emission*, *induced emission* and *absorption* during dipole transitions of atoms and molecules.

Spontaneous emission and absorption

The dominant de-excitation channel of electronically excited levels in low pressure plasmas is represented by the spontaneous emission of a photon:

$$A(i) \longrightarrow A(k) + h\nu \tag{2.41}$$

with $i > k$. The energy of the emitted photon corresponds to the energy difference of the participating states i and k with $E_{\mathrm{ph}} = h\nu = E(i) - E(k)$, where ν is the frequency of the emitted photon and h denotes Planck's constant. The *emissivity* ϵ_{ik} of the transition gives the number of photons emitted per volume and second,

$$\epsilon_{ik} = n_i A_{ik}, \tag{2.42}$$

and depends on the population density n_i of the upper state and the *Einstein coefficient for spontaneous emission* A_{ik}. According to equation (2.42), measuring the emissivity of a transition allows access to the population density n_i of the corresponding upper state and provides the basic principle for emission spectroscopy. The reverse process — absorption — leads to excitation or ionization of the particle depending on the photon energy.

Reabsorption and radiation trapping

An emitted photon can be absorbed on its way through the plasma volume with a certain probability by another atom or molecule in the plasma. The iteration of photon emission and absorption within the plasma is called *radiation trapping* [Fuj04]. If this process prevents a significant portion of photons from leaving the discharge volume, the corresponding radiative transition is named *optically thick* or *opaque*. Only a reduced emissivity can be measured outside the plasma volume which has to be considered regarding the application of emission spectroscopy to optically thick transitions. Solving the *equation of radiative transfer*,

$$\frac{\mathrm{d}L_{ik}}{\mathrm{d}l} = \epsilon - \alpha L_{ik}, \tag{2.43}$$

gives information about the radiance L_{ik} of an emission line along a line of sight l. L_{ik} is given in units of $\mathrm{W}/(\mathrm{m}^2\ \mathrm{sr})$ while ϵ denotes the spectral emission coefficient $[\mathrm{W}/(\mathrm{m}^3\ \mathrm{sr\ nm})]$ and α is the spectral absorption coefficient $[\mathrm{nm}^{-1}]$. Generally, $L_{ik}(l)$ is dependent on the wavelength and the Einstein coefficient of the transition, the population densities and the statistical weights of the participating states as well as on the emission and absorption line profiles. The line profile can be affected by several mechanisms, e.g. natural broadening, Doppler broadening or pressure broadening [TLJ99, HL65]. For a detailed description of the radiative transfer equation and its solution, it is referred to [Beh98, TLJ99, Bri11].

Reabsorption effects can be considered via so-called *escape factors* Θ $(0 \leq \Theta \leq 1)$ [Hol51, Iro79] which allow to count absorption in the form of negative emission.

In this way, the Einstein coefficient of opaque transitions reduces to an effective value of $A_{ik}\Theta$ [s^{-1}]. The calculation of Θ has to be performed individually for the specific application [Beh98].
In order to treat opacity for emission spectroscopy measurements *line escape factors* Θ_{line} are deduced which describe the ratio of the radiation leaving the plasma along the line of sight of the spectrometer in the optically thick case. The density of the upper state i, which is obtained from an emission line following equation (2.42), can be then corrected to

$$n_i = \frac{\epsilon_{ik}}{A_{ik}\Theta_{\text{line}}}. \tag{2.44}$$

Depending on the specific transition, reabsorption effects can significantly contribute to the population density of the upper states and, therefore, have to be included as additional population process in population models (see section 2.4.3).

2.3.3 Heavy particle processes

2.3.3.1 Excitation of vibrational and rotational states in the ground state

Since the vibrational levels in molecules are much closer compared to the individual electronic states, already the kinetic energy of a heavy particle suffices to induce a vibrational excitation. Apart from electron impact excitation, hence, the vibrational population in the ground state X of a molecule A can be determined by collisions with other heavy particles B:

$$A(X, v'') + B \longleftrightarrow A(X, v') + B \tag{2.45}$$

with the vibrational quantum numbers v' and v'' ($v'' < v'$).
Being in the range of few 10^{-3} eV [FK11], the spacing between sequent rotational levels is much smaller than for vibrational levels. For this reason, the low kinetic energy of a heavy particle C can dominate the rotational excitation in a vibrational level v of the molecular ground state X via

$$A(X, v, J'') + C \longleftrightarrow A(X, v, J') + C. \tag{2.46}$$

J' and J'' denote the corresponding rotational quantum numbers with $J'' < J'$. In comparison, inelastic collisions with electrons play a minor role due to the

higher density of heavy particles [Bri11].
Even if the nascent rotational distribution of the ground state is non-Boltzmann, the long lifetime of the ground state allows enough collisions with gas particles for a thermalization. As a consequence, in the majority of the cases, the rotational population in the ground state follows a Boltzmann distribution [BSSL14]. A rotational temperature T_{rot} which is equal to the gas temperature can be assigned. Unless they belong to metastable states, depopulation of rotational levels mainly takes place via spontaneous emission with applying the selection rules (2.34) - (2.36).

2.3.3.2 Diffusion to the vessel walls

In general, diffusion processes occur as a result of density gradients due to local particle generation or sink mechansims. In the case of charged particles, they result from electric fields. The following short summary of the corresponding diffusion processes is limited to the case without external magnetic or electric fields and is mainly based on [Möl93]. As already briefly mentioned above, neutrals, e.g. in metastable states, and ions are not entirely confined within the plasma. The main loss channel is given by diffusion to and subsequent recombination at the vessel walls.
The *confinement time* τ describes the effective time that a particle remains within the plasma volume before it is lost at the vessel wall. In contrast, the lifetime of an excited state is given by the mean time until de-excitation of the state occurs. Diffusion becomes a relevant de-population process for excited states of heavy particles if the corresponding lifetimes are comparable to the individual confinement times. The *mean free path* $\lambda_{\mathrm{mean},i}$ of the diffusing particle species i represents the mean travel distance between two collisions with a particle of the background gas. It depends on the gas pressure and temperature as well as on the kinetic energy of the diffusing particle. Together with the dimensions of the vessel, it allows a classification of the different diffusion regimes:
The *laminar diffusion* regime is present at high pressure when the mean free path is smaller than the effective vessel dimension. The motion of a particle is characterized by a series of collisions with the background gas until it finally reaches the vessel wall. In contrast at low pressure, where the mean free path exceeds the effective vessel dimension, *molecular* or *free fall diffusion* occurs. A nascent particle does not undergo any collision with the background gas before colliding with the wall surface. The mean free path in the investigated discharges

in this work is determined to be in the range of several cm which is comparable to the plasma vessel's dimensions (see section 3.1). Therefore, the discharges are located in the transition region between molecular and laminar diffusion. Expressions of the confinement time for both regimes, τ_{mol} and τ_{lam}, are stated in the following for neutrals and ions. The total resulting confinement time τ is estimated by the sum $\tau = \tau_{\mathrm{mol}} + \tau_{\mathrm{lam}}$.

Neutral particle diffusion

In the molecular or so-called 'free' fall regime the mean free path, the confinement time τ_{mol} of a neutral particle (e.g. in the ground state or a metastable state) with mass m,

$$\tau_{\mathrm{mol}} = \frac{\Lambda_{\mathrm{mol}}}{< v >}, \tag{2.47}$$

depends on its thermal speed $< v >$ according to equation (2.6) and its average distance Λ_{mol} from the walls. Assuming a Maxwellian ensemble of particles, the former is characterized by the corresponding temperature which is assumed to be equal to the gas temperature T_{gas}. The expression of Λ_{mol} is dependent, amongst others, on the vessel geometry and can be found in [Cha87].

In contrast, if the mean free path is small in comparison with the effective vessel's dimension laminar diffusion of the neutrals through a background gas with a particle mass of m_0 occurs. In this case, the confinement time τ_{lam} is determined by a *mean diffusion length* Λ_{lam} and the *normal diffusion coefficient* D_n:

$$\tau_{\mathrm{lam}} = \frac{\Lambda_{\mathrm{lam}}^2}{D_n} \quad \text{with} \quad D_n = \frac{3\sqrt{\pi}}{8}\lambda_{\mathrm{mean}}\sqrt{k_{\mathrm{B}}T_{\mathrm{gas}}\frac{m+m_0}{2mm_0}}. \tag{2.48}$$

Equal temperatures for the diffusing and background particles corresponding to the gas temperature are assumed. Analogously to the molecular diffusion case, Λ_{lam} includes the vessel geometry as well as the adsorption properties of the wall surface and is given in [Möl93].

Ion diffusion

As discussed in section 2.1 the quasi-neutrality of the plasma evokes an electric field that repells the electrons and simultaneously attracts the ions towards the vessel walls. This effect leads to an ambipolar diffusion of the electrons and positive ions. According to [TL29], the following collection is based on the as-

sumption of an ion production being proportional to the spatial electron density distribution and leading to the 'free' fall confinement time of

$$\tau_{\mathrm{mol,ion}} = \frac{\Lambda_{\mathrm{mol,ion}}}{v_{\mathrm{ion}}}. \tag{2.49}$$

It is determined analogously to equation (2.47) from the velocity of the ions v_{ion} and the effective vessel dimension $\Lambda_{\mathrm{mol,ion}}$ that is given in [Möl93]. The laminar confinement time $\tau_{\mathrm{lam,ion}}$ of ions can be expressed with

$$\tau_{\mathrm{lam,ion}} = \frac{\Lambda^2_{\mathrm{lam,ion}}}{D_a} \quad \text{with} \quad D_a = \frac{3\sqrt{\pi}}{8}\lambda_{\mathrm{mean,ion}}\frac{T_{\mathrm{e}}}{T_{\mathrm{gas}}}\sqrt{\frac{k_{\mathrm{B}}T_{\mathrm{gas}}}{m_{\mathrm{ion}}}} \tag{2.50}$$

assuming $T_{\mathrm{ion}} \approx T_{\mathrm{gas}} << T_{\mathrm{e}}$. D_a is referred to as *ambipolar diffusion coefficient*. The calculation formulas for $\Lambda_{\mathrm{lam,ion}}$ depending on the plasma geometry can be again found in [Möl93].

2.4 Population models

The plasma parameters electron density n_{e}, electron temperature T_{e} as well as the ground state density strongly depend on the supply gas (mixture) and on the operating parameters, e.g. applied power and discharge pressure. They determine the population density of excited states and, therefore, the plasma emission, particularily those in the VUV range, and are of high diagnostic interest.
The following section based on [Fuj04] will give an overview about the basics of population models which are applied to derive a diagnostic access to the significant plasma parameters. Depending on the specific plasma conditions, these models can range from rather simple balances to arbitrarily complex models with regard to the resolution of energy levels, the particle species as well as to the included de-/population channels.

The simplest population model treats a system of two states 1 and 2 with the energies E_1 and E_2 ($E_2 > E_1$) in thermodynamic equilibrium. It is characterized by a temperature T and the states can represent electronic, vibrational or rotational levels. According to the *Boltzmann's distribution*, the ratio of the population

densities n_1 and n_2 of state 1 and 2, respectively, can be expressed by

$$\frac{n_2}{n_1} = \frac{g_2}{g_1} \exp\left(-\frac{E_2 - E_1}{k_\mathrm{B} T}\right). \tag{2.51}$$

The statistical weights g_1 and g_2 include the degeneracy of the corresponding states [TLJ99].
However, since low pressure discharges are usually highly non-equilibrium plasmas, the population densities do not neccessarily follow a Boltzmann distribution.

2.4.1 Rate coefficients

As presented in the previous section, a multitude of different processes are simultaneously taking place in plasma discharges and are leading to population and de-population of electronic and ro-vibrational states in atoms and molecules. Each process is linked to its probability. The Einstein coefficients A_{ik} and B_{ki} give the transition probabilities for spontaneous emission and absorption, respectively, while collision-induced processes are characterized by *cross sections* σ or *rate coefficients* X. The former represents the fundamental statistical quantity to describe the process probability and depends on the specific type of interaction as well as the relative initial speed of the collision partners. Assuming two particle ensembles, the rate coefficient X of a reaction process is defined as the convolution of the corresponding cross section σ with the particle ensembles' relative velocity v_rel and is given in units of $\mathrm{m}^{-3}\mathrm{s}^{-1}$:

$$X = < \sigma \cdot v_\mathrm{rel} > . \tag{2.52}$$

Under the assumption that the two particle ensembles follow the Maxwell-Boltzmann energy distribution f_M accordingly to equation (2.5), the rate coefficient is given by

$$X = \int_0^\infty \sigma(E_\mathrm{rel}) \sqrt{\frac{E_\mathrm{rel}}{2\mu}}\, f_\mathrm{M}(E_\mathrm{rel})\, \mathrm{d}E_\mathrm{rel} \tag{2.53}$$

with

$$E_\mathrm{rel} = \frac{1}{2}\mu v_\mathrm{rel}^2 \tag{2.54}$$

and the reduced mass μ of the participating particle species.
In the case of electron-impact processes with heavy particles, the high difference of the particle masses allows the approximations $E_{\mathrm{rel}} \approx E_{\mathrm{e}}$ and $\mu \approx m_{\mathrm{e}}$ with the electron energy E_{e} and electron mass m_{e}. In most cases, a Maxwell-Boltzmann distribution function $f_{\mathrm{M}}(E_{\mathrm{e}}, T_{\mathrm{e}})$ is applied.
The following equation exemplarily describes the population rate of the density n_p of an electronic state p via electron excitation from the ground state

$$\frac{\mathrm{d}n_p}{\mathrm{d}t} = n_0 \cdot n_{\mathrm{e}} \cdot X_{0p}^{\mathrm{exc}}(T_{\mathrm{e}}), \tag{2.55}$$

where n_0 denotes the ground state density, n_{e} the electron density and $X_{\mathrm{exc}}^{0p}(T_{\mathrm{e}})$ is the corresponding rate coefficient for electron excitation from the ground state to the state p which depends on the electron temperature T_{e}. Analogously, all relevant excitation and de-excitation channels for the specific level p can be included with the corresponding rate coefficients and particle and population densities, respectively.

2.4.2 Power and Ionization balance

The most common representatives of population balances are the *ionization balance* and the *power balance* which allow access to the qualitative behaviour of the electron temperature T_{e} and density n_{e}.

Ionization balance and the electron temperature

As already briefly discussed in section 2.3, the main generation process of positive ions is electron impact ionization of gas particles while the dominant loss channel is given by diffusion to the vessel walls. Assuming only one neutral particle species in the ground state with density n_0 and one ion species with density n_{ion} leads to the ionization balance

$$n_0 n_{\mathrm{e}} X^{\mathrm{ion}}(T_{\mathrm{e}}) = \frac{n_{\mathrm{ion}}}{\tau_{\mathrm{ion}}}. \tag{2.56}$$

$X^{\mathrm{ion}}(T_{\mathrm{e}})$ denotes the rate coefficient for ionziation taking place from the ground state. The right hand side of the equation describes the rate of ion losses with τ_{ion} being the ion confinement time within the plasma volume. Considering quasi-neutrality according to equation (2.2) and assuming laminar ion diffusion accord-

ing to equation (2.50), one obtaines

$$X^{\mathrm{ion}}(T_{\mathrm{e}}) = \frac{1}{n_0 \tau_{\mathrm{ion}}} \propto \frac{\lambda_{\mathrm{mean,ion}}}{n_0 \sqrt{m_{\mathrm{ion}}}} \tag{2.57}$$

with the mean free path $\lambda_{\mathrm{mean,ion}}$ of the ions, the ion mass m_{ion}. Neglecting the T_{e}-dependency of τ_{ion} compared to $X^{\mathrm{ion}}(T_{\mathrm{e}})$, it can derived that T_{e} increases with decreasing n_0.

Power balance and electron density

The power balance describes the equilibrium between the power deposited in the plasma and the occuring loss mechanisms of heavy particles due to excitation, ionization or dissociation by electrons. The following description is focused on the situation in the bulk region of the plasma and is mainly based on [Beh91]. Since the external energy is predominantely transferred to the electrons, ions are not considered and exclusive power absorption by electrons is assumed [CB11]. In general, electrons distribute the absorbed power P_{abs} via inelastic collisions with feed gas particles leading to excitation, ionization or dissociation. On the other hand, elastic collisions occur within the plasma volume with an impact on the gas temperature. Since the latter process as well as losses to the wall play a minor role [Beh91], the power balance can be written as

$$P_{\mathrm{abs}} = P_{\mathrm{exc}} + P_{\mathrm{ion}} + P_{\mathrm{diss}}. \tag{2.58}$$

P_{exc}, P_{ion} and P_{diss} denote the power dissipated into excitation, ionization and dissociation processes in cases of molecular gases, respectively. The power consumption of these processes strongly depends on the energetic structure of the gas atoms and molecules. The presence of molecules enables losses via dissociation and via a multitude of excitation channels due to additional ro-vibrational energy levels especially in the ground state. According to [Beh91], it follows:

$$V_{\mathrm{plasma}} n_{\mathrm{e}} \propto \frac{P_{\mathrm{abs}}}{n_0 \sum_j X_{0j}^{\mathrm{exc}}(T_{\mathrm{e}}) E_j} \tag{2.59}$$

with the neutral particle density n_0, the electron density n_{e}, the excitation rate coefficient $X_{0j}^{\mathrm{exc}}(T_{\mathrm{e}})$ from the ground state into a state j and the threshold energy E_j of the excitation process. According to this expression, the electron density is increasing with increasing the absorbed power and is decreasing with increasing

T_e and n_0.
In the case of pure atomic discharges, e.g. noble gases, the loss mechanisms are limited to excitation and ionization. The relation

$$V_{\text{plasma}} n_e \propto P_{\text{abs}} \tau_{\text{ion}}. \tag{2.60}$$

can be derived [Beh91] with the plasma volume V_{plasma}, the electron density n_e and the ion confinement time T_{ion}. Again, the electron density increases with increasing power absorbed in the plasma.

2.4.3 Corona & CR model

Corona model

Based on the condition in the solar corona with high electron temperatures $T_e \approx 100\,\text{eV}$ and low electron densities in the range of $n_e \approx 10^{12}\,\text{m}^{-3}$ [GMK+99], the *corona model* allows a simple approach to the population density n_i of an excited state i for plasmas with a rather low electron density. In this case, the contribution of electron collisions to the de-population is negligable, and the radiative decay to lower states k dominates the de-excitation. Moreover, recombination processes do not occur due to the high electron temperature. Inelastic electron collisions with heavy particles in the ground state are balanced with spontaneous emission in the so-called *corona equilibrium*:

$$n_0 n_e X_{0i}^{\text{exc}}(T_e) = n_i \sum_{k<i} A_{ik}. \tag{2.61}$$

The left side of the equation describes the electron excitation from the ground state into level i with the corresponding rate coefficient $X_{0i}^{\text{exc}}(T_e)$. Usually, the ground state density n_0 equals the neutral particle density in a good approximation. Spontaneous emission is given on the right side with the Einstein coefficients A_{ik} for the individual radiative channels.
In molecular gases, dissociation processes might play an important role and must be included in the model. In this work, a simple implementation is followed to determine the neutral particle densities in oxygen and nitrogen plasmas from the measured emissivity of atomic lines. Direct electron collision excitation of the corresponding upper state from the atomic ground state and dissociative electron collision excitation from the molecular ground state are balanced with spontaneous emission to all lower lying atomic states j with

$$n_{\mathrm{atom}} n_{\mathrm{e}} X^{\mathrm{exc}}_{\mathrm{atom}}(T_{\mathrm{e}}) + n_{\mathrm{mol}} n_{\mathrm{e}} X^{\mathrm{exc}}_{\mathrm{mol}}(T_{\mathrm{e}}) = n_i \sum_{j<i} A_{ij}. \tag{2.62}$$

The resulting rate balance equation contains the excitation rate coefficients for the electron excitation processes, $X^{\mathrm{exc}}_{\mathrm{atom}}(T_{\mathrm{e}})$ and $X^{\mathrm{exc}}_{\mathrm{mol}}(T_{\mathrm{e}})$, the Einstein coefficients A_{ij} and the electron density n_{e}. According to equation (2.42), the density n_i of the upper state can be expressed with the measured emissivity $\epsilon_{ik} = n_i A_{ik}$. *Emission rate coefficients*

$$X^{\mathrm{em},ik}_{\mathrm{atom,mol}}(T_{\mathrm{e}}) = X^{\mathrm{exc}}_{\mathrm{atom,mol}}(T_{\mathrm{e}}) \cdot \underbrace{\frac{A_{ik}}{\sum_{j<i} A_{ij}}}_{branching\ ratio} \tag{2.63}$$

are introduced for direct excitation and dissociative electron excitation, respectively. Taking into account the so-called *branching ratio*, they can be calculated from excitation rate coefficients which, in turn, are computed with cross sections from literature assuming a Maxwellian EEDF via equation (2.53). In the event that *emission* cross sections instead of *excitation* cross sections are provided, emission rate coefficients are directly obtained already including the branching ratio. However, emission cross sections may also include contributions from higher excited states due to cascade processes [MZ71] which might depend on the specific plasma discharge.

Depending on the gas and the specific transition, additional excitation processes (e.g. electron excitation from metastable levels) might have to be considered which refers to an *extended* corona model.

Collisional radiative model

Collisional radiative (CR) models provide the opportunity of a more global access to the population situation in plasmas closing the gap between the application ranges of corona models and the thermodynamic equilibrium in which each process is in equilibrium with its reverse process. The following description of the general structure of CR models is taken from [Wün04]. The core of CR models is a set of rate equations completely balancing the occuring population processes

for each state. The rate equation for an atomic or molecular state p,

$$\frac{\mathrm{d}n_p}{\mathrm{d}t} = \underbrace{\sum_{q\neq p} n_\mathrm{e} n_q X_{qp}^\mathrm{exc}}_{\substack{electron\ impact\\ population}} + \underbrace{\sum_{q>p} n_q A_{qp}}_{\substack{radiative\\ cascading}} - \Big(\underbrace{\sum_{q\neq p} n_\mathrm{e} n_p X_{pq}^\mathrm{exc}}_{\substack{electron\ impact\\ de-population}} + \underbrace{\sum_{q<p} n_p A_{pq}}_{\substack{spontaneous\\ emission}} \Big), \tag{2.64}$$

includes for example populating and de-populating electron collisions, spontaneous emission and population via spontaneous emission from higher lying states, and describes the temporal evolution of the population density n_p. The first two terms represent population channels while the bracket contains de-population processes. The rate equation (2.64) is set up for each state which is considered in the CR model. In the case of 'steady state' equilibrium, the population density of each state remains constant which leads to $\frac{\mathrm{d}n_p}{\mathrm{d}t} = 0$. Consequently, the differential rate equations transform into a set of coupled linear equations which can be expressed in matrix notation as

$$\mathbf{X} \cdot \mathbf{R} = \mathbf{V}. \tag{2.65}$$

On the right hand side, the rate coefficients of all excited states corresponding to electron excitation from the ground state are summarized in the vector $\mathbf{V}$. The left hand side contains the rate matrix $\mathbf{X}$, whose entries are given by rate coefficients of the interaction processes between excited states, and the coupling vector $\mathbf{R}$. The latter is composed of the *population coefficients*

$$R_{0p} = \frac{n_p}{n_0 n_\mathrm{e}} \tag{2.66}$$

of all considered states which depend on the electron temperature, electron density and further parameters. The population coefficients indicate the population density of a state p with respect to the product of ground state density n_0 and electron density n_e. They represent the solution of collisional radiative models and allow the determination of the population density according to

$$n_p = R_{0p} n_0 n_\mathrm{e}. \tag{2.67}$$

Additional particle species, e.g. ions, and coupling processes can be integrated. For general aspects and further details on collisional radiative models, it is again

referred to [Fuj04] as well as to [Kun09].
Finally, it is stressed that the accuracy of the presented population models crucially depends on the accuracy of the included cross sections and rate coefficients.

3 Experimental setup *PlanICE* and general diagnostics

3.1 Experimental setup *PlanICE*

At the experimental setup *PlanICE* (**Plan**ar **I**nductively **C**oupled **E**xperiment), the absolute intensity calibration of the VUV spectrometer (see section 4.1.2), the investigations of the spectral ranges (see chapter 6) as well as the calibration and the benchmark of the diode system (see section 4.2.4 and chapter 7) are performed. An exploded view of the setup is depicted in figure 3.1.

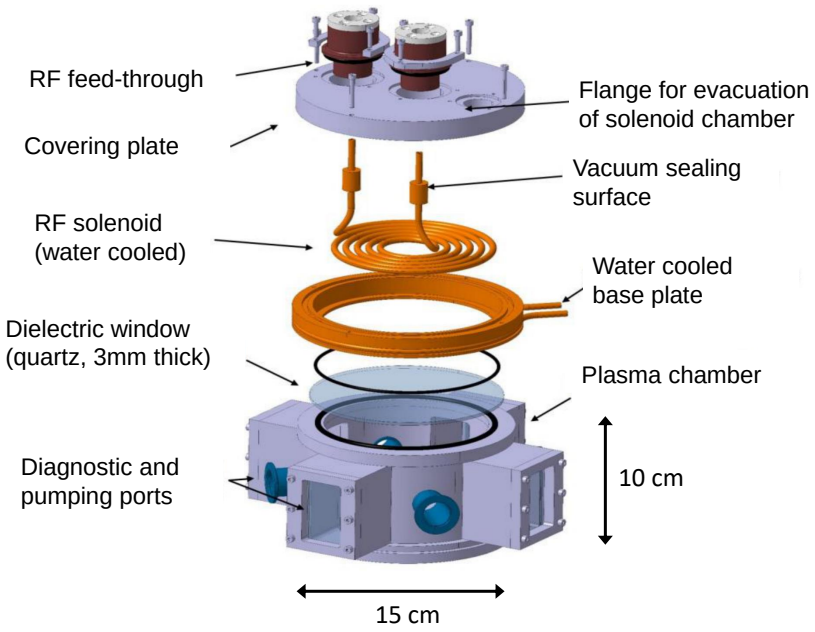

Figure 3.1: Exploded view of the planar ICP experiment *PlanICE*. The sketch was kindly provided by [Eck19].

A radio frequency (RF) generator (*CESAR type 0220*) is used for the plasma generation. It delivers a power up to 2 kW at a frequency of 2 MHz. To obtain an

optimal power transfer from the generator to the discharge, a matching network consisting of two tunable capacitors is applied. The goal of the matching process is to adapt the overall impedance of the load (including the capacitors, the RF cables, the solenoid as well as the discharge itself) to 50 Ω. This value is given by the generator and specifies the condition for maximum power output. The RF coil has 5.5 windings made of a copper tube with a diameter of 6 mm and is water cooled to reduce losses due to ohmic heating.

The cylindrical plasma chamber with a diameter of 15 cm and a height of 10 cm is made of stainless steel and is also water cooled. Both the vessel and the chamber containing the RF coil are pumped by combinations of roughing and turbomolecular pumps achieving background pressures of some 10^{-4} Pa which are monitored with a cold cathode gauge (*Pfeiffer Vacuum PRK 251*). Gas is inserted into the vessel by mass flow controllers which allow flow rates up to 10 sccm (molecular gases) or 20 sccm (noble gases). During plasma operation, the discharge pressure is adjusted with a butterfly valve between the plasma vessel and the vacuum system. It is gradually closed or opened in order to manipulate the effective pumping rate. In the presented work, discharge pressures in the range between 0.3 Pa and 10 Pa were used which are measured with a capactive pressure gauge (*Pfeiffer Vacuum CMR 375*). Several ports and optical windows allow an extensive diagnostic access to the plasma.

The RF power drives an AC current through the RF coil which consequently causes an oscillating magnetic field $\boldsymbol{B}$ that reaches through the dielectric quartz window into the cylindral plasma chamber [LL05, CC03]. Following *Faraday's law*,

$$\nabla \times \boldsymbol{E} = -\frac{\partial \boldsymbol{B}}{\partial t}, \tag{3.1}$$

an electric field $\boldsymbol{E}$ is induced inside the vessel with an orientation antiparallel to the antenna current. Heating of primary electrons that are present in the gas occurs due to the electric field within a thin layer below the dieelectric window. For a detailed description of the underlying processes it is referred to [LL05].

An important control parameter in plasma applications is the input power that is applied to the discharge. Regarding RF systems, ohmic losses within the circuit, the antenna coil, the matching system or due to induced eddy currents in close components occur. They are summarized to P_{loss}. Therefore, only the fraction P_{plasma} of the delivered generator power $P_{\mathrm{RF,del}}$ is absorbed by the plasma.

Following [CB11], the ratio

$$\eta = \frac{P_{\text{plasma}}}{P_{\text{RF,del}}} = \frac{P_{\text{RF,del}} - P_{\text{loss}}}{P_{\text{RF,del}}} \tag{3.2}$$

describes the *RF power transfer efficiency* of the system. The dissipated power P_{loss} with

$$P_{\text{loss}} = I^2_{\text{rms,plasma}} \cdot R_{\text{network}} \tag{3.3}$$

is assessed via a *subtractive method* [Hop94, Hor83, RBF17] measuring the current $I_{\text{rms,plasma}}$ through the coil as well as the resistance of the network R_{network}.
An in-line RF voltage and current probe ($V-I$ probe, *Bird, VIP system 7001A500 series*) plus a current transformer (*Pearson, current monitor model 4997*) are used in the setup depicted in figure 3.2. The current transformer enclosing the cable from the matching system to the RF solenoid is conneceted to an oscilloscope (*Tektronix TDS 2002B*) and measures the antenna current $I_{\text{rms,plasma}}$. The voltage and current probe gives the delivered power by the generator.

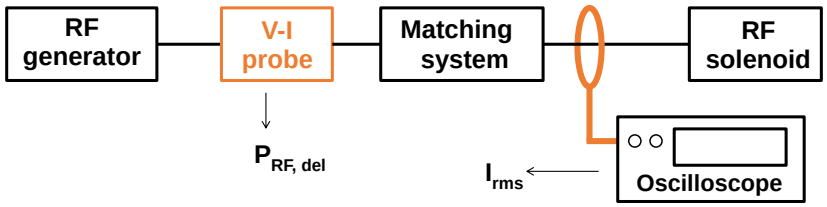

Figure 3.2: Diagnostics for determination of the RF transfer power efficiency and the estimation of the power absorbed by the plasma.

An extensive description of the components, the setup as well as the measurement technique and the data analysis can found in [Rau18]. In the presented work, the technique using the $V-I$ probe is applied in order to estimate the power which is absorbed by the discharge and which serves as an important parameter for the plasma emission.
Due to the geometry and experimental setup of *PlanICE*, the plasma shows a cylindrical symmetry with vertical variations across the discharge. Therefore, the applied diagnostics for plasma characterization as well as the determination of particle and photon fluxes are attached at the same height at radial symmetric lines of sight. One exception is the mass spectrometer which is installed at the plasma vessel's bottom with a vertical line of sight. It has to be noted that the viewing volumes of the diagnostics are different.

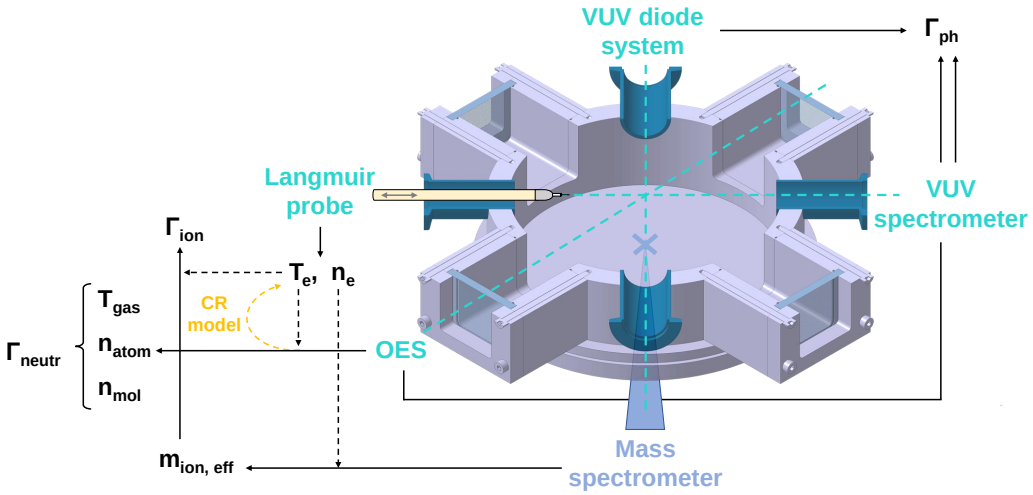

Figure 3.3: Diagnostic systems at *PlanICE*, including the obtained plasma parameters (e.g. T_e, n_e, T_{gas}) and their contribution to quantify the particle fluxes Γ_{ion} and Γ_{neutr}. The photon flux Γ_{ph} is directly derived from the emission spectroscopy system. The sketch of the vessel was provided by [Eck19].

Figure 3.3 shows a horizontal section through the plasma vessel indicating the diagnostics' orientation and the lines of sight, however, without scaled viewing volumes. Moreover, the obtained quantities, their interdependence and their contribution to determine particle and photon fluxes are stated.
In the following, the instrumental hardware of the diagnostics are described. Details on the evaluation of the measurements in order to quantify the positive ion flux Γ_{ion}, the neutral particle flux Γ_{neutr} and the photon flux Γ_{ph} are presented in section 5.

3.2 General diagnostics

3.2.1 Langmuir probe

For a local determination of plasma parameters, electrostatic probes are commonly used whose most widespread representative is the Langmuir probe [MSL26]. It allows measuring the electron temperature and density as well as the floating and the plasma potentials. These parameters are crucial for the quantification of the ion and neutral particle fluxes Γ_{ion} and Γ_{neutr} (see figure 3.3). Additionally, the determination of the EEDF and the ion density are accessible. The technique is based on a thin wire being inserted into the plasma and being biased with a varying voltage with respect to a reference electrode. Generally, the reference is

given by the plasma vessel wall. As a result, a voltage dependent current, which flows between the plasma and the wire, is measured. Its $I - V$ characteristic provides information about the plasma parameters. A sketch of the probe setup as well as the electric circuit is depicted in figure 3.4.

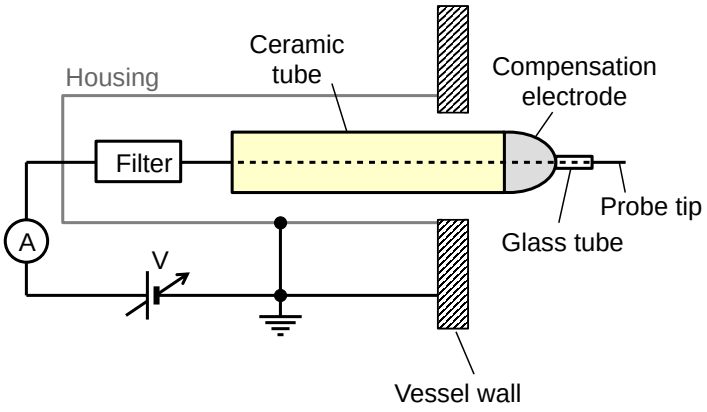

Figure 3.4: Schematic setup and electric circuit of the applied Langmuir probe type following [MDCK$^+$08]. The Langmuir probe is enlarged and is not drawn to scale. The diameter of the ceramic tube is around $7 - 8$ mm.

A ceramic tube gives mechanical stability and serves for insulation as well as for protection of the electric connection from the plasma. The Langmuir probe is flanged to the plasma vessel. Due to a membrane bellow, a stepper motor can gradually move the whole ceramic arm within the plasma vessel or remove the probe tip from the discharge. In this work, radial distances from the vessel wall up to 80 mm (which is 5 mm beyond the vessel center) are investigated in 10 mm steps. The probe tip is represented by a thin wire with a diameter of 50 - 300 µm. It is made of a high-melting material with a cylindrical tip geometry for which tungsten is often used. During plasma operation, the probe is regularly cleaned with a sufficiently high positive voltage such that the wire starts to glow in order to remove contaminations from the probe tip. A glass tube limits the current collecting area of the tip to a range of few millimeters and provides an electrical insulation from the metallic compensation electrode which has to be on floating potential. Together with a passive filter system, the compensation electrode accounts for a reduction of RF oscillation problems [SFAP01, MDCK$^+$08] which would obstruct an accurate evaluation.
The acquisition of the $I - V$ characteristic with a voltage step of 0.1 V as well as the evaluation of the plasma parameters are performed automatically with the probe software *PlasmaMeter, version 5.3.42*. In each step, the corresponding

voltage is applied for a certain time interval during which the current between plasma and probe tip is measured. The specific time interval is defined by the duty cycle given in percentage of the time interval for which the voltage is applied. Low duty cycles of 1 % or 10 % were chosen in order to reduce a thermal electron emission from the tip which would lead to a falsification of the $I-V$ characteristic. For details regarding the evaluation of the probe measurements, it is referred to section 5.1.1.
Too high probe currents reduce the accuracy of the measurements due to undesired ohmic resistances in the probe circuit. They lead to ohmic losses of the applied voltage and might affect the $I-V$ characteristic and, thus, the evaluation of the plasma parameters. For this reason, the length of the tip was set to around 1 mm in argon. Due to its reactive properties, a fast degradation of the tungsten wire and the probe signal, respectively, were observed in oxygen plasmas. It was found that a platinum tip allowed reproducible measurements in these cases.

3.2.2 Mass spectrometer

The composition of the positive ion species and the corresponding effective positive ion mass m_{ion} in the different plasma discharges is crucial for the quantification of the positive ion flux Γ_{ion}. Although the positive ion density n_{ion}^{+} equals the electron density n_{e} due to the quasineutrality of the plasma, however, the composition of the ion species is not a priori obvious. Apart from noble gas discharges in disregard of different ionisation levels, this applies for pure plasmas and especially for gas mixtures.
The effective ion mass considers the mass and the density of the different ion species in the plasma and is determined by ion mass spectrometry. At *PlanICE*, a quadrupol mass spectrometer (*Balzers PPM 421 plasma monitor*) is installed in the bottom plate of the plasma vessel. In general, the system is capable of measuring ions as well as neutral particles. The following description of the setup which is depicted in figure 3.5 (a) and the operation mode of the mass spectrometer is based on [Pfe, Bal, Dem16].
As can be seen in figure 3.5 (b), an electrically insulated extraction cap with a diameter of 6 cm extends roughly 3 cm into the plasma vessel. Particles can enter through a small aperture with a diameter of 100 µm into the mass spectrometer. The main parts are an ion optic system including an ionisation chamber and serving as ion source, an energy filter (Cylindrical Mirror Analyzer, CMA) which is followed by a mass filter (Quadrupol Mass Analyzer, QMA) and a secondary

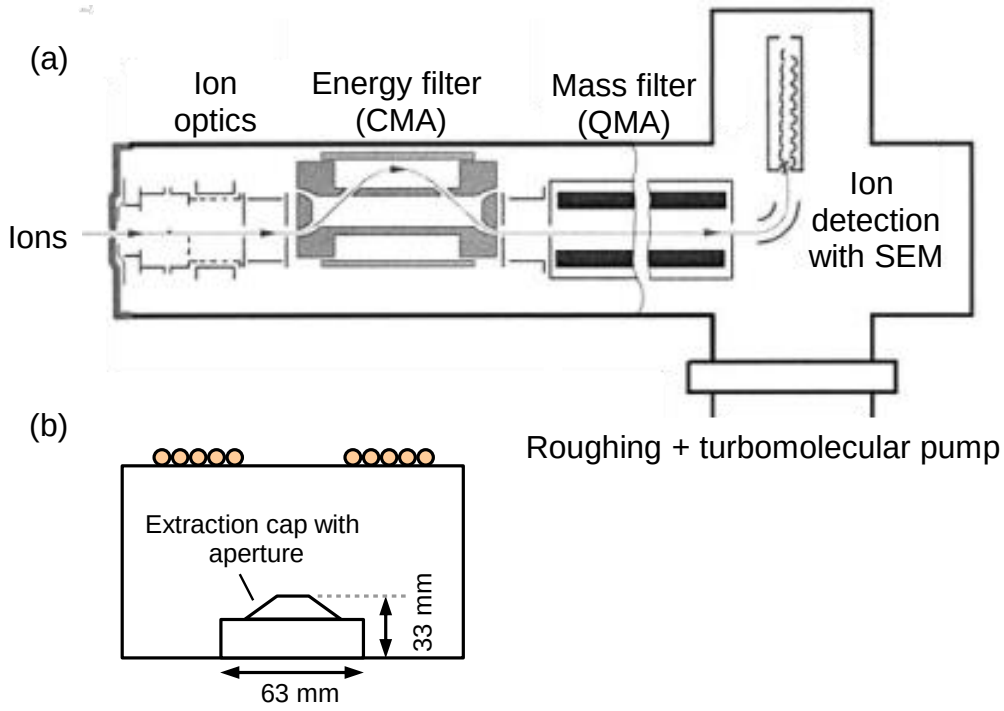

Figure 3.5: Energy resolved mass spectrometer for ion detection at *PlanICE*. (a) Plasma monitor *PPM 421* taken from [Pfe]. (b) Dimensions of extraction cap and installation at the experiment.

electron multiplier (SEM) for ion detection.

Ions passing the aperture of the extraction cap are accelerated or slowed down, respectively, by the so-called entrance lense potential depending on the extraction cap's potential. The ions enter the ion transfer optics where coordinated potentials are applied to focus and lead them into the energy filter. If neutrals are investigated, the ion source provides ionisation by electron impact without changing the direction and the energy of the particles. In this case, electrons are emitted from a current-carrying and, therefore, heated filament. The ionized particles are focused on the entrance of the CMA.

Energy selection in the CMA is based on two concentrically interlaced cylinders. The electrical field in the space between the cylinders inflects the trajectory of incoming ions. Only ions with a specific kinetic energy are deflected appropriately and can leave the CMA. Ions with a higher or lower energy are filtered by hitting the cylinders. Further details on the CMA can be found in [Se67].

Subsequently, the ions enter the quadrupol mass filter. The description of its basic design and functionality is based on [PRZ58, Pfe13]. In principle mass selection is achieved using an electric quadrupol field which is generated by four

parallel metal rods arranged in a square. A voltage with DC and periodic AC component is applied in the way that opposite rods are on the same potential. Axially induced ions approximately with the same kinetic energy are forced by the quadrupol field into a helical movement along the longitudinal axis. The ions move with constant speed through the system and follow the so-called *Mathieu's differential equations*.
For stable solutions which depend on the ions' charge-to-mass ratio, the amplitude of the oscillation stays small enough that the corresponding ions do not hit the rods and can pass the mass filter. The mass of 'stable' ions can be selected with the applied DC and AC voltages and the resolution is tuned by their ratio.
In the last step, the filtered ion beam is deflected by 90° and finally detected by a secondary electron multiplier (SEM). The signal output is given in counts per second.
A background pressure below 10^{-5} mbar is required for a proper functionality of the ion optics and to prevent particle collisions within the mass spectrometer [Pfe]. Therefore, the system is differentially pumped with a combination of a roughing and a turbomolecular pump maintaining a pressure of approximately three orders of magnitude below the pressure in the plasma vessel.
In this work, the mass spectrometer was not applied to neutral particles since the ionisation process in the ionisation chamber requires detailed knowledge about molecular *cracking patterns* which consider possible dissociation of neutral molecules induced by electron impact. Although the relative distribution of the fragmentation products is characteristic for the specific molecule, it further depends on the temperature, the electron energy as well as properties of the applied mass spectrometer [DH66]. In order to circumvent these error-prone considerations, the neutral particle density was obtained by optical emission spectroscopy.
Details on the calibration of the mass spectrometer as well as on the evaluation of the measurements are summarized in section 5.1.2.

3.2.3 Optical emission spectroscopy

Optical emission spectroscopy (OES) provides a convenient and non-invasive insight into the plasma. In general, an emission spectrometer measures the line of sight integrated emission arising from atomic and molecular transitions in the discharge. In combination with population models, it allows access to many plasma parameters like the gas temperature, electron temperature, particle densities, the

vibrational as well as rotational distribution of the involved states and provides information about plasma processes [HL65].

At *PlanICE*, the optical emission spectroscopy system is composed of a survey optical spectrometer (*Plasus Emicon*, 195 - 1100 nm, FWHM $\approx$ 1 nm) for monitoring the plasma stability together with a high resolution spectrometer (*Acton SP2750*, 180 - 933 nm, Gaussian profile with FWHM = 18 pm at 650 nm [BRF17], grating with 1800 lines/mm, CCD camera) for the analysis of plasma parameters. Regarding the latter spectrometer, radiation is collected by an achromatic mirror system and focalized spectrally independently into a UV enhanced fibre. The spectrometer exhibits an almost cylindrical acceptance volume with a diameter of 1 cm.

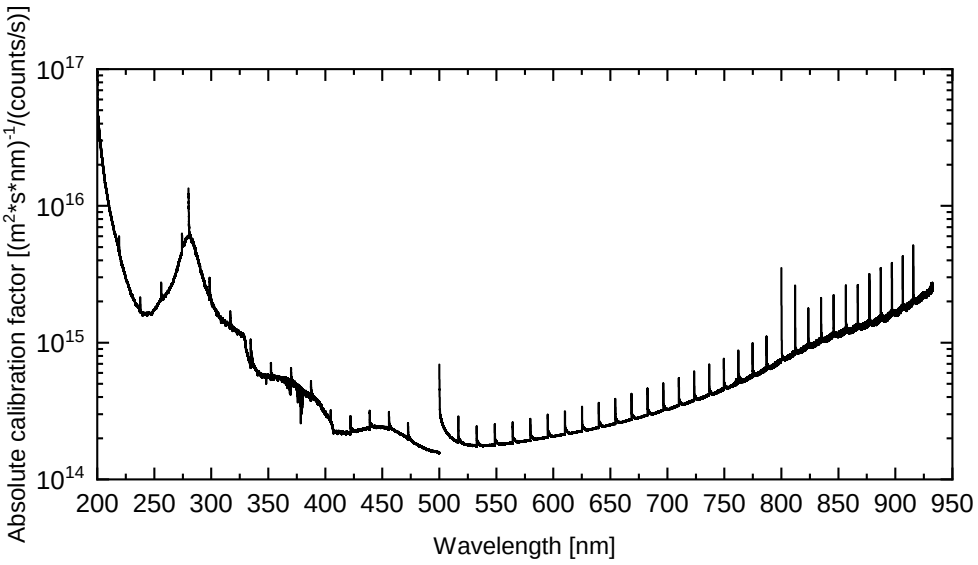

Figure 3.6: Absolute intensity calibration curve of the applied optical high resolution spectrometer in the wavelength range 200 - 933 nm. The 'spikes' arise from the spatial variation of the CCD sensor's sensitivity.

Both spectrometers are wavelength calibrated. The survey spectrometer is solely used to observe the behavior of prominent emission features of the investigated discharges without any intensity calibration. The relative and absolute intensity calibration of the high resolution spectrometer were performed in the wavelength range 380 - 933 nm using an absolutely calibrated Ulbricht sphere. With the continuum radiation of a relatively calibrated deuterium arc lamp, an extension of the absolute intensity calibration down to 200 nm is achieved[1] using the overlapping

[1]It has to be noted that the calibration above 800 nm had become necessary during this work in the course of emission spectroscopy on pure oxygen plasmas and was performed only for this purpose. For other gases, calibrated spectra had been taken in the range 200 - 800 nm.

wavelength range of the two sources.
The corresponding calibration curve is depicted in figure 3.6. The general trend of the calibration factor arises from the overall sensitivity of the system's optical components (e.g. mirror system, optical fibre, the grating, ...). Since the spectrum is recorded stepwise by the spectrometer's CCD sensor, 'spikes' in the absolute calibration curve occur which are due to the spatial variation of the sensors's pixel sensitivity.
In this way, the absolute spectral intensity $I_\lambda(\lambda)$ can be determined in units of $(\mathrm{sm}^2\mathrm{nm})^{-1}$. Dividing by the length l of the line of sight leads to the spectral emissivity

$$\epsilon_\lambda(\lambda) = \frac{I_\lambda(\lambda)}{l}. \tag{3.4}$$

The emissivity of an emission line or a certain emission range is obtained by integrating the spectral emissivity in the corresponding wavelength of the line or molecular band interval.

4 VUV spectroscopy systems

4.1 VUV spectrometer

The following sections describe the instrumental setup of the applied VUV spectrometer and its absolute intensity calibration which have both been published and discussed in [FBFBF21].

4.1.1 Instrumental setup

The VUV spectrometer is a monochromator *Model 225* by *McPherson* and is operated in scanning mode. It has a direct vacuum connection to the plasma vessel. A pumping system with roughing and turbolmolecular pumps achieve a background pressure around several 10^{-5} Pa. The pumps are oilfree in order to avoid a degradation of the grating due to adsorbed oil vapour under VUV irridation [BHH$^+$83]. To reduce absorption of radiation inside the spectrometer and to fulfill crucial operating parameters of one detector, the pressure within the VUV spectrometer is kept below 10^{-3} Pa during plasma operation. It is achieved by an additional differential pumping system within the line of sight based on the two tubes together with a roughing and turbolmolecular pump.
The VUV spectromter is characterized by a focal length of 1 m with single reflection at a concave diffraction grating in normal incidence configuration. The enclosed total angle of incoming and reflected line of sight is 15°. The standard grating is made of a borosilicate crown glass and an Al/MgF_2 coating. It has 1200 grooves per mm and is blazed at a wavelength of 120 nm. Depending on the detector, the accessible wavelength region ranges down to 30 - 50 nm [McP86] while the upper limit of 300 nm is given by the mechanics of the spectrometer. A scanning speed of 10 $\frac{\text{nm}}{\text{min}}$ is chosen as a compromise between the time needed for taking one spectrum and the wavelength resolution. The reproducibility of the wavelength is within ± 1 % and the plasma stability is checked by the optical survey spectrometer during the measurement. A mercury lamp served for the wavelength calibration of the VUV spectrometer by means of the emission line at

253.6 nm and the zeroth order. Due to the entrance and exit slit width of 50 µm, a Gaussian line profile is achieved. Its FWHM (full width at half maximum) varied between 30 pm and 37 pm over the total wavelength range 46 - 300 nm which is accessible applying a combination of two detectors — a solar-blind photomultiplier tube (PMT, *EMR 51F-08-18*, 18 stages, 2800 V operating voltage) and a channel electron multiplier (CEM, *Model 425, McPherson*, 1600 V operating voltage).
The former is based on a semitransparent cesium-telluride photocathode on a lithium fluoride window. Its cut-on wavelength is typically around 104.5 nm [SE00] and determines the lower wavelength limit. In contrast, the CEM is built without window. A MgF_2 layer on the inner surfaces of the device determines the sensitivity range of 30 - 180 nm. Both detectors provide the detected intensity of the radiation as voltage signal which is then measured by a digital multimeter (*DMM 5017, PREMA*) with the integration time set to 100 ms. A manual filter wheel in front of the entrance slit contains a quartz filter which is applied during measurements above 200 nm for the purpose of suppressing higher diffraction orders. A shutter is inserted as long as no spectrum is taken to reduce aging effects of the optical components due to intense VUV radiation.
Apertures and two tubes (with a length of 7 cm and 20 cm, diameter of 0.4 cm each) in front of the entrance slit limit the accessible solid angle to roughly $4.8 \cdot 10^{-5}$ sr. This leads to a viewing cone with a diameter ranging between 4.3 mm where the line of sight enters the plasma chamber and 5.5 mm at the opposite vessel wall. These values were analytically estimated based on the geometry of the setup's components and serve for comparison reasons regarding the viewing volumes of other diagnostics.

4.1.2 Absolute intensity calibration

An absolute intensity calibration of the VUV spectrometer is required for the intended quantification of photon fluxes. It considers the spectral sensitivity of the corresponding detector, the transmission of the window if necessary, the wavelength dependency of the reflective grating and apertures along the line of sight. The choice of the detector directly affects the sensitivity of the VUV spectrometer.
The general principle of intensity calibration procedures relies on reproducible radiation standard sources and a comparison of their known spectral intensity distribution $I_{\mathrm{stand}}(\lambda)$ with a spectrum $I_{\mathrm{meas}}(\lambda)$ measured with the VUV spectrometer here in units of volts. The wavelength calibration of the instrument

serves as prerequisite.
The inverse spectral sensitivity (or calibration curve) $\rho^{-1}(\lambda)$ is characterized by

$$\rho^{-1}(\lambda) = \frac{I_{\text{stand}}(\lambda)}{I_{\text{meas}}(\lambda)}. \tag{4.1}$$

in the units of photons/s/m^2/nm/V.
For an absolute calibration, electron storage rings emitting synchrotron radiation typically constitute the primary standard. Due to the related high transport effort and operating costs as well as a limited access time, a calibration procedure based on different secondary standard sources and plasmas directly at the experiment *PlanICE* has been developed in this work which has been already published in [FBFBF21]. It extends the established procedure for the wavelength range 116 - 300 nm from 116 nm down to 46 nm.
The emission solid angle of the standard source as well as the collection solid angle of the VUV spectrometer are of crucial importance in order to connect the emitted photon number and the produced signal output. Special attention has to be paid concerning a full illumination of the spectrometer's acceptance volume by the radiation source [Kun09] and a conservation of the illuminated grating area while calibrating and measuring [TLJ99]. Especially the latter condition might not be given using point like radiation sources in contrast to the usually spatial extension of a plasma discharge. Recalling these two requirements, extended radiation sources should be applied with priority for an absolute intensity calibration.
In the following sections, an overview of the applied standard sources and the calibration procedure will be presented. For an extensive description including a detailed uncertainty discussion, it is again referred to [FBFBF21].

a. Standard radiation sources

The VUV spectrometer can be applied with two different detectors — CEM and PMT — providing access to the wavelength ranges 30 - 180 nm (CEM) and 105 - 300 nm (PMT), respectively. In the following, two deuterium arc lamps, a high current hollow cathode and branching ratios in nitrogen discharges which serve as standard sources are described.

Deuterium arc lamp I: 190.0 - 400.0 nm

The deuterium lamp I (*Model 6316, L.O.T. Oriel GmbH*) allows to derive a relative calibration curve for the VUV spectrometer. Inside the glass bulb, a deu-

terium discharge at a pressure around several hundreds of Pascal is produced by a filament driven by a stabilized power supply (*Model 68840, L.O.T. Oriel GmbH*). Radiation is emitted through a fused silica window and an apperture with a diameter of 1 mm which characterizes the extent of the deuterium discharge. The source was calibrated against a secondary standard [Mar96] whose absolute calibration in units of $\mu W/cm^2/nm$ can be traced back to the *Physikalisch-Technische Bundesanstalt Braunschweig und Berlin (PTB)*. The relative uncertainty is wavelength dependent with ±16 % (190 - 195 nm), ±10 % (195 - 240 nm) and ±9 % (240 - 350 nm), respectively. Due to the point like emission of the deuterium lamp I and its limited emission wavelength range in the VUV through the quartz window, it serves for the relative calibration of the VUV spectrometer equipped with the PMT.

Deuterium arc lamp II: 116.0 - 400.0 nm

The deuterium lamp II (*L9841, Hamamatsu*) allows to derive a relative calibration curve for the CEM as well as the PMT. Unlike the first type of deuterium lamp, a direct vacuum connection to the plasma vessel and an operation under vacuum is possible. The deuterium discharge is enclosed in a glass bulb with a MgF_2 window and is sustained by a current-stabilized power supply (*C9559, Hamamatsu*). The emitting solid angle is limited by an aperture with a diameter of 0.5 mm. The absolute radiometric calibration was carried out at the *Physikalisch-Technische Bundesanstalt Braunschweig und Berlin* in units of $\mu W/mm^2/sr/nm$ using the electron storage ring BESSY II [Tho15]. The resulting uncertainties are 7 % in the range 116.0 - 120.4 nm, 18 % for 120.6 - 122.6 nm, 7 % in the interval 122.8 - 170.0 nm and 3.5 % from 172.0 nm up to 400.0 nm [Tho15]. Being a point like source, the deuterium lamp II was applied for extending the relative calibration curve of the VUV spectrometer down to 116.5 nm. This lower limit results from the cut-on wavelength of the MgF_2 window.

High current hollow cathode (HCHC): 46.1 - 123.6 nm

An intensity calibration reaching down to the deep ultraviolet region below 100 nm can be performed with a high current hollow cathode. The applied model *DKK 042* relies on a glow-discharge and was applied for the relative calibration of the VUV spectrometer below 116.5 nm for both detectors. The setup of the source is described in detail in [DGF+88, HKW94, HKHW02]. The rare gases helium, neon, argon, krypton or xenon serve as feed gas with flow rates around 60 sccm

resulting in a discharge pressure in the range of 20 - 120 Pa. Controlling the gas flow with a needle valve enables to stabilize the discharge at the working point of 500 V and 1 A [Hoh05]. The solid angle of the radiation emitted by the source is restricted due to an aperture with a diameter of 1.2 mm.

Being a secondary standard, the hollow-cathode exhibits the characteristic that the absolute intensity calibration of an original prototype is transfered onto its replicas. An absolute calibration of line emissivities of the original source prototype had been performed by the PTB at a beam line of the electron storage ring BESSY in units of μW/sr. Radiation from atomic and ionic transitions of the working gas covers the range between 46.1 nm (Ne II) and 123.6 nm (Kr I). Calibrated values are given in [HKW94] with an uncertainty of $\pm 5\,\%$ [DKK] for the applied replica.

***PlanICE* nitrogen plasmas - Branching ratio technique: 116.4 - 212.7 nm**
Branching ratios of nitrogen atoms and molecules are standardly applied for a relative intensity calibration of a VUV spectrometer [MZ71]. The ratio of emissivities of two transitions with the same upper level corresponds to the ratio of their transitions probabilities. Atomic line radiation as well as vibrational bands of molecules can be used. In this work, a nitrogen plasma (3 Pa, 600 W) was operated at *PlanICE* and the branching ratio technique was applied to the molecular Lyman-Birge-Hopfield system (100 - 260 nm [LK77]) and two atomic transitions at 116.4 nm and 131.1 nm with the common upper state $2p^2 3d\ ^2\mathrm{D}$. Atomic transition probabilities are taken from the *NIST* database [KYRa19b]. Vibrational transitions of the Lyman-Birge-Hopfield system with initial quantum numbers v'=0-6 were evaluated. Corresponding relative emission intensities from [Mum72] were used. Due to the molecular transitions, a nearly continuous relative calibration in the interval 127.3 - 212.7 nm was obtained while the atomic radiation allowed an extension down to 116.4 nm. Nevertheless, a lack of appropriate emission lines in the available gases prevents to obtain a calibration between 116.4 nm and 127.3 nm. An interpolation was performed by default [MZ71]. However, this wavelength range characterizes an important emission range of various discharges, especially for hydrogen plasmas which emit the very prominent L_α line at 121.6 nm. Therefore, this calibration technique was limitedly applied for the wavelength range 169.5 - 198.2 nm.

b. Calibration technique

The calibration of the VUV spectrometer taking into account the respective detector and all other components is referred to as 'calibration of the PMT/CEM' in the following description. It is worthwile noting that the calibrations of the two detectors are mutually dependent and interwoven. The piecewise extension of the PMT's and CEM's calibration curves is based on overlapping wavelength regions of the applied radiation sources and techniques. Their different accessible and considered wavelength ranges are taken from [FBFBF21] and summarized in the appendix C.

Photomultiplier tube (PMT),
Measurements with the PMT equipped on the VUV spectrometer were performed from 200 nm up to 300 nm with the quartz filter installed in the line of sight while no filter is applied below 200 nm .

(a) The deuterium lamp I allows a relative calibration in the interval 190 - 300 nm (without quartz filter chosen in the manual filter wheel in front of the VUV spectrometer) and 200 - 300 nm (with quartz filter). The first measurement is required for absolute scaling factors which are obtained in step (c).

(b) Branching ratios in a nitrogen discharge (3 Pa, 500 W) continue the results without the quartz filter down to 116.4 nm.

(c) An absolute scaling of the derived relative calibration curve was performed by simultaneous measurements with the VUV spectrometer and the absolutely calibrated optical spectrometer at a helium plasma (5.2 Pa, 400 W). The discharge's symmetry was confirmed to be within $\pm 10\%$ for the rotation-symmetric lines of sight of the two spectrometers. The absolute radiometric calibration of the VUV spectrometer is based on five helium lines at 269.61 nm ($1s9p\ ^3\mathrm{P^o}$), 272.32 nm ($1s8p\ ^3\mathrm{P^o}$), 276.38 nm ($1s7p\ ^3\mathrm{P^o}$), 282.91 nm ($1s6p\ ^3\mathrm{P^o}$) and 294.51 nm ($1s5p\ ^3\mathrm{P^o}$). The electronic configuration together with the related spectroscopic term of the upper states are indicated in brackets. Absolute scaling factors at the corresponding wavelengths were generated by a comparison of the measured signal with the VUV spectrometer and the absolute emissivity observed simultaneously with the optical spectrometer. The relative calibration curves were shifted in such a way to achieve an agreement with the absolute values.

(d) The calibration curve without quartz filter was extended down to 116.5 nm using the deuterium arc lamp II.

(e) An absolute calibration of the PMT below 116.5 nm was obtained through measurements with both detectors at corresponding discharges at *PlanICE* with the prerequisite of an absolute calibration of the CEM. Emission lines in the interval 107.4 - 120.1 nm produced from xenon, nitrogen and oxygen atoms and ions, respectively, were investigated with the PMT as well as the CEM. Several operating pressures (0.3 - 10 Pa) and generator powers (300 - 600 W) were chosen to minimize their effect on the calibration factor. Since a change of the detectors requires venting the spectrometer, the measurements cannot be performed simultaneously and, therefore, reproducible conditions are crucial. Applying the optical emission survey spectrometer, the plasma emission was monitored showing a reproducibility within ±10 %. The same procedure using the emission of the high current hollow cathode with argon and xenon as feed gas gave further absolute calibration factors at 104.8 nm (Ar I), 106.7 nm (Ar I), 116.4 nm (Xe I) and 123.6 nm (Xe I). As mentioned above, the lower limit of the accessible spectral range of the PMT is given by its lithium fluoride window.

The emission of the deuterium arc lamp I directly gives a continuous calibration curve in the wavelength range 200 - 300 nm. However, the calibration procedure in the range below 200 nm only provides calibration factors at specific wavelength values characterized by the source. These calibration factors range over several orders of magnitude across the entire wavelength interval of the PMT and show a great variation of the slope. Therefore, a number of fit functions is required which were obtained by the curve fitting tool *Datafit* (Oakdale Engineering).
The results of the calibration procedure are presented in figure 4.1 (a). There, the applied source standards and techniques are characterized by different colours. Full symbols refer to calibration factors finally taken into account into the calibration curve while open values are presented to indicate overlap ranges. The solid red line refers to the combination of the obtained fit functions.

Channel electron multiplier (CEM)
If the CEM is installed on the VUV spectrometer, the system is absolutely calibrated as follows:

(a) In a first step, a relative calibration curve was obtained with the deuterium

arc lamp II in the region 116.5 - 160 nm. The range above 160 nm is affected by a low signal-to-noise ratio due to a decrease of the dectector's sensitivity together with a poor intensity of the deuterium emission.

(b) The PMT's absolute calibration in the wavelength range above 140 nm which is independent from the CEM's calibration allowed an absolute scaling of the relative CEM calibration factors using the deuterium arc lamp II. The scaling factor corresponds to the fraction of the source emission getting into the VUV spectrometer and was determined with the PMT via comparing the measured intensity with the calibrated source radiation. It remains unaffected by a change of the detector. Hence, it can be applied as scaling factor to the relative calibration curve of the CEM which is obtained in the previous step.

(c) The high current hollow cathode was operated with helium, neon, argon, krypton and xenon, and relative calibration factors in the range 46.1 - 123.6 nm are derived. The overlap with the values obtained in step (b) allows to continue the absolute calibration of the CEM down to 46.1 nm.

Like with the PMT, *DataFit* was finally applied to derive a composition of fit functions. The results are shown in figure 4.1 (b).

Over-all inverse sensitivity of the VUV spectrometer

Figure 4.1 gives an overview about the results from the applied calibration procedure of the VUV spectrometer for both detectors. Symbols in different colours refer to the applied source standards or techniques. Full symbols indicate that the corresponding calibration factors have been considered in the resulting calibration curve. If they are open, they are shown to give an impression about overlap intervals.

The VUV spectrometer with the two detectors gives access to the entire wavelength interval 46 - 300 nm. The inverse sensitivity is characterized by a maximum near 120 nm which is present both for the PMT and the CEM. The calibration curves show a minimum at each side of the maximum with another rise towards the upper and lower wavelength limits. This yields to the application ranges of 104.8 - 300 nm of the PMT and 46.1 - 160 nm of the CEM, respectively.

The strong rise of the inverse sensitivity of the VUV spectrometer equipped with the PMT below 108 nm can be traced back to the LiF window in the PMT housing which shows a highly reduced transmission towards the typical cut-on

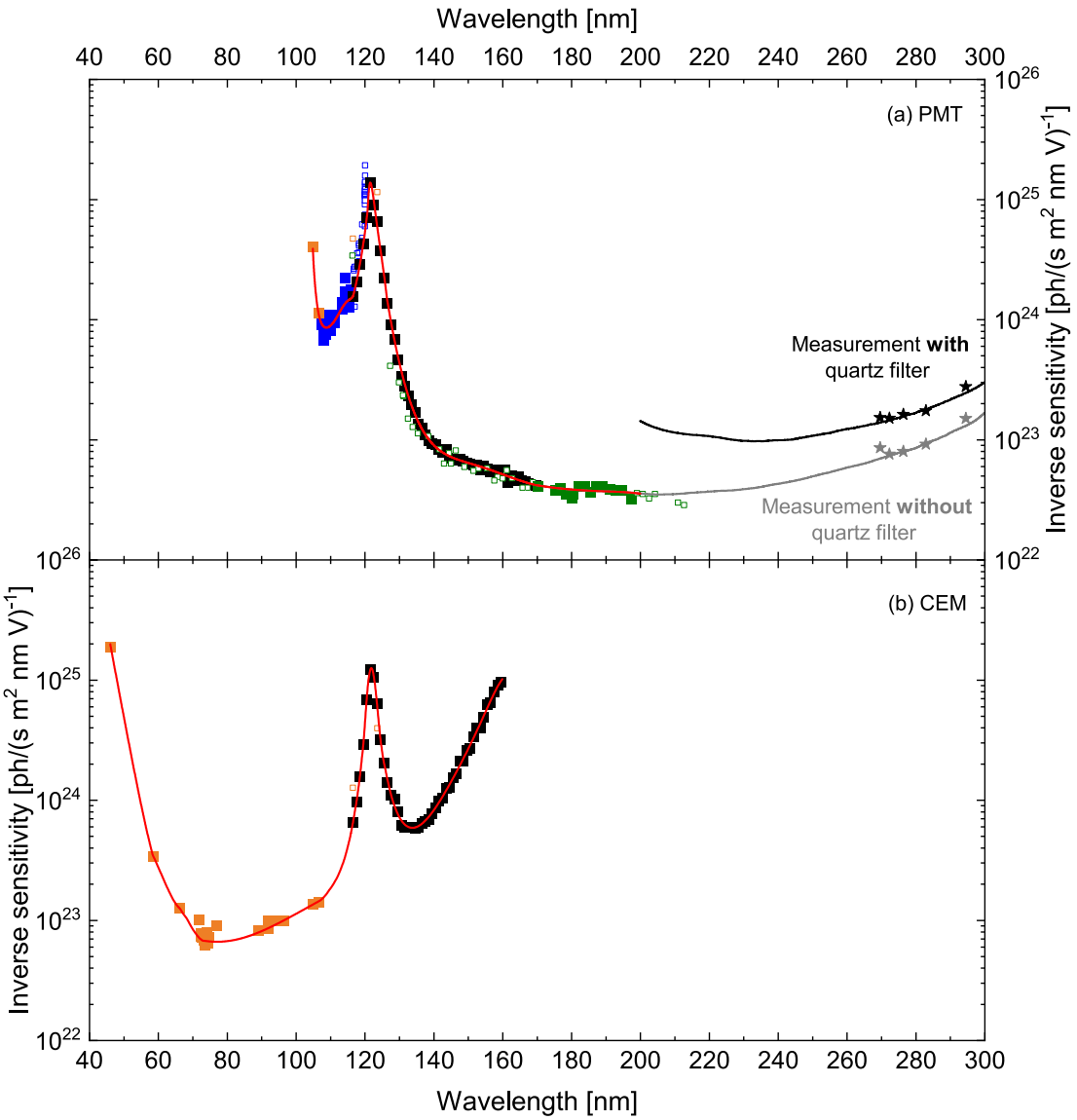

Figure 4.1: Inverse spectral sensitivity of the VUV spectrometer equipped with **(a) PMT** and **(b) CEM** published in [FBFBF21]. The intensity calibration is based on several source standards including a high current hollow cathode (orange squares), Xe, N_2 and O_2 plasmas (blue squares), a number of nitrogen branching ratios (green squares) and two deuterium arc lamps (with fused silica window, black/grey line, or with MgF_2 window, black squares) and a helium discharge (black/grey stars refering to measurements with and without quartz filter). Calibration factors taken into account in the calibration the inverse sensitivity curve are given by full symbols, open symbols illustrate overap ranges. The final combination of fit functions derived with *DataFit* is characterized by the red lines.

wavelength. Dependent on the ambient temperature, fabrication and storage, the cut-on wavelength is in the range of 104.5 nm [Sam67,SE00]. Regarding the PMT, the highest sensitivity of the VUV spectrometer corresponding to a minimum in the calibration curve could be determined in the wavelength region 150 - 230 nm. The additional quartz filter results in higher calibration factors for measurements above 200 nm. The absolute shift is given by the spectral transmission of the quartz filter which has the cut-on wavelength around 160 nm. The minimum of the inverse sensitivity is slightly shifted to 235 nm. The increase of the calibration curve above ≈260-270 nm can be assigned to the semitransparent cesiumtelluride cathode of the PMT. Its sensitivity drastically decreases in this wavelength range [Sam67, FSM$^+$73].

In contrast, the VUV spectrometer equipped with the CEM exhibits the highest sensitivity in the range around 80 nm. A steep rise of the calibration curve can be observed below 60 nm and for a wavelength greater than 140 nm.

The peak around 120 nm in the calibration curves of both detectors could be confirmed as a characteristic of the applied grating in [FBFBF21]. Following the standard calibration procedure presented in [MZ71] would underestimate the calibration factor in the wavelength range of the L_α line by one order of magnitude.

The over-all inverse sensitivity presented in figure 4.1 might be traced back to contrasting effects of the blaze wavelength and absorbing carbon films on the grating surface. The deposition of hydrocarbon films might have occured due to oil-lubricated vacuum pumps which had been in operation at the VUV spectrometer for about fourty years. In this case, back-diffusing oil vapour into the vacuum chamber of the spectrometer cannot be excluded and might degrade the grating's spectral reflectivity crucially if being irridated [BHH$^+$83]. In recent years, the VUV spectrometer was mainly applied to hydrogen discharges with an intense radiation in the VUV range, e.g. from the L_α line. Additional effects due to ambient humidity might result from storage conditions and venting processes. Concluding, a routine investigation of the VUV spectrometer's inverse sensitivity in the affected wavelength range is crucial.

In [FBFBF21] an extensive and wavelength-dependent evaluation of the uncertainty of the presented absolute intensity calibration has been performed. The results are given in the tables C.3 and C.4 in the appendix.

Since the uncertainty of the CEM exceeds the values of the PMT by 7 - 10 % at a

wavelength greater than 116.5 nm, the following application regions are specified for the two detectors: The CEM is used in the wavelength range below 116.5 nm. In contrast, the VUV spectrometer is equipped with the PMT for the region 116.5 - 300 nm.

4.2 VUV diode system

Due to the necessary periphery equipment, VUV spectrometers are rather stationary instruments. Therefore, the development of flexible diagnostic tools for the VUV range has grown over the last years. Mainly these devices are based on diodes with known sensitivities [BLC+14, KTK+15] or on the familiar principle of converting VUV radiation into photons in the optical range by a sodium salicylate surface [IMF+17].
With prospect to a flexible absolute quantification of photon fluxes in industry and science, the main goal of this work was the development of a small and portable VUV diagnostic tool based on a VUV diode. In the subsequent sections, the device is described in detail including the setup, the applied filter set, characteristic properties as well as its absolute intensity calibration against the VUV spectrometer. Many of the presented aspects will be published in [FFBF22] together with results from chapter 6, chapter 7 and chapter 8.

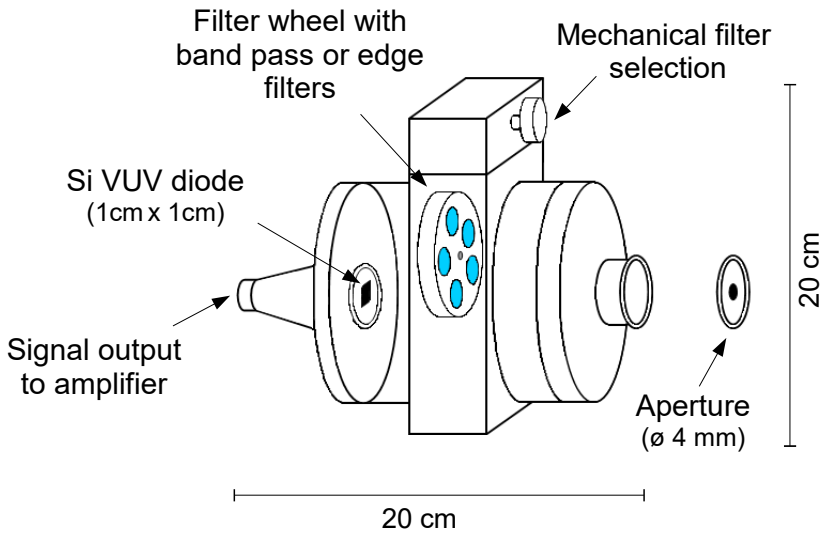

Figure 4.2: Design of the portable VUV diode system.

A sketch of the resulting diode system is is depicted in figure 4.2. With the

dimensions of 20 cm x 20 cm x 20 cm and a weight in the range of one to two kilogram, the diode system can be easily carried by hand.
The detector element is a silicon VUV photodiode (*AXUV100G*[1], Opto Diode) with an active area of 1 cm x 1 cm which is commercially available. The diode itself is based on a silicon n-p-junction with a 6 - 8 nm thick silicon oxide (SiO_2) layer on top. With its passivating characteristic, the SiO_2 window protects against dead regions and, therefore, against recombination losses [KPC+03] which leads to an internal quantum efficiency of 100%. The device is sensitive to incoming photons with a wavelength roughly in the range 10 - 1100 nm as well as electrons. The photon response of the VUV diode is depicted in figures 4.3 and 4.4.

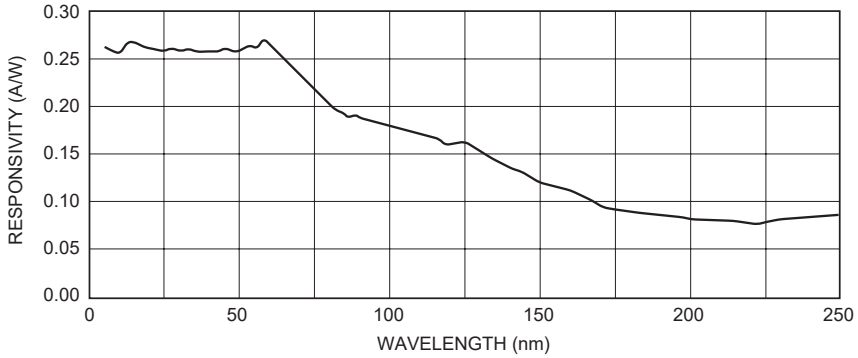

Figure 4.3: Photon response of the AXUV100G diode from the ultraviolet region down to the extrem ultraviolet spectral range, taken from the corresponding data sheet [Opt19].

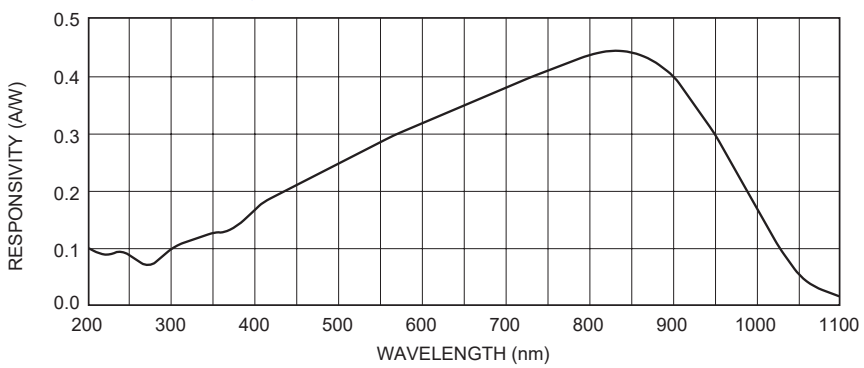

Figure 4.4: Photon response of the AXUV100G diode from the near infrared to the UV spectral range, taken from the corresponding data sheet [Opt19].

The resulting input current is amplified and converted by a pre amplifier (*Model 671, McPherson*) into a voltage output signal. The conversion/amplification

[1] A detailed characterization of the silicon diode can be found in [KPC+03, KRR+98]

factor was set to $10^4\,\mathrm{V/A}$ by default. The typical voltage range measured in this work was below 1 V. The signal is recorded with the same data acquisition system which is used for the VUV spectrometer.
To obtain a certain spectral resolution, band pass or edge filters are inserted into the mechanical filter wheel in front of the diode which has five available positions. One position is permanently occupied by a cover which is selected during two measurements in order to reduce aging effects of the filter and the diode by incoming VUV radiation. The filter set of four filters is chosen with respect to the investigated gas as well as to the photon energy region of interest and is selected manually during the measurement. Since the device has a very small volume, it is directly attached to the plasma chamber. The inserted filters do not prevent the gas flow, thus, no additional pumping system is required.
An aperture stop between the diode system and the plasma limits the solid angle to approximately 0.02 - 0.04 sr which is three orders of magnitude higher than the corresponding value of the VUV spectrometer. The diameter of the resulting viewing volume of the diode system at *PlanICE* is approximately 2 cm at the entrance into the plasma vessel and increases up to 5 cm at the opposite wall. Compared to the VUV spectrometer, the diode system detects photons from an horizontally and vertically enlarged volume including the plasma close to the top plate of the plasma vessel. In order to keep a sufficient signal-to-noise ratio, it was decided to waive a more narrow aperture in front of the diode system to adjust the viewing volumes of both diagnostics. However, it must be kept in mind for a proper interpretation of the measurements and the absolute intensity calibration of the device against the VUV spectrometer. The latter is presented in section 4.2.4.

4.2.1 Applied filters

The *filter transmission function* is given by the wavelength dependent ratio of the transmitted to the incoming radiation. It allows the definition of a specific wavelength interval in which the filter is transparent. It is referred to as *filter interval* in the following.
The filters were chosen with respect to relevant spectral emission ranges of photon fluxes which were identified for pure argon, hydrogen, nitrogen and oxygen plasmas as well as mixtures of them in section 6. The available filters include band pass and edge filters which are listed in table 4.1. The former type lets pass a rather narrow wavelength interval while radiation beyond is absorbed or

reflected. Usually, they are realized as interference filters which are made up of a substrate material with a series of semitransparent metallic films separated by a dielectric layer. The wavelength selection is based on the principle of a Fabry-Perot etalon and can be adjusted by the used materials and the layer thickness. Characteristic specifications are the central wavelength λ_0, the peak transmission and the FWHM of the transmitted wavelength interval. In contrast, edge filters are transparent for the entire spectrum *above* or *below* a specific wavelength which is commonly referred to as *cut-on* or *cut-off wavelength*, $\lambda_{\mathrm{cut-on}}$ and $\lambda_{\mathrm{cut-off}}$, respectively. According to their transmission range, edge filters are classified into long pass and short pass filters. Easily available window materials like MgF_2 or fused silica are suitable to serve as long pass filters. Regarding the VUV range, LiF is the material with the shortest known cut-on wavelength at roughly 105 nm. However, MgF_2 has been chosen due to the much lower vulnerability to water vapor [SE00]. The complete filter set of the diode system is summarized in table 4.1.

The transmission function of ideal filters which is depicted as a blue broken curve in figure 4.5 is characterized by a rectangular function resulting in a distinct filter interval and a sharp wavelength selection. In contrast, real filters exhibit a less steep behaviour at the edges of the transmission interval which can be exemplarily seen in the measured transmission curve of the bandpass filter 313BP. It is depicted as solid line in figure 4.5. In this case, the assignment of the corresponding filter interval is not unambiguous. Another difference to ideal filters is given by absorption or reflection within the transparent range which leads to a transmission of less than 1. The cut-on wavelength of long pass filters as well as the transmission range of band pass filters can slightly vary with the purity of the materials, the preparation process and the temperature. In general, a degradation due to aging might occur for all types of filters depending on the storage conditions (e.g. ambient pressure versus vacuum) and the handling. Moreover, high energetic radiation, e.g. VUV photon fluxes, contribute to the aging effects and lead to a gradual change of the filter transmission. Therefore, the transmission functions of all applied filters have been determined inhouse.

The transmission curves of the filters were measured using different radiation sources (e.g. a deuterium arc lamp, an Ulbricht sphere, a hydrogen discharge) together with the VUV or an optical spectrometer. They are summarized in the appendix (see figures D.1 and D.2). In the depicted example, the peak transmission is determined to 15.5 % at 312.8 nm and the FWHM accounts to 10 nm.

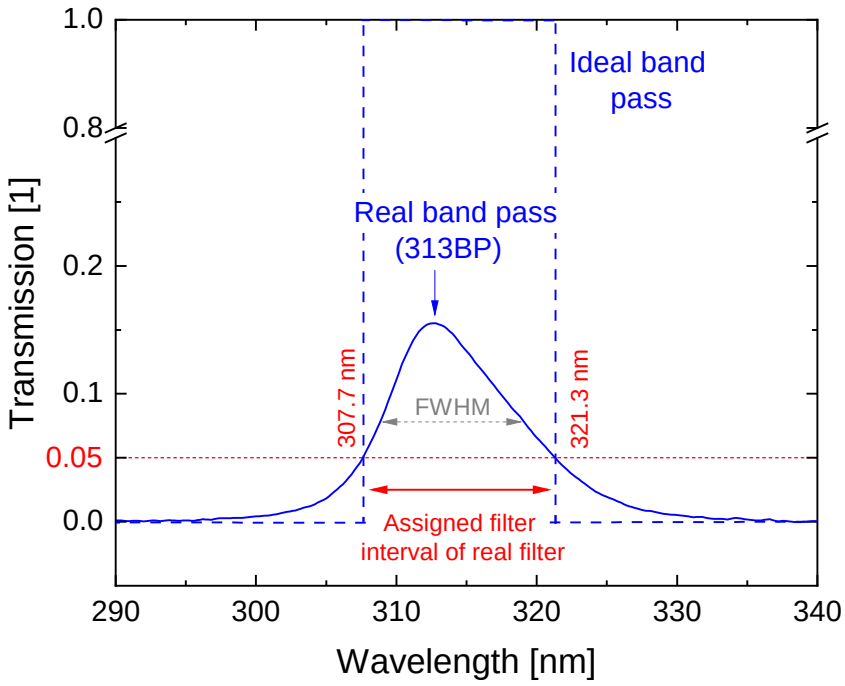

Figure 4.5: Transmission curve of the band pass filter 313BP measured with the deuterium arc lamp I and the optical emission survey spectrometer. The measured FWHM of 10 nm is indicated in gray and the peak transmission is 15.5 % at 312.8 nm. The filter interval corresponding to a transmission of equal or greater than 5 % is shown in red. The broken line represents an ideal filter transmission function with the limits of the determined filter interval.

If not otherwise stated, a transmission of greater or equal to 5 % was used for the definition of the filter interval in the present work which leads to an assigned filter interval of 307.7 - 321.3 nm for the given example.

Regarding the 337BP filter, the measured peak transmission is around 4 % and the standard definition of the corresponding filter interval is not applicable. Since the transmission curve is very narrow around the central wavelength, the limits of the filter interval were obtained at these wavelengths where the measured signal significantly exceeds the noise level.

The 122BP filter is an exception since the corresponding transmission curve could not be directly measured due to the lack of continuous radiation sources in the corresponding wavelength range. Using a hydrogen discharge revealed that only a narrow wavelength range around the L_α line is transmitted[1]. Hence, for this filter

[1]The peak transmission could be determined to roughly 6.3 % instead of 16.2 % given by

the manufacturer's value of the FWHM is given in table 4.1. Consequently, the Lyman-α line in the spectrum taken with the VUV spectrometer was exclusively assigned to the filter interval of the 122BP filter.

Table 4.1: Available filter set for the diode system consisting of (a) band pass and (b) long pass filters with measured central and cut-on wavelengths, respectively, as well as the FWHM for the band pass filters. Regarding the 122BP, the FWHM is given by the manufacturer.

Filter name	Central wavelength	FWHM	Filter interval
122BP	122 nm	14 nm	L_α
154BP	154 nm	30 nm	147 - 187 nm
230BP	230 nm	37 nm	196 - 268 nm
313BP	313 nm	10 nm	308 - 312 nm
337BP	337 nm	10 nm	330 - 344 nm

(a) Band pass filters

Filter name	Cut-on wavelength
MgF_2	113 nm
Fused silica	153 nm
BK7	281 nm
400LP	397 nm
500LP	500 nm

(b) Long pass filters

Depending on the spectral region of interest and the specific discharge gas, band pass filters are commercially available. If this is not the case, a combination of two long pass filters can act as a band pass filter with the wavelength interval limited by their cut-on wavelengths. Complementary measurements with a long pass filter and without any filter are also possible. In practice, a differential measurement techniques is applied where the two corresponding signals are measured with the diode system and then subtracted. In the following, such a filter combination will be indicated as "filter 1 – filter 2". An example for a filter combination consisting of two ideal long pass filters is shown in figure 4.6. The transmission curves are depicted in red and blue (right axis) while a the spectral emissivity of a nitrogen discharge at *PlanICE* is given in gray and black (left axis), respectively. The black part of the spectrum corresponds to the transmission interval if the differential measurement technique with filter 1 and filter 2 is applied.

the manufacturer.

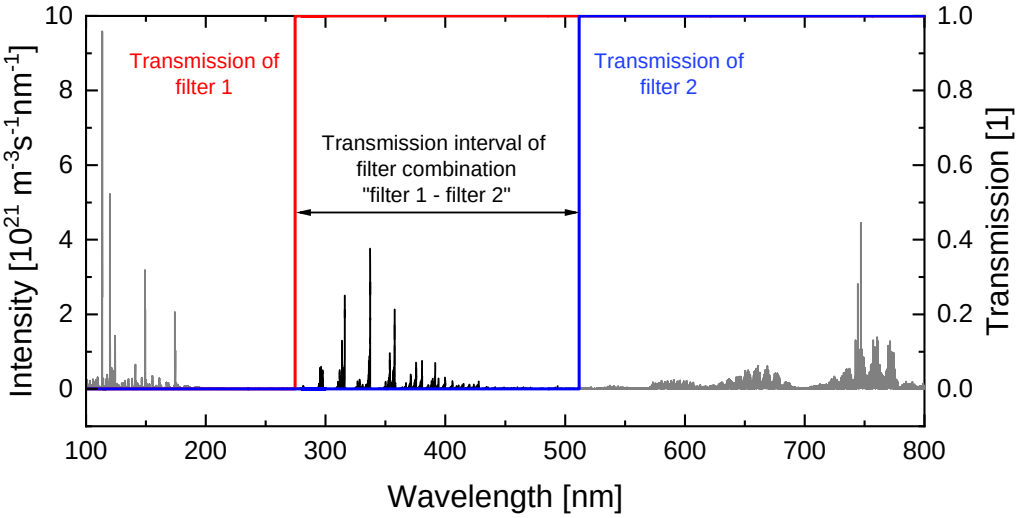

Figure 4.6: Example for the differential measurement technique using the a filter combination "filter 1 — filter 2" consisting of two ideal long pass filters. The transmission curves are depicted in red and blue (right axis), the spectral emissivity of a nitrogen discharge at *PlanICE* is shown in gray and black (left axis).

A coarse spectral resolution roughly into the VUV and the UV region is obtained with the filter combinations given in table 4.2. According to the particular plasma and energy ranges of interest, a gas specific filter set can be flexibly compiled for measurements with the diode system. The tables 4.3 to 4.7 give on overview of relevant emission features in the investigated gases argon, hydrogen, nitrogen, oxygen as well as mixtures thereof and the filter combination to select the corresponding emission range. For a detailed description how the emission ranges were identified, it is referred to section 6.

Table 4.2: Filter combinations for a coarse resolution into VUV and UV range.

Spectral range	Filter combination	Filter interval
VUV	No filter – fused silica	$\leq$ 153 nm, $\geq$ 8.1 eV
UV	Fused silica – 400LP	153 nm - 396 nm, 8.1 - 3.1 eV

Table 4.3: Filter combinations in argon with corresponding filter interval.

Gas	Emission feature	Filter combination	Filter interval
Ar	Ar^+ & Ar lines	No filter – MgF_2	$\leq$ 113 nm, $\geq$ 11.0 eV

Table 4.4: Filter combinations in hydrogen plasmas with corresponding filter interval.

Gas	Emission feature	Filter combination	Filter interval
H_2	L_α	122BP	$\approx$122 nm, $\approx$10.2 eV
H_2	Lyman band (B-X)	154BP	147 - 187 nm, 8.4 - 6.6 eV
H_2	Continuum (a-b)	230BP	196 - 268 nm, 6.3 - 4.6 eV
H_2	Werner band (C-X), $L_\beta, L_\gamma, \ldots$	No filter – MgF_2	$\leq$ 113 nm, $\geq$ 11.0 eV

Table 4.5: Filter combinations in nitrogen with corresponding filter interval (LBH: Lyman-Birge-Hopfield system, SPS: Second positive system).

Gas	Emission feature	Filter combination	Filter interval
N_2	N lines, part of LBH (a-X)	154BP	147 - 187 nm, 8.4 - 6.6 eV
N_2	N lines	No filter – MgF_2	$\leq$ 113 nm, $\geq$ 11.0 eV
N_2	LBH (a-X), N lines	MgF_2 – BK7	113 - 281 nm, 11.0 - 4.4 eV
N_2	SPS (C-B)	BK7 – 500LP	281 - 500 nm, 4.4 - 2.5 eV

Table 4.6: Filter combinations in oxygen with corresponding filter interval.

Gas	Emission feature	Filter combination	Filter interval
O_2	O and O^+ lines	No filter – Fused silica	$\leq$ 153 nm, $\geq$ 8.1 eV

Table 4.7: Filter combinations in gas mixtures with corresponding filter interval (LBH: Lyman-Birge-Hopfield system, SPS: Second positive system).

Gas mixture	Emission feature	Filter combination	Filter interval
N_2/H_2	NH band (A-X)	337BP	330 - 344 nm, 3.8 - 3.6 eV
N_2/H_2	SPS (C-B), NH band	BK7 – 500LP	281 - 500 nm, 4.4 - 2.5 eV
N_2/H_2	Emission of N, N_2, H, H_2	No filter – BK7	$\leq$ 281 nm, $\geq$ 4.4 eV
H_2/O_2	OH band (A-X)	313BP	308 - 312 nm, 4.0 - 3.9 eV
N_2/O_2	NO γ band (A-X)	230BP	196 - 268 nm, 6.3 - 4.6 eV
N_2/O_2	LBH (a-X), N & O lines, NO γ band	MgF_2 – BK7	113 - 281 nm, 11.0 - 4.4 eV

4.2.2 Remarks on the energy resolution

Broad filter transmission edges might set limitations regarding the energy resolution of the diode system, especially when applying the differential measurement techniques "filter 1 – filter 2".

The effect of the broad transmission curve of the MgF_2 window on the energy resolution of the diode system is illustrated in figure 4.7 with the spectra of a nitrogen/hydrogen mixture (50:50) at 0.3 Pa and 500 W generator power[1].

Absolute intensities (left axis) and the transmission curves of the MgF_2 window (broken lines, right axis) are displayed. The upper part represents the ideal case of a rectangular function (red) with the step at 113 nm which has been defined as the cut-on wavelength of the real MgF_2 window. The lower part shows the measured transmission curve (blue) of the real window. The spectra depicted in gray are directly obtained with the VUV spectrometer and correspond to the plasma emission observed by the diode system with "No filter". Applying the ideal or real filter transmission to the measured intensity gives the spectrum detected by the diode system with an ideal or real MgF_2 window, respectively. The red and blue intensities recreate the spectra corresponding to the applied differential

[1]The spectrum chosen for the illustration since the spectral distribution allows to clearly demonstrate the qualitative effect and is not intended for a physical interpretation.

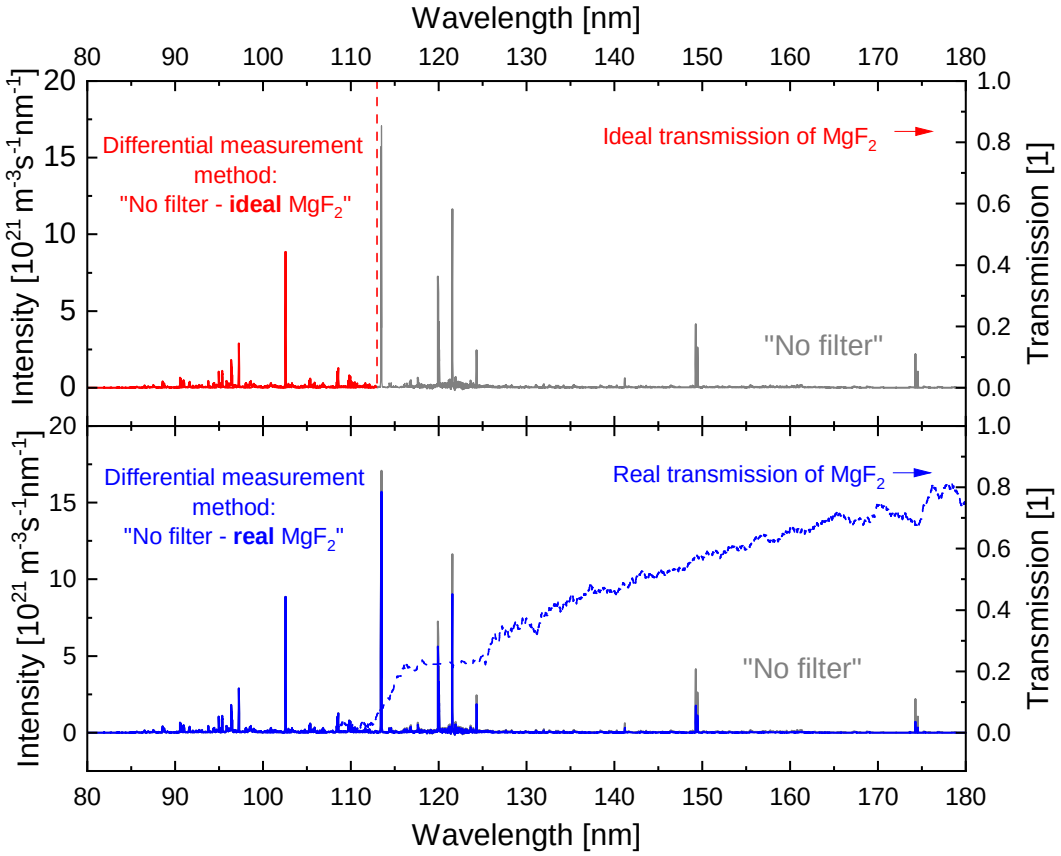

Figure 4.7: Influence of the broad transmission edge of the MgF_2 window on the energy resolution of the diode system. Absolute intensities of a hydrogen/nitrogen (50:50) plasma at 0.3 Pa and 500 W measured with the VUV spectrometer are depicted in gray (left axis) and represent the spectrum detected by the diode system with "No filter". The coloured solid lines represent the spectra corresponding to the differential measurement method "No filter – MgF_2" (upper part/red: ideal MgF_2, lower part/blue: real MgF_2). The corresponding filter transmissions are depicted with broken lines (right axis).

measurement technique using the filter combination "No filter – MgF_2".

In the ideal case, the resulting spectrum is sharply restricted to the filter interval. In contrast, the real filter transmission leads to the effect that 'additional' emission features above the filter interval limit of 113 nm are detected and the energy resolution does not fully agree with the given filter interval.

In the presented example, these are the L_α line at 121.6 nm and several atomic nitrogen lines, e.g. at 113.5 nm, 120 nm, 124.3 nm and at 149.3 nm. The 'additional' emission might produce a significant contribution to the measured diode signal. In the example, it even exceeds the total emissivity in the filter interval and would lead to an overestimation of the measured photon flux. The exact

portion of the additional emission might also vary with the operating parameters and is dependent on the specific gas composition.

In the same manner, this applies to the emission range corresponding to the Werner band together with parts of the Lyman serie in hydrogen which is accessible with the filter combination "No filter – MgF_2". Although the L_α line lies outside the definded filter interval of lower or equal to 113 nm, it is mostly detected by the diode system due to the transmission edge of the MgF_2 window. For gases which do not produce significant emission within the transmission edge of the MgF_2 window (e.g. argon), a better representation of the energy resolution is given by the filter interval.

Since the transmission edges of the fused silica window and the BK7 window are less broad (see figure D.2 in the appendix), the described effect is expected to be less pronounced for filter combinations in which these windows are applied for the upper limit of the filter interva, e.g. for the VUV range ("No filter – Fused silica").

On the other hand, if filters with a broad transmission edge serve for the lower limitation of the filter combination's interval, the reverse effect might arise during the differential measurement technique with a underestimation of the corresponding photon flux.

In order to minimize the described effects, filters or windows with a transmission edge as narrow as possible are highly preferable. For the optical region, edge pass filters with an almost ideal transmission are commercially available. However, the situation appears to be much more challenging regarding the UV and VUV range.

4.2.3 Effective volume

The interplay of the diode system's viewing volume and the specific geometry of the experiment determine the fraction of the isotropic radiation reaching the surface of the silicon diode. The portion of the photons being emitted at an arbitrary location $\mathbf{r}$ in the plasma and being detected by the diode system is calculated by the ratio of the solid angle $\Omega(\mathbf{r})$ spanned by the surface A_{diode} of the silicon diode and the solid angle of the whole space given by 4π. Considering the distance d of $\mathbf{r}$ from the center of the silion diode and its possible tilting by

the angle θ, $\Omega(\mathbf{r})$ is calculated with

$$\Omega(\mathbf{r}) = \frac{A_{\text{diode}}\cos(\theta)}{d^2}. \tag{4.2}$$

θ describes the angle between $\mathbf{r}$ and the normal of the diode surface with the coordinates' origin in the center of the diode area. Taking into account the viewing volume V_{diode} of the diode system, the *effective volume* is determined by

$$V_{\text{eff}} = \int_{V_{\text{diode}}} \frac{\Omega(\mathbf{r})}{4\pi} \mathrm{d}V. \tag{4.3}$$

In this definition, a total illumination of the diode area by each plasma volume element is assumed. The effective volume depends on the specific setup in use. Therefore, the absolute calibration factors for the diode system obtained at *PlanICE* are inherently linked to the corresponding effective volume $V_{\text{eff,PlanICE}}$. When the diode system is transferred to other experiments, a careful evaluation of the respective effective volume V_{eff} is crucial. The measurement results must be divided by the factor $\frac{V_{\text{eff}}}{V_{\text{eff,PlanICE}}}$.
A simplification of the setup's geometry allows to determine the effective volume analytically. In this approach, the square surface of the diode is approximated by circular areas, one with the diameter corresponding to the diode's edge length and one with the diameter corresponding to the diode's diagonal. Finally, the results are averaged. The simplified geometry of the diode system at an exemplary plasma vessel is displayed in figure 4.8. The viewing volume of the diode system is depicted in blue and the solid angle for an example location $\mathbf{r}$ is shown in orange. Choosing cylindrical coordinates, the effective volume can be expressed and solved analytically as

$$\begin{aligned} V_{\text{eff}} &= \int_0^{2\pi} \int_{z_0}^{z_1} \int_0^R \frac{\Omega(\mathbf{r})}{4\pi} r \mathrm{d}\varphi \mathrm{d}z \mathrm{d}r \\ &= \int_0^{2\pi} \int_{z_0}^{z_1} \int_0^R \frac{A_{\text{diode}}}{4\pi(r^2+z^2)} \frac{zr}{\sqrt{r^2+z^2}} \mathrm{d}\varphi \mathrm{d}z \mathrm{d}r \\ &= \frac{A_{\text{diode}}}{2}(z_1 - z_0)\Big[\Big(\frac{R^2}{z_1^2}+1\Big)^{-\frac{1}{2}} + 1\Big]. \end{aligned} \tag{4.4}$$

In the case of an experimental setup with a rather complex geometry, ray tracing algorithms are a convenient tool for calculating the effective volume which

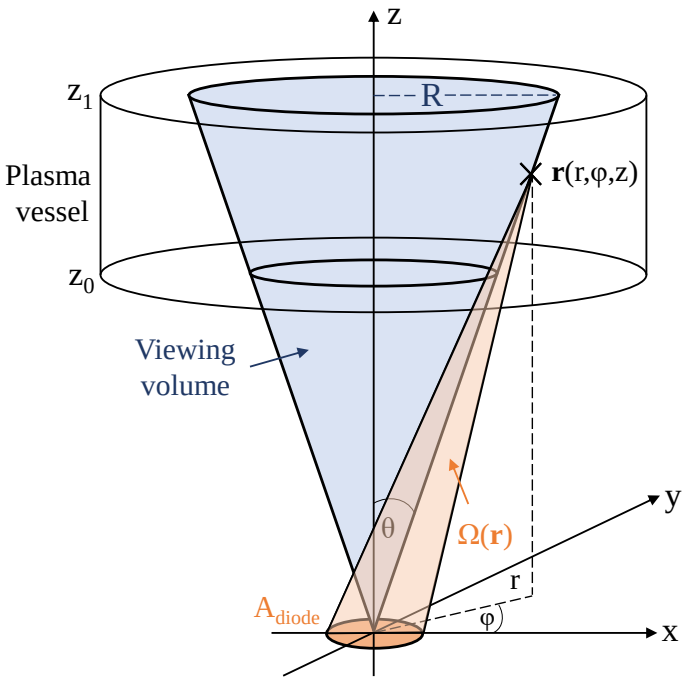

Figure 4.8: Simplified geometry and effective volume of the diode system at an exemplary plasma vessel.

is seen by the diode system. Basically, they calculate the integral in equation (4.2.3) considering the geometrical arrangement and including masking effects of components. In this work, results from the ray tracing code described in [Hur20] are applied in section 8.3.

4.2.4 Calibration against the VUV spectrometer

The intensity calibration of the diode system was performed in pure gases via simultaneous measurements together with the absolutely intensity calibrated VUV spectrometer as well as with the high resolution optical spectrometer at *PlanICE*. Obtained calibration factors directly include the wavelength dependent sensitivity of the silicon diode, the transmission curve of the filters as well as properties of the pre amplifier and of the voltage measurement device, respectively.
Due to the diagnostics' different viewing volumes and their applied lines of sight, a homogeneous plasma emission across the cones and a rotational symmetry of the discharge have to be provided.
Vertical emission profiles in the plasma vessel originate from a vertical profile of the plasma parameters, e.g. electron temperature and density, and evolve with increasing pressure in molecular discharges. The viewing volume of the diode sys-

tem is more expanded in vertical direction compared to the one of the reference spectrometer. Therefore, the diode system is able to detect the intense part of the discharge which is progressively constricted in the region below the quartz plate with increasing pressure. Considering the respective diffusion coefficients of neutral atoms and ions in equation (2.48) and (2.50), a homogeneous vertical plasma emission is predominantly expected at low pressure and high generator power. The vertical plasma homogeneity was investigated in pure nitrogen, hydrogen and argon with the optical survey emission spectrometer. Vertical profiles of exemplar emission ranges were recorded for a pressure variation. The power was adjusted individually for the specific feed gas in order to avoid excessive heating of the experiment's components. Results for nitrogen are exemplarily deicted in figure 4.9, those for hydrogen and argon are given in figures E.1 and E.2 of the appendix. The measurements confirm a homogeneous emission across the vertical section through the plasma vessel within ±11 % in nitrogen, ±12 % and ±9 % in argon at 1 Pa.

The rotational symmetry of the plasma was confirmed with the moveable Langmuir probe and optical emission spectroscopy at different rotation-symmetric lines of sight. The results agree within the limits given by the measurement errors below ±10 %.

The discharges rarely produce a continuous emission within the identified filter intervals. Moreover, the intensity distribution strongly varies with the feed gas. In combination with the nonideal filter transmission curves and the wavelength dependency of the diode's responsitivity, a calibration specifically for each filter combination and gas is required.

Calibration measurements have been performed at two different generator powers, and the results are averaged. The final calibration factor $K_{\mathrm{Gas}}^{\mathrm{Filter}}$ is determined by the ratio of the absolute emissivity $\epsilon_{\mathrm{Gas}}^{\mathrm{Filter}}$ integrated over the corresponding filter interval in the spectrum measured with the VUV spectrometer and the respective voltage signal $S_{\mathrm{Gas}}^{\mathrm{Filter}}$ from the diode system,

$$K_{\mathrm{Gas}}^{\mathrm{Filter}} = \frac{\epsilon_{\mathrm{Gas}}^{\mathrm{Filter}}}{S_{\mathrm{Gas}}^{\mathrm{Filter}}}. \tag{4.5}$$

The absolute calibration then allows to convert the voltage signal measured with

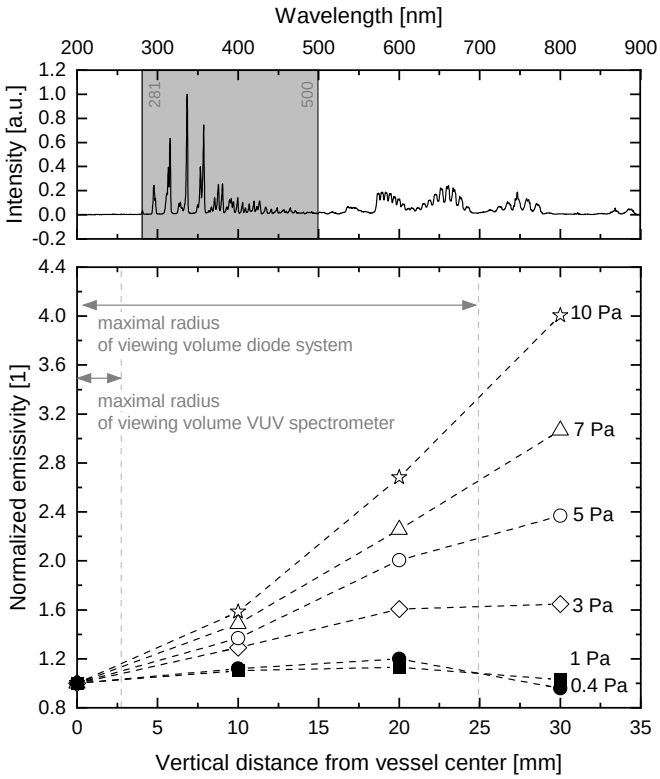

Figure 4.9: Pressure dependent vertical emission profile in nitrogen at a generator power of 400 W. The upper part shows a spectrum at 1 Pa taken with the optical survey spectrometer taken at the vessel center. The investigated wavelength range roughly corresponds to the second positive system of N_2. The integrated emissivities are displayed in the lower part with a normalization at the vessel center. The maximal radii of the viewing volumes of the diode system and the VUV spectrometer are indicated.

the diode system into the emissivity $\epsilon_{\mathrm{Gas}}(E_1, E_2)$ by

$$\epsilon_{\mathrm{Gas}}(E_1, E_2) = K_{\mathrm{Gas}}^{\mathrm{Filter}} \cdot S_{\mathrm{Gas}}^{\mathrm{Filter}} \tag{4.6}$$

in units of $\mathrm{m}^{-3}\mathrm{s}^{-1}$. With equation (5.21) and a volume-to-surface ratio at *Plan-ICE* of 0.021 m, the resulting photon flux can be calculated. The energy of the detected photons is in the range between E_1 and E_2 which are determined by the transmission interval of the selected filter.

Figure 4.10 illustrates the calibration procedure exemplarily in hydrogen for the filter combination "No filter – MgF_2" as well as the bandpass filters 154BP and 230BP. They are assigned to the Lyman lines $L_\beta, L_\gamma, \ldots$ together with the Werner band, the Lyman band and the Continuum, respectively. The absolute intensity

(black, left axis) and the measured transmission curves (coloured lines, right axis) are displayed. The corresponding filter intervals with a transmission greater or equal to 5 %, in which the intensity is integrated, are highlighted in the corresponding colour.

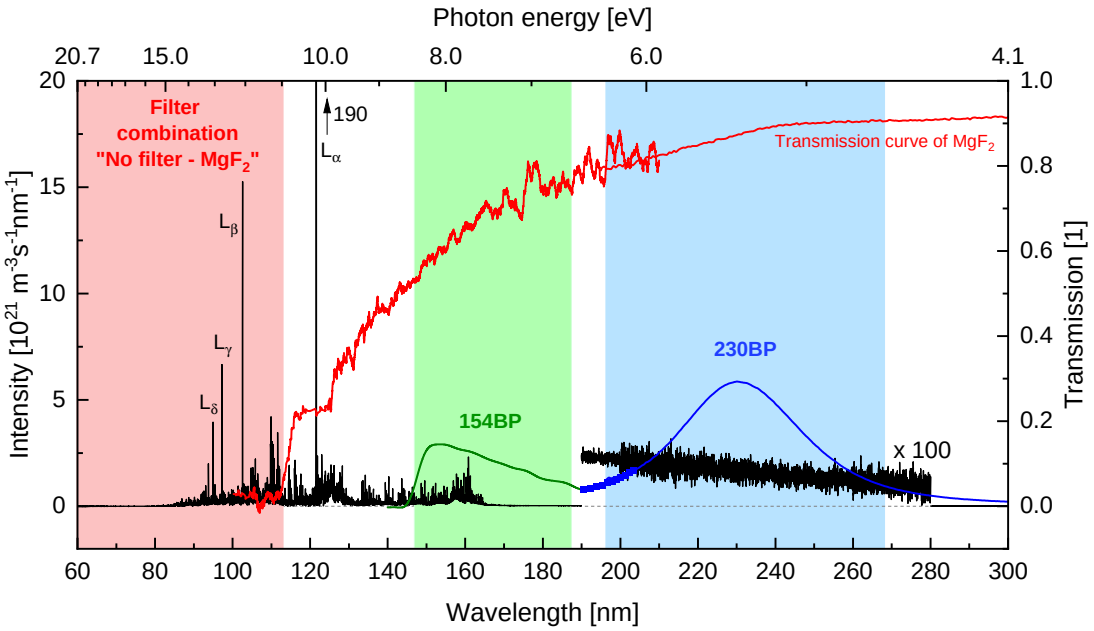

Figure 4.10: Example of an absolutely calibrated hydrogen spectrum (black line, intensity on left axis) at 1 Pa and 1100 W generator power with the measurend transmission curves of the 154BP and 230BP filter as well as the MgF_2 window (coloured lines, right axis). The corresponding wavelength ranges, which are integrated in the spectrum for the calibration of the diode system, are highlighted. The wavelength range 190 - 280 nm is displayed with an amplification factor of 100.

In general, the calibration of a specific filter combination is performed in pure gases. For example, the filter combinations for the VUV and UV range were independently calibrated in the pure gases argon, hydrogen, nitrogen and oxygen. The resulting calibration factors are summarized in table 4.8. In the same manner, the calibration of the diode system with the filter combinations corresponding to the emission ranges listed in table 4.9 was performed individually in the pure gases.

If a filter combination is applied in a gas mixture, a linear combination of the pure gas calibration factors according to the gas composition is recommended. For example, for determining photon fluxes from the VUV range in the hydrogen/oxygen mixture (85:15) the calibration factor was calculated according to

Table 4.8: Calibration factors of the diode system in units of $10^{22}\,\mathrm{m^{-3}s^{-1}V^{-1}}$ for the VUV and UV range in **pure gases**. The related measurement range of the voltmeter is indicated and the last column gives the calculated relative uncertainty of the absolute calibration. The corresponding filter combinations and filter intervals are summarized in table 4.2.

Spectral Range	Ar 300 mV	Ar 3 V	H_2 300 mV	N_2 300 mV	O_2 300 mV	Relative uncertainty
VUV	35	36	20	19	22	60 %
UV	1	0.1	33	25	27	25 %

Table 4.9: Calibration factors of the diode system in units of $10^{22}\,\mathrm{m^{-3}s^{-1}V^{-1}}$ in **pure gases**. The voltmeter's measurement range is "300 mV" with the exception of argon (first value: "300 mV", second value: "3 V"). For the band pass filters in hydrogen, two values are given since two calibrations have been performed: The first values is valid for measurements before January 2019, the latter for subsequent measurements. The last column gives the calculated relative uncertainty of the absolute calibration. The corresponding filter combinations and filter intervals are summarized in the tables 4.3 to 4.6.

Gas	Emission feature	Calibration factor	Relative uncertainty
Ar	Ar & Ar^+ lines	38; 39	60 %
H_2	L_α	61; 53	24 %
H_2	Lyman band (B-X)	160; 100	17 %
H_2	Continuum (a-b)	145; 123	25 %
H_2	Werner band (C-X), $L_\beta, L_\gamma, \ldots$	15	60 %
N_2	N lines, part of LBH (a-X)	126	17 %
N_2	N lines (below 113 nm)	12	60 %
N_2	LBH (a-X), N lines	23	60 %
N_2	SPS (C-B)	30	10 %
O_2	O and O^+ lines	22	60 %

$K^{\mathrm{VUV}}_{\mathrm{H2/O2}} = 0.85 \cdot 20 + 0.15 \cdot 22 = 20.3$ with the pure gas values taken from table 4.8.

However, if only one of the mixture's constituent gases produce a significant emission in the filter interval, the calibration factor of the corresponding pure gas was applied. This was the case in the investigated nitrogen containing plasmas for the filter combinations "BK7 – 500LP", "No filter – BK7" and "MgF_2 –

BK7" since the corresponding filter intervals are mainly dominated by emission from molecular nitrogen, e.g. Second positive system and Lyman-Birge-Hopfield system. This context is the responsibility of the experimental user at the specific setup where the diode system is applied.
If additional emission ranges exist in gas mixtures arising from composite molecules (e.g. the NO band in nitrogen/oxygen discharges), the corresponding filter combination was exemplarily calibrated at a fixed gas composition in this work. The results are summarized in table 4.10.

Table 4.10: Calibration factors of the diode system in units of $10^{22}\,\mathrm{m^{-3}s^{-1}V^{-1}}$ for emission ranges of composite molecules in **gas mixtures**. The values were directly obtained in the mixture at the fixed gas composition which is given in brackets. The voltmeter's measurement range is "300 mV". The last column gives the calculated relative uncertainty of the absolute calibration. The corresponding filter combinations and filter intervals are summarized in table 4.7.

Gas mixture	Emission feature	Calibration factor	Relative uncertainty
N_2/H_2 (50:50)	NH band (A-X)	1110	10 %
H_2/O_2 (85:15)	OH band (A-X)	489	10 %
N_2/O_2 (80:20)	NO γ band (A-X)	112	25 %

Uncertainty sources

The quantification of photon fluxes with the diode system is subject to several uncertainties including the contribution assigned to the diode system's signal and to the intensity calibration against the VUV spectrometer. The former was determined to a value of ±3 % in section 4.2.5 and the latter will be discussed in the following.
The relative uncertainty of the absolute calibration of the VUV spectrometer and the optical spectrometer (±10 %) is directly transferred. Due to the wavelength dependency of the VUV spectrometer's calibration, the relative uncertainty of the diode systems' calibration is determined indivually for each filter combination. Since the uncertainty of the VUV spectrometer might vary within the corresponding filter interval, the maximum uncertainty value is applied for the diode system.
The results for the relative uncertainty of the calibration factor, which are obtained with a Gaussian error propagation, are summarized in the last column of

the tables 4.8, 4.9 and 4.10. They range from 10 % up to 60 % depending on the specific filter (combination). For evaluating the emissivity with equation (4.6) and in the following the photon flux, the diode's signal relative uncertainty of ±3 % has to be applied again in a Gaussian error propagation[1].
For the sake of completeness, a qualitative remark about the calibration of the diode in oxygen is given. In oxygen plasmas, photon fluxes from atomic and ionic oxygen lines can be obtained with the diode system and filter combination "No filter – Fused silica". In this case, the filter interval is crucially determined by the sensitivity of the silicon diode. As can be seen in figure 4.3, the diode's sensitivity reaches a maximum plateau in the range of roughly 10 - 60 nm. In contrast, absolute measurements with the VUV spectrometer are restricted to the wavelength range 46 - 300 nm. If photon fluxes arise below 46 nm, e.g. from oxygen ions at 43.0 nm ($2p^2 3d\ ^4\mathrm{P} \rightarrow 2p^3\ ^4\mathrm{S}^\circ$, $A_{ik} = 4.3 \cdot 10^9\,\mathrm{s}^{-1}$) [KYRa19e], they are exclusively recorded by the diode system and might falsify the calibration factor. This effect is expected to occur at very low pressure, however, a quantitative estimation of the effect is not possible. Apart from very specific plasma applications, e.g. impurity studies in the extreme ultraviolet region on fusion plasmas [KCF+18], the effect is considered to be of small importance.

4.2.5 Stability and performance aspects

The following section deals with the basic aspects regarding the performance of the diode system, e.g. the accessible dynamic range, the linearity of the signal output, the temporal stability as well as aging effects have been studied.

Dynamic range

The dynamic range of the diode system is characterized by the maximum and the minimum of the measurable photon flux which, in turn, is determined by the dynamic range of the output voltage signal weighted with the specific calibration factor. Since the latter is dependent on the energy range as well as on the investigated gas, this is also the case for the accessible dynamic range of the photon flux.
The upper detection limit is determined by the maximum voltage output of the pre amplifier which is given as ±14 V. However, it is recommended by the manufacturer not to exceed ±10 V and to choose the amplification setting accordingly. An amplification factor of 10^4 has been chosen.

[1] The volume-to-surface ratio of the vessel is assumed to be accurate.

The lower limit of the dynamic range is characterized by noise which may arise from all components of the diode system and may be composed of different contributions, e.g. thermal noise or shot noise [Mül90]. Additionally, the noise level might be increased by stray RF radiation which, in turn, is influenced by the discharge pressure and the generator power. This effect is depending on the specific experimental setup and might be influenced by the generator frequency, the distance of the diode system from the RF components and the grounding concept of the setup.

The noise level was investigated during offset measurements (i.e. no illumination of the diode due to the cover) in pressure and power scans. It depends on the gas and slightly on the pressure and power parameters. No significant influence of the measurement range of the digital multimeter was observed. The absolute value ranges between $6.2 \cdot 10^{-6}\,\mathrm{V}$ in oxygen up to $7 \cdot 10^{-4}\,\mathrm{V}$ in argon.

Exemplarily for the resonant atomic argon lines at 104.8 nm and 106.7 nm which are accessible with the filter combination "No filter – MgF_2", these voltage limits result in photon fluxes in the range from $5.9 \cdot 10^{18}\,\mathrm{m^{-2}s^{-1}}$ to $8.4 \cdot 10^{22}\,\mathrm{m^{-2}s^{-1}}$. The corresponding calibration factor of $39 \cdot 10^{22}\,\mathrm{m^{-3}s^{-1}V^{-1}}$ for the diode system's 3 V measurement range was taken from table 4.9.

Linearity

Using the emission from a plasma at *PlanICE*, the linear response of the diode system was roughly tested during power scans at constant pressure of 1 Pa. They were performed during the benchmark measurements with the diode system in argon, hydrogen, oxygen and nitrogen as well as the mixtures nitrogen/hydrogen (50:50), hydrogen/oxygen (85:15) and nitrogen/oxygen (80:20) which are described in detail in chapter 7.

Based on the power balance and considering only electron excitation, a linear dependence of the radiation intensity on the absorbed power is expected.

Exemplary results for the resonant atomic argon lines at 104.8 nm and 106.7 nm measured with filter combination "No filter – MgF_2" and obtained in the power scan are depicted in figure 4.11 together with the electron temperature T_e and the electron density n_e. The horizontal axis gives the power transferred to the plasma considering the coupling efficiency of the discharges. The electron temperature stays constant while the electron density increases linearly with the transferred power. Also, the resulting photon fluxes follow a linear trend, however, with a slightly different slope.

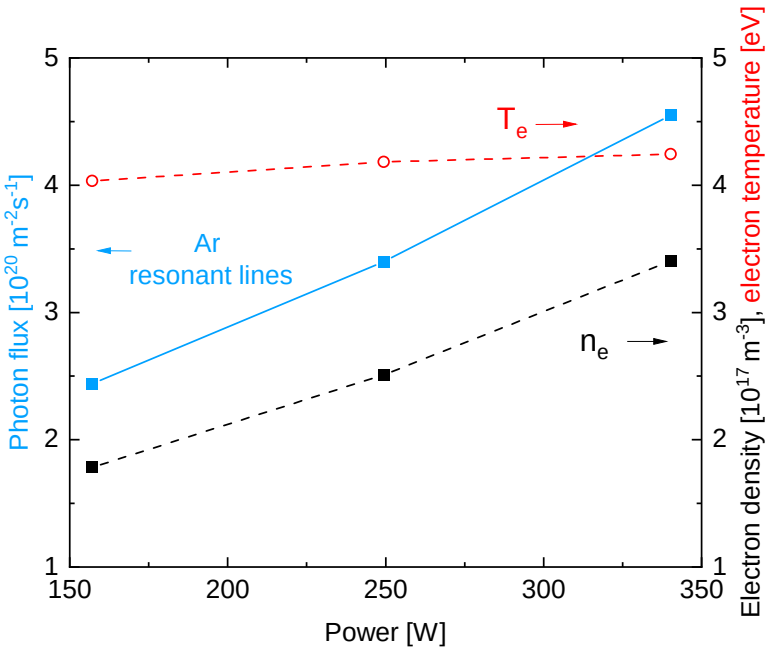

Figure 4.11: Power scan in argon at 1 Pa. The horizontal axis give the power transferred to the plasma considering the coupling efficiency. The photon flux arising from the atomic resonant argon emission lines is depicted in blue (left axis). The right axis refers to the electron density (black) and the electron temperature (red).

The photon fluxes from all investigated gases which were determined during power scans at *PlanICE* are summarized in section F of the appendix. In a good approximation, they show a linear increase with the power transferred to the plasma. Taking into account that the diode output voltages[1] were in the range between $4.4 \cdot 10^{-5}$ V (NH band in nitrogen/hydrogen at 1 Pa and 300 W generator power) and 0.18 V (VUV range in hydrogen/oxygen at 1 Pa and 1100 W generator power), the diode system's linearity was checked in a voltage interval extending over more than three orders of magnitude.

Temporal stability and measurement procedure

The temporal behaviour of the output signal during a illumination of several minutes by a hydrogen discharge has been monitored exemplarily with the bandpass filters for the L_α line and the Lyman band at a hydrogen discharge. The corresponding filters, 122BP and 154BP, are representatives of a bandpass filter

[1] The investigated signals were offset corrected. For filter combinations based on subtracting the signals of two edge filters, the difference signal was used.

with a very narrow filter interval selecting only one atomic line and a bandpass filter with a rather broad filter interval around 40 nm applied for molecular emission. Measurement intervals of 5 minutes and 7 - 8 minutes, respectively, have been chosen. Figure 4.12 presents the evolution of the voltage measured with the diode system for both filters (left axis, black curves)[1]. Additionally, the relative intensity of corresponding transitions in the optical region have been recorded with the survey optical emission spectrometer (right axis, gray lines in figure 4.12) in order to check on the stability of the plasma. The atomic H_α line was chosen regarding the L_α line measured with the 122BP filter while the signal of the 154BP filter assigned to the Lyman band was compared with the integrated emissivity of the molecular Fulcher transition. The atomic emission measured with the optical spectrometer shows an overall decrease of -10 % over the entire measurement period, the molecular emission declines by -4 %.

As can be seen from the figure 4.12, the output of the diode system is not constant during the time of illumination and shows a filter or transition specific variation. The 122BP (L_α) and the 154BP filter (Lyman band) exhibit both a temporal dynamic directly connected to the exposure to the plasma: The signal with the 122BP filter is increasing during the illumination of 5 minutes. In contrast, a decrease of the signal is observed for the 154BP filter. Maybe, this different behaviour might be traced back to different substrate materials. According to the manufacturer, the substrate of the 122BP filter is MgF_2 while the substrate of the 154BP filter is cultured quartz [Pen22]. Since the observed standard variation of the output signal from the averaged value taking into account the entire recording interval of 5 - 8 minutes is below ± 1 % for both filters, the different behaviour was not further investigated.

It appears that the curves flatten with time, but no distinct saturation of the signal occurs. During the periods without illumination between two measurement intervals, a recovery of the signal intensity indicated in green in figure 4.12 (b) can be detected for both filters. The starting values of the corresponding previous measurement interval, which are given as gray dashed horizontal lines, are roughly reached.

The dependence of the recovery effect on the length of the (non-)illumination

[1]The presented measurements were performed to derive conclusions about the diode system's qualitative temporal behaviour at a preliminary stage and, thus, prior to the absolute calibration against the VUV spectrometer presented in section 4.2.4. The setup of the VUV spectrometer was changed in between these stability measurements and, therefore, its absolute calibration. Hence, a quantification of the incoming photon fluxes from the results in figure 4.12 is not possible.

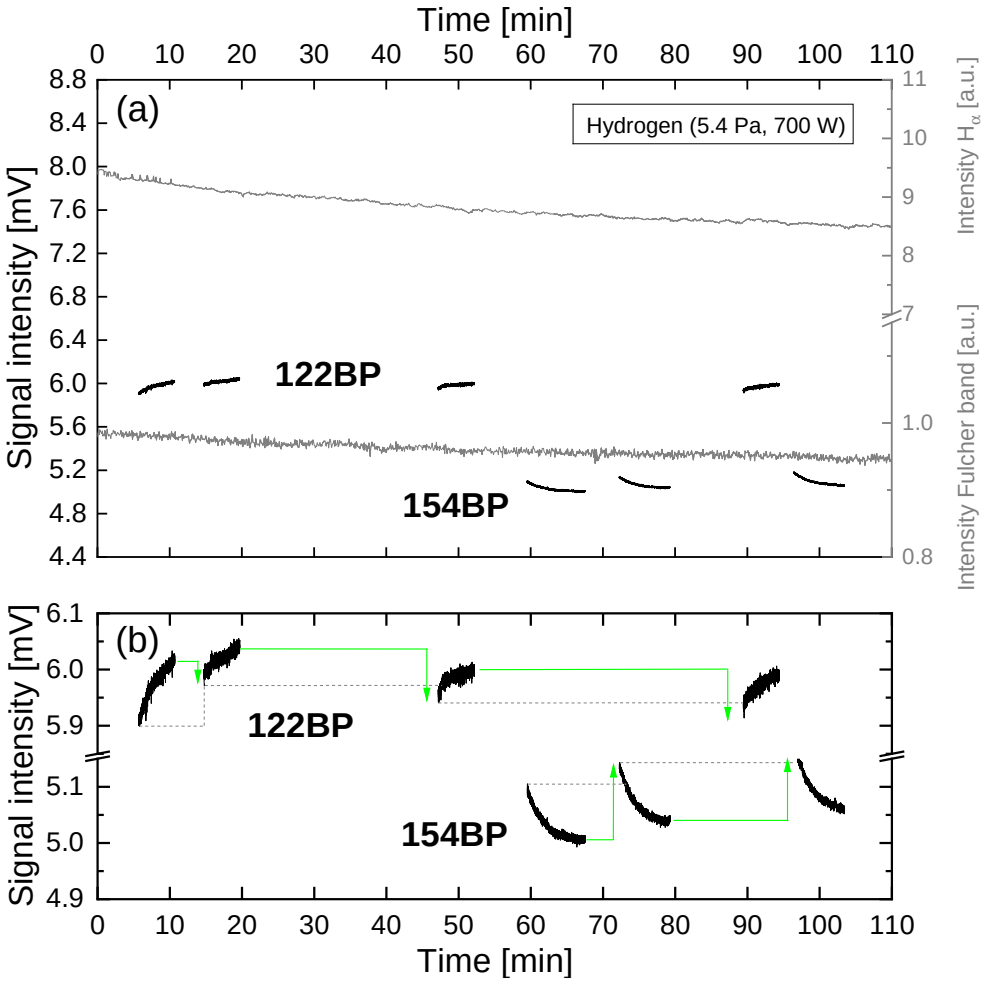

Figure 4.12: Temporal behaviour of the diode signal with the 122BP for the L_α line and the 154BP filter for the Lyman band (black, left axis) in hydrogen at 1 Pa and a generator power of 700 W. (a) Additionally, the relative intensity of the H_α line and the Fulcher band (gray lines, right axis) are depicted in arbitrary units to give an impression about the plasma stability. (b) The diode system's output signals for the for both filters are shown on a enlarged scale to give an impression about the temporal dynamic under illumination. The standard deviation from the averaged value of the diode signal within the measurement interval of 5 - 8 minutes each is below ±1 %. The observed recovery of the diode signal without illumination with respect to the starting values of the previous measurement is indicated in green.

periods between the measurement intervals has not been examined. The observed aspects might indicate the production of so-called colour centers within the filter material in contact with ionising radiation with subsequent recovery without illumination. These lattice defects produce wavelength and material de-

pendent absorption bands which underlie temporal dependent reverse bleaching processes [Sei46, Sei54, DV57].

In order to achieve a reproducible data acquisition, the exposure of the filters to radiation should be kept as short as possible during the measurements with the diode system as well as during the time interval between two measurements. The latter is achieved by inserting the aluminum cover. For the former, a standard measurement procedure has been developed: One measurement cycle starts with an offset measurement followed by measurements with the filters in the four remaining positions in the filter wheel. A measurement interval (i.e. with illumination) of 30 seconds was chosen for each filter in the filter wheel as well as for the offset measurement with the aluminium cover. A second offset measurement closes the measurement cycle.

The average of the last 15 seconds gives the voltage signal $S_{\mathrm{Gas}}^{\mathrm{Filter}}$ of the diode system and the corresponding filter or the aluminium cover. Regarding the two offset measurements, the resulting values are averaged and subtracted from the results obtained with the filters. Using equation (4.6) together with the corresponding calibration factor gives the emissivity arising from the respective energy range which is defined by the filter interval.

In figure 4.13, an example for a single measurement with the diode system and the 122BP filter for the L_α line in hydrogen at 1 Pa and 1100 W generator power is shown. The diode's output voltage measured with the filter is already corrected by the average of both offset measurements (green lines). The red line indicates the average of the signal during the second 15 seconds leading to a value of 10.54 mV. Applying equation (4.6) with the corresponding calibration factor of $53 \cdot 10^{22}\,\mathrm{m^{-3}s^{-1}V^{-1}}$, which is taken from table 4.9, gives an emissivity of $5.6 \cdot 10^{21}\,\mathrm{m^{-3}s^{-1}}$. With the vessel's volume-to-surface ratio of 0.021 m, a photon flux of $1.2 \cdot 10^{20}\,\mathrm{m^{-2}s^{-1}}$ is obtained.

During the benchmark measurements presented in section 7, the variation of the diode's signal in the second 15 seconds has been examined for the filters in each corresponding gas (mixture). For this investigation, plasmas at the crossing point of the power and pressure scans were chosen (e.g. H_2: 1 Pa, 700 W generator power). The standard deviation of the diode signal within the second 15 seconds from the averaged value, which was obtained from the presented evaluation, is less that 3 %. Therefore, a reproducible data acquisition with the described method is assumed.

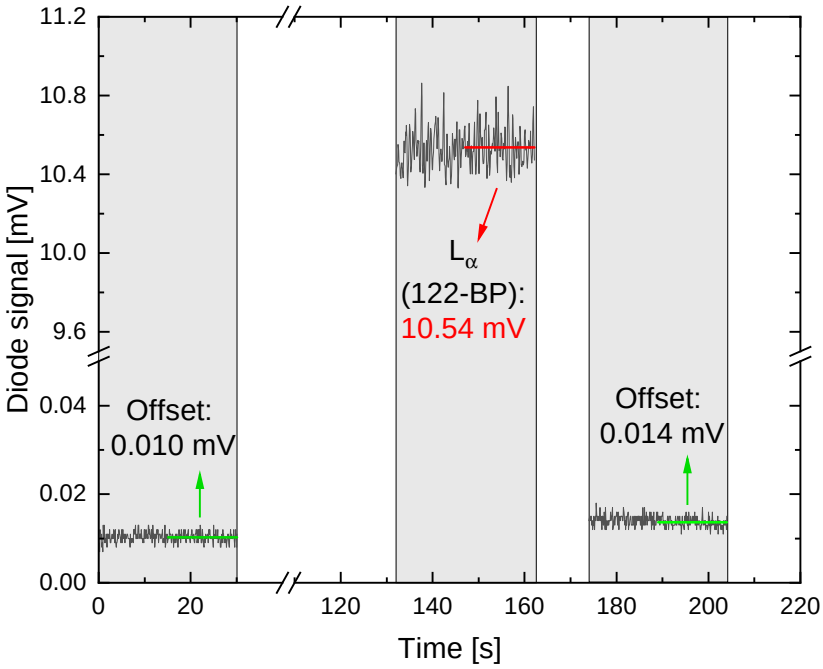

Figure 4.13: Example for the measurement procedure with the diode system and the 122BP filter for the L_α line in hydrogen (1 Pa, 1100W generator power). The voltage signals are depicted in black. The diode's signal with the filter is already offset-corrected by the average of the two offset-measurements (green lines, average of 0.010 mV and 0.014 mV). Averaging the diode's signal with the 122BP filter within the second 15 seconds of the measurement interval leads to a value of 10.54 mV (red line).

Apart from the dynamic behaviour during illumination within the measurement interval, the reproducibility of $S_{\text{Gas}}^{\text{Filter}}$ obtained from the presented evaluation has been exemplarily investigated for the L_α line with the 122BP filter. For this purpose, a series of successive measurements of the L_α line with the diode system and the VUV spectrometer in a hydrogen/oxygen discharge has been performed extending over the period of roughly two hours. It is accompanied by a continuous monitoring of the H_α emission. Each sequence consists of three measurements with the diode system (full squares) with an offset measurement (i.e. no illumination) in between and one scan of the L_α line with the VUV spectrometer (open squares). The standard measurement procedure was applied for the diode system. Normalized signals are presented in figure 4.14.

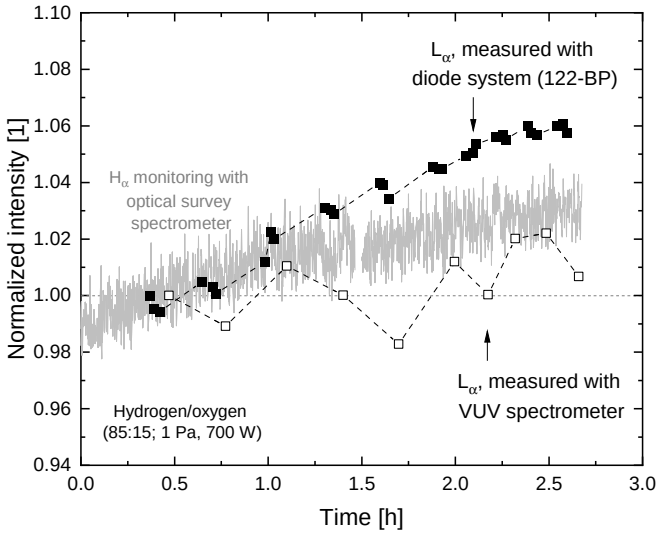

Figure 4.14: Reproducibility of the diode system expemplarily investigated with the 122-BP filter (full squares). For comparison, the emissivity of the L_α line was measured with the VUV spectrometer (open symbols). The stability of the plasma is monitored with optical emission spectroscopy via the H_α line (gray curve). Intensities normalized to the values roughly after 3.5 hours of plasma operation are displayed.

The intensity of the H_α line shows a minor increase by 3 % which is roughly followed by the intensity of L_α measured with the VUV spectrometer. Regarding the diode system, the relative standard deviation of the results with respect to the mean value is below 1 % for each series of three successive measurements and below 3 % considering all measurements. The long term behaviour of the L_α line measured with the diode system shows an increase of 6 %. The deviation of the absolute emissivity calculated with the corresponding calibration factor from the value obtained with the VUV spectrometer can be traced back to the spectral distribution in hydrogen/oxygen plasmas' emission within the transparent interval of the 122BP filter. Since the temporal variation of the relative standard deviation is less than 3 % at least within the two investigated hours of plasma operation, the diode system is considered to allow long-term measurements with a sufficient reproducibility.

Degradation and aging effects

Possible aging effects concern the applied filters as well as the silicon diode itself. The latter can not be assessed individually with the present experimental setup.

Visual surface modifications over time have been observed for the interference filters 122BP (L_α), 154BP (H_2 Lyman band) and 230BP (H_2 Continuum). An exemplary picture of the latter was taken after the completion of all measurements presented in this work and is shown in figure 4.15. This roughly corresponds to about 6000 seconds of total irradiation including direct exposure to plasmas ($\approx$ 4600 seconds) as well as radiation from the deuterium arc lamp I ($\approx$ 1400 seconds). The image indicates a transformation of the reflective surface material which is illuminated by photon fluxes (within red circle). The previously smooth and totally flawless surface exhibits an opaque haze and scattered dim spots extending into the filter material and reminding of dust beneath the surface. Additionally, a slight attrition at the edges of the filter due to the bearing area within the filter wheel can be observed. The 122BP and the 154BP filter show similar modifications as can be seen in figure D.3 in the appendix. For the other filters, the visual analysis did not show any apparent change.

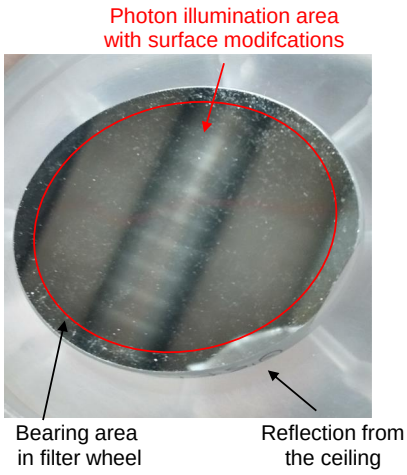

Figure 4.15: Picture of 230BP filter indicating material modifications after 6000 seconds total illumination.

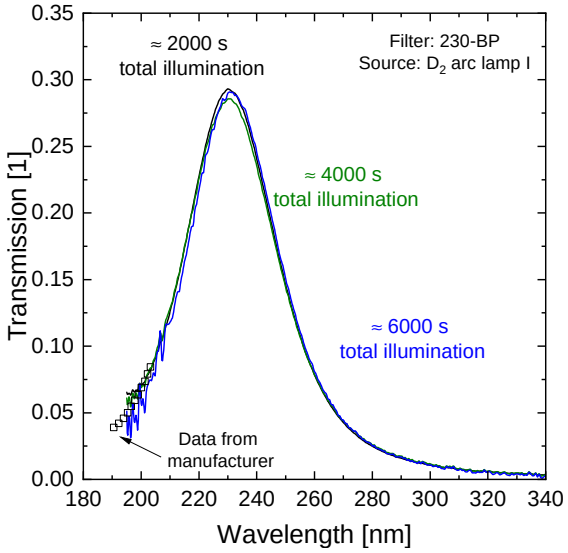

Figure 4.16: Monitoring of the 230BP filter's transmission after 2000 seconds, 4000 seconds and 6000 seconds of total irradiation. The curve taken after 2000 seconds corresponds to the determined filter transmission curve presented in figure D.1 in the appendix.

The deuterium arc lamp I together with the optical survey spectrometer allowed an easy monitoring of the 230BP filter's transmission. The results of the trans-

mission monitoring are presented in figure 4.16. The transmission was measured after roughly 2000 seconds, 4000 seconds and 6000 seconds of total irradiation of the filter. During the observation period, no significant change of the filter transmission could be observed. Minimal variations might arise from a slight tilt of the filter or from a minor shift of the measurement spot on the filter surface. Moreover, they are not monotonic over the transmission interval. Therefore, no evidence for a degradation of the transmission could be detected for the 230BP filter.

A long term reproducibility study of the diode system was carried out measuring the emissivity of the L_α line, the Lyman band and the Continuum with the 122BP, 154BP and 230BP filter, respectively. The measurements were performed at a hydrogen plasma at a pressure of 5 Pa and a generator power of 700 W with a temporal distance of roughly two years. The first measurement had been carried out in 2018 and it was repeated in 2020. As a reference, the emissivities of the Balmer lines H_α up to H_ϵ were recorded in both discharges with the high resolution optical emission spectrometer. They showed a reproducibility of the plasma better than $\pm 10\,\%$ with respect to the mean value of the two measurements. The emission of the Fulcher band[1] did not change with a variation of less than 1 %.

The emissivities in the VUV range obtained from the standard evaluation of the diode system measurements are summarized in table 4.11. The emissivities of the L_α (122BP) and the Continuum (230BP) are in the range of $\pm 10\,\%$, those of the Lyman band (154BP) agree within $\pm 15\,\%$ with respect to the mean values.

Table 4.11: Emissivities in units of $10^{21}\,\mathrm{m^{-3}s^{-1}}$ obtained with the diode system in a hydrogen discharge (5 Pa, 700 W) in comparative measurements performed in 2018 and 2020.

Emission range (Applied filter)	L_α (122BP)	Lyman band (154BP)	Continuum (230BP)
2018:	2.9	4.2	1.3
2020:	2.7	3.1	1.0

It is followed that no significant degradation of these filters as well as the diode itself in the corresponding wavelength range has occurred during this work. A comparable behaviour is also assumed for the remaining filters which do not show

[1] In 2020, no Langmuir probe measurements have been performed. Thus, for the evaluation the electron temperature measured in 2018 has been applied.

any visual modifications and which, therefore, have not been investigated individually.

Within the framework of this work, no degradation effects have been detected and the diode system allowed reproducible measurements over a period of two years. If indications for a degradation occur in the future, either a recalibration against the VUV spectrometer is required or the accuracy of the diode system will suffer. Therefore, it is recommended to carefully and regularly check the applied filters and the diode itself on visible modification which might be related to aging. A periodic reproducibility measurement of the diode system at a reference discharge is suggested.

Uncertainty sources

The uncertainty arising from the temporal behaviour of the diode signal is based on its dynamic during the measurement interval. As described above, the signal's relative variation of less than $\pm 3\,\%$ was observed.

The silicon diode is also sensitive to electrons and ions with the responsitivity being dependent on the incident particle energy [FSRK97, FRHK01]. A possible contribution of charged particles to the output signal is restricted to measurements without any filter and might be considered in the error estimation depending on the specific application. At *PlanICE*, the effect of ions and/or electrons on the diode system was roughly investigated in argon and hydrogen discharges. A removeable horse shoe magnet was adjusted in a way that possible charged particles are deflected and the influence on the measured signal without any filter was monitored together with the plasma emission via the survey optical spectrometer. An effect of the magnet on the output signal of the diode system below $\pm 8\,\%$ could be observed. However, the interpretation is rather difficult since the plasma was affected simultaneously due to the vicinity of the magnet to the discharge. Therefore, the variation of the signal can not be unambiguously assigned to an influence of impinging ions. No further uncertainty is considered in this work, but might play a role in a specific setup where the diode system will be applied. Concluding, only the uncertainty of $\pm 3\,\%$ due to the variation of the diode's signal within the measurement interval is applied for the diode system's results in the following.

5 Quantification of fluxes in low pressure plasmas

In plasma discharges, the plasma species of heavy particles, electrons as well as photons contribute to a flux onto the reactor walls or a surface inserted for treatment processes. According to their energy, the emitted photons can be classified into the infrared region (IR, $\lessapprox 1.8\,\mathrm{eV}$), the visible region (VIS, $\approx 1.8 - 3.1\,\mathrm{eV}$), the ultraviolet (UV, $\approx 3.1 - 6.2\,\mathrm{eV}$) and the vacuum ultraviolet (VUV, $\gtrapprox 6.2\,\mathrm{eV}$) range. In particular, photons from the VUV/UV range with exceeding 3.1 eV and may play an important role in plasma processing [SZDE12, TGYH11, LWY01].
In this work, emission ranges with relevant photon fluxes are identified with respect to the neutral particle flux and the positive ion flux in several gases and gas mixtures. The following sections describe how these fluxes are calculated and how the relevant parameters are determined with the diagnostic system at *PlanICE*.

5.1 Determining relevant parameters for particle fluxes

Every species with the density n and particle velocity v inside the plasma creates a flux according to

$$\mathbf{\Gamma} = n \cdot \mathbf{v}. \tag{5.1}$$

The sheath between bulk plasma and surface has a repelling effect on negatively charged particles like electrons and negative ions. Hence, atomic and molecular neutrals from the feed gas as well as their positive ions play the major role regarding the influence on surface materials [HKSS08].
The neutrals' movement through the plasma is driven by diffusion and collisions with other plasma particles. Assuming a Maxwellian distribution of the particles'

velocity, the directed flux is given by

$$\Gamma = n \cdot \langle v \rangle \tag{5.2}$$

with the mean velocity $\langle v \rangle$ from equation (2.6). In the context of neutral particles, it is called thermal velocity v_{therm} and is determined by the mass and the temperature of the neutral species. It has to keep in mind, that selective plasma processes may result in a difference in the temperatures of the different particle species. The flux of neutral atoms and molecules, respectively, is given by

$$\Gamma_{\mathrm{neutr}} = \frac{n_{\mathrm{neutr}}}{4} \cdot v_{\mathrm{therm}} = \frac{n_{\mathrm{neutr}}}{4} \cdot \sqrt{\frac{8 k_{\mathrm{B}} T_{\mathrm{gas}}}{\pi m_{\mathrm{neutr}}}}. \tag{5.3}$$

In atomic discharges, the corresponding neutral particle density n_{neutr} is directly obtained from the pressure using the ideal gas law. In the case of molecular gases where dissociation takes place, the atomic and molecular densities are derived from the pressure via the atomic-to-molecular density ratio which can be obtained by optical emission spectroscopy and population models. In hydrogen and nitrogen containing plasmas, the gas temperature T_{gas} can be obtained from optical emission spectroscopy using the rotational temperature T_{rot} as it is described in section 5.1.3. The mass of the particular atomic or molecular species is denoted by m_{neut}.

In contrast, positive ions from the plasma produce a directional flux onto the surface material due to the potential drop across the plasma sheath. After entering the sheath region with a minimum velocity of v_{B} in agreement with the Bohm criterion according to equation (2.9), the ions are accelerated towards the surface with the flux remaining constant. Assuming single ionization and one ionic species, the ion density $n^{+}_{\mathrm{ion,s}}$ at the sheath edge equals 60 % of the positive ion density $n^{+}_{\mathrm{ion,b}}$ in the bulk plasma. Following [CC03, F18], the approximation $n^{+}_{\mathrm{ion,s}} = \frac{1}{2} n^{+}_{\mathrm{ion,b}}$ can be made. Using the quasineutrality within the bulk plasma one obtains $n^{+}_{\mathrm{ion,s}} = \frac{1}{2} n_{\mathrm{e}}$ resulting in

$$\Gamma_{\mathrm{ion}} = n^{+}_{\mathrm{ion,s}} \cdot v_{\mathrm{B}} = \frac{n_{\mathrm{e}}}{2} \cdot \sqrt{\frac{k_{\mathrm{B}} T_{\mathrm{e}}}{m_{\mathrm{ion}}}} \tag{5.4}$$

for the positive ion flux. The electron temperature T_{e} and density n_{e} are typically obtained by Langmuir probe measurements. The ion mass is denoted by m_{ion}. In

the case of N different ion species in the plasma, the weighted mean ion mass

$$m_{\text{ion,mean}} = \frac{1}{n_\text{e}} \cdot \sum_{i=1}^{N} m_i \cdot n_i^+ \tag{5.5}$$

is used. In this case, equation (5.4) describes an effective ion flux. The density n_i^+ of the individual ion species with mass m_i can be determined by the use of the mass spectrometer in the center of the plasma vessel in combination with Langmuir probe results.

5.1.1 Plasma parameters from the Langmuir probe

The following introduction to underlying processes as well as the analyzing technique to obtain plasma parameters from Langmuir probe measurements is based on [CB11, CC03, SS70, LL05] and is restricted to electrons and positive ions.
A current-voltage characteristic of an argon discharge at *PlanICE* at 5 Pa and 300 W generator power obtained with the Langmuir probe is exemplarily shown in figure 5.1.
The measured probe current is the sum of the electron and the ion current. The current carried by electrons is counted per definition with a positive sign. A very high negative biasing creates a sheath around the probe tip that accelerates positive ions and suppresses the electron current from the plasma. As the corresponding name already indicates, positive ions dominate the measured current within the *ion saturation regime*. The cylindrical probe tip and the resulting increase of the sheath dimensions prevents, however, a real saturation. The recombination of the ions at the tip results into a negative sign of the current in the ion saturation regime. Increasing the voltage in positive direction reduces the electron repelling effect of the sheath and the electron current starts to rise. If the probe voltage reaches the floating potential V_fl, the ion and electron currents are equal and no net current is measured. A further increase of the probe voltage allows more slow electrons to overcome the decreasing repulsive effect of the sheath and to contribute to the probe current in the *transition region*. Simultaneously, the ion current on the probe is decreasing. Assuming a Maxwellian energy distribution of the electrons according to equation (2.5) and subtracting the contribution from the positive ions, the electron current follows an exponential function

$$I_\text{e}(V) = \frac{eA}{4} n_\text{e} \langle v \rangle \cdot \exp\left[\frac{\text{-}e(V_\text{pl} - V)}{\text{k}_\text{B} T_\text{e}}\right] \tag{5.6}$$

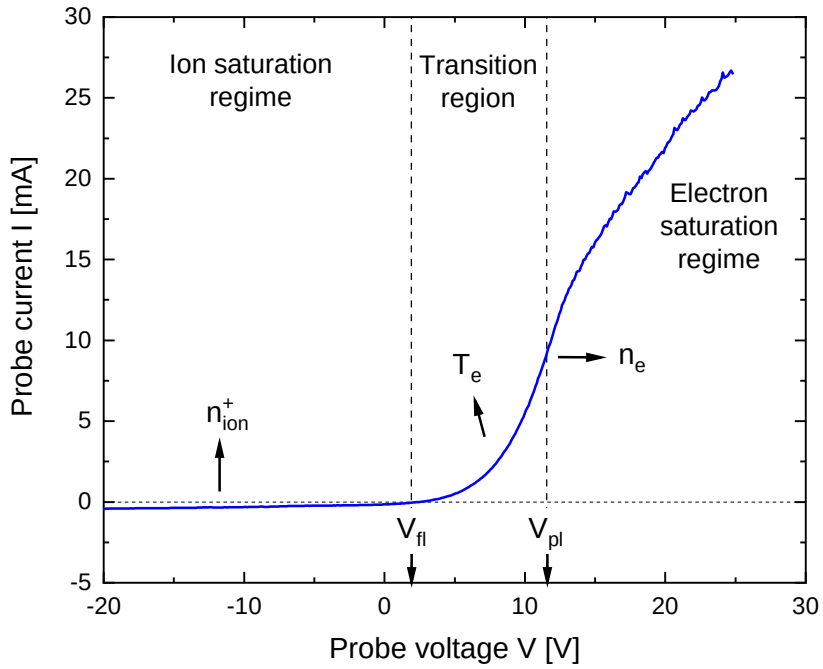

Figure 5.1: Measured current-voltage characteristic in argon at 5 Pa and 300 W generator power with indication of typical regimes accordingly to [CC03] and determinable plasma parameters.

with the probe tip surface area A that is exposed to the plasma, the elementary charge e and the electron density n_e. V_{pl} represents the plasma potential and $\langle v_e \rangle = \sqrt{\frac{8k_B T_e}{\pi m_e}}$ is the mean electron velocity resulting from the Maxwellian distribution according to the electron temperature T_e.

At $V = V_{pl}$, the probe is at the same potential as the plasma, no sheath region is present and the electron density equals the ion density. The ion contribution to the measured current is negligible. A further increase of the applied voltage beyond the plasma potential ($V > V_{pl}$) prohibits the ions from the probe tip where only electrons arrive. The corresponding range is called *electron saturation region*. However, an increase of the sheath dimensions where electrons are collected prevents a real saturation above V_{pl} [MSL26].

The floating potential V_{fl} can be derived directly from the current-voltage characteristic from the zero-crossing of the curve. The plasma potential is marked by the inflection point in the $I - V$ characteristic. For determining V_{pl}, it is suitable to use $\frac{d^2 I(V)}{dV^2}$ considering the property of the second derivative to be zero at inflection points of the initial function and, therefore, at V_{pl}. The *PlasmaMeter*

software applies a smoothing procedure for the second derivative from which the EEDF and EEPF can be obtained as described below. The specific smoothing voltage interval can be adjusted manually for each $I - V$ characteristic and has an influence on the results. The second derivative of the exemplary characteristic from figure 5.1 is shown in figure 5.2 (a).

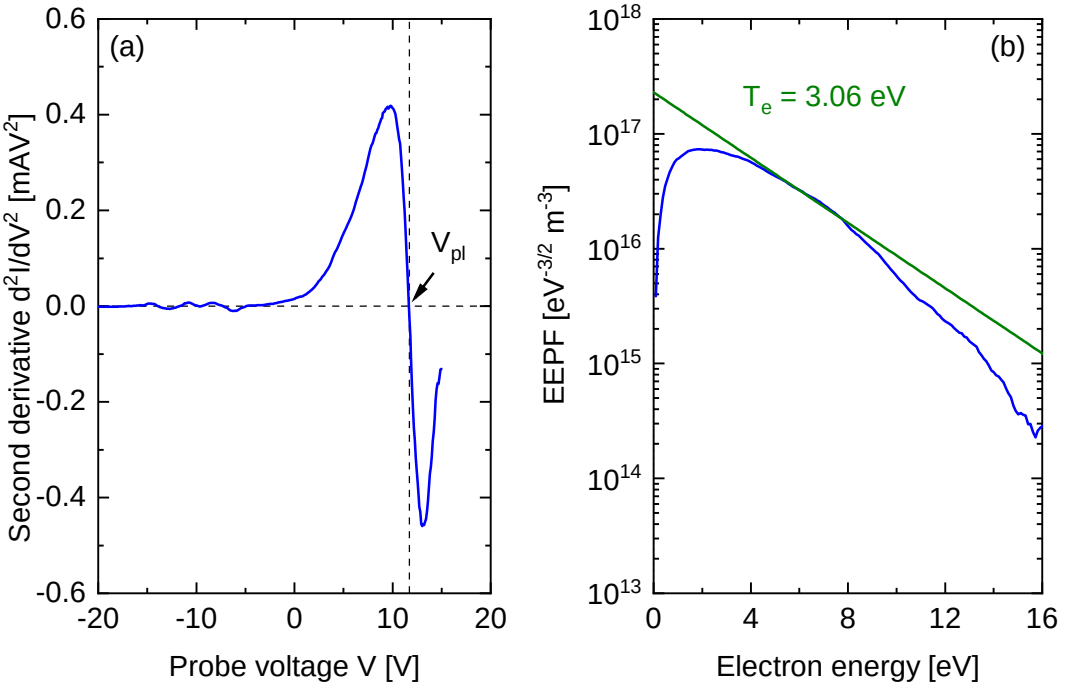

Figure 5.2: Determination of plasma parameters from the probe $I - V$ characteristic. (a) Plasma potential from the second derivative. (b) EEPF and corresponding electron temperature obtained with the probe software *PlasmaMeter*.

The electron energy distribution function $f(E_\mathrm{e})$ as well as the electron energy probability function $g(E_\mathrm{e})$ can be deduced from the second derivative of the probe characteristic in the range $V \leq V_\mathrm{p}$. The electron energy is given by $E_\mathrm{e} = e(V_\mathrm{pl} - V)$. According to [Dru30], the EEDF is related to the second derivative and can be written as

$$f(E_\mathrm{e}) = \frac{\sqrt{8 m_\mathrm{e} E_\mathrm{e}}}{e^{3/2} A} \cdot \frac{\mathrm{d}^2 I}{\mathrm{d}V^2}. \tag{5.7}$$

According to equation (2.8), the EEPF results in

$$g(E_\mathrm{e}) = \frac{\sqrt{8m_\mathrm{e}}}{e^{3/2}A} \cdot \frac{\mathrm{d}^2 I}{\mathrm{d}V^2}. \tag{5.8}$$

The EEDF and EEPF are given in $[\mathrm{eV}^{-1}\mathrm{m}^{-3}]$ and $[\mathrm{eV}^{-3/2}\mathrm{m}^{-3}]$, respectively, with the equation above. In the case of a Maxwellian distribution function, it applies $\ln\big(g(E_\mathrm{e})\big) \propto \frac{E_\mathrm{e}}{k_\mathrm{B}T_\mathrm{e}}$ from the equations (2.5) and (2.8). Therefore, the electron temperature T_e can be deduced from a linear fit's slope of $\ln\big(g(E_\mathrm{e})\big)$. An example of a calculated $g(E_\mathrm{e})$ from the measured $I-V$ characteristic is depicted in semilogarithmic scale in figure 5.2 (b). The green line represents a Maxwellian EEPF according to the electron temperature of $T_\mathrm{e} = 3.06\,\mathrm{eV}$ which has been determined automatically with the *PlasmaMeter* software. The voltage interval for the linear fit is set by the software routine individually for each measurement and was not changed manually. The range corresponding to high electron energies might be affected by a poor signal-to-noise level in cases of low probe currents. On the other hand, the very low energy range is influenced by different aspects, e.g. the probe circuit resistance, contaminations of the probe surface or insufficiently suppressed RF distortions [GPA92].
The electron density can be determined from the current-voltage characteristic by evaluating equation (5.6) at the plasma potential V_pl. Hence, n_e can be calculated with

$$n_\mathrm{e} = \frac{I(V_\mathrm{pl})}{eA}\sqrt{\frac{2\pi m_\mathrm{e}}{k_\mathrm{B}T_\mathrm{e}}} \qquad \text{and} \qquad A = 2\pi r l, \tag{5.9}$$

r being the radius and l the length of the probe tip exposed to the plasma.
For evaluating the positive ion density n_ion^+ from the ion saturation region, several theories are available with different approaches regarding the movement of the ions towards the probe tip. Details can be found in the literature [CC03, CB11, All92, ABR57]. In the present work, the plasma's immanent property of quasi-neutrality described by equation (2.2) is exploited to derive n_ion^+ directly from the electron density.
In order to compare the results from Langmuir probe measurements with the line of sight integrated optical emission spectroscopy, radial profiles of the discharge were taken across the region from a distance of 0 mm up to 80 mm from the vessel wall in 10 mm steps. Radial profiles of the electron density and electron temperature in argon at 5 Pa and 300 W are exemplarily shown in figure 5.3. The

evaluation is performed as follows: The determined local plasma parameters T_e and n_e are mirrored at the vessel axis to obtain a full profile over the whole plasma diameter. For each profile, the determined values of n_e (depicted as green squares) are fitted using a Bessel function with the maximum at the center of the plasma vessel. The fit function gives fitted values of n_e at the different measurement positions. Finally, these are averaged to obtain the axially integrated electron density. For the corresponding value of T_e, the determined local values (black circles) are averaged. This procedure leads to $n_e = 1.07 \cdot 10^{18} \mathrm{m}^{-3}$ and $T_e = 3.09\,\mathrm{eV}$ for the presented example.

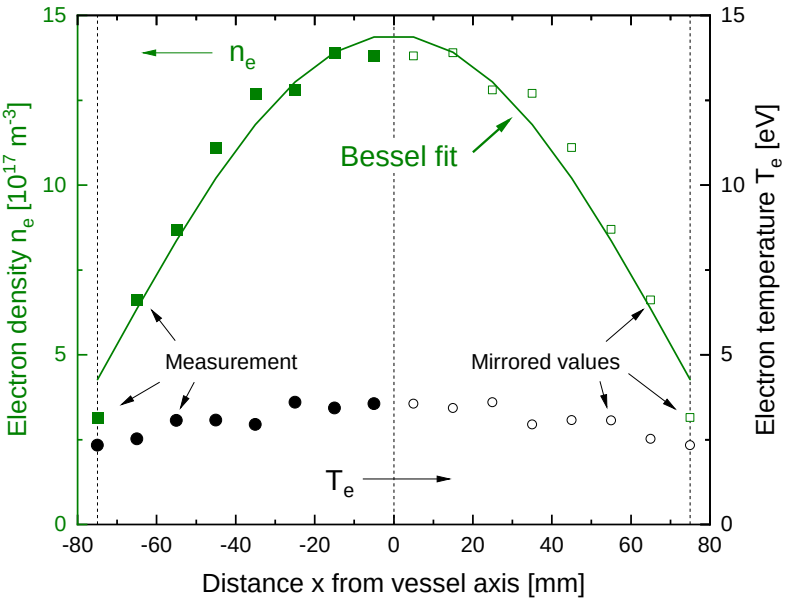

Figure 5.3: Determined profiles of n_e and T_e in argon at 5 Pa and 300 W generator power. The vessel's walls are located at the positions ± 75 mm.

Limitations and uncertainty sources

The Langmuir probe is an invasive measurement technique for which an object is directly inserted into the plasma. Therefore, mutual effects between the probe and the plasma are present. For example, changes of the impedance matching and the power transfer efficiency while moving the probe were detected. Although these effects are usually rather slight, however in some extreme cases, the discharge turned off.

RF power is known to have an influence on probe measurements and on the eval-

uation of the plasma parameters [GD11]. A temporal variation of the plasma potential is impressed on the measured $I - V$ characteristic leading to distorted results [SC94, LL05]. Despite of the passive filter system, a complete compensation might be not achieved.

In the following, the consideration focuses on the uncertainty contribution arising from the measurement and evaluation procedure and their effect on the uncertainty of the determined plasma parameters. For this purpose, [Hei18] is used as reference since the same probe system was applied and intensively studied there.

The accuracy of the electron temperature determination depends on the assumption of a Maxwellian distribution and significantly on the chosen interval for the linear fit. To estimate the uncertainty due to the choice of the fit interval by the software, a comparison with a manual evaluation was exemplarily performed for the pure gases argon, nitrogen, oxygen and hydrogen at 5 Pa and a fixed probe distance of 20 mm to the vessel wall. The medium pressure of 5 Pa was chosen for which a stable plasma operation was possible for each gas. The distance of 20 mm was selected with the idea of preventing the probe characteristic from the influence of the vessel wall as well as from RF solenoid. Different voltage intervals for the linear fit of $\ln(g(E_\mathrm{e}))$ were investigated. It appeared that the absolute difference between the maximum and the minimum determined value is in the range of $0.4 - 1.4\,\mathrm{eV}$. Therefore as an approximation, $\Delta T_\mathrm{e} = \pm 1\,\mathrm{eV}$ was chosen. Considering the maximum and minimum electron temperature determined in this work, $T_\mathrm{e} = 10.9\,\mathrm{eV}$ in nitrogen at 0.3 Pa and 400 W and $T_\mathrm{e} = 2.3\,\mathrm{eV}$ in hydrogen/nitrogen at 10 Pa and 500 W, respectively, it leads to a relative uncertainty range of $\frac{\Delta T_\mathrm{e}}{T_\mathrm{e}} = 0.1 - 0.4$. The value of 10 % given in [Hei18] corresponds to the lower limit of the presented uncertainty estimation.

According to equation (5.9), the uncertainty of the electron density depends on ΔT_e, the accuracy of the probe dimensions as well as the plasma potential current $I(V_\mathrm{pl})$ and, therefore, on the uncertainty of the plasma potential V_pl. In [Hei18], the overall uncertainty of the plasma potential determined with the applied probe type was summarized to $\Delta V_\mathrm{pl} = \pm 0.5\,V$. This value includes the influence of the smoothing procedure for the second derivative, the size of the voltage steps in the measurement as well as a general error of $\pm 0.15\,\mathrm{V}$ due to the noise level.

The error resulting from the determination of the probe radius is assumed to be $\frac{\Delta r}{r} = \pm 10\,\%$ according to the manufacturer of the tungsten wire. The same assumption is made for the platinum wire due to missing information from the manufacturer. The probe tip's length was measured manually with a sliding

calliper. An uncertainty of $\Delta l = \pm 0.5\,\mathrm{mm}$ is estimated for this procedure.
The aforementioned exemplary investigation in pure gases at 5 Pa and a distance of 20 mm from the vessel gives a relative uncertainty of $\frac{\Delta n_\mathrm{e}}{n_\mathrm{e}} = 0.7$ in argon. For the other gases, the corresponding value is in the range of $0.3 - 0.5$. Hence, an averaged relative uncertainty of 0.4 was chosen for these discharges. The difference is mainly due to a different length of the tip which was around 1 mm for argon discharges and in the range 5 - 10 mm for the other gases.

5.1.2 Plasma parameters from the mass spectrometer

The hardware components of the applied mass spectrometer have been described in section 3.2.2. Either scans of m/q at a fixed energy-to-charge ratio E/q or, vice versa, scans of E/q with a constant mass-to-charge ratio m/q can be performed. In the following, these scan modes are abbreviated and referred to as energy and mass scan, respectively. In both cases, counts per second are detected. Typical spectra obtained in these scan modes are shown exemplarily for a pure nitrogen discharge in the figures 5.4 (a) and (b).

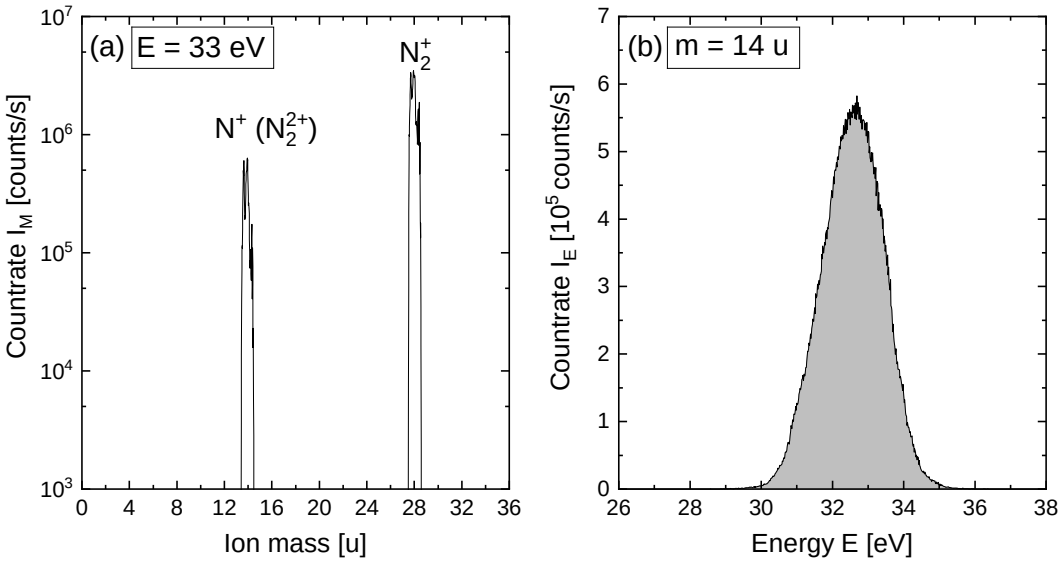

Figure 5.4: Typical spectra obtained with the ion mass spectometer in nitrogen at 0.3 Pa and 400 W generator power. (a) Mass scan at fixed energy of 33 eV. (b) Energy scan at fixed mass of 13.94 u.

The measurements with the mass spectrometer in order to derive the densities n_i^+ of the ion species in the plasma and an effective ion mass $m_{\mathrm{ion,eff}}$ were performed in two steps: first the ion mass is scanned at a fixed but arbitrary energy to get insight into the present ion species. The exemplary mass scan in figure 5.4

(a) reveals peaks around a mass of 14 u and 28 u corresponding to singly ionized atomic and molecular nitrogen, respectively. However, doubly ionized nitrogen molecules would also contribute to the peak at 14 u. In a second step, energy scans are performed separately for each ion species that was detected during the mass scan. A typical measured energy distribution $I_{\mathrm{E}}(E)$ is shown in figure 5.4 (b) for atomic nitrogen at a peak mass of 13.94 eV.
It has to be stressed that the measured quantity with the plasma monitor is not directly the density of an ion species but the flux reaching the detector. This, in turn, is proportional to the product of the area below the measured intensity curve $I_{\mathrm{E},i}$ and a mass dependent relative transmission factor $T_{\mathrm{r}}(m_i)$. Using the quasineutrality

$$\sum_i n_i^+ = n_{\mathrm{ion}}^+ = n_{\mathrm{e}}, \tag{5.10}$$

the density of the ion species i can be determined with

$$n_i^+ = \frac{\int I_{\mathrm{E},i}(E)\ \mathrm{d}E \cdot T_{\mathrm{r}}(m_i) \cdot \sqrt{m_i}}{\sum_j \int I_{\mathrm{E},j}(E)\ \mathrm{d}E \cdot T_{\mathrm{r}}(m_j) \cdot \sqrt{m_j}} \cdot n_{\mathrm{e}}. \tag{5.11}$$

The fraction represents the density ratio of species i with respect to the total positive ion density n_{ion}^+. The relative factor $T_{\mathrm{r}}(m_i)$ is necessary to consider the directional and mass dependent transmission of the mass spectrometer and will be discussed in more detail later. The factor $\sqrt{m_i}$ arises from the assumption of an ion speed equal to the Bohm velocity when entering the mass spectrometer. The electron density n_{e} is obtained from local Langmuir probe measurements directly above the entrance aperture of the mass spectrometer. According to equation (5.5), an effective mass $m_{\mathrm{ion,eff}}$ of the positive ions can be calculated for the quantification of the positive ion flux from the plasma.

Calibration procedure

The calibration of the energy scale was provided already by the manufacturer. Prior to calibrating the mass dependent transmission of the plasma monitor, an optimization of the ion optics is carried out in an argon discharge. In this way, the signal output is maximized. Different potentials correspond to components of the ion transfer system, the energy and mass filter as well as to the 90° deflection of the ion beam into the SEM which were described in section 3.2.2. Those are

varied in order to result in a maximal signal intensity and optimized signal-to-noise ratio.

With these optimized parameters, the calibration of the mass dependent directional transmission of the plasma monitor can be performed to obtain the factors $T_\mathrm{r}(m_i)$ in equation (5.11). For this purpose, the noble gases helium, neon and argon are used in gas phase. The mass dependent transmission is assumed to apply equally for neutrals and ions. The plasma monitor is operated in neutral particle mode with the ion source activated in order to ionize incoming neutrals by electrons. The energy of the electrons is given by an applied potential difference of 100 V between the emitting filament and the ion formation chamber. Therefore, electron impact ionization cross sections σ_gas for each gas at an electron energy of 100 eV have to be considered. The corresponding values were taken from [WBHF87]. The density n_gas can be calculated via the ideal gas law from the gas pressure and the room temperature $T = 300\,\mathrm{K}$.

Energy scans are performed for the main isotopes of the specific noble gas, i.e. $m = 4\,\mathrm{u}$ (99.99999 %) for helium, $m = 20\,\mathrm{u}$ (90.48 %) and $m = 22\,\mathrm{u}$ (9.25 %) in neon and $m = 40\,\mathrm{u}$ (99.60 %) using argon. The numbers in the brackets correspond to the isotopic ratio $c_\mathrm{gas}(m)$ of each isotope [Int91]. The calibration factor is calculated with

$$T(m) = \frac{n_\mathrm{gas} \cdot \sigma_\mathrm{gas}}{\int I_{\mathrm{E},m}(E)\ \mathrm{d}E} \cdot c_\mathrm{gas}(m) \tag{5.12}$$

for $m = 4\,\mathrm{u}$, $20\,\mathrm{u}$, $22\,\mathrm{u}$ and $40\,\mathrm{u}$. The resulting values are arbitrarily normalized at a mass of 3 u corresponding to H_3^+ in hydrogen plasmas which leads to relative factors $T_\mathrm{r}(m_i)$. Since no general statement about the mass dependency of the instrument can be made, a fit function has been applied to derive calibration factors for arbitrary masses. The corresponding calibration curve up to a mass of 41 u is shown in figure 5.5. It has to be noted that the fit function cannot be derived from theoretical results.

Limitations and uncertainty sources

As can be seen in figure 3.5 (b), the extraction cap constitutes a rather large metallic volume inserted into the plasma which has a significant influence on the radial profiles of the plasma parameters. This leads to a decrease of the electron density and a slight increase of the mean electron energy in the center of the plasma vessel [SFAP01]. However, an influence on axial emission profiles could

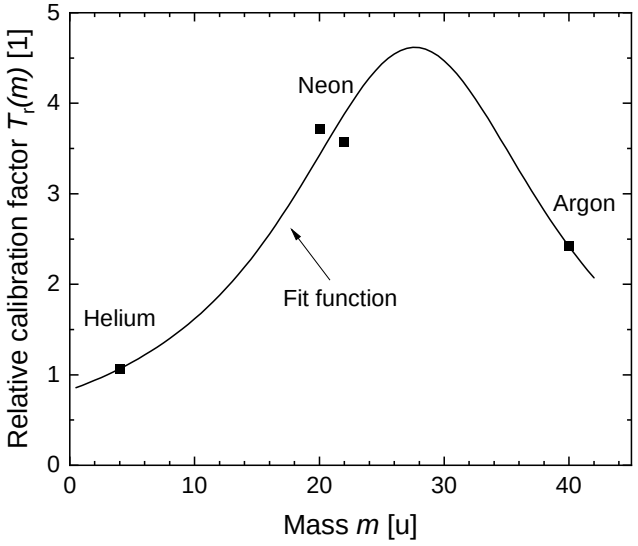

Figure 5.5: Mass dependent relative calibration factors and fit function obtained for the *PPM 421* mass spectrometer.

not be observed in the present setup by optical emission spectroscopy. Vertical Langmuir probe measurements are not possible while the mass spectrometer is mounted.

The temporal stability of the mass spectrometer's signal was analyzed exemplarily in pure nitrogen discharges. A series of energy scans at constant mass revealed a rather large deviation regarding absolute values of $\int I_{\mathrm{E},m}(E)\mathrm{d}E$. Nevertheless, the ratios between different species showed a satisfactory reproducibility under the terms of a sufficient signal intensity: in nitrogen, the ratio of molecular ions ($m = 28\,\mathrm{u}$) to atomic ions[1] ($m = 14\,\mathrm{u}$) exhibited a standard deviation of around 10 %. This value will be applied as typical relative uncertainty.

Furthermore, the mass dependent calibration procedure contributes to the uncertainty in several ways. The calibration factors in helium, neon and argon depend on the uncertainty of the pressure measurement, on the accuracy of the ionization cross sections as well as on uncertainties arising from the assumed room temperature, the isotopic distribution and again from the reproducibility. However, the main contribution arises from the fit function in figure 5.5. The highest accuracy can be expected for the rare gases applied during the calibration procedure. In contrast, the ranges below 4 u and above 40 u were extrapolated. These range and the maximum of the fit function which is not well-defined are highly error-

[1] It has to be noted that a contribution from molecular ion N_2^{2+} can not be excluded.

prone. The resulting uncertainty of the calibration for arbitrary masses cannot be assessed quantitatively since reproducibility measurements only were carried out exemplarily for one nitrogen discharge. For this reason, the relative uncertainty of $\pm 10\,\%$ which was obtained from stability investigations in nitrogen is applied to the relative density of ion species i corresponding to the fraction in equation (5.11).

A Gaussian error propagation and the uncertainty of the electron density n_e, which was determined individually in argon and in the molecular gases by Langmuir probe measurements, result in a relative uncertainty $\frac{\Delta n_i^+}{n_i^+}$ of 71 % in argon and 41 % in the other discharges, respectively.

5.1.3 Plasma parameters from the optical spectrometer

The following section gives an overview about the plasma parameters that can be obtained from optical emission spectroscopy and which are necessary to calculate neutral particle fluxes. The underlying principles and evaluation methods are discussed.

a. Gas temperature

For determining the gas temperature, it is convenient to investigate ro-vibronic transitions of molecules in the optical region with emission spectroscopy. It has to be noted that upper states of the investigated transitions are labeled with one prime (') and lower states without prime in the following section[1].

Provided a Maxwellian distribution, the kinetic energy of heavy neutral particles is characterized by the gas temperature T_gas. As discussed in section 2.3.1, the population of rotational levels in the molecular ground state $(X, v = 0)$ can be usually described by a Boltzmann distribution function with $T_\mathrm{rot}(X, v = 0) = T_\mathrm{gas}$. It can be assumed that it is directly mapped into an excited state (A, v') via electron impact excitation, i.e. $\Delta J = 0$. The rotational population of the state A is accessible with emission spectroscopy and the corresponding rotational temperature $T'_\mathrm{rot}(A, v')$ can be deduced.

If the rotational relaxation in the upper state occurs slowly enough compared to the emission lifetime, the gas temperature is connected to $T'_\mathrm{rot}(A, v')$ with the gas

[1] In section 2.3, the lower state was denoted with a double prime (").

temperature [BSSL14]

$$T_{\text{gas}} = T_{\text{rot}}(X, v = 0) = \frac{B_{v=0}(X)}{B'_{v'}(A)} \cdot T'_{\text{rot}}(A, v'). \tag{5.13}$$

Therefore, the ratio of the rotational constants $B_{v=0}(X)$ and $B'_{v'}(A)$ corresponding to the ground state and to the excited state is used as scaling factor.
In this work, the gas temperature in hydrogen and nitrogen plasmas was determined by means of molecular emission.

Hydrogen:
The following section shortly summarizes the evaluation procedure of the gas temperature in hydrogen discharges based on optical emission spectroscopy which is presented in detail in [BRF17].
In hydrogen, the assumption of a rotational distribution in the ground state following a Boltzmann distribution and the validity of $T_{\text{rot}}(\text{X}, v = 0) = T_{\text{gas}}$ is restricted to low rotational quantum numbers J. The high lying rotational states suffer from overpopulation due to recombination of hydrogen atoms at the walls to rotationally excited molecules [VSE04, GSE08].
The Fulcher transition d $^3\Pi_\text{u} \rightarrow$ a $^3\Sigma_\text{g}^+$ provides diagnostic access to the rotational temperature of the d $^3\Pi_\text{u}$ state in pure hydrogen and hydrogen containing plasmas. Ro-vibrational transitions from $(v' = 0 - 3, J')$ to (v, J) with $\Delta v = 0$ and $\Delta J = 0$ are investigated. According to equation (2.42), absolute emissivities are given by

$$\epsilon_{\text{a},v,J}^{\text{d},v',J'} = n^{\text{d},v',J'} \cdot A_{\text{a},v,J}^{\text{d},v',J'} \tag{5.14}$$

with the Einstein coefficient $A_{\text{a},v,J}^{\text{d},v',J'}$. The emissivities allow the determination of the rotational population in the excited state.
Technically, the evaluation of the gas temperature is based on the comparison of simulated and measured rotational and vibrational density distributions in an iterative process. The simulation assumes a 'cold' ensemble of hydrogen molecules arising from the plasma volume and a 'hot' ensemble due to surface recombination of H atoms at the wall.
Therefore, two-temperature Boltzmann distributions of the rotational and vibrational levels in the ground state X with the same weighting factor are included. The colder rotational temperature is assigned to the gas temperature [BRF17] which serves together with the 'cold' vibrational temperature and the weighting

factor as fitting parameters. The 'hot' rotational and vibrational temperature are set to be equal and also work as additional fitting parameters. All fitting parameters are determined in an iterative optimization approach: The simulation projects the rotational distribution of X according to the corresponding temperatures into the upper Fulcher state d following $\Delta J = 0$. The contribution of each ro-vibrational level (v, J) of the ground state to the population of a specific state (v', J') via electron collision excitation is considered. Vibrationally resolved and T_e dependent rate coefficients for electron impact excitation based on a Maxwellian EEDF and Frank-Condon factors [MTG72, WF16] are used. As a result, a fitting routine that allows the best accordance between simulated and measured rotational distribution provides the fitted values for the cold and hot rotational and vibrational temperatures of the ground state as well as the weighting factor. As mentioned above, the former temperature corresponds to the gas temperature.

Nitrogen:

The rotational lines of transitions in molecular nitrogen cannot be separated with the available optical spectrometer. Therefore, a different approach evaluating the gas temperature [BSSL14] is necessary: The emission spectra of the second positive system C $^3\Pi_u \rightarrow$ B $^3\Pi_g$ is measured and compared with a synthetic spectrum. As a standard, the vibrational transition $v' = 0 - v = 2$ is used whose emission is located in the wavelength range 376 - 381 nm.

The simulation provides the relative intensity distribution of the $v' = 0 - v = 2$-band according to the calculated rotational population density of $v' = 0$ with the rotational temperature $T_{rot}(C, v' = 0)$ as fitting parameter. The Doppler broadening of an emission line and the apparatus profile of the spectrometer are included into the synthetic spectrum. By varying $T_{rot}(C, v' = 0)$, the simulated spectrum is adjusted to the measurement. More details about the simulation and the used input data can be found in [BRF17, Sie15].

From $T_{rot}(C, v' = 0)$ with the best accordance between measured and synthetic spectra, the gas temperature can be calculated with equation (5.13) and the rotational constants taken from the NIST Chemistry WebBook [HH18]. Figure 5.6 exemplarily shows a result of the fitting procedure with the measured relative emission spectra and the matched simulation results. A rotational temperature of 550 K was determined for the upper state which leads to a gas temperature of 603 K.

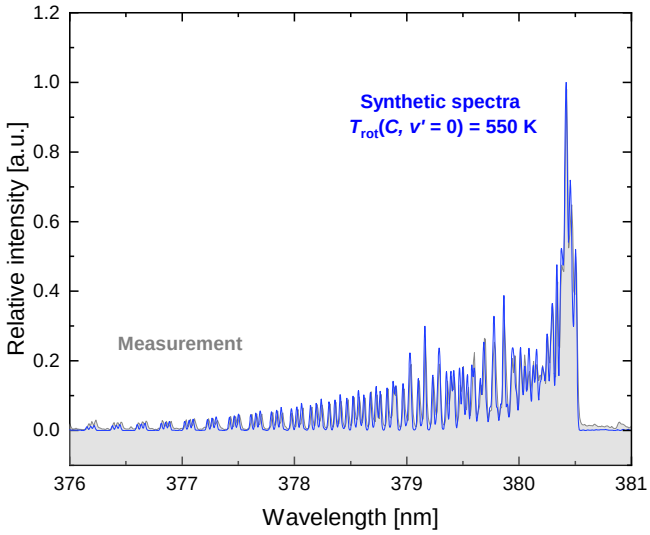

Figure 5.6: Example showing the result of the fitting procedure with synthetic (blue) and measured emission spectra (grey) of the $v' = 0 - v = 2$ transition in the second positive system of nitrogen (0.3 Pa, 400 W generator power). A rotational temperature of 550 K in the upper state is obtained.

b. Neutral particle density and atomic-to-molecular density ratio

Following the ideal gas law and neglecting electrons as well as ions due to the low ionization degree, the total neutral particle density

$$n_0 = n_{\mathrm{atom}} + n_{\mathrm{mol}} \tag{5.15}$$

can be calculated directly from the gas pressure and the gas temperature, however, without any information about the atomic and molecular portion. To obtain n_{atom} and n_{mol}, optical emission spectroscopy can be applied in combination with population models.

In nitrogen as well as oxygen discharges, the emissivity of appropriate atomic lines was measured and connected to the ground state density of the corresponding atoms n_{atom} by using extended corona models describes in section 2.4.3. The molecular ground state density n_{mol} can then be derived from equation (5.15) and the atomic-to-molecular density ratio $\delta = \frac{n_{\mathrm{atom}}}{n_{\mathrm{mol}}}$ can be calculated. Regarding gas mixtures (e.g. N_2/O_2), the gas composition is considered for calculating the total neutral density with equation (5.15) for the individual gas constituents (e.g. N_2 and O_2). Spontaneous emission is the only depopulation process considered

for nitrogen as well as for oxygen in the corona model given in equation (2.62). The corresponding Einstein coefficients are taken from the NIST atomic spectra database [KYRa19c].
With $n_{\mathrm{atom}} = \frac{n_0}{1+1/\delta}$ and $n_{\mathrm{mol}} = \frac{n_0}{1+\delta}$ as well as emission rate coefficients, equation (2.62) transforms to

$$\frac{n_0 n_{\mathrm{e}} X_{\mathrm{atom}}^{\mathrm{em},ik}(T_{\mathrm{e}})}{1+1/\delta} + \frac{n_0 n_{\mathrm{e}} X_{\mathrm{mol}}^{\mathrm{em},ik}(T_{\mathrm{e}})}{1+\delta} = \epsilon_{ik}. \tag{5.16}$$

This equation cannot be solved analytically for δ and was evaluated numerically using *Python*[1].

Oxygen:
Oxygen containing discharges produce several intense atomic emission lines in the optical region as well as in the VUV range (see the energy scheme in figure A.1 in the appendix).
In the triplet system, two emission lines at 130.5 nm ($3s\ ^3\mathrm{S}^\circ \rightarrow 2p^4\ ^3\mathrm{P}$) and at 844.6 nm ($3p\ ^3\mathrm{P} \rightarrow 3s\ ^3\mathrm{S}^\circ$) occur. Resulting from a resonant transition with $A_{130.5\,\mathrm{nm}} = 6.12{\cdot}10^8\,\mathrm{s}^{-1}$, the former line might be strongly affected by reabsorption and is, therefore, not used in the evaluation.
In the present plasma parameter regime, direct and dissocative electron excitation are considered to be the dominant population processes of $3p\ ^3\mathrm{P}$ [FBA20]. Hence, the absolute intensity of the 844.6 nm line was applied for the quantification of the ground state density of atomic oxygen. On the basis of a Maxwellian EEDF, emission rate coefficients for the direct excitation from the atomic ground state were obtained from excitation cross sections [II90, TH88]. For dissociative excitation, corresponding emission cross sections were taken from [SSC+85]. Both cross sections can be found in the appendix G.1 and G.2 while the emission rate coefficients are presented in figure 5.7. The branching ratio of the 844.6 nm line can be calculated to be 1.00003 and was considered as equal 1.
In the quintet system, a candidate for the application in the corona model is the intense emission line at 777.4 nm ($3p\ ^5\mathrm{P} \rightarrow 3s\ ^5\mathrm{S}^\circ$). However as described in the following, it appeared that this line is less suitable for this purpose: at low pressure, population from the lower state $3s\ ^5\mathrm{S}^\circ$ becomes important for the upper state $3p\ ^5\mathrm{P}$ of the 777.4 nm line [CP20]. Therefore, the population density of $3s\ ^5\mathrm{S}^\circ$ is of crucial importance for the corona model. However, this state exhibits

[1]The function *scipy.optimize.fsolve* included in the *SciPy* library was used.

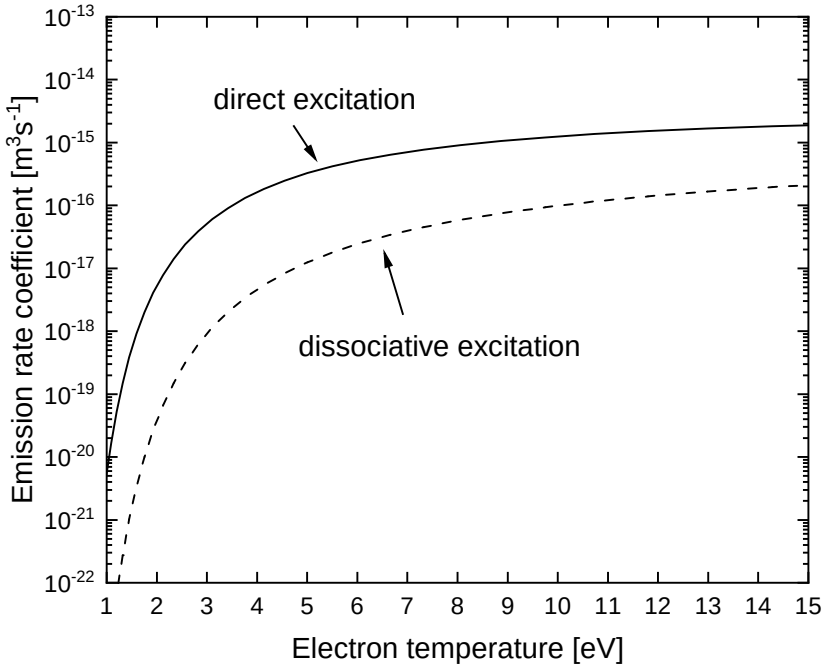

Figure 5.7: Emission rate coefficients of the atomic oxygen line at 844.6 nm for direct excitation from the atomic ground state (solid line) and dissociative excitation from the molecular ground state (dashed line). They were obtained from excitation and emission cross sections by [II90, TH88] and [SSC$^+$85], respectively.

an extensive excitation and de-excitation pattern including several atomic oxygen states in all three spin systems Moreover, it can be considered as metastable due to the small emission transition probability of the emission line at 135.7 nm ($3s\ ^5\mathrm{S}^\circ \rightarrow 2p^4\ ^3\mathrm{P}$, $A_{135.7\,\mathrm{nm}} = 5.56 \cdot 10^3\,\mathrm{s}^{-1}$). Therefore, diffusion to the vessel walls might play an important role as depopulation process. As a consequence, a collisional radiative model exceeding the capability of a simple corona model is required to accurately reproduce the (de-)population processes of the $3s\ ^5\mathrm{S}^\circ$ and $3p\ ^5\mathrm{P}$ states. Different corona models were set up and evaluated for the 777.4 nm line starting from the basic approach with only direct and dissociative excitation included. In a stepwise extension additional (de-)population processes were considered, e.g. electron excitation of $3p\ ^5\mathrm{P}$ from $3s\ ^5\mathrm{S}^\circ$, diffusion losses and/or cascading into $3s\ ^5\mathrm{S}^\circ$ or a direct quantification of the $3s\ ^5\mathrm{S}^\circ$ state's population with the VUV spectrometer in order to reduce uncertainties. Nevertheless, no model configuration allowed reliable results in the investigated pressure range.

Therefore, the evaluation of the atomic and molecular neutral oxygen densities

was performed using the emission line at 844.6 nm and the corresponding corona model described above.

Nitrogen:
In the case of nitrogen, the emission spectrum in the optical spectral region is dominated by molecular bands. However, some atomic emission lines in the VUV/UV range can be applied for the evaluation of the neutral ground state density. The atomic line ocurring at 174.3 nm ($3s\ ^2\mathrm{P} \rightarrow 2p^3\ ^2\mathrm{P}^\circ$, see energy scheme in figure A.2) which is accessible with the VUV spectrometer is applied. Corona models with the purpose of a neutral density determination had been already developed and benchmarked for several VUV lines including the one above in [Mei00]. Besides dissociative electron excitation from the molecular ground state and direct electron excitation from the atomic ground state, the model for nitrogen also includes the population from two metastable states. For convenience, the ground state is designated with m_1 while the metastable states are denoted with m_2 and m_3, respectively. Their energy difference with respect to the ground state is rather small which can be seen in table 5.1 and figure A.2 in the appendix. Hence, a population of the metastables states following a Boltzmann distribution with the electron temperature is assumed [Mei00] and diffusion losses to the vessel walls are not considered.

State	Configuration	ΔE [eV]	g
m_1	$2s^2 2p^3\ (^4S^\circ)$	0	4
m_2	$2s^2 2p^3 (^2D^\circ)$	2.38	10
m_3	$2s^2 2p^2\ (^2P^\circ)$	3.58	6

Table 5.1: Atomic nitrogen states included in the extended corona model for emission of the 174.3 nm line (m_1: ground state, $\mathrm{m}_{2,3}$: metastable states). The energy differences with respect to the ground state as well as the statistical weights g are given.

Corresponding emission rate coefficients for direct electron excitation from the states m_1, m_2 and m_3 were calculated using the collisional radiative model ADAS[1] with an electron density of $1 \cdot 10^{17}\,\mathrm{m}^{-3}$. Regarding the dissociative excitation of $3s\ ^2\mathrm{P}$, emission cross sections can be found in [MZ71].

[1] Atomic Data and Analysis Structure [Sum04]. For cross sections that are included in the model, it is referred to [FASB98].

Assuming a Maxwellian EEDF, it is converted into the emission rate coefficient $X^{\mathrm{em}}_{\mathrm{mol}}(T_{\mathrm{e}})$. The emission rate coefficients are presented in figure 5.8.

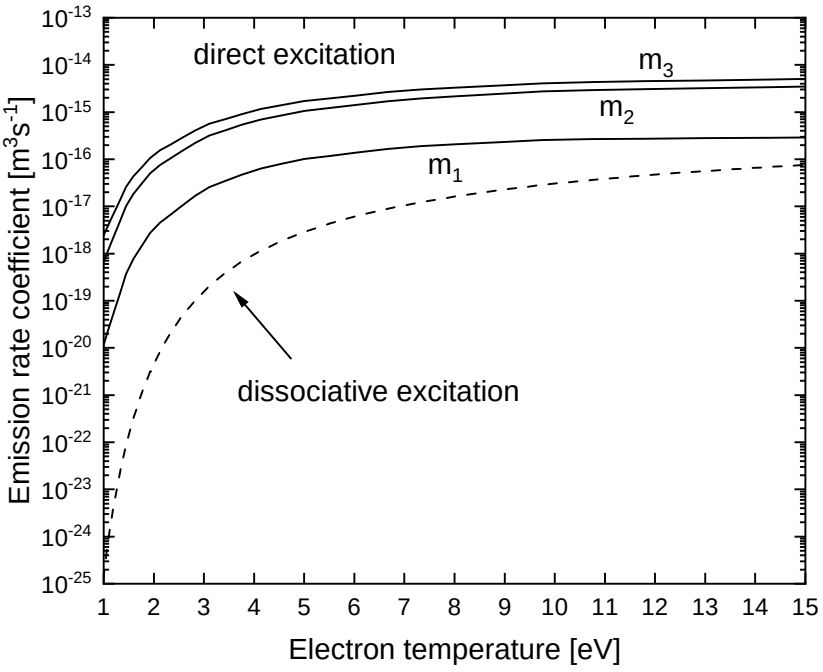

Figure 5.8: Emission rate coefficients of the atomic nitrogen line at 174.3 nm for direct excitation (solid line) from the atomic ground state m_1 and the metastable states m_2 and m_3 as well as for dissociative excitation (dashed line). The former are obtained with the CR model ADAS [Sum04], the latter are calculated from cross sections given in [MZ71].

Hydrogen:

In hydrogen, the atomic-to-molecular density ratio $n_{\mathrm{H}}/n_{\mathrm{H_2}}$ is directly accessible by measuring the emissivities of the Balmer H_γ line and the molecular Fulcher transition, $\epsilon_{\mathrm{H}_\gamma}$ and ϵ_{Ful}, respectively, together with the collisional radiative population models *Yacora H* and *Yacora* H_2. As results, the models provide the population coefficients

$$R_{\mathrm{H},n=4}(T_\mathrm{e}, n_\mathrm{e}) = \frac{n_{\mathrm{H},n=4}}{n_\mathrm{H} n_\mathrm{e}} = \frac{X^{\mathrm{em,eff}}_{\mathrm{H}_\gamma}(T_\mathrm{e}, n_\mathrm{e})}{A_{\mathrm{H}_\gamma}},$$
$$R_{\mathrm{H}_2,d}(T_\mathrm{e}, n_\mathrm{e}) = \frac{n_{\mathrm{H}_2,d}}{n_{\mathrm{H}_2} n_\mathrm{e}} = \frac{X^{\mathrm{em,eff}}_{\mathrm{Ful}}(T_\mathrm{e}, n_\mathrm{e})}{A^{\mathrm{eff}}_{\mathrm{Ful}}} \tag{5.17}$$

of the atomic state $n = 4$ and the molecular state $d^3\Pi_u$ which are the upper states of H_γ and the Fulcher transition. The corresponding population densities are denoted with $n_{\mathrm{H},n=4}$ and $n_{\mathrm{H}_2,d}$. In general, a population coefficient R_{0p} of a given state p multiplied by the corresponding Einstein coefficient of a transition from p into a state k ($k < p$) leads to the *effective emission rate coefficient* $X^{\mathrm{em,eff}}_{0p}$. Therefore, the population coefficients in equation (5.17) can be expressed with the effective emission rate coefficients $X^{\mathrm{em,eff}}_{\mathrm{H}_\gamma}$ and $X^{\mathrm{em,eff}}_{\mathrm{Ful}}$ and the Einstein coefficients A_{H_γ} and $A^{\mathrm{eff}}_{\mathrm{Ful}}$. This is shown on the right side of equation (5.17). $A^{\mathrm{eff}}_{\mathrm{Ful}}$ represents the effective transition probability which is the sum of the vibrationally resolved Einstein coefficients weighted with the relative population density of the specific vibrational level [Wün04, Fan06]. Combining the equations (2.42) and (5.17), the atomic-to-molecular density ratio

$$\frac{n_\mathrm{H}}{n_{\mathrm{H}_2}} = \frac{\epsilon_{\mathrm{H}_\gamma}}{\epsilon_{\mathrm{Ful}}} \cdot \frac{X^{\mathrm{em,eff}}_{\mathrm{Ful}}(T_\mathrm{e}, n_\mathrm{e})}{X^{\mathrm{em,eff}}_{\mathrm{H}_\gamma}(T_\mathrm{e}, n_\mathrm{e})} \tag{5.18}$$

is obtained from the measured emissivity ratio. Finally, the atomic ground state densities of atoms and molecules can be calculated with

$$n_\mathrm{H} = \frac{n_0}{1 + \left[\frac{n_\mathrm{H}}{n_{\mathrm{H}_2}}\right]^{-1}}, \qquad n_{\mathrm{H}_2} = \frac{n_0}{1 + \left[\frac{n_\mathrm{H}}{n_{\mathrm{H}_2}}\right]} \tag{5.19}$$

using the total neutral particle density from equation (5.15).

The intensity of the Balmer lines can be significantly increased by opacity of the Lyman series and dissociative excitation of hydrogen molecules due to electron collisions. The contribution of these processes decrease with increasing main quantum number of the upper state from which the particular Balmer line is emitted. Therefore, H_γ turned out to be a convenient compromise between being less influenced and providing a sufficient signal-to-noise ratio [Fan04]. Depending on the specific hydrogen discharge, different population processes can be included in *Yacora H*. In the model, electron-impact cross sections from [MTG72] were used for hydrogen molecules.

Argon:
In this work, pure argon discharges were investigated for which the neutral particle density can be directly determined from the ideal gas law with the natural isotope ratio. Since the gas temperature is not accessible with the diagnostic system, $T_{\mathrm{gas}} = 700\,\mathrm{K} \pm 300\ \mathrm{K}$ is used.

c. Electron temperature and density in hydrogen

In the case of hydrogen, the population models *Yacora H* and *Yacora* H_2 can also be applied in order to determine the electron temperature and density which serve as fitting parameters. Together with T_{e} and n_{e}, the composition of the hydrogen species is varied to optimize the aggreement between the simulated and measured emissivities of the Balmer series H_α to H_ϵ as well as their line ratios and the Fulcher transition ϵ_{Ful}. The variation of the parameters takes place within a given confidence range of the measured emissivities, e.g. $\pm 20\,\%$.

Limitations and uncertainty sources
Due to the intensity calibration procedure of the optical high resolution spectrometer with the Ulbricht sphere and a limited reproducibility of the spectra acquisition, the uncertainty of measured emissivities in the optical range has a typical range of $\pm 10\,\%$. Regarding the gas temperature evaluation, a typical absolute uncertainty of $\pm 25\,\mathrm{K}$ is applied in hydrogen and $\pm 50\,\mathrm{K}$ in nitrogen [BRF17], respectively. Using the CR models *Yacora H* and *YacoraH*$_2$, the uncertainties ΔT_{e} and Δn_{e} can be derived from the values for which simulation and measurement agree within the chosen confidence range. As mentioned in section 2.4, the uncertainty of the determined plasma parameters depends on the accuracy of the used cross sections. A quantification of this influence eludes the frame of this work. If not otherwise stated, a Gaussian error propagation was used for all calculations. For the determination of the atomic density, the uncertainties Δn_0 and Δn_{e} as well as the uncertainty of the measured emissivity were considered. Due to the ideal gas law, the former value includes ΔT_{gas} and a relative uncertainty of $\pm 1\,\%$ regarding the pressure setting.
The corona models for nitrogen and oxygen using the atomic-to-molecular density ratio are restricted to numerical solutions and the standard evaluation of the error propagation cannot be applied directly. Therefore, the uncertainty of the atomic density Δn_{atom} is calculated from the basic form of the corona models including the particle densities instead of δ (see equation 2.62). Due to the

interdependence of the quantities, the uncertainties $\Delta n_{\mathrm{mol}} = |\Delta n_{\mathrm{atom}}| + |\Delta n_0|$ and $\frac{\Delta\delta}{\delta} = |\frac{\Delta n_{\mathrm{atom}}}{n_{\mathrm{atom}}}| + |\frac{\Delta n_{\mathrm{mol}}}{n_{\mathrm{mol}}}|$ result for nitrogen and oxygen discharges. No additional error arising from the numerical solution is taken into account.
In hydrogen, a relative uncertainty of $\pm 2\,\%$ for the atomic-to-molecular density ratio was quantified in [Fri13]. The uncertaintes Δn_{H} and $\Delta n_{\mathrm{H_2}}$ are determined from equation (5.19) using an Gaussian error propagation.

From equation (5.3), the uncertainty of the neutral particle fluxes

$$\Delta\Gamma_{\mathrm{neut}} = \left|\left(\frac{8k_{\mathrm{B}}T_{\mathrm{gas}}}{\pi m_{\mathrm{neut}}}\right)^{1/2}\frac{\Delta n_{\mathrm{neut}}}{4}\right| + \left|\left(\frac{8k_{\mathrm{B}}T_{\mathrm{gas}}}{\pi m_{\mathrm{neut}}}\right)^{-1/2}\frac{n_{\mathrm{neut}}k_{\mathrm{B}}}{\pi m_{\mathrm{neut}}}\Delta T_{\mathrm{gas}}\right| \tag{5.20}$$

can be derived with $n_{\mathrm{neut}} = n_{\mathrm{atom,mol}}$ and the corresponding atomic and molecular mass $m_{\mathrm{neut}} = m_{\mathrm{atom,mol}}$.

5.2 Determining photon fluxes

The quantification of photon fluxes relies on intensity calibrated spectroscopy systems. In this work, the photon fluxes arising in the VUV/UV range were determined by the VUV spectrometer and the VUV diode system. Because of strong absorption in air below 200 nm, they demand a direct connection to the plasma and sufficient vacuum conditions. Photon fluxes in the optical region were obtained with the optical high resolution spectrometer.
The isotropic photon emission of a plasma is described by the spectral emissivity $\epsilon_\lambda(\lambda)$ in the unit photons/($\mathrm{m^3\,s\,nm}$). An integration over a certain wavelength range leads to the emissivity[1] ϵ which gives the total number of photons being radiated per cubic meter and second into the whole solid angle of 4π.
The total number of photons emitted per second by the plasma is obtained by integrating the emissivity over the emitting plasma volume V. Assuming a homogeneous and isotropic emission, an averaged photon flux

$$\Gamma_{\mathrm{ph}} = \epsilon \cdot \frac{V}{S} \tag{5.21}$$

onto the surface S enclosing the plasma volume and being hit by the photons can be calculated. In the case of *PlanICE*, it corresponds to the inner surface of

[1] The emissivity ϵ_{ik} of an atomic transition was already introduced in equation (2.42) and results from the integration over the corresponding atomic spectral line.

the plasma vessel. Considering the bottom plate, top plate as well as the lateral surface of the cylindrical vessel leads to a value of $S \approx 0.1\,\mathrm{m}^2$.

6 Characterization of emission ranges and photon fluxes in pure gases and gas mixtures

As introductorily mentioned, the impact of photons on surfaces facing a plasma is crucially determined by the photon energy and the corresponding absolute photon flux. Depending on the particular treatment process, different spectral ranges may play a relevant role. With the filter set presented in section 4.2.1, the diode system provides the user the possibility to flexibly determine photon fluxes from the most significant energy ranges in the specific plasma setup.

In order to compile the filter set given in table 4.1 and the gas specific filter combinations presented in the tables 4.3 to 4.6, the most relevant photon energy ranges which are characteristic for the common feed gases and gas mixtures were identified. Therefore, a systematic energy resolved quantification of photon fluxes in the pure gases argon, hydrogen, nitrogen and oxygen as well as in the gas mixtures nitrogen/hydrogen (50:50), hydrogen/oxygen (85:15) and nitrogen/oxygen (80:20) was carried out at *PlanICE* in power and pressure scans. On overview of the performed measurement series is given in table 6.1.

Absolute photon fluxes were determined using the absolute intensity calibrated VUV spectrometer together with the high resolution optical emission spectrometer. Photon fluxes from the VUV range are related to a high photon energy range, those from the UV range are attributed to a medium energy. Photons from the visible region are assigned to a rather low energy range. For the filter set of the diode system, filters were chosen which correspond to spectral ranges in the high energetic VUV and medium energetic UV region. With a view to a classification in order to guide the reader, the measured photon fluxes are compared to the occuring ion fluxes. A photon-to-ion flux ratio $\Gamma_{ph}/\Gamma_{ion} \gtrapprox 0.5$ is classified as "high flux ratio", a value below 0.5 is assigned to a "low flux ratio".

Gas (mixture)	Power scan	Pressure scan
Ar	1 Pa: 200 W, 300 W, 400 W	300 W: 0.5 Pa, 1 Pa, 3.5 Pa, 5 Pa, 7 Pa, 10 Pa
H_2	1 Pa: 700 W, 900 W, 1100 W	700 W: 1 Pa, 3 Pa, 5 Pa, 7 Pa, 10 Pa
N_2	1 Pa: 300 W, 400 W, 600 W	400 W: 0.3 Pa, 1 Pa, 3 Pa, 5 Pa, 7 Pa, 10 Pa
O_2	1 Pa: 400 W, 500 W, 600 W	600 W: 0.3 Pa, 1 Pa, 2 Pa, 3 Pa, 5 Pa, 7 Pa, 10 Pa
N_2/H_2 (50:50)	1 Pa: 300 W, 500 W, 700 W	500 W: 0.3 Pa, 1 Pa, 3 Pa, 5 Pa, 7 Pa, 10 Pa
H_2/O_2 (85:15)	1 Pa: 700 W, 900 W, 1100 W	700 W: 1 Pa, 3 Pa, 5 Pa, 7 Pa, 10 Pa
N_2/O_2 (80:20)	1 Pa: 300 W, 500 W, 700 W	500 W: 0.4 Pa, 1 Pa, 3 Pa, 5 Pa, 7 Pa, 10 Pa

Table 6.1: Measurement series with pressure and power scans performed at *PlanICE* in different gases and mixtures. The given power values refer to the generator power.

The following sections give an overview of the identified relevant spectral ranges individually for each investigated gas (mixture) and indicate the corresponding filters chosen for the diode system. Broadband spectra in the range of 60 - 900 nm with absolute intensities present the spectral composition arising from the most prominent atomic and molecular emission features of the investigated plasmas. The region below 300 nm was obtained with the VUV spectrometer while the optical spectrometer was applied for the range above 300 nm. Below the lower wavelength limit, the spectra are characterized by noise due to the rise of the VUV spectrometer's calibration factor in combination with less or no intensity from the plasmas. In general, the identification of atomic and ionic lines is performed with the help of the NIST database [KYRa19d, KYRa19c]. The molecular emission ranges are derived from literature for which the specific reference will be indicated individually.

The results obtained in the power scans are summarized in detail for each gas or gas mixture in the appendix F. Additionally, the measured plasma parameters

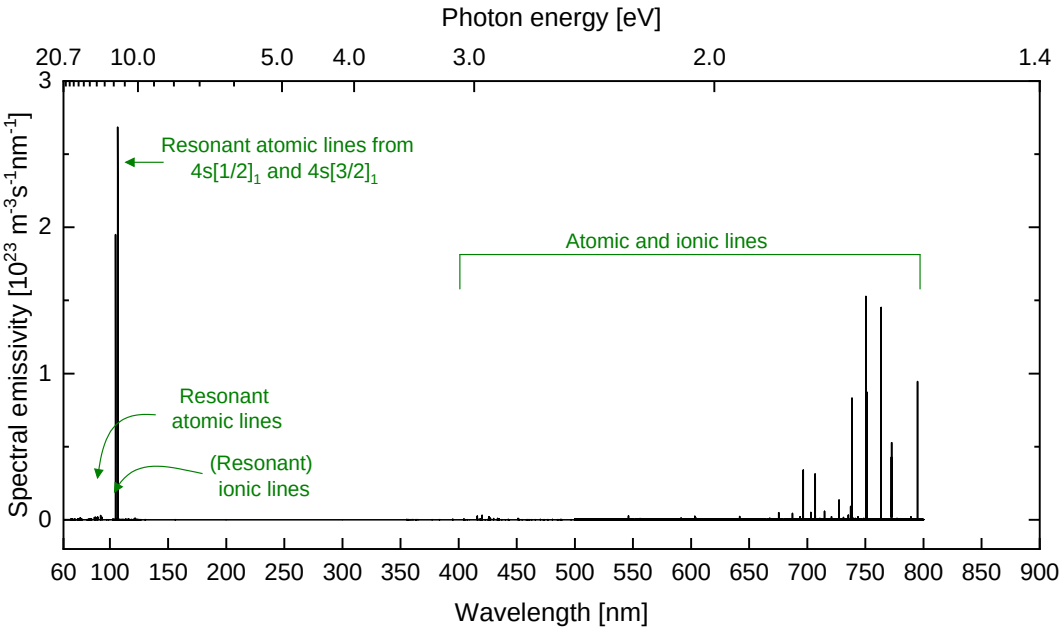

Figure 6.1: Absolute intensities of an argon discharge at 1 Pa and 300 W generator power.

(T_e, n_e, T_{gas}) together with the ion composition whose interplay determine the ion flux are also compiled there. In the following, the results of the pressure scans will be given. Additionally, the highest photon energy, for which a significant emission was measured, will be stated for each investigated gas and gas mixture.

6.1 Pure gases

6.1.1 Argon

The noble gas argon is widely used for industrial coating applications, e.g. regarding films with a low dielectric constant [LRR+17, YS08]. It exhibits a line spectrum produced by neutral and ionic atoms which is exemplarily depicted in figure 6.1 for 1 Pa and 300 W generator power. Resonant atomic emission lines occur below 110 nm (11.3 eV) [Min73] while transitions between excited states are restricted to the range above 300 nm. The most prominent and very intense atomic lines in the VUV range are located at 104.8 nm (11.8 eV) and 106.7 nm (11.6 eV). They are assigned to the resonant transitions from the states $(^2P_{1/2}{}^\circ)4s[1/2]_1$ and $(^2P_{3/2}{}^\circ)4s[3/2]_1$ into the ground state ^{1}S. The highest detected photon energy ranges around 21.4 eV at 0.3 Pa arising from further resonant ionic lines in the wavelength range below 100 nm. The corresponding emissivity is, however, in-

significant. Argon produces a minor emission in the UV and the visible range. The second emission range with significant intensity arising from atomic and ionic lines can be observed in the near infrared region with a wavelength greater or equal to 670 nm with an energy lower or equal to 1.9 eV, respectively.

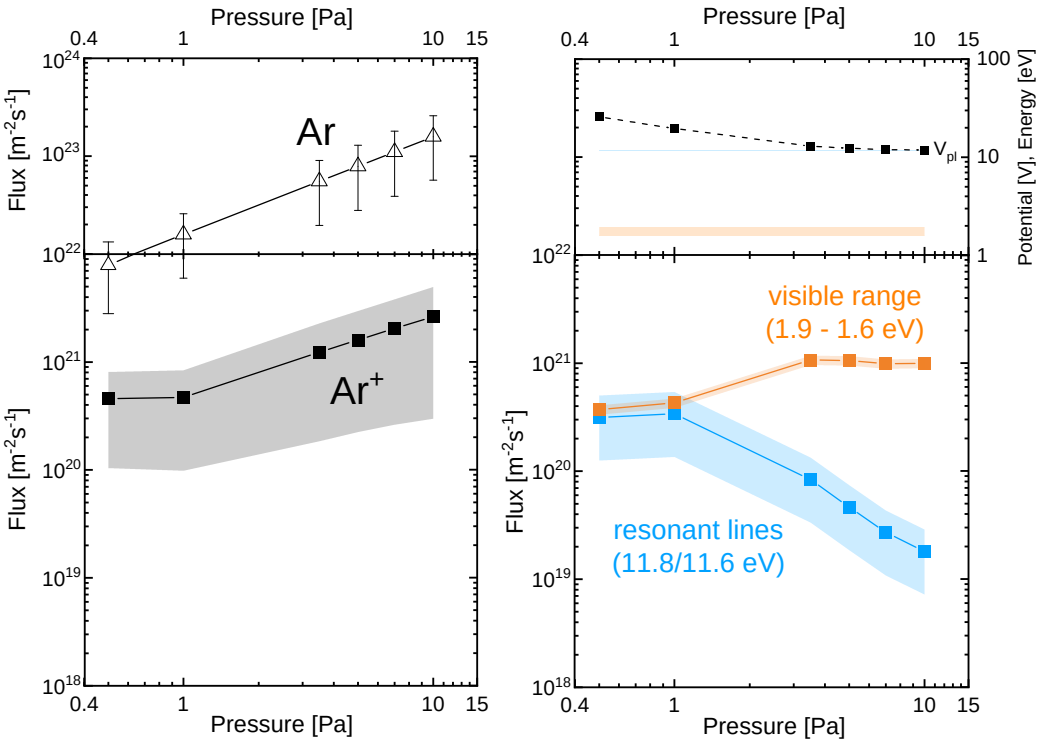

Figure 6.2: Particle and photon fluxes measured in argon (pressure scan at 300 W). Please note the different scaling of the vertical axis in the left lower and upper part. The right upper part illustrates the corresponding photon energy ranges and the plasma potential as upper ion energy limit. The plasma parameters used in the particle fluxes' calcuation are given in figure F.1 in the appendix.

Figure 6.2 exemplarily shows the results of the particle fluxes (left side) and photon fluxes (right side) for the pressure scan. It is pointed out that the vertical axis is differently scaled in the lower and upper part of the left figure. The energy ranges of the photon fluxes are depicted in the right upper part as horizontal lines or bands in corresponding colours. The plasma potential V_{pl} serves for estimating the ions' upper energy limit when hitting the vessel walls and is also included as black squares. It is assumed that an ion from the bulk plasma passes the complete potential drop to the vessel surface without energy loss due to collisions. In this example, the estimated ion energy decrease from roughly 26 eV to 12 eV with

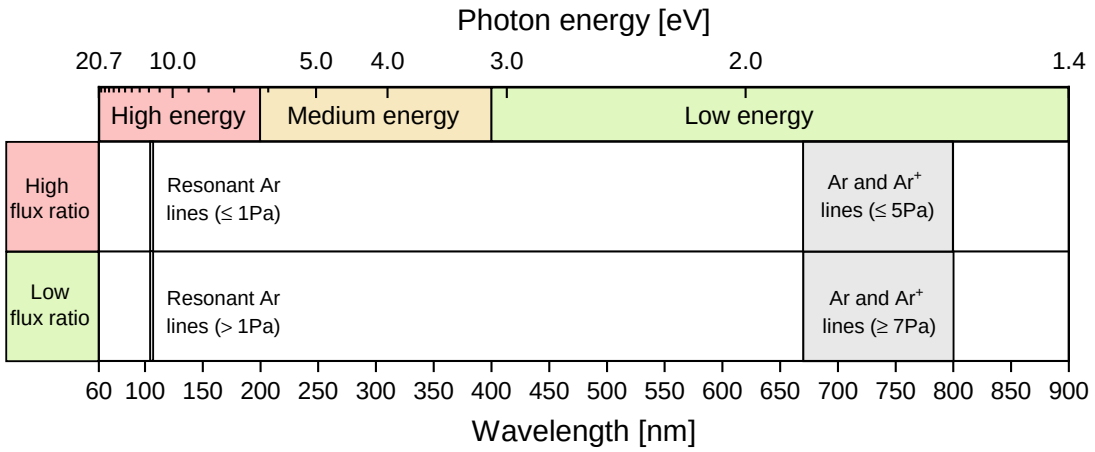

Figure 6.3: Characterization scheme of the identified emission ranges in argon discharges (at a generator power of 200 W, 300 W and 400 W at 1 Pa as well as pressure scans between 0.5 Pa and 10 Pa at 300 W generator power). Main emission ranges are highlighted in gray. The resonant atomic lines at 104.8 nm and 106.7 nm have been identified as the relevant emission range.

increasing pressure. The plasma parameters required for the determination of the particle fluxes are summarized in the appendix in figure F.1.

The left part shows an increase of the atomic and ion fluxes with pressure which can be traced back to an increase of the corresponding particle densities. The ion flux is determined assuming only the ion species Ar^+ with a mass according to the natural isotopic ratio. The photon fluxes with low energy (1.9 - 1.6 eV) also increase with pressure.

Special focus should be laid on the resonant atomic argon lines at 104.8 nm (11.8 eV) and 106.7 nm (11.6 eV) since significant damaging effects on low-k material induced by them have been reported in [SRN+12, RRM+13]. At pressures lower or equal to 1 Pa, the photon flux from these resonant lines is in the range of $3 \cdot 10^{20}\,\mathrm{m^{-2}s^{-1}}$ and thus comparable to the ion flux Γ_{ion}. Following the results in [RRM+13], the corresponding photon fluxes would have a significant effect on the Si-CH_3 bonds in the investigated material after an exposure of few minutes to the plasma. With increasing pressure, the photon flux from the resonant atomic lines is rapidly decreasing and much lower than the ion flux The photon-to-ion flux ratio accounts for 0.07 at 3.5 Pa and further decreases to 0.01 at 10 Pa.

The emission range in the near infrared region exhibits a photon-to-ion flux ratio from 0.66 up to 0.91 for pressures lower or equal to 5 Pa. The results are summarized in table 6.3.

Since no bandpass filters are commercially available below 113 nm, the filter com-

bination "No filter – MgF_2" was chosen to select the resonant atomic argon lines in the VUV with the diode system. At low pressure, they produce photon fluxes comparable to the ion flux and whose possible crucial influence on material has been exemplarily discussed above.

6.1.2 Hydrogen

Hydrogen discharges or plasmas with hydrogen admixture are widely studied, e.g. in fusion research [SFF+06, vRVG+07], for x-ray lithography [ZKL+11] or for reducing oxide layers on metals [SRP+14].

Characteristic features of hydrogen discharges are the atomic Lyman series in the VUV range and the Balmer series in the optical region which are indicated in figure 6.4. The former summarizes resonant atomic transitions from excited states n' into the ground state $n'' = 1$ while the latter corresponds to transitions ending on the first excited state $n'' = 2$. The most well-known representatives are the L_α line at 121.6 nm (10.2 eV) and the H_α line at 656.3 nm (1.9 eV). Besides, various molecular bands occur. In the VUV/UV range, they are represented by the resonant Werner band (C $^1\Pi_u \rightarrow$ X $^1\Sigma_g^+$, ≈80 - 130 nm, 15.5 - 9.5 eV), the resonant Lyman band (B $^1\Sigma_u^+ \rightarrow$ X $^1\Sigma_g^+$, ≈130 - 190 nm, 9.5 - 6.5 eV) as well as the continuum (a $^3\Sigma_g^+ \rightarrow$ b $^3\Sigma_u^+$, ≈190 - 280 nm, 6.5 - 4.4 eV) ending in a non-binding state. Since these bands partly overlap, the indicated intervals assign the corresponding main emission range. The Fulcher-α transition ($d\,^3\Pi_u \rightarrow a\,^3\Sigma_g^+$) in the optical region is predominantly located in the wavelength range 590 - 650 nm (2.1 - 1.9 eV). Beyond, further non-resonant molecular bands occur with minor intensity and corresponding to small photon energies.

Figure 6.5 presents the measured photon fluxes as well as the determined particle fluxes. As depicted in the left part, both the molecular and atomic flux increase with the pressure. The molecular flux ranges between $\Gamma_{\mathrm{mol}} = 8.1 \cdot 10^{22}\,\mathrm{m^{-2}s^{-1}}$ and $\Gamma_{\mathrm{mol}} = 6.7 \cdot 10^{23}\,\mathrm{m^{-2}s^{-1}}$ while the atomic flux is roughly one order of magnitude below. An atomic-to-molecular density ratio δ in the range of 0.09 - 0.15 is obtained in the pressure scan. In the power scan, it increases up to 0.25.

The ion flux roughly stays constant around $\Gamma_{\mathrm{ion}} = 1.5 \cdot 10^{20}\,\mathrm{m^{-2}s^{-1}}$. The plasma parameters required for the calculation of the ion fluxes are summarized in figure F.3 in the appendix. There, also the composition of the ions species derived with the mass spectrometer is shown. At pressures above 1 Pa, H_3^+ is almost the exclusively detected ion species. At 1 Pa, H_3^+ is also the dominant species, followed by H_2^+ and to a less extend by H^+.

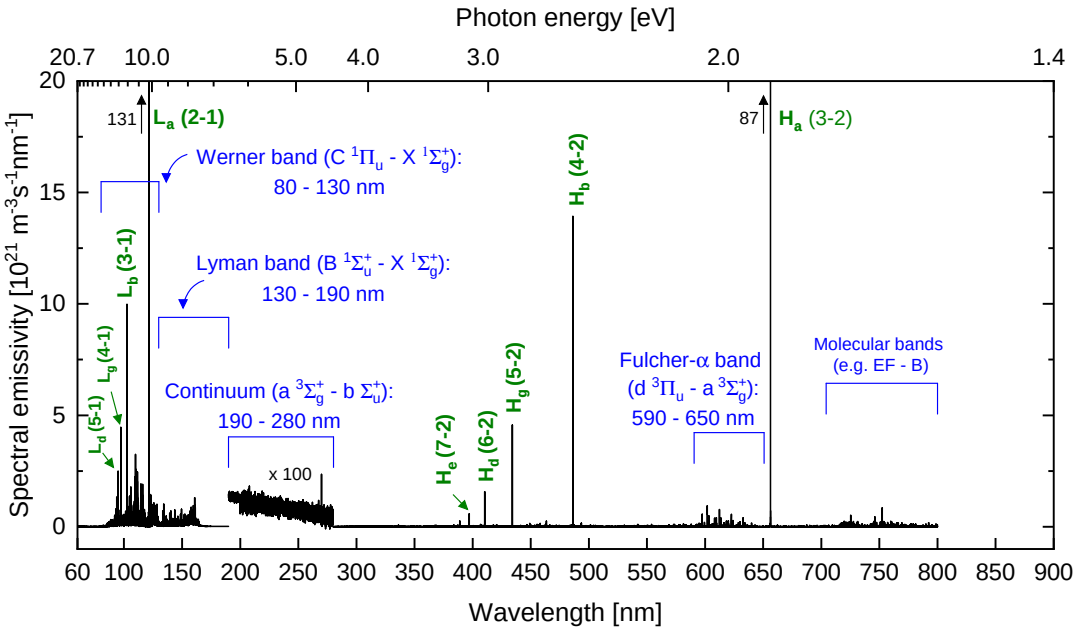

Figure 6.4: Absolute intensities of a hydrogen discharge at 1 Pa and 900 W generator power. The continuum is displayed with a multiplication factor of 100. Emission ranges of molecular hydrogen are displayed in blue. The Lyman and Balmer series of atomic hydrogen are indicated in green and the levels of the corresponding transition are given in brackets (n'-n").

The upper right part of figure 6.5 shows the photon energies of the identified spectral ranges and a decreasing plasma potential with pressure from 32 V at 1 Pa to 11 V at 10 Pa. The highest detected photon energy in hydrogen was 15.4 eV at 1 Pa. At this pressure, the ion energy exceeds the highest photon energy while it is in the energy range of photons from the Werner band and L_α line for pressures above 1 Pa.

Photons from hydrogen discharges cover wide ranges of fluxes as well as corresponding energies. Pressure dependent photon fluxes arising from the identified emission ranges are depicted in the lower right section of figure 6.5. They all show a maximum at 3 Pa with values between $9.7 \cdot 10^{18}\,\mathrm{m^{-2}s^{-1}}$ from the Fulcher band up to $2.7 \cdot 10^{20}\,\mathrm{m^{-2}s^{-1}}$ from the Werner band and Lyman series.

The H_α line as well as the Fulcher-α transition both located in the low energy range produce minor photon fluxes in comparison with the determined ion flux. Their photon-to-ion flux ratio does not exceed 0.23 and 0.08, respectively. Therefore, both the Fulcher band as well as the H_α are assigned to a low energy and a low flux ratio in figure 6.6. For the continuum, the photon-to-ion flux ratio is comparable to the one of the H_α line. However, the corresponding photon

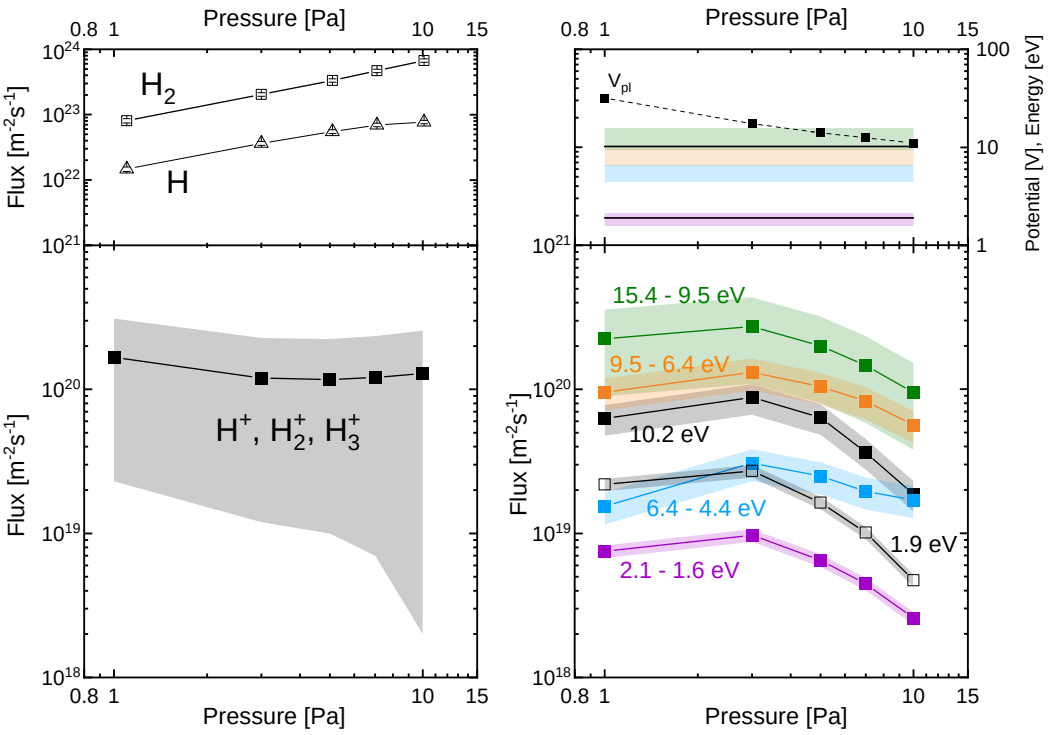

Figure 6.5: Particle and photon fluxes measured in hydrogen (pressure scan at 700 W generator power). Please note the different scaling of the vertical axis in the left lower and upper part.

energy is higher and can be predominantly assigned to the medium energy range reaching into the high energy range. For this reason, the bandpass filter 230BP is selected for the diode system to determine photon fluxes from the Continuum (see table 4.4).

The molecular emission ranges in the VUV range are identified to play an even more relevant role. The Lyman band exhibits flux ratios between 0.54 and 1.08 below 10 Pa with a slight decrease to 0.44 at 10 Pa. The wavelength range below 130 nm—assigned to the Werner band together with the Lyman series—reaches highly significant absolute photon fluxes. The corresponding photon-to-ion flux ratio ranges between 0.73 and 2.26. Considering only the L_α line, the value stays below 0.49 at 1 Pa and at pressures greater or equal to 7 Pa but achieves a maximum of 0.73 at 3 Pa.

The filter set of the diode system includes bandpass filters for the Continuum (230BP), the Lyman band (154BP) and the L_α line (122BP) as well as the filter

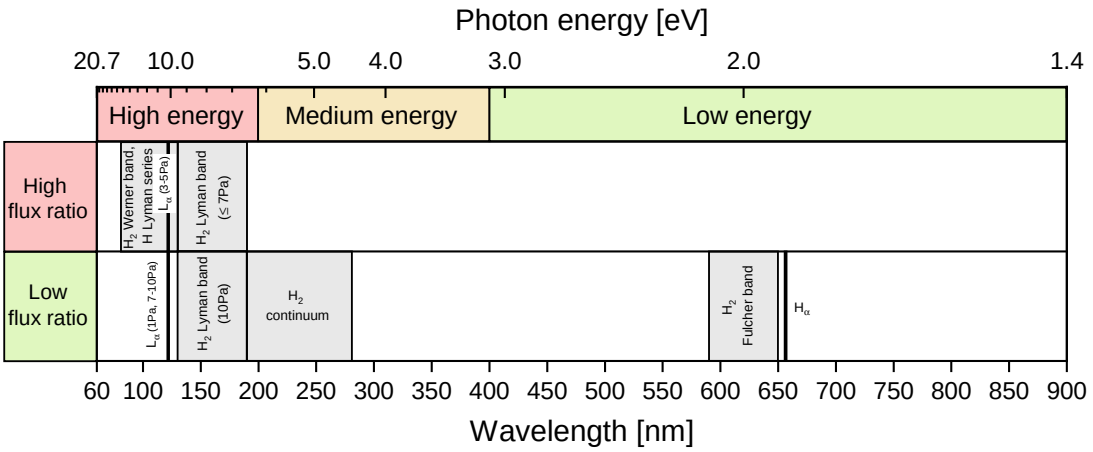

Figure 6.6: Characterization scheme of the identified emission ranges in hydrogen discharges at a generator power of 700 W, 900 W and 1100 W at 1 Pa as well as pressure scans between 1 Pa and 10 Pa at 700 W generator power. The Lyman band, the L_α as well as the range assigned to the Werner band together with the Lyman series are identified as most relevant emission ranges.

combination "No filter – MgF_2" for the Werner band together with L_β, L_γ. They are summarized in table 4.4.

6.1.3 Nitrogen

Figure 6.7 presents a spectrum of nitrogen at 1 Pa and a generator power of 400 W. In the investigated wavelength range between 60 nm and 900 nm, neutral nitrogen molecules produce three well separated systems for which the emission ranges are taken from [LK77]. The First positive system (B $^3\Pi_g \rightarrow$ A $^3\Sigma_u^+$, ≈480 - 2500 nm, 2.6 - 0.5 eV) covers broad parts of the visible and near infrared region. Vibronic transitions with $\Delta v = +5, \ldots, +1$ lie within the accessible range of the spectrometers. In this range, several atomic emission lines are also located.
The UV range is dominated by the Second positive system (C $^3\Pi_u \rightarrow$ B $^3\Pi_g$, ≈270 - 550 nm). The main emission is observed in the range 270 - 475 nm (4.6 - 2.6 eV) including the vibronic transitions with $\Delta v = +3, \ldots, -4$ which are indicated in figure 6.7. Additionally, emission from the First negative system of the molecular nitrogen ion (B $^2\Sigma_u^+ \rightarrow$ X $^2\Sigma_g^+$, ≈330 - 470 nm) occurs in the UV and overlaps with the Second positive system of neutral nitrogen molecules. If the emissivity axis is enlarged, vibronic transitions corresponding to $\Delta v = +2, \ldots, -2$ can be identified with a minor intensity. For reasons of clarity, they are not indicated individually in figure 6.7. Due to the overlap with the second positive system,

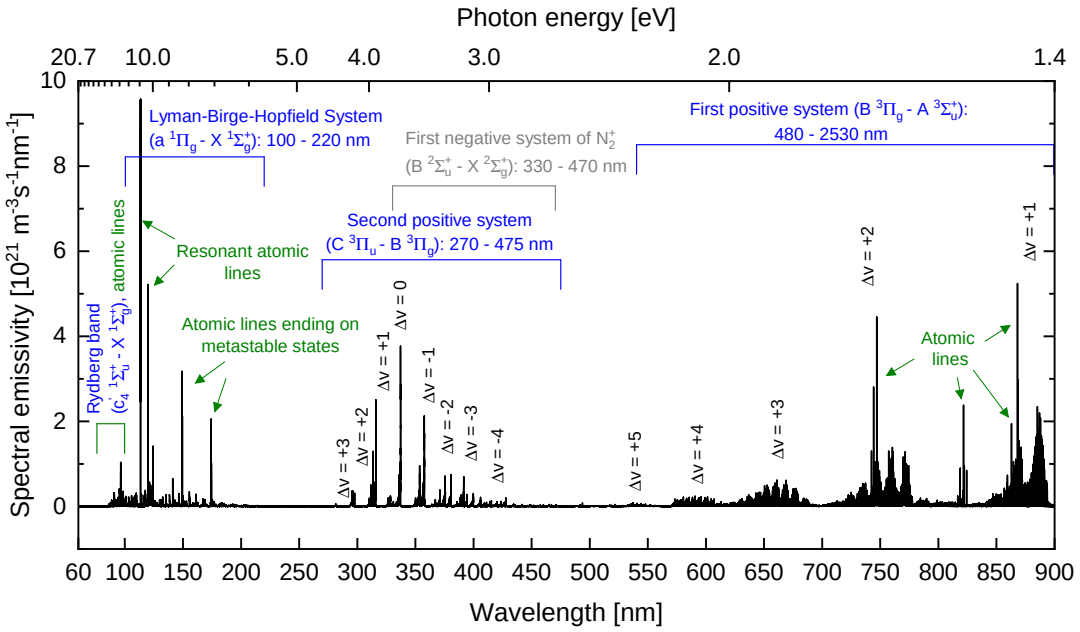

Figure 6.7: Absolute intensities of a nitrogen discharge at 1 Pa and 400 W generator power. Molecular emission ranges are indicated in blue [LK77] and atomic lines are given in green.

photon fluxes from the first negative system could not be separately investigated. The resonant Lyman-Birge-Hopfield system ($a\ ^1\Pi_g \rightarrow X\ ^1\Sigma_g^+$, 100 - 220 nm, 12.4 - 5.6 eV) reaches down to the vacuum ultraviolet region and is superimposed by several intense atomic lines. These include the resonant atomic multiplets[1] at 113.5 nm (10.9 eV, $2s2p^4\ ^4\mathrm{P}_{\frac{1}{2},\frac{3}{2},\frac{5}{2}} \rightarrow 2s^22p^3\ ^4\mathrm{S}^\circ_{\frac{3}{2}}$) and at a wavelength of 120.0 nm (10.3 eV, $2s^22p^23s\ ^4\mathrm{P}_{\frac{1}{2},\frac{3}{2}} \rightarrow 2s^22p^3\ ^4\mathrm{S}^\circ_{\frac{3}{2}}$). Additionally, intense atomic multiplets arising from $2s^22p^23s\ ^2\mathrm{P}_{\frac{1}{2},\frac{3}{2}}$ and ending on the metastable states $^2\mathrm{D}^\circ_{\frac{3}{2},\frac{5}{2}}$ and $^2\mathrm{P}^\circ_{\frac{1}{2},\frac{3}{2}}$, both with electron configuration $2s^22p^3$, occur at 149.3 nm (8.3 eV) and 174.4 nm (7.1 eV), respectively.

Further atomic lines lie within the range of the First positive system and below 110 nm, respectively. In the latter range, another band structure can be detected whose shape differs from the Lyman-Birge-Hopfield system. It might be assigned to the Rydberg band ($\mathrm{c}'_4\ ^1\Sigma_\mathrm{u}^+ \rightarrow \mathrm{X}\ ^1\Sigma_\mathrm{g}^+$) of molecular nitrogen [BSS+81]. Vibronic (v', v'')-transitions occur e.g. at 94.4 nm (3,2), 95.8 nm (0,0), 96.4 nm (3,3) and 98.1 nm (0,1) [GLTM99] which coincidence with the wavelength position of observed peaks in the spectrum.

[1] Atomic emission lines arising or ending on levels with a multiplicity $2S + 1 > 1$ are called multiplets and occur clustered in the spectra. In the case of two or three such lines, it is referred to a *doublet* or a *triplet*, respectively.

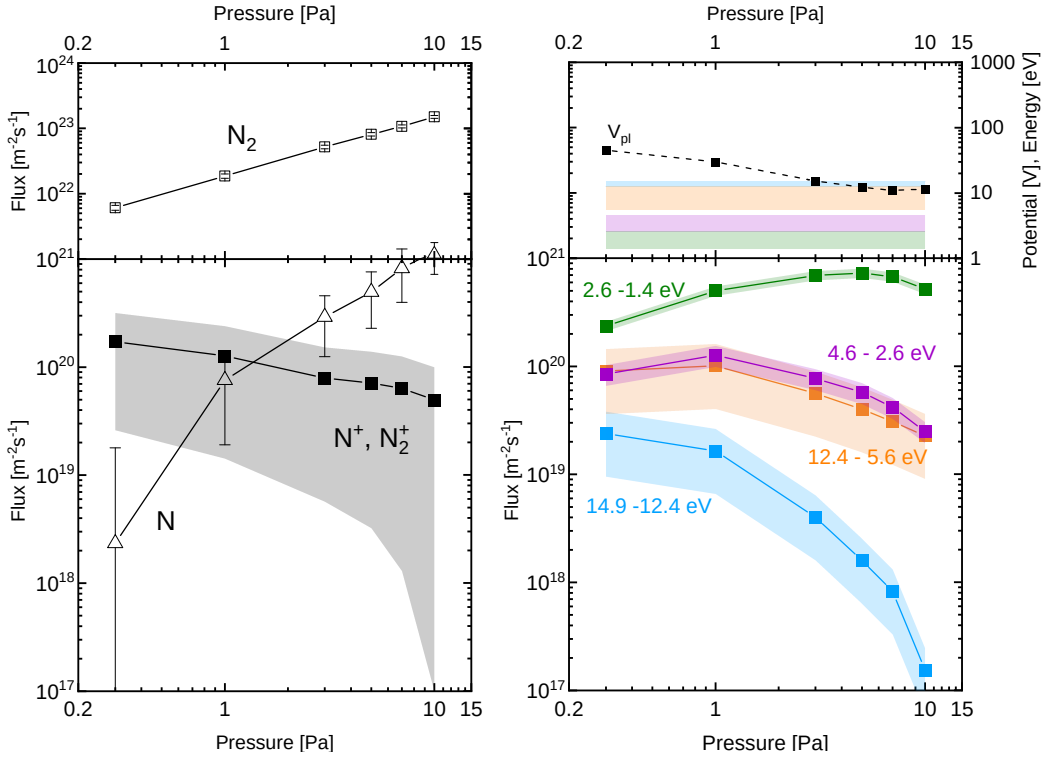

Figure 6.8: Particle and photon fluxes determined in nitrogen during the pressure scan at 400 W generator power. Please note the different scaling of the vertical axis in the left lower and upper part.

The results for the pressure scan are presented in figure 6.8, those for the power scan in figure F.6 in the appendix. As can be seen, the neutral atomic and the molecular particle fluxes are both increasing with the pressure in the range $2.3 \cdot 10^{18}$ - $1.2 \cdot 10^{21}\,\mathrm{m^{-2}s^{-1}}$ and $6.1 \cdot 10^{21}$ - $1.5 \cdot 10^{23}\,\mathrm{m^{-2}s^{-1}}$, respectively. The atomic-to-molecular density ratio increases from δ=0.0003 at 0.3 Pa to δ=0.006 at 10 Pa. It is rather low compared to hydrogen discharges with values in the range of 0.09 - 0.15 between 1 Pa and 10 Pa. Moreover, it shows an opposite pressure dependency.

The ion flux is decreasing with the pressure from $1.7{\cdot}10^{20}\,\mathrm{m^{-2}s^{-1}}$ to $5.0{\cdot}10^{19}\,\mathrm{m^{-2}s^{-1}}$ and the corresponding maximal ion energy shows also a decrease from 45 eV to 11 eV. For pressures below 10 Pa, N_2^+ is the dominant ion species with a small fraction of N^+. At 10 Pa, the latter is dominating, and also a contribution from NH^+, N_2H^+ or $N_2H_4^+$ occurs. Hydrogen might arise from trace amounts of water released from the vessel walls due to a rising gas temperature (see figure F.5 in the appendix).

Nitrogen produces high photon fluxes with respect to the ion flux in the entire energy range below 12.4 eV. The classification of the spectral ranges can be seen in figure 6.9. Especially the part of the First positive system, which is accessible with the diagnostic system, is characterized by high photon fluxes in the range of (2.4 - 7.3)·10^{20} $m^{-2}s^{-1}$ with corresponding photon-to-ion flux ratios between 1.37 (at 0.3 Pa) and 10.6 (at 7 Pa). Since only a fraction of the First positive system can be detected, the flux from the total transition is even higher. However, due to the rather low photon energy of less than 2.6 eV, the relevance of the assigned photon fluxes is considered as minor. Thus, no corresponding filter combination is chosen for the diode system. In contrast, the Second positive system and the Lyman-Birge-Hopfield system (together with the atomic lines) dominate the medium and high energy range until 12.4 eV. Moreover, they exhibit high photon-to-ion flux ratios of at least 0.46 each with a maximum of 0.79 and 1.00, respectively, at 1 Pa. Therefore, the combinations "MgF_2 – BK7 " and "BK7 – 500LP" are selected for the diode system. They are given in table 4.5.
Photon fluxes with a photon energy exceeding 12.4 eV show a photon-to-ion flux ratio of less than 0.14 throughout the investigated parameter range. However, due to the very high photon energy (with a maximal observed value up to 14.9 eV) the filter combination "No filter – MgF_2" can additionally be applied for nitrogen plasmas. Furthermore, the bandpass 154BP allows to select a narrow wavelength interval including a fraction of the Lyman-Birge-Hopfield system and several atomic lines. The corresponding filter set for nitrogen plasmas is summarized in table 4.5.

6.1.4 Oxygen

Although being a molecular gas,the invested oxygen plasmas produce radiation which is dominated by atomic lines. A spectrum taken at 1 Pa and a generator power of 600 W is presented in figure 6.10. The most intense representatives of atomic lines are the triplets located around 777.3 nm (1.6 eV, $2s^22p^33p\ ^5P_{1,2,3} \rightarrow 2s^22p^33s\ ^5S^\circ_2$) and 844.6 nm (1.5 eV, $2s^22p^33p\ ^3P_{0,1,2} \rightarrow 2s^22p^33s\ ^3S^\circ_1$). In the VUV range, emission lines including resonant transitions ending on the ground state arise at 98.9 nm (12.5 eV, $2s^22p^33s\ ^3D^\circ_{1,2,3} \rightarrow 2s^22p^4\ ^3P_2$), 130.3 nm (9.5 eV, $2s^22p^33s\ ^3S^\circ_1 \rightarrow 2s^22p^4\ ^3P_{0,1,2}$) and 135.7 nm (9.1 eV, $2s^22p^33s\ ^5S^\circ_2 \rightarrow 2s^22p^4\ ^3P_{1,2}$). Lines ending on metastable states occur for example at 115.2 nm (10.8 eV, $2s^22p^33s\ ^1D^\circ_2 \rightarrow 2s^22p^4\ ^1D_2$). Several atomic and ionic lines can be detected up to a photon energy of 17.2 eV at 0.3 Pa.

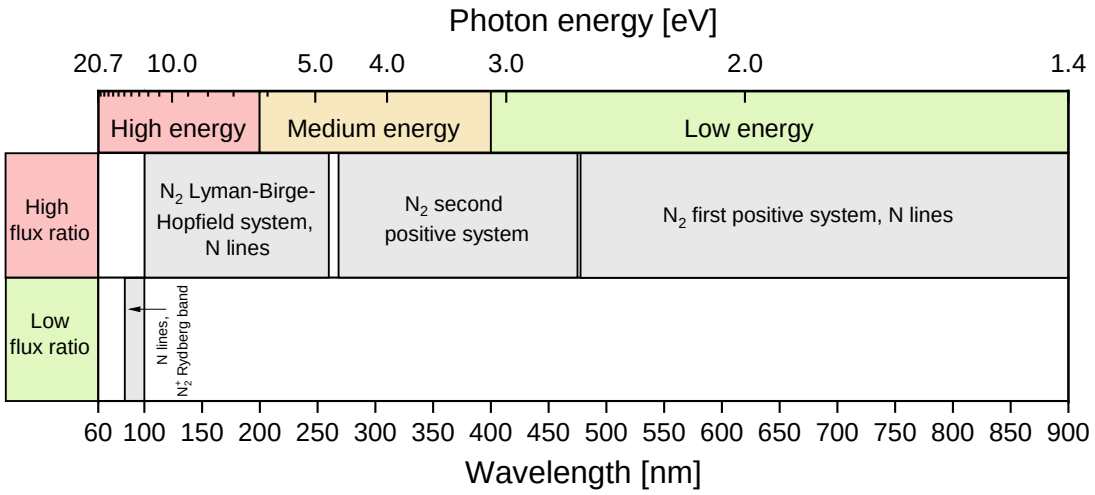

Figure 6.9: Characterization scheme of the identified emission ranges in nitrogen discharges at a generator power of 300 W, 400 W and 600 W at 1 Pa as well as pressure scans between 0.3 Pa and 10 Pa at 400 W generator power. The second positive system and the Lyman-Birge-Hopfield system of molecular nitrogen as well as the energy range above 12.4 eV are indentified as the most relevant emission ranges. Despite the high photon-to-ion flux ratio of the first positive system, it is not further considered due to the low photon energy.

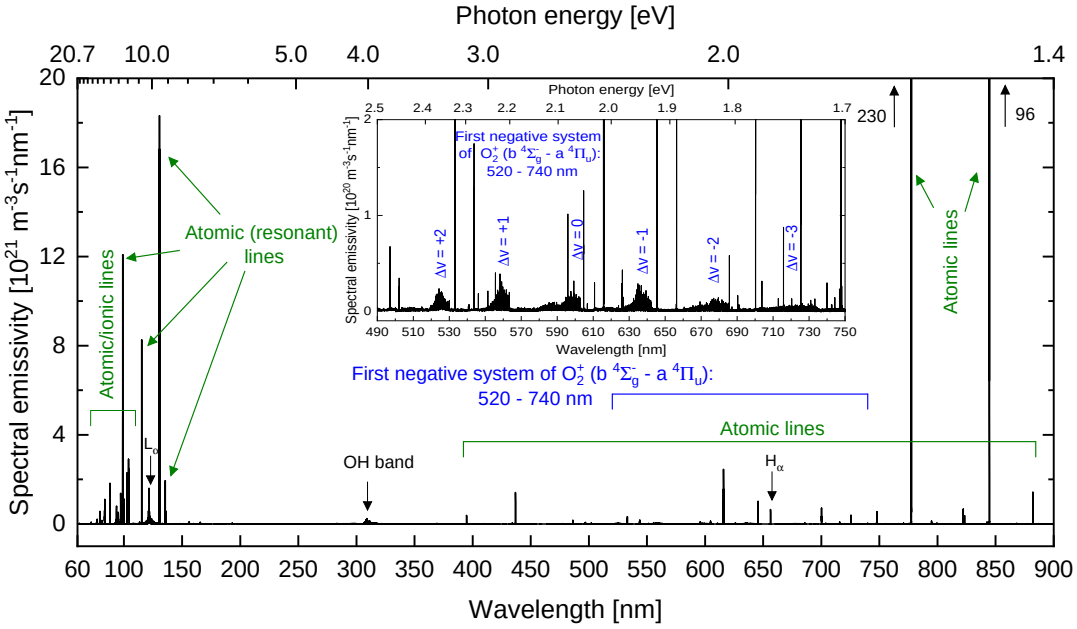

Figure 6.10: Absolute intensities of an oxygen discharge at 1 Pa and 600 W generator power. Atomic lines are given in green. Molecular emission ranges are indicated in blue [Kru72] and depicted in enlarged scale in the inset.

With almost negligible intensity, vibronic bands of the First negative system of

O_2^+ (b $^4\Sigma_g^-$ → a $^4\Pi_u$) with $\Delta v = +2, \ldots, -3$ are observed within 520 - 740 nm (2.4 - 1.7 eV). Additionally, slight emission from hydrogen impurities (L_α, H_α, OH band) are detected. It might be traced back to adsorbed water at the vessel walls which is released preferably in oxygen plasmas due to the very high wall temperatures. Those arise from typical high power transfer efficiencies up to 77 % compared to other plasmas inducing a rich surface chemistry.

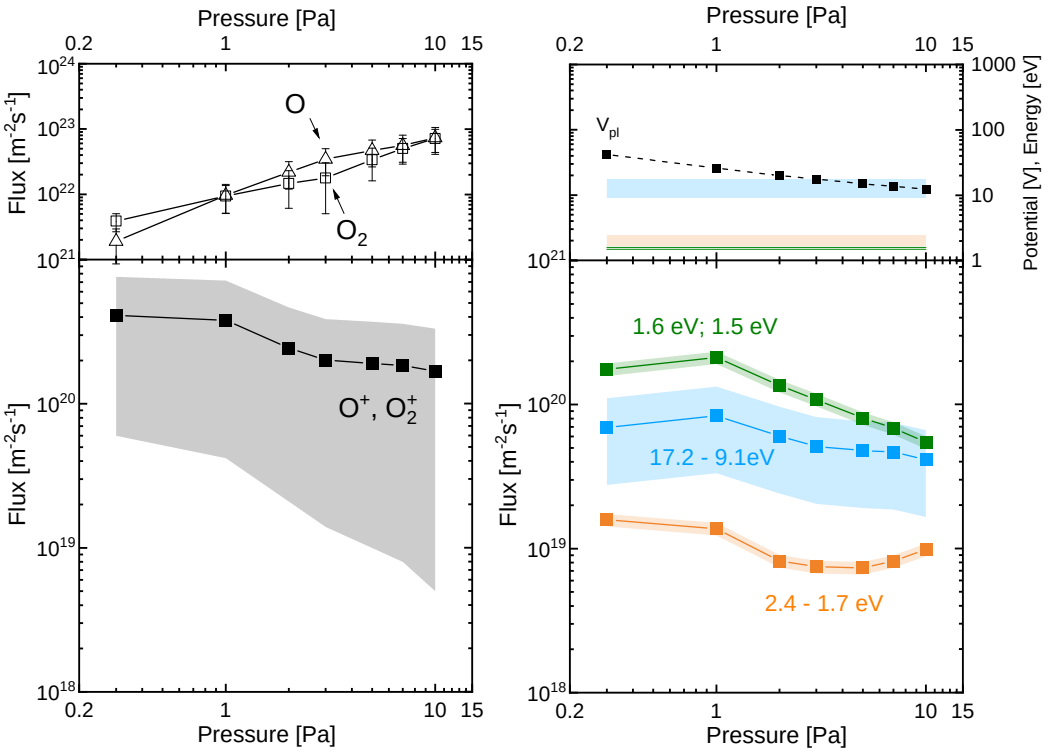

Figure 6.11: Particle and photon fluxes determined in oxygen during the pressure scan at 600 W generator power. Please note the different scaling of the vertical axis in the left lower and upper part.

The results of the pressure scan are summarized in figure 6.11, those of the power scan in figure F.8 in the appendix. The atomic and molecular fluxes of neutral oxygen are in the same order of magnitude and increase with pressure from several $10^{21}\,\mathrm{m^{-2}s^{-1}}$ at 0.3 Pa up to roughly $7 \cdot 10^{22}\,\mathrm{m^{-2}s^{-1}}$ at 10 Pa. The atomic-to-molecular density ratio was determined to be in the range 0.3 - 1.4.
The positive ion flux consists of the species O^+ and O_2^+ with the former being the dominant species below 3 Pa. With increasing pressure, the distribution is reversing in the sense that O_2^+ is the predominant species. In the investigated pressure scan, the ion flux is slightly decreasing from $4.1 \cdot 10^{22}\,\mathrm{m^{-2}s^{-1}}$ to $1.7 \cdot$

$10^{22}\,\mathrm{m^{-2}s^{-1}}$. The maximal ion energy declines from 42 eV to 12 eV with increasing pressure. For pressures above 1 Pa, the photon energies related to the (resonant) atomic and ionic lines in the VUV range are comparable to the ions' energy. These lines are the only observed emission features in the investigated oxygen plasmas corresponding to the high energy range. For the diode system, the filter combination "No filter – Fused silica" is selected according to table 4.6.
However, the photon flux including these lines does not exceed $8.4 \cdot 10^{19}\mathrm{m^{-2}s^{-1}}$ resulting in low flux ratios of 0.17 - 0.25 in comparison with the ion flux. In particular, the resonant atomic lines at 130.3 nm and 135.7 nm reach their maximum photon flux at 1 Pa with values of $3.6 \cdot 10^{19}\mathrm{m^{-2}s^{-1}}$ and $1.8 \cdot 10^{18}\mathrm{m^{-2}s^{-1}}$, respectively.
An overview of the classification of all investigated emission ranges is depicted figure 6.12.

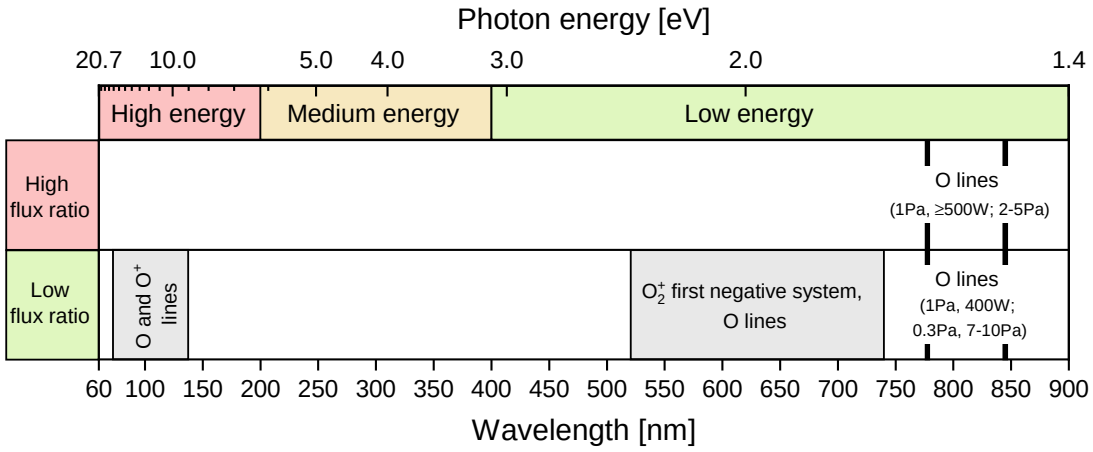

Figure 6.12: Characterization scheme of the identified emission ranges in oxygen discharges at a generator power of 400 W, 500 W and 600 W at 1 Pa as well as a pressure scan between 0.3 Pa and 10 Pa at a generator power of 600 W. The atomic and ionic lines corresponding to high photon energies exceeding 9.1 eV are identified as most relevant emission ranges in oxygen discharges.

6.2 Gas mixtures

In gas mixtures, further spectral emission features occur in addition to the emission from the pure gases since compounds (e.g. NH, OH, NO) are produced in the plasma volume. They are highlighted in the presented spectra in the insets.
The gas mixtures nitrogen/hydrogen (50:50), hydrogen/oxygen (85:15) and nitrogen/oxygen (80:20) with the mixing ratios in brackets were investigated. The

former mixture is typically applied for surface nitriding processes by plasmas, e.g. [Ric97]. The properties of the treated layer is influenced by the hydrogen admixture in nitrogen. Effects on stainless steal are studied for hydrogen concentrations between 5 % and 75 % in [KBF+00]. The ratio 50:50 was selected exemplarily. The composition of the hydrogen/oxygen mixture was selected in order to produce a significant emission from oxygen, on the one hand, and to comply with the restrictions of the pumping system, on the other hand. The latter gas mixture was chosen to represent the main air constituents.

6.2.1 Nitrogen/hydrogen (50:50)

In general, the emission spectra of the nitrogen/hydrogen discharges are mainly dominated by atomic hydrogen lines together with molecular nitrogen emission ranges. However, with decreasing pressure, the significance of the latter is reducing and atomic nitrogen lines gain importance.

Figure 6.13 shows a hydrogen/nitrogen spectrum in the entire accessible wavelength range taken at 1 Pa and 500 W generator power. In the UV range, a minor emission band, identified as the resonant A-X system ($A\,^3\Pi \rightarrow X\,^3\Sigma^-$) of the NH molecule, emerges around 336.0 nm. It appears more pronounced with increasing pressure. An enlarged inset of the NH emission is shown for 10 Pa where the vibrational band with $\Delta v = 0$ can be identified [PG76]. Normalized intensities are displayed with the emission of the pure nitrogen Second positive system depicted in gray for comparison reasons.

Due to the medium energy in the range of 3.7 eV of the NH band, the bandpass filter 337BP with the center wavelength at 337 nm was selected for the diode system (see table 4.7). Depending on the plasma setup and operating parameters, the NH band might be more or less superimposed by the Second positive system of N_2 which is the case in the investigated plasmas at *PlanICE*. Therefore, photon fluxes measured with the diode system together with the 337BP filter cannot be directly assigned to the NH band but only to the corresponding energy range. For further interpretation, a distinct knowledge about the spectral composition of the specific plasma is inevitable. In the following, photon fluxes from the NH band and the Second positive system are not categorized separately.

The results of the pressure scan can be seen in figure 6.14, results of the power scan are shown in figure F.10 in the appendix.

For the neutral particle fluxes, atomic and molecular fluxes of pure nitrogen as well as of hydrogen were calculated. They increase with increasing pressure. The high-

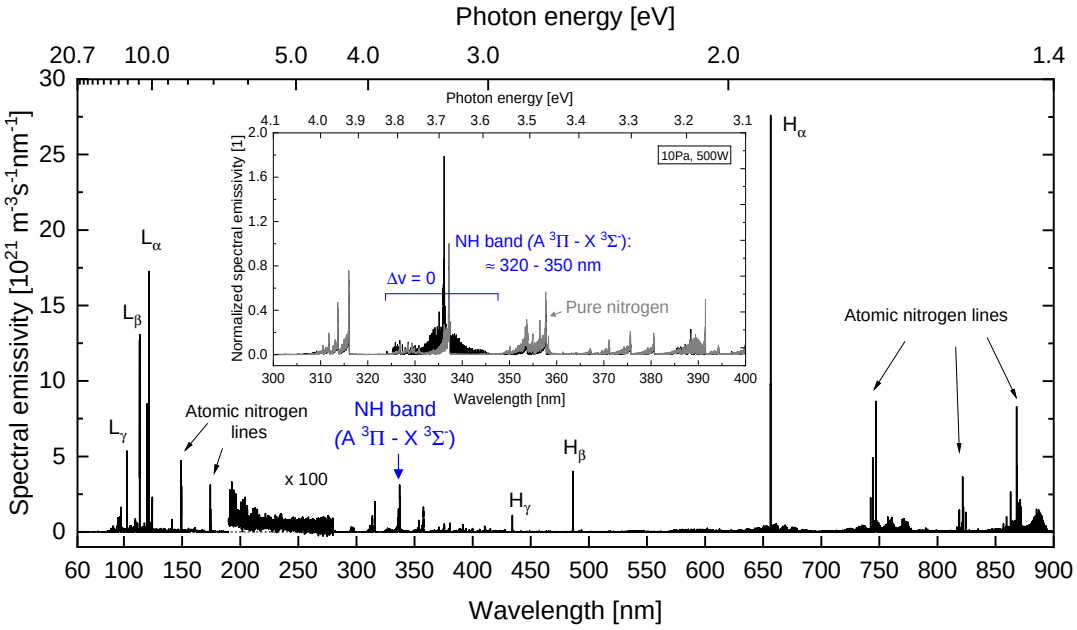

Figure 6.13: Absolute intensities of a nitrogen/hydrogen mixture (50:50) at 1 Pa and 500 W generator power. The spectrum in the wavelength region 190 - 280 nm is depicted with an amplification factor of 100. Since the NH band can be separated more easily from the Second positive system of N_2 with increasing pressure, the inset shows normalized intensities at 10 Pa and 500 W. The spectrum of pure nitrogen is presented for comparison in gray to give an impression about the relevance of the NH band. The emission ranges of the pure gases nitrogen and hydrogen are presented in the figures 6.7 and 6.4, respectively.

est fluxes are produced by hydrogen molecules in the range from $8.2 \cdot 10^{21}\,\mathrm{m^{-2}s^{-1}}$ to $2.2 \cdot 10^{23}\,\mathrm{m^{-2}s^{-1}}$. The atomic hydrogen flux accounts to 49 - 65 % of the molecular hydrogen flux while the molecular nitrogen flux is roughly 40 % and the atomic nitrogen flux is less than 1 % with respect to the molecular hydrogen flux. At a pressure below 3 Pa, the ion flux is dominated by the N_2^+ and N^+. With increasing pressure, their significance declines and composed ion species like N_2H^+, NH_3^+, H_2O^+ become dominant (see figure F.9 in the appendix). In figure 6.14, it can be seen that the ion flux decreases from $1.8 \cdot 10^{20}\,\mathrm{m^{-2}s^{-1}}$ at 0.3 Pa to $4.7 \cdot 10^{19}\,\mathrm{m^{-2}s^{-1}}$ at 10.3 Pa. The plasma potential decreases as well from 37 V to 11 V with pressure. The highest detected photon energy is 19.2 eV at 0.3 Pa.

In contrast to pure hydrogen and nitrogen discharges, photon fluxes from emission ranges of molecular and atomic hydrogen and nitrogen, repectively, below 280 nm are not displayed separately in figure 6.14. They are summarized to photon fluxes with energies above 4.4 eV. Only photon fluxes arising from the L_α line are given individually.

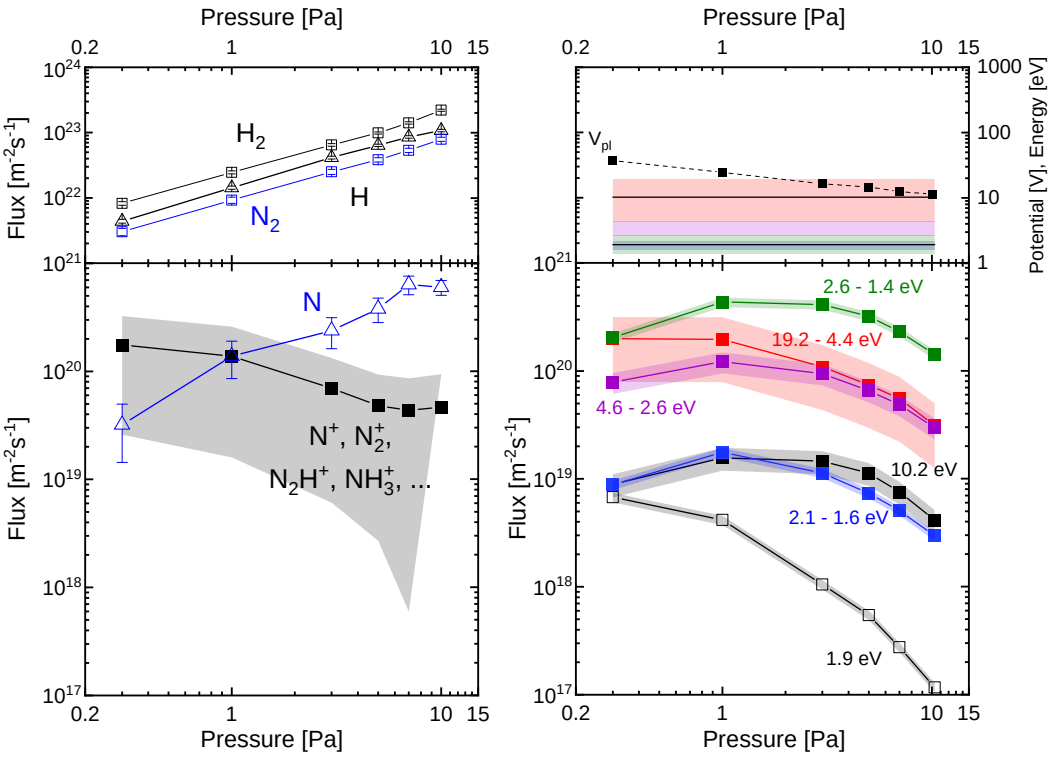

Figure 6.14: Particle and photon fluxes measured in the nitrogen/hydrogen mixture (pressure scan at 500 W generator power). Please note the different scaling of the vertical axis in the left lower and upper part.

In accordance with the measurements in pure nitrogen, high photon fluxes are produced in the wavelength range 478 - 900 nm exceeding the ion flux and with photon-to-ion flux ratios between 1.16 and 6.66. They are composed mainly by the First positive system of molecular nitrogen and a minor proportion of several atomic nitrogen lines. The contributions from the Fulcher band of hydrogen and the atomic H_α line are below 0.05 each. The corresponding characterization according to the photon energy and the photon-to-ion flux ratio of the described emission ranges can be found in table 6.15. The photon flux from the L_α line compared to the determined ion flux does not exceed 0.23. For the Second positive system of N_2, and thus including the NH band, photon-to-ion flux ratios of Γ_{ph}/Γ_{ion} = 0.64 - 1.39 are determined at a discharge pressure of greater or equal to 1 Pa. A slightly lower value of 0.45 is obtained at 0.3 Pa.

The molecular hydrogen Lyman band and the Continuum are superimposed by the Lyman-Birge-Hopfield system (LBH). The photon-to-ion flux ratio in both wavelength ranges does not exceed 0.49. In contrast, the energy range including

the Werner band, the Lyman series of atomic hydrogen as well as a part of the nitrogen Lyman-Birge-Hopfield system provides values between 0.80 and 0.98 in the pressure range lower or equal to 7 Pa. At higher pressure, the photon-to-ion flux ratio falls to 0.39.

The total emission range below 280 nm corresponding to photon energies above 4.4 eV produces photon fluxes comparable to the ion flux with high photon-to-ion flux ratios between 1.27 and 1.56. The flux is distributed over the medium and high energy range in the pressure range below 7 Pa. At 10 Pa, the flux ratio accounts to 0.67. To take account of this result, filter combination "No filter – BK7" was chosen for the diode system. If desired, filter combination "MgF_2 – BK7" from the nitrogen filter set can be applied.

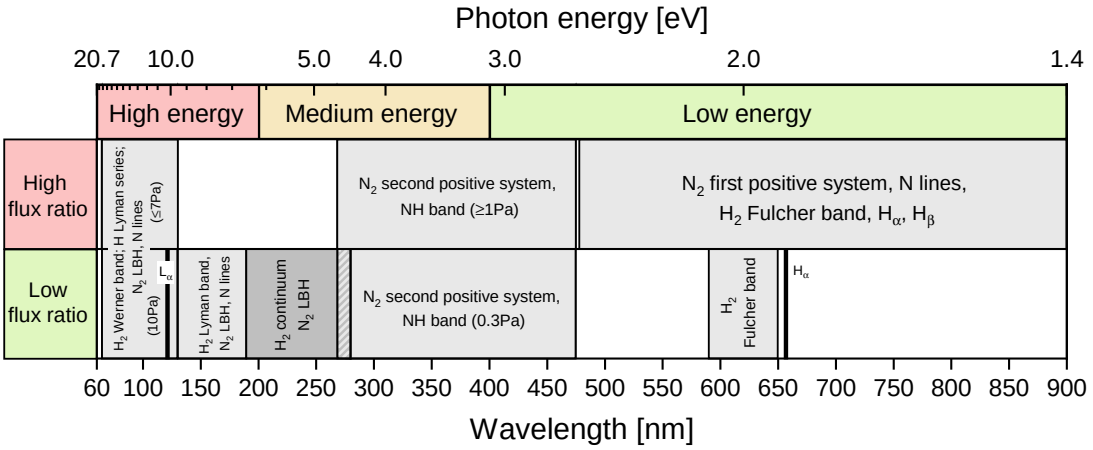

Figure 6.15: Characterization scheme of the identified emission ranges in the nitrogen/hydrogen mixture (50:50) at a generator power of 300 W, 500 W and 700 W at 1 Pa as well as a pressure scan from 0.3 Pa to 10.3 Pa at 500 W generator power.

6.2.2 Hydrogen/oxygen (85:15)

The spectra of the investigated hydrogen/oxygen discharges are characterized by the highly pronounced emission from the Lyman and Balmer series of atomic hydrogen. An example taken at 1 Pa and a generator power of 700 W is presented in figure 6.16. Emission from hydrogen molecules is observed as well as emission from the resonant atomic oxygen lines around 130.3 nm. The highest photon energy is observed at 1 Pa around 17.2 eV resulting from the molecular hydrogen Werner band. The atomic lines in the visible range at 777.3 nm and 844.6 nm have

been detected only with the survey optical spectrometer and absolute photon fluxes were not determined. Molecular oxygen emission could not be observed.
In addition to the emission features of the pure gases, a strong emission from the resonant OH band ($A\ ^2\Sigma^+ \rightarrow X\ ^2\Pi$) occurs in the UV range around 310 nm (4.0 eV). In figure 6.16, the observed vibrational sequences ($\Delta v = 0, +1$) are indicated [DC62]. A bandpass filter 313BP to account for the OH band was selected for the diode system.

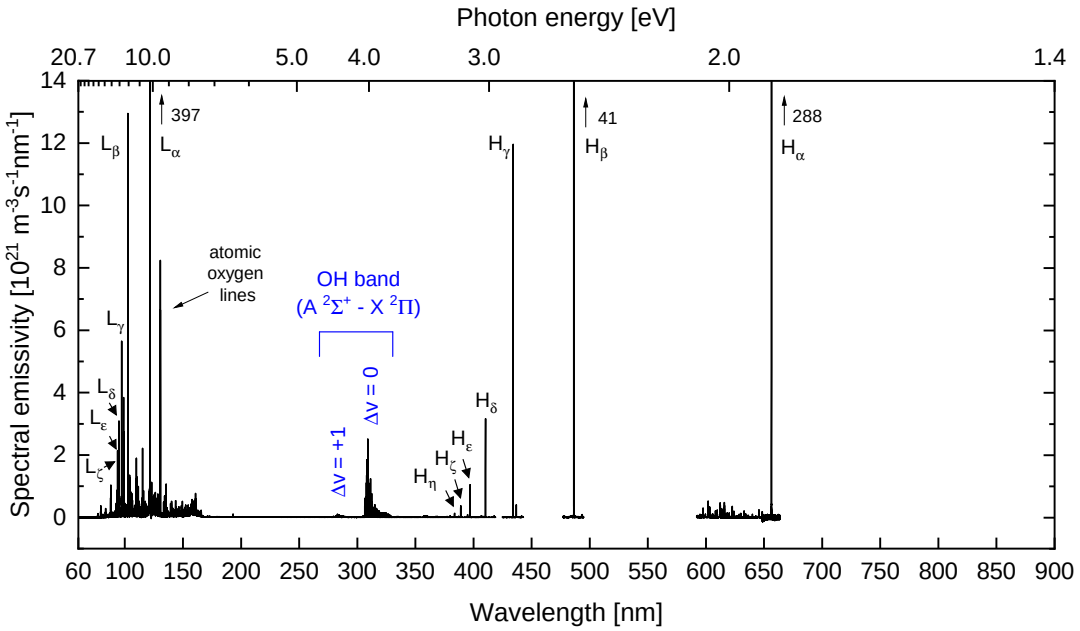

Figure 6.16: Absolute intensities of a hydrogen/oxygen mixture (85:15) at 1 Pa and 700 W generator power in the VUV/UV range. The vibronic transitions $v = +1$ and $v = 0$ of the OH band are indicated. Single spectra taken for the evaluation of the Balmer series and the Fulcher band are included.

In the hydrogen/oxygen mixture (85:15), power and pressure scans were performed at the same parameters chosen for the hydrogen discharges. Results from the pressure scan can be found in the figure 6.17, those from the power scan are summarized in figure F.12 of the appendix.
The neutral atomic and molecular particle fluxes of hydrogen as well as oxygen increase with the pressure. For hydrogen, the fluxes of atoms and molecules are comparable with values in the range of $3 \cdot 10^{22}$ - $3 \cdot 10^{23}\,\mathrm{m^{-2}s^{-1}}$. Below 10 Pa, the atomic flux is even higher than the molecuar flux which is in accordance with the atomic-to-molecular density ratio decreasing from 1.3 to 0.5 with pressure. These values strongly exceed the corresponding values determined in pure hydrogen which are in the range 0.09 - 0.15.

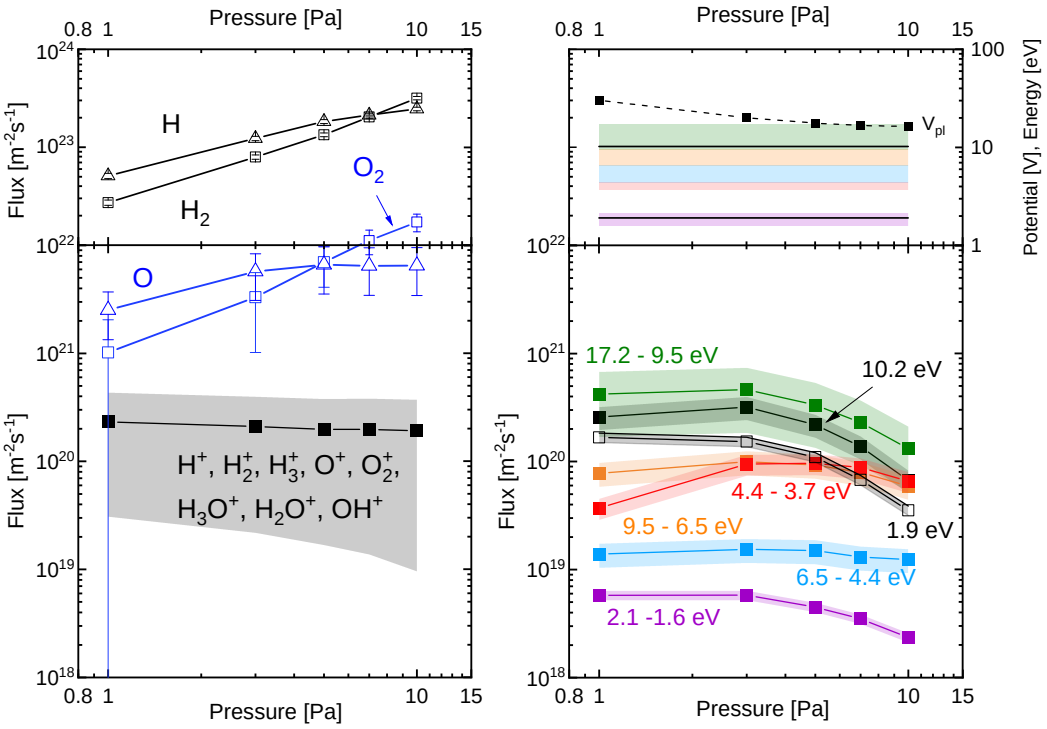

Figure 6.17: Particle and photon fluxes determined in the hydrogen/oxygen mixture during the pressure scan at 700 W generator power. Please note the different scaling of the vertical axis in the left lower and upper part.

For oxygen, the atomic and molecular fluxes are also comparable to each other but are roughly one order of magnitude below the fluxes of hydrogen. Similarily, the atomic particle flux exceeds the molecular flux in the low pressure range. The atomic-to-molecular density ratio decreases from 1.7 down to 0.3 for oxygen with pressure.

The positive ion flux determined during the pressure scan stays constant around $2 \cdot 10^{20}\,\mathrm{m^{-2}s^{-1}}$. At 1 Pa, the main contributing ion species are H_2O^+, H_3O^+, OH^+ followed by O_2^+ and O^+. Low amounts of the hydrogen ions H_3^+, H_2^+ and H^+ are observed whose significance even further declines with pressure. At 10 Pa, the dominant ion species is H_3O^+ (see figure F.11 in the appendix). The corresponding ions' maximum energy show a decrease from 30 eV to 16 eV.

Compared to the pure hydrogen case, the photon-to-ion flux ratios for the Fulcher band and the Continuum decrease to low values of below or equal to 0.03 and 0.08, respectively. The emission ranges are classified accordingly in figure 6.18.

Although the wavelength region 130 - 190 nm assigned to the Lyman band of

molecular hydrogen is superimposed by the atomic oxygen triplet at 135.7 nm, the photon-to-ion flux ratio does not exceed 0.48 in this range. In contrast, the emission from the atomic hydrogen lines L_α and H_α significantly increases which can be traced back to the increased atomic-to-molecular density ratio given above. For the former, the corresponding photon-to-ion flux ratio ranges between 0.70 and 1.52 below 10 Pa and 0.35 at 10 Pa. Regarding the Balmer line, values up to a maximum of 0.73 are reached in the pressure range lower or equal to 5 Pa while the photon-to-ion flux ratio is does not exceed 0.34 for higher pressures. Photon fluxes from the atomic oxygen lines have not been investigated separately.
Due to the admixture of oxygen, the energy range above 9.5 eV additionally includes the atomic oxygen lines decribed in section 6.1.4. The corresponding photon fluxes in this energy range reach ratios of 0.69 up to 2.21 compared to the ion flux.
The OH band produces UV photon fluxes in the range of $(3.7 - 9.6) \cdot 10^{19}\,\mathrm{m^{-2}s^{-1}}$ leading to rather low ratios compared to the ion flux between 0.16 and a maximum value of 0.49 at 5 Pa.

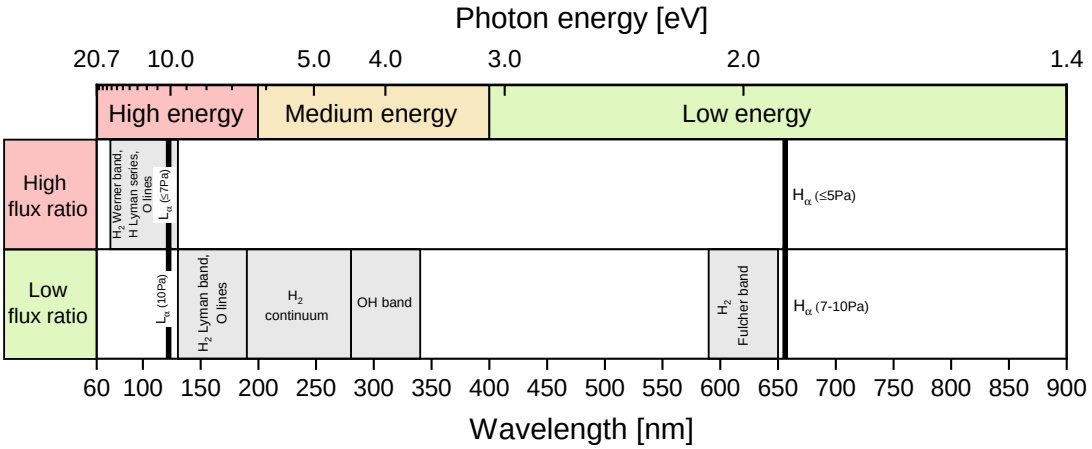

Figure 6.18: Characterization scheme of the identified emission ranges in the hydrogen/oxygen mixture (85:15) at a generator power of 700 W, 900 W and 1100 W at 1 Pa as well as a pressure scan from 1 Pa to 10 Pa at 700 W generator power.

6.2.3 Nitrogen/oxygen (80:20)

In synthetic air (i.e. nitrogen/oxygen mixture with gas composition 80:20), the molecular nitrogen systems (Lyman-Birge-Hopfield system, First and Second positive system) as well as the atomic nitrogen and oxygen lines in the VUV and

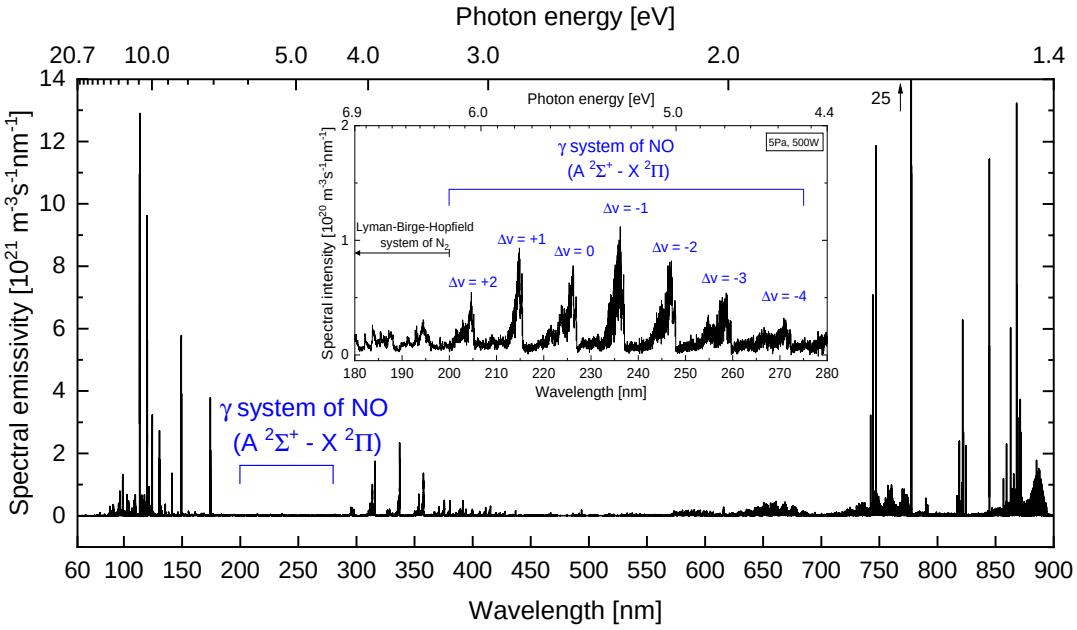

Figure 6.19: Absolute intensities of a nitrogen/oxygen mixture (80:20) at 1 Pa and 500 W generator power. An enlarged spectrum including the emission of the γ system of NO is depicted in the inset.

VIS region are the main emission ranges. The atomic lines are characterized in the investigated nitrogen/oxygen discharges by a very high intensity. Molecular oxygen emission could not be detected. However, a slight emission occurs in the range of 200 - 275 nm (6.2 - 4.5 eV) which can be assigned to the γ system (A $^2\Sigma^+ \rightarrow$ X $^2\Pi$) of NO. The observed vibronic transitions corresponding to $\Delta v = +2, \ldots, -4$ [PG76] are displayed in the inset of figure 6.19. If requested for a specific plasma application, an appropriate filter for this energy range is given by the 230BP filter.

The results from the pressure scan can be seen in figure 6.20, those from the power scan are shown in figure F.14 in the appendix.

The atomic and molecular neutral particle fluxes of nitrogen and oxygen increase with pressure, whereas the atomic nitrogen flux stays constant for pressures above 3 Pa. The molecular nitrogen flux grows in the range from $5.0 \cdot 10^{21}\,\mathrm{m^{-2}s^{-1}}$ to $1.1 \cdot 10^{23}\,\mathrm{m^{-2}s^{-1}}$ while the atomic flux is more than two orders of magnitude below. The fluxes of atomic and molecular oxygen are more or less comparable and roughly one order below the molecular nitrogen flux.

In contrast, the positive ion flux decreases from $2.6{\cdot}10^{20}\,\mathrm{m^{-2}s^{-1}}$ to $6.7{\cdot}10^{19}\,\mathrm{m^{-2}s^{-1}}$ with pressure. For pressures lower or equal to 1 Pa, it mainly consists of the ion species N_2^+ and N^+ and to a lower extend by NO^+ and O^+. With increasing

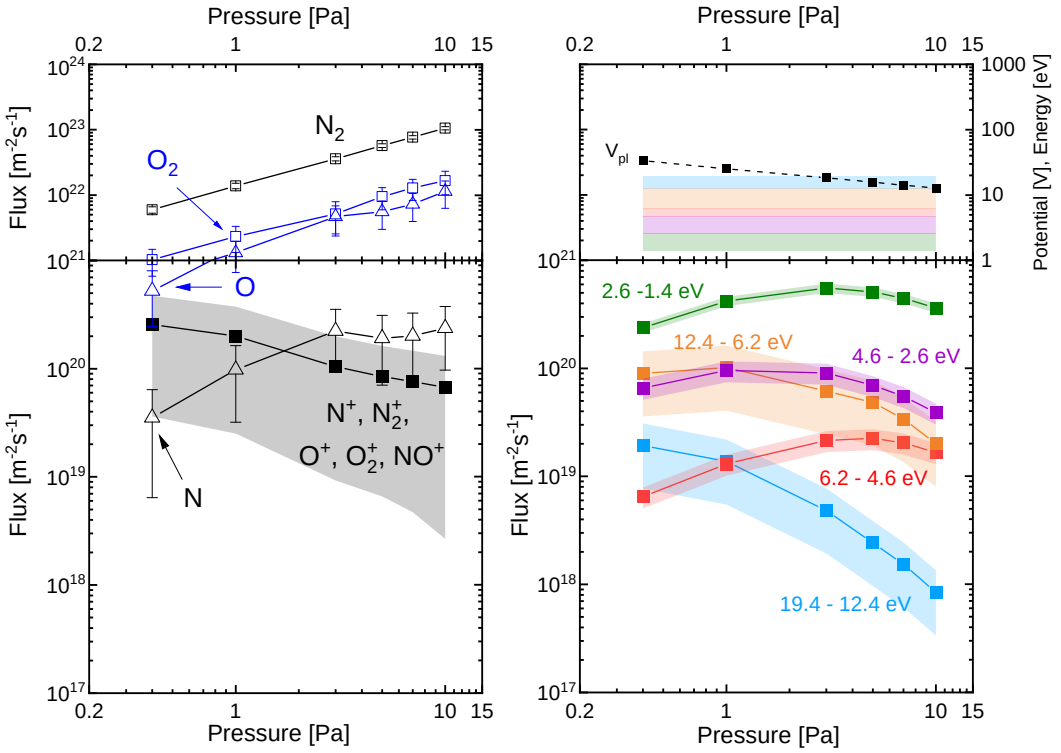

Figure 6.20: Photon and particle fluxes determined in the nitrogen/oxygen mixture during the pressure scan at 500 W generator power. Please note the different scaling of the vertical axis in the left lower and upper part. These results will be published in [FFBF22].

pressure, the proportion of NO^+ strongly increases until being the dominant species at 10 Pa (see figure F.13 in the appendix). The corresponding maximal ion energy decreases from 33 eV to 13 eV.

A maximum photon energy of 19.4 eV was detected at 0.4 Pa. The energy range 2.6 - 1.4 eV including the First positive system of N_2 as well as atomic nitrogen and oxygen lines produce high photon fluxes clearly exceeding the ion flux. Similar to the results in pure nitrogen and in the nitrogen/hydrogen mixture, high photon-to-ion flux ratios up to 6.02 were determined.

The Second positive system shows a photon-to-ion flux ratio of below or equal 0.48 at low pressure ($\leq$ 1 Pa: 500 W) and/or high generator power (1 Pa: 500 W, 700 W). Apart from that, values between 0.58 and 0.87 are achieved.

The γ system of the NO molecule produces photon fluxes with a photon-to-ion flux ratio ranging up to 0.27. In order to avoid an overlap with the NO band, the wavelength range corresponding to the Lyman-Birge-Hopfield system of molecular

nitrogen is compressed to the interval 100 - 200 nm compared to the pure nitrogen case. Besides the atomic oxygen lines at 115.2 nm, 130.3 nm and 135.7 nm, it also contains the atomic nitrogen lines at 113.5 nm, 120.0 nm, 149.3 nm and 174.4 nm. The photon-to-ion flux ratio is roughly around 0.5 in the power scan at 1 Pa. Regarding the pressure scan, the value ranges between 0.30 at 10 Pa and a maximum value of 0.59 at 3 Pa. Due to the lack of an appropriate edge filter with a desired cut-on wavelength around 200 nm, no filter combination corresponding to the wavelength range 100 - 200 nm was found. Therefore, also the filter combination "MgF_2 – BK7" cutting the spectral range 113 - 280 nm, was selected for the filter set applied to synthetic air plasmas. It corresponds to parts of the N_2 Lyman-Birge-Hopfield system together with oxygen and nitrogen lines as well as the NO band.

The photon-to-ion flux ratio from atomic nitrogen together with atomic as well as ionic oxygen below 100 nm does not exceed 0.08. With respect to the high photon energy, the filter combination "No filter – MgF_2" which is also applied in pure nitrogen and oxygen can be selected.

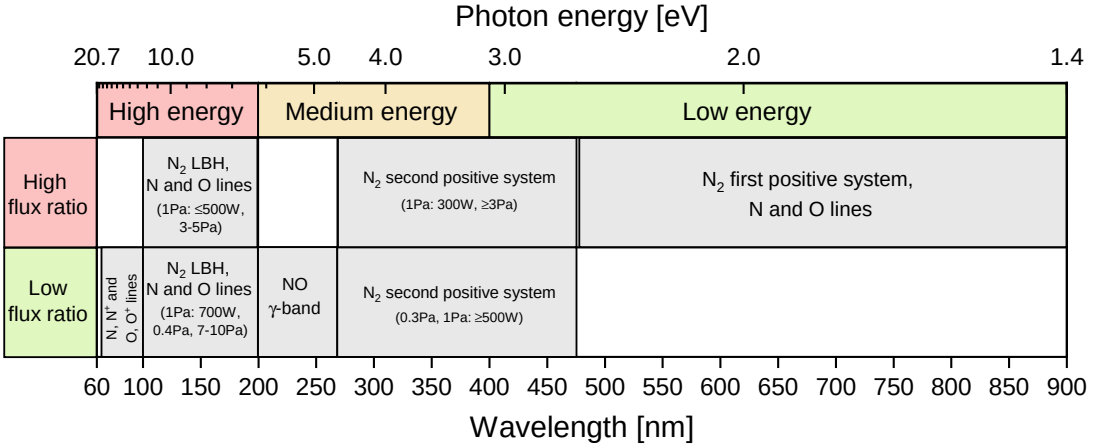

Figure 6.21: Characterization scheme of the identified emission ranges in the nitrogen/oxygen mixture (80:20) at a generator power of 300 W, 500 W and 700 W at 1 Pa as well as a pressure scan from 0.4 Pa to 10 Pa at 500 W generator power.

Finally, some concluding remarks will be given regarding the photon-to-ion flux ratio of the total VUV range with respect to the ion fluxes in the discharges.

The investigated pure argon plasmas exhibited a VUV photon-to-ion flux ratio of 0.69 at 0.3 Pa and 300 W which can be traced back to resonant atomic lines with photon energies of 11.6 eV and 11.8 eV, respectively, as well as emission from the

ionic lines. However, at high pressure ($\geq$7 Pa and 300 W) it drastically decreases to the lowest value of around 0.01. Pure oxygen plasmas showed low absolute VUV photon fluxes compared to the ion flux and do not exceed a flux ratio of 0.25.

The applied hydrogen containing plasmas produced VUV photon fluxes comparable to the ion flux or even exceeding it. At 3 Pa, the maximum VUV photon-to-ion flux ratios are obtained with a value of 1.5 in nitrogen/hydrogen plasmas at 500 W and a value of 2.7 in hydrogen/oxygen plasmas at 700 W, respectively. Pure hydrogen plasmas were identified to produce the highest VUV photon-to-ion flux ratio of 3.3 at 3 Pa.

No significant dependency of the VUV photon flux compared to the ion flux on the generator power could be detected.

7 Benchmark of the diode system at *PlanICE*

In order to demonstrate the capability of the diode system and the validity of its absolute intensity calibration, extended benchmark measurements at *PlanICE* were performed in pure gases as well as gas mixtures. Exemplar results will be published in [FFBF22]. The VUV spectrometer and/or the high resolution optical spectrometer served as reference standard. Derived emissivities for the applied filter combinations are compared to results simultaneously obtained with the reference in power and pressure scans. A constant discharge pressure of 1 Pa is chosen for the former.

7.1 Example for the successful benchmark

As an example for the successful benchmark of the diode system, figure 7.1 shows the measured emissivities in hydrogen during a power scan (left side) and a pressure variation at a constant generator power of 700 W (right side). The emissivities are assigned to the Lyman band (green, measured with the 154BP filter) and the Continuum (blue, measurend with the 230BP filter). The open symbols represent the integrated intensity in the corresponding filter intervals measured with the VUV spectrometer while the full symbols refer to the diode system. Since the absolute values of both diagnostics and their uncertainty are directly related via the calibration of the diode system, only the uncertainty arising from the reproducibility is considered which lies within the depicted symbols. To give an impression about the quality of the agreement, a tube with ±25 % is indicated around the results of the VUV spectrometer. Analogous formatting is chosen for the corresponding graphs through the entire section.
In both the power and the pressure scan, the diode system shows a very good agreement with the emissivities obtained by the VUV spectrometer. The relative behaviour is reflected and the absolute values are within ±25 % for both energy

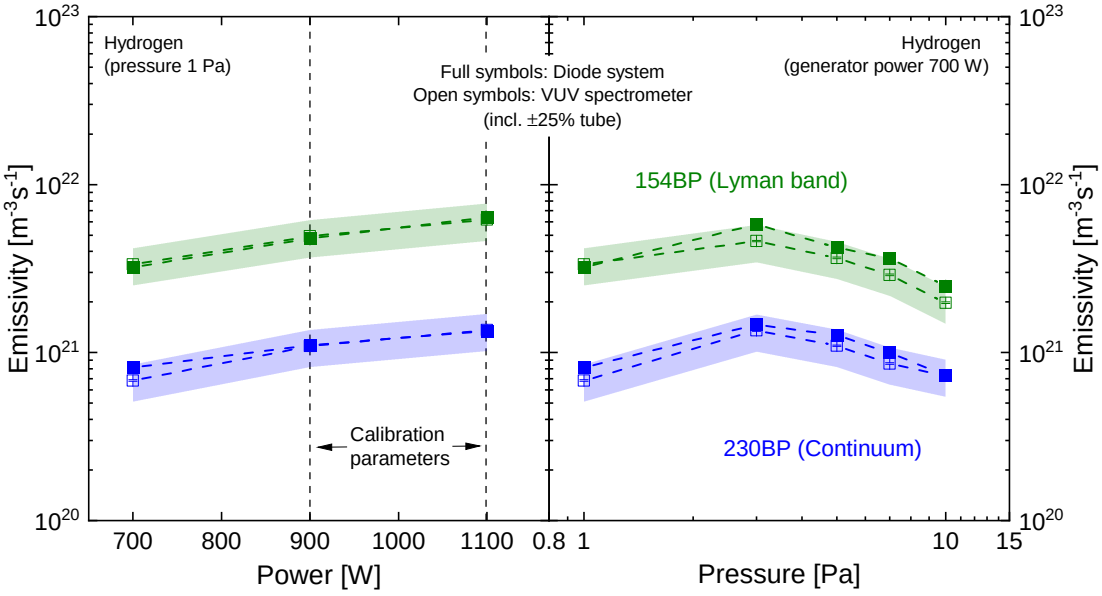

Figure 7.1: Example of the successful benchmark of the diode system in hydrogen for the 154BP (Lyman band, green) and 230BP filter (Continuum, blue) with the power scan at 1 Pa (left side) and the pressure scan with 700 W generator power (right side). The emissivities measured with the diode system are depicted with full symbols, the open symbols correspond to the VUV spectrometer. The uncertainty of ±3 % due to the reproducibility of the diode's signal lies within the symbols. A tube with ±25 % around the values of the VUV spectrometer is depicted to given an impression about the relative agreement between the results. The calibration points at 1 Pa and 900 W generator power and 1 Pa and 1100 W generator power are indicated with dashed lines.

ranges showing a successful benchmark of the diode system.

A complete assembly of the benchmark measurements for all investigated gases and mixtures is presented in the appendix (see sections H and I).

7.2 Influences on the benchmark

Deviations between the diode system and the reference were observed at *Plan-ICE* depending on the specific filter combination, feed gas and the operating parameters. They can be assigned to different effects arising from experimental conditions and properties of the diode system. Being aware of them is essential for a correct interpretation of the results from the diode system. Since these effects might occur at any plasma setup in-use, their occurrence and implication will be discussed in detail. The following compilation does not claim for completeness but shall sensitize the diode system's user to possible effects. An estimation of

their occurence requires a detailed knowledge about the specific plasma setup.

Vertical emission profiles

Figure 7.2 presents emissivities of the Second positive system of molecular nitrogen measured with the diode system measured with the filter combination "BK7 – MgF_2" in pure nitrogen at a generator power of 400 W. The high resolution optical spectrometer served as reference whose results are given by open symbols. An excellent agreement for pressures below 3 Pa is achieved. Above, the diode system starts to deviate and the difference is increasing with the discharge pressure. At the maximum accessible pressure of 10 Pa, it exists a factor of 3.4 between the results of the diode system and the optical spectrometer.

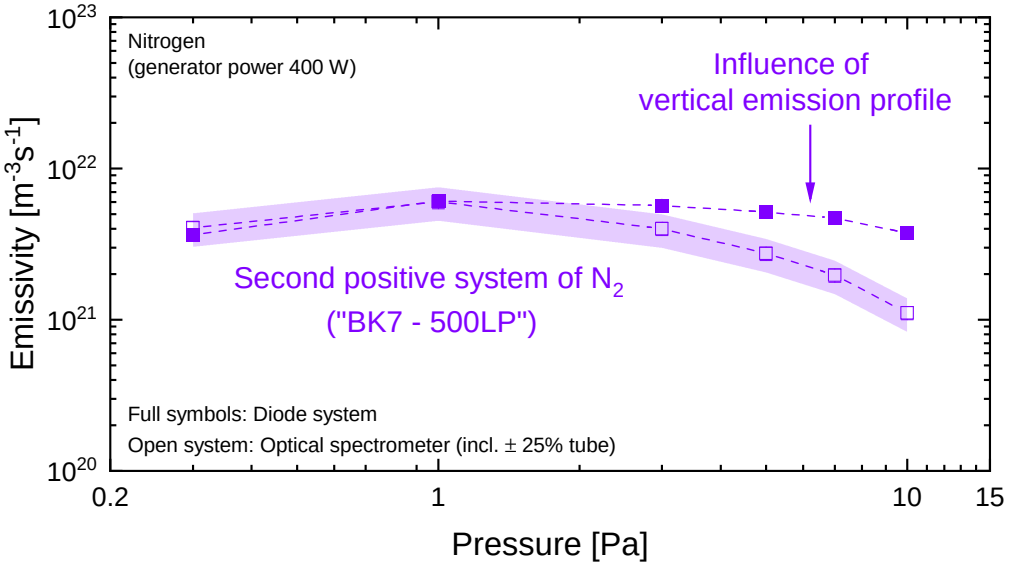

Figure 7.2: Influence of the vertical emission profile observed in nitrogen with the diode system for the Second positive system ("BK7 – MgF_2").

The deviation can be traced back to the pressure dependent vertical emission profile of nitrogen plasmas at *PlanICE* (see figure 4.9) in combination with the different viewing volumes of the diode system and the reference which has been discussed in section 4.2.4. The absolute manifestation might depend on the specific atomic and molecular transition and, hence, on the corresponding wavelength range.

Filter transmission curves of the filters

A further effect arises from the specific transmission curves of the applied filters.

It is mostly pronounced in cases with a broad transmission edge which is especially present for MgF_2 as well as for BK7 and to a slightly lesser extend for the fused silica window. For the corresponding wavelength dependent transmission curves, it is referred to figure D.2. A deviation from the rectangular function, which characterizes an ideal filter, leads to several consequences that must be considered for the evaluation of the benchmark.

Figure 7.3 displays the benchmark pressure scan at 300 W generator power in argon for the VUV range. Results of the diode system were determined with the filter combination "No filter – Fused silica" corresponding to the wavelength range equal or below 153 nm. The measurements show a perfect agreement between the results of the diode system and the VUV spectrometer at pressures below 3 Pa. A deviation for higher pressures is observed. Since argon discharges do not exhibit a significant vertical emission profile, this deviation cannot be traced back to the previously described effect.

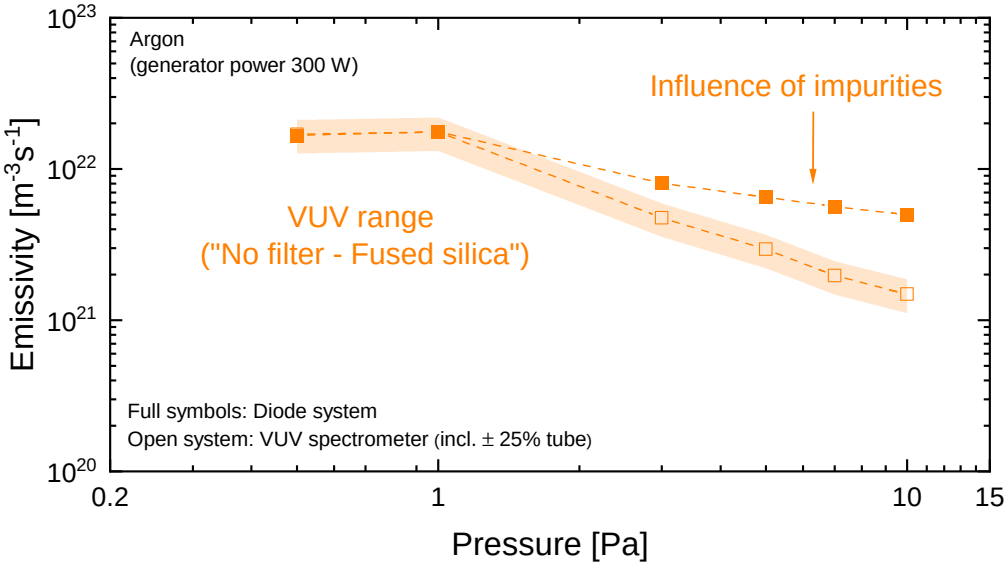

Figure 7.3: Influence of the impurities observed in argon with the diode system for the VUV range ("No filter – Fused silica").

A careful investigation of the spectra taken with the VUV spectrometer revealed that a significant emission from carbon lines ($2s2p^3\ ^3\mathrm{D}^\circ \rightarrow 2s^2 2p^2\ ^3\mathrm{P}$) emerges at 156.1 nm which is within the transmission edge of the fused silica window. The emission is increasing with the pressure above 1 Pa. At *PlanICE*, carbon impurities might be released, for instance, by the interaction of plasma particles with the sealing rings or are residues of detergents applied at the plasma vessel. The

transmission of the fused silica is approximately 62 % at 156.1 nm. Consequently, 38 % of the carbon emission is detected applying the differential measurement technique of the diode system. This portion is not considered in the results of the VUV spectrometer which are obtained from integrating the intensity over the wavelength range lower or equal to 153 nm. This leads to results of the diode system exceeding the values measured with the VUV spectrometer. In the investigated pressure range, the carbon emission is continuously increasing up to a factor higher than 40 at 10 Pa with respect to 1 Pa. In this case, the carbon emission accounts for 9 % of the total emission arising in the filter interval. Additionally, the intensity distribution within the transmission edge of the fused silica window highly differs from the one during the calibration of the diode system and might amplify the described deviation.
A changing spectral distribution within the filter interval compared to the situation during the calibration might have a further effect on the diode system's results. In the hydrogen/oxygen mixture, the emissivity of the L_α line (122BP) was underestimated by the diode system. At 1 Pa and 700 W generator power, a deviation of 52 % from the VUV spectrometer reference was detected (see figure I.3 in the appendix). It might be traced back to the additional molecular emission from the Werner band within the filter transmission range which was neglected during the calibration process in pure hydrogen.
This observation underlines again that the qualitative spectral distribution of the plasma emission and its deviation from the calibration spectrum are important to be known.

Absorption effects in nitrogen/oxygen plasmas

In nitrogen/oxygen plasmas, the benchmark measurements in power and pressure scans showed a good relative agreement of the diode system and the VUV spectrometer. However, a significant absolute deviation of the diode system around a factor of 2 was observed for some emission ranges, e.g. the VUV range ("No filter - Fused silica", see figure I.4 in the appendix). A rough estimation based on Beer's Law regarding the diagnostics' different lines of sight, gave hints that this effect might be traced back to absorption of radiation in air in the wavelength range 38 - 160 nm [Sch40].

Summary

The benchmark of the diode system against the VUV and/or optical spectrometer

was carefully analyzed for each filter combination and each gas composition.
For the performed power scans, the absolute agreement between the diode system and the reference was better than ±30 % for all gases with the following two exceptions. The first was observed for the L_α line (measured with the 122BP filter) in hydrogen mixtures with a relative deviation up to +168 % in hydrogen/nitrogen and -52 % in hydrogen/oxygen. As described above, these deviations could be traced back to the spectral distribution within the specific filter transmission compared to the situation during the calibration of the diode system. The second exception occurs in nitrogen/oxygen for several investigated emission ranges with a maximum deviation of 68 % from the reference value which might be assigned to absorption effects in the plasma.
In the pressure scans, the maximum deviation of +237 % was obtained for the Second positive system ("BK7 – 500LP") nitrogen which results from pressure dependent vertical emission profiles in the plasma vessel in combination with different viewing volumes of the diode system and the reference spectrometer.
For details, it is referred to the tables in the appendix (see tables H.1 - I.5).

The benchmark and the observed effects underline the importance of an appropriate knowledge about the emission characteristics of the investigated plasmas (e.g. impurities), the wavelength dependent transmission of the applied filters (e.g. broad transmission edges) as well as operating properties of the setup in use (e.g. emission profiles). They are an essential prerequisite for reliable measurements with the diode system. Following this, the diode system proofed to be a valid measurement tool with an absolute measuring scale in the range of orders of magnitude which allows an easy and flexible determination of absolute photon fluxes down to the VUV range in various gases and gas mixtures.

8 Transfer of the diode system

After its absolute calibration and the benchmark at *PlanICE*, the diode system was transferred to three other plasma experiments.
The first transfer was made to the inhouse laboratory experiment *ACCesS* (Augsburg Comprehensive CESium Setup) where the geometry of the hydrogen plasmas is very similar to *PlanICE*. Optical emission spectroscopy is available, however, the VUV spectrometer cannot be applied there. The main purpose was to test the flange-mounting of the diode system and to achieve stable measurements. Example results obtained at *ACCesS* and presented in the following section will be published in [FFBF22].
In the next step, the diode system was transferred to the double inductively coupled plasma experiment *PlasmaDecon* at the Institute for Electrical Engineering and Plasma Technology (AEPT, Ruhr-Universität Bochum). The setup is applied for studies on sterilizing properties of plasmas, in particular, using argon mixtures (e.g. Ar/H_2, Ar/N_2, Ar/O_2) [FOA17]. Simultaneous measurements with another portable VUV detector were performed [IMF+17].
In a last step, the diode system was applied to the ion source of the *Batman Upgrade* test stand at the Max-Planck-Institut für Plasmaphysik (IPP, Garching) [SFF+06, HFF+15, HFK+17] in order to perform the very first measurements on photon fluxes in the VUV/UV range there. Some of the presented results can be found already in [WBFF21] and will be published in [FFBF22].

8.1 Laboratory experiment *ACCesS*

The laboratory experiment *ACCesS* (Augsburg Comprehensive CESium Setup) is engaged in research studies on low work function surfaces exposed to low pressure hydrogen plasmas. A main research area is the investigation of the effect on cesiated surfaces. For this purpose, the setup allows an in-situ cesiation of material samples und the direct determination of the work function using photoelectric measurements [CFF20a, FF17]. Moreover, further low work

function materials in contact with hydrogen plasmas have been recently investigated [HFF+21, CFF20b, FCF18].

The work function might be influenced by plasma interaction, e.g. by atomic or ionic particle fluxes onto the surface or by the impact of photons. In this respect, the diode system provides information about incoming photon fluxes and might allow insights into plasma-material interacting processes.

The plasma vessels of *ACCesS* and *PlanICE* are identical in construction. The plasma generation also takes place via an inductive planar coil on top, however at an RF frequency of 27.12 MHz and a power up to 600 W. The similar properties of the setups allowed basic studies on the transferability of the diode system, e.g. flange-mounting, RF noise, stability of measurements. At *ACCesS*, a substrate of the investigated material can be mounted on a sample holder located close to the center of the vessel. A detailed description of the experimental setup and the extended diagnostic system can be found in the given references. A rough bottom view sketch of the setup together with the attached diode system is shown in figure 8.1. The viewing volume of the diode system depicted in blue was still defined by the aperture in front of the diode system but might be affected by the sample holder.

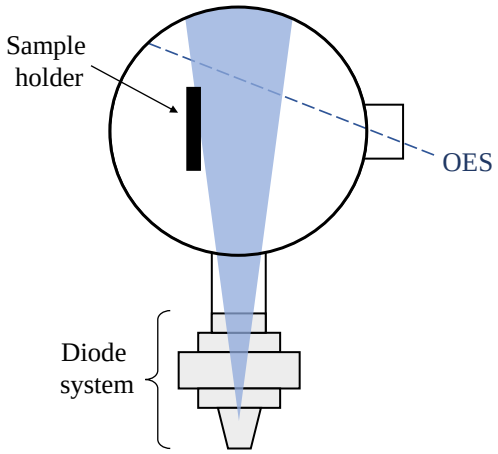

Figure 8.1: Viewing volume of the diode system and line of sight of the optical emission spectrometer at *ACCesS* (bottom view).

The consequence on the effective volume of the diode system is difficult to assess and was estimated by equation (4.4) together with "empirical corrections" which are explained in the following. For this purpose, a comparison of the measured emission from the L_α line and the corresponding value simulated with the CR model *Yacora H* was aimed. The atomic L_α was preferred since it can be

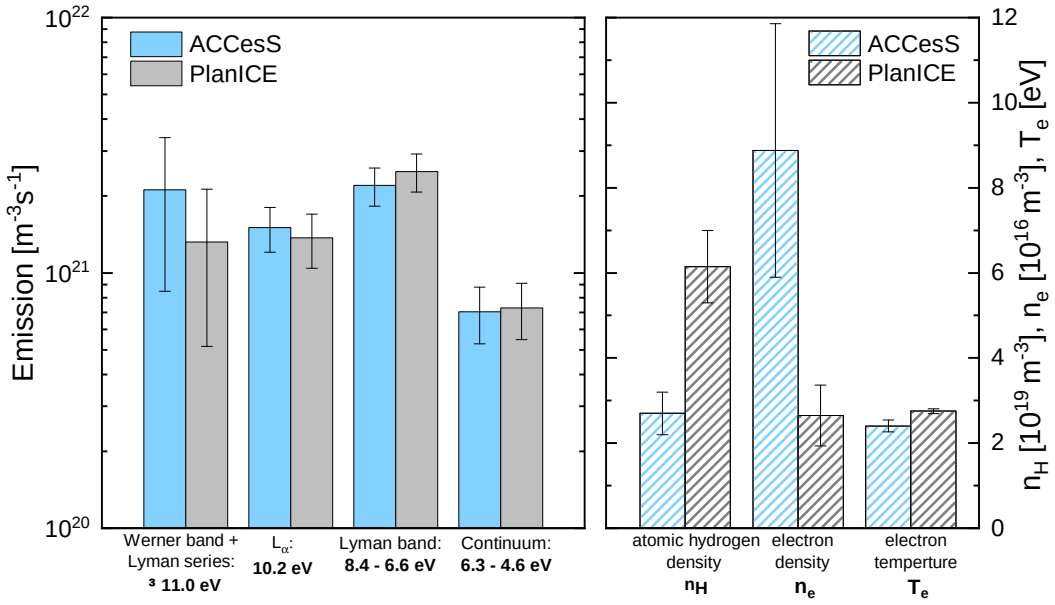

Figure 8.2: Comparison of the measurement results in a hydrogen plasma at 10 Pa at *ACCesS* (blue, generator power 450 W) and *PlanICE* (grey, generator power 700 W). On the left side, the emission from the L_α (measured with 122BP), the Lyman band (measured with 154BP), the Continuum (measured with 230BP) and the Werner band including L_β, L_γ, ... (measured with "No filter – MgF_2) was determined with the diode system. The values at *ACCesS* include the correction of the shadowing due to the sample holder (see text). On the right side, the atomic density n_H, the electron density n_e and the electron temperature T_e are summarized.

completely detected by the diode system with the 122BP filter. This is not the case regarding the molecular Lyman band, Werner band or the Continuum of which the diode system only observes a limited range with the corresponding filter combinations.

The emission from the molecular Fulcher band und the Balmer lines $H_\alpha, \ldots, H_\epsilon$ as well as the gas temperature were investigated with an absolutely calibrated optical emission spectrometer. The electron temperature T_e, the electron density n_e as well as the atomic hydrogen ground state density n_H were determined by the use of the collisional radiative models *Yacora H* and *Yacora* H_2 [WF16]. The molecular model was used with excitation rate coefficients by Miles [MTG72] and the atomic model with escape factors from [Bri20] considering opacity effects. Using the input parameters from the optical emission spectroscopy, the emissivity of the L_α line can be simulated with *Yacora H*. A comparison of the modeled

L_α emission with the value obtained with the diode system is used to address the question whether the sample holder partly obstructs the diode's viewing volume. A comparison at 10 Pa and 450 W reveals a ratio of 0.51 of the measured value with respect to the simulated L_α emission. As a consequence, the measurements with the diode system at *ACCesS* will be corrected by a factor of 2 in the following.

The emission of the L_α (measured with 122BP), the Lyman band (measured with 154BP), the Continuum (measured with 230BP) and the Werner band including L_β, L_γ, ... (measured with the filter combination "No filter – MgF_2) was determined with the diode system. Figure 8.2 shows the comparison of the corresponding emissivities at 10 Pa obtained with the diode system both at *ACCesS* (450 W, blue) and *PlanICE* (700 W, grey). It includes the emission from the L_α line measured with the diode system for *PlanICE* and the corrected measured value for *ACCesS*. The error bars correspond to the relative uncertainty of the diode system. On the right side, the figure is supplemented with the plasma parameters deduced from optical emission spectroscopy together with *Yacora H* and *Yacora* H_2. At both experiments, a similar emission in the investigated energy ranges was observed. Since the geometry of the plasma vessels is equal, this corresponds directly to similar photon fluxes onto the vessel walls.

The comparison of the results at *ACCesS* and *PlanICE* demonstrates the applicability and the first successful transfer of the diode system.

8.2 Low pressure sterilization *PlasmaDecon*

The diode system was applied to the double inductively coupled plasma experiment *PlasmaDecon*. The experiment is located at the Institute for Electrical Engineering and Plasma Technology (AEPT, Ruhr-Universität Bochum) and described explicitly in [FOA17]. It is operated to investigate the sterilization effect of various plasma mixtures on medical instruments. The cylindrical vessel (diameter 40 cm, height 20 cm) is made of stainless steel and is equipped with two planar coils at the top and bottom. The volume-to-surface ratio is 0.05 m. Low pressure plasmas with an accessible range of 1 Pa to 50 Pa are driven at a frequency of 13.56 MHz and RF powers up to 5 kW.

In addition to the diode system, another portable VUV detector designed at the AEPT [IMF+17] has been applied. It converts incoming VUV/UV photons into radiation with a wavelength between 350 nm and 550 nm by a sodium salicylate

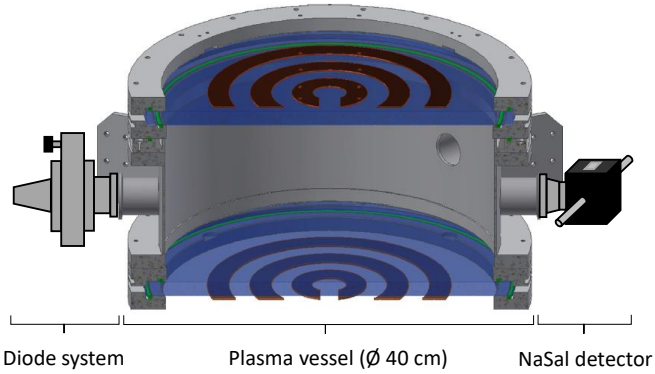

Figure 8.3: Diode system and NaSal detector at *PlasmaDecon*. The sketch of the experimental setup is taken from [FOA17].

(NaSal) layer. In the following, it is referred to as NaSal detector. The resulting signal is measured either spectrally resolved by an absolutely calibrated broadband echelle spectrometer [BHAW07] or spectrally integrated by a photomultiplier tube. The absolute calibration of the NaSal detector is performed against an absolutely intensity calibrated deuterium arc lamp. Together with an appropriate filter combination, an absolute calibration factor for the NaSal detector in the range 225 - 325 nm is obtained which is also applied for other emission ranges in the VUV [IMF$^+$17]. Additionally, the quantum efficiency of the specific sodium salicylate layer and its wavelength dependency has to be taken into account. By inserting several combinations of edge filters in front of the NaSal layer, different wavelength intervals can be selected. For more details regarding the NaSal detector, its absolute calibration procedure and the measurement technique, it is referred to [IMF$^+$17, IHM$^+$19].

Figure 8.3 shows a cross section through the experimental setup taken from [FOA17] and complemented by the two VUV diagnostic systems.

Due to the large dimensions of the plasma vessel, the diameter of the diode system's viewing cone on the opposite vessel wall ranges between 8 cm and 10 cm. The ratio of the corresponding effective volumes was calculated to $\frac{V_{\mathrm{eff,DICP}}}{V_{\mathrm{eff,PlanICE}}} = 2.7$.

At the *DICP*, argon discharges with different gas admixtures in the pressure range 3 - 10 Pa were investigated at a fixed generator power of 500 W with the diode system and the NaSal detector simultaneously. The gas mixtures argon/nitrogen (100:5), argon/oxygen (100:5) and argon/hydrogen/oxygen (100:4:2) were chosen with the flow rates in sccm given in brackets.

The transfer of the diode system allowed a comparative study which requires a similar wavelength range accessible with both diagnostics. Due to the applied fil-

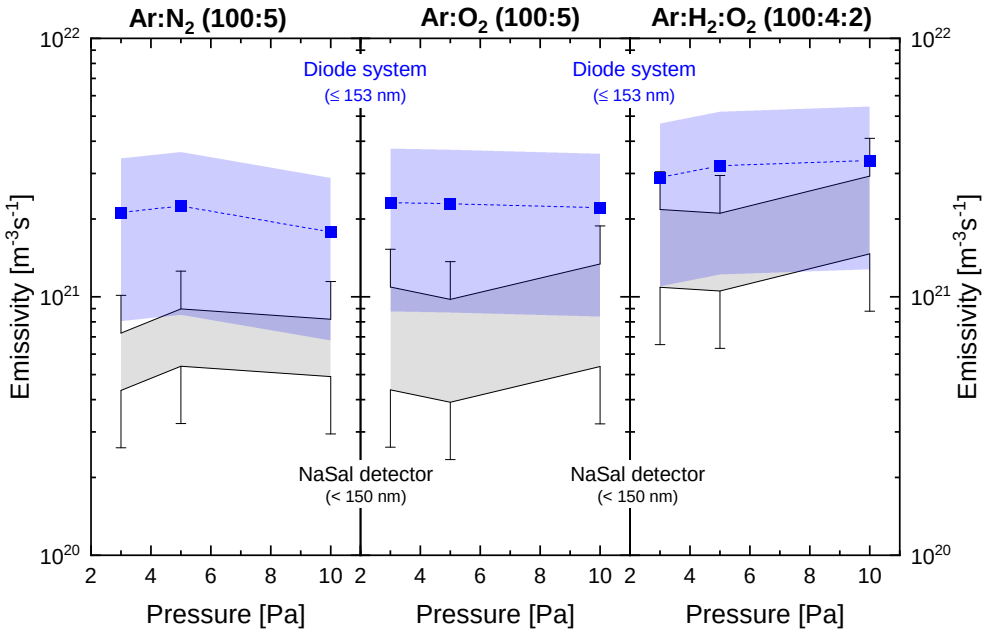

Figure 8.4: Emissivities of the VUV range in different argon mixtures measured at *PlasmaDecon* in the pressure range 3 - 10 Pa and a fixed generator power of 500 W. The results obtained with the diode system ("No filter - Fused silica", *leq* 153 nm) are depicted in blue. The blue tubes correspond to the relative uncertainty of ±60 %. For comparison, results with the NaSal detector in the wavelength range below 150 nm are given in black with error bars of ±40 % [Igl19]. The lower limit is determined under the assumption of a constant quantum efficiency of NaSal in the VUV range, the upper limit includes the wavelength dependendy of the quantum efficiency accordingly to [MBVR07] (see figure 8.5).

ter sets, the VUV range appears to be suitable. The respective filter combination "No filter – Fused silica" of the diode system corresponds to the wavelength range lower or equal to 153 nm. The applied filter combination of the NaSal detector detects the wavelength range lower or equal to 150 nm. Due to the mixture ratio of the supply gases, the most dominant emission can be expected from the resonant atomic argon lines at 104.8 nm and 106.7 nm. Admixtures of nitrogen, oxygen and hydrogen produce additional radiation from atomic lines and molecular systems as has been extensively described in section 6.

The emissivities measured in the argon mixtures at the *PlasmaDecon* are summarized in figure 8.4. The results with the diode system are given in blue applying a linear combination of the pure gas calibration factors taken from table 4.9 according to the gas mixture. The relative uncertainty of the absolute emissivities is depicted as tube and amounts to ±60 %. The emissivities obtained by the NaSal

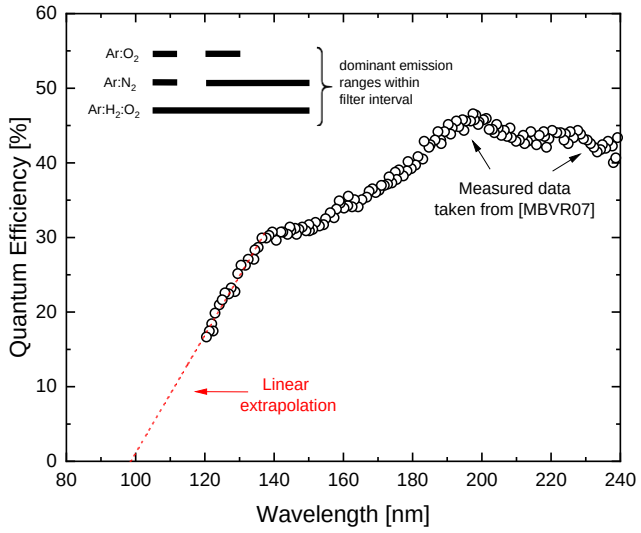

Figure 8.5: Quantum efficiency of sodium salicylate taken from [MBVR07]. Below 120 nm the data points are linearly extrapolated. Moreover, dominant emission ranges in the argon mixture within the filter interval below 150 nm are indicated.

detector as well as the error bars of ±40 % due to the calibration technique and the measurement procedure were kindly provided by [Igl19]. They are depicted in black.

The lower limit of the measured emissivity in figure 8.4 is obtained with the assumption of a constant quantum efficiency of NaSal which is independent of the wavelength. In contrast, the upper limit includes the wavelength dependency of sodium salicylate below 200 nm according to the following approach: figure 8.5 presents the quantum efficiency of sodium salicylate in the wavelength range of 120 - 240 nm taken from [MBVR07] as open dots. Additionally, the most dominant emission wavelength ranges of the investigated argon mixtures in the corresponding filter wavelength interval are indicated. Below 120 nm, a linear extrapolation of the data points was performed. An average value of the quantum efficiency in the gas specific most prominent emission range was obtained for each gas mixture. Its ratio with respect to the averaged quantum efficiency in the wavelength range 225 - 240 nm from figure 8.5 is then considered in the emissivity calculation. The result can be considered as upper limit.

The pressure scans performed in the different argon mixtures and presented in figure 8.4 reveal a minor pressure dependency of the emissivities in the investi-

gated wavelength interval. The variation of the emissivities is below $\pm 15\,\%$ in the pressure range of 3 - 10 Pa for each mixture.
The exchange of the admixed gas has a small influence on the overall emissivity of the VUV range. The argon/nitrogen as well as the argon/oxygen discharges produce emissivities in the range of $(2.1-2.3)\cdot 10^{21}\,\mathrm{m^{-3}s^{-1}}$. Slightly higher emissivities around $3.2\cdot 10^{21}\,\mathrm{m^{-3}s^{-1}}$ are detected in the argon/hydrogen/oxygen mixture. The increase might be traced back to the Lyman series of atomic hydrogen and to the molecular Werner and Lyman emission bands in the investigated wavelength range. The corresponding photon fluxes are of the order of $10^{20}\,\mathrm{m^{-2}s^{-1}}$.
The results obtained with the NaSal detector represent 20 % up to 70 % of the values from the diode system depending on the pressure and the gas mixture. A detailed quantitative comparison requires a deepened insight into the basics of the NaSal detector's calibration procedure and underlying prerequisites concerning the NaSal layer (e.g. homogeneity, degradation, impurities). The two diagnostics agree well regarding the minor pressure dependency and the observed influence of the hydrogen admixture on the emissivity in the VUV range.
The performed measurements demonstrate the transferability of the diode system to a new plasma setup and underline the benefit regarding the direct VUV photon detection as well as the gas and filter combination specific absolute calibration.

8.3 Ion source at *Batman Upgrade*

The diode system provided the very first measurements of VUV photon fluxes in hydrogen plasmas at the ion source of the *Batman Upgrade* test stand at the Max-Planck-Institut für Plasmaphysik (IPP, Garching) [SFF+06, HFF+15, HFK+17] where fundamental research on neutral beam heating for future fusion power plants is carried out. Figure 8.6 shows a vertical section through the setup. Following the concept of the neutral beam injection (NBI) as a heating mechanism of fusion plasmas, the ion source produces negative ions which are subsequently accelerated and neutralized. The ion source is based on low pressure hydrogen or deuterium plasmas generated in the driver which is equipped with a helical coil (RF frequency of 1 MHz, RF power up to 80 kW). The plasma expands into the expansion chamber where the production of negative ions at the plasma grid (PG) takes place. In-situ cesiation of the plasma grid establishs a surface with a low work function to facilitate the surface conversion process. A magnetic filter field is induced by a current through the plasma grid in order to reduce the

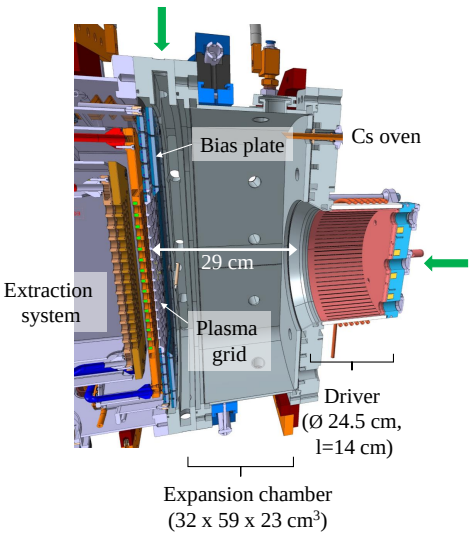

Figure 8.6: Vertical section through the ion source at *Batman Upgrade* with the driver and the expansion chamber. It is provided by [Eck19]. The diode system has been applied at two different positions indicated with green arrows. The first position is axially centered at the driver. In the second position, the diode system is located in front of plasma grid with the viewing volume being parallely orientated to the grid.

electron temperature and the electron density in front of the plasma grid and, therefore, to prevent the produced negative ions from collisional destruction by plasma particles. The ion source is equipped with a series of diagnostics (e.g. optical emission spectroscopy, Langmuir probe) to monitor and characterize the plasma in the driver as well as in the expansion chamber. The plasma parameters in the expansion region are subject to a steep gradient from the exit of the driver to the plasma grid. The region directly in front of the plasma grid, the so-called extended boundary layer, plays an important role regarding the production of negative ions. Moreover, a mutual interplay between the grid surface and the plasma takes place with an influence on the source performance.

A low work function of the plasma grid material is required regarding the hydrogen ion generation. However, it additionally favours the production of photoelectrons by impinging VUV/UV photons. These photoelectrons as well as co-extrated electrons might have a crucial influence on the plasma sheath and the plasma in front of the plasma grid. In this regard, a quantification of corresponding VUV/UV photon fluxes onto the plasma grid can give insight into the relevance of the photoelectrons and might help to extend plasma simulation models. Another point of interest is the possible effect of the VUV/UV photons

on the cesium layer.

For both effects, the contributions arising from the driver plasma as well as from the expansion chamber have to be considered. Due to its flexible applicability, the diode system is particularly suitable for this purpose for which the device was installed at two different positions at the setup — axially centered at the driver and vertically aligned in front of and parallel to the plasma grid. The corresponding effective volume of the position at the driver was calculated following section 4.2.3. Since the emissivity measured at this port is expected to be dominantly produced by the driver plasma, the calculation of the effective volume is restricted to the driver volume. In contrast, the position in front of the plasma grid exhibits a more complex situation, especially since the bias plate, which is also depicted in figure 8.6, cuts the viewing volume of the diode system. This geometry exceeds the capability of the simple analytical approach which necessitates the application of a ray tracing code [Hur19]. The results are $\frac{V_{\mathrm{eff,Driver}}}{V_{\mathrm{eff,PlanICE}}} = 0.94$ and $\frac{V_{\mathrm{eff,PG}}}{V_{\mathrm{eff,PlanICE}}} = 3.2$ for the driver port and the port in front of the plasma grid, respectively.

For the driver, the volume-to-surface-ratio to derive photon fluxes from measured emissivities takes into account only the dimensions of the driver vessel leading to a value of 0.03 m. Due to the aforementioned gradient across the expansion region, the volume-to-surface ratio for the measurements close to the plasma grid does not include the whole expansion chamber but is restricted to the section directly in front of the plasma grid which is accessible with the diode system. Therefore, a limited geometry is applied considering the height (59 cm) and width (32 cm) of the expansion chamber while the maximum diameter of the diode system's viewing volume ($\approx$ 5 cm) is taken as reduced length. This leads to a volume-to-surface ratio of 0.02 m which is used to calculate the photon flux onto the inner walls of the 'reduced' expansion chamber close to the plasma grid.

The investigations were carried out in hydrogen plasmas without cesiation. The diode system was equipped with the filters 122BP and 154BP as well as with the filter combination "No filter – MgF_2" corresponding to the L_α line, the Lyman band and the wavelength range lower or equal to 113 nm where the Werner band and Lyman lines L_β, L_γ, ... are located. Standard conditions of the ion source are referred to an operation pressure of 0.3 Pa, a RF power of 40 kW and a current of 1 kA through the plasma grid. According to [SWF18], this current roughly corresponds to a magnetic field strength around 1.5 mT at the center of the plasma grid. If not otherwise stated, applied representative plasma parameters obtained

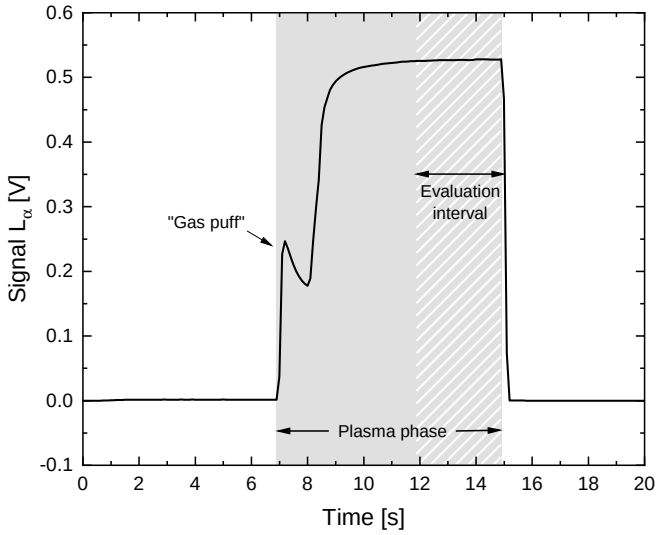

Figure 8.7: Temporal characteristic of the L_α emission during a standard pulse at *Batman Upgrade* recorded with diode system at the driver port. The plasma phase of seven seconds and the evaluation interval of three seconds to the end of the pulse for the analysis of the measurements are indicated.

from optical emission spectroscopy are taken from [Bri19].

The temporal characteristic of the L_α signal during a standard pulse at *Batman Upgrade* recorded with the diode system at the driver port is exemplarily presented in figure 8.7. The driver plasma is ignited at the maximum of a temporary increase of the pressure in the driver which arises from opening the gas feed valve ("gas puff"). Shortly after adjusting the operating pressure, the plasma emission reaches a stable level. The duration of the overall plasma phase is set to seven seconds. The last three seconds of this short-time pulse were used for analyzing the measured diode system signals. The diode system perfectly reflects the temporal dynamic of the pulse. For comparison with timetraces of the Balmer lines and the emission from molecular hydrogen monitored by optical emission spectroscopy at *Batman Upgrade*, it is referred to [HFK$^+$17]. The diode system is characterized by a low noise level as well as a high temporal resolution.

The measured emissivities under standard conditions are summarized in figure 8.8 both for the driver as well as the region in front of the plasma grid. The electron temperature and the electron density are intended as representative values valid for the standard pulse and have been obtained from optical emission spectroscopy in combination with the collisional radiative model *Yacora H* [Bri19].

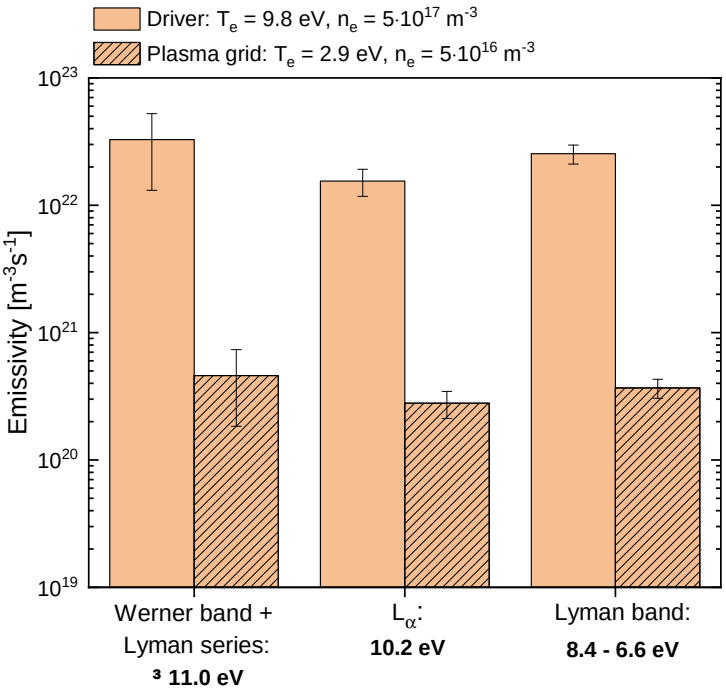

Figure 8.8: Emissivities measured with the diode system at the driver port (blank) and in front of the plasma grid (ruled) at *Batman Upgrade*. The given eletron temperature T_e and electron density n_e are obtained from optical emission spectroscopy. These results have been published in [WBFF21].

The driver plasma is characterized by a high electron temperature and high electron density ($T_\mathrm{e} = 9.8\,\mathrm{eV}$, $n_\mathrm{e} = 5 \cdot 10^{17}\,\mathrm{m}^{-3}$). It produces an emissivity of $3.3 \cdot 10^{22}\,\mathrm{m}^{-3}\mathrm{s}^{-1}$ linked to the energy range above 11.0 eV corresponding to the Werner band and the Lyman series $L_\beta, L_\gamma \ldots$. It is followed by the Lyman band with an emissivity of $2.5 \cdot 10^{22}\,\mathrm{m}^{-3}\mathrm{s}^{-1}$ while the atomic L_α line exhibits an emissivity of $1.5 \cdot 10^{22}\,\mathrm{m}^{-3}\mathrm{s}^{-1}$. In contrast, the plasma in front of the plasma grid has a significantly reduced electron temperature of $T_\mathrm{e} = 2.9\,\mathrm{eV}$ and the electron density is lower by one order of magnitude. As a consequence, this leads to emissivities of $4.6 \cdot 10^{20}\,\mathrm{m}^{-3}\mathrm{s}^{-1}$, $3.7 \cdot 10^{20}\,\mathrm{m}^{-3}\mathrm{s}^{-1}$ and $2.8 \cdot 10^{20}\,\mathrm{m}^{-3}\mathrm{s}^{-1}$ obtained for the respective spectral ranges. Therefore, the emissivity in front of the plasma grid is decreased by a factor in the range of 55 - 71 compared to the driver plasma.

The absolute emissivities of the molecular bands are in rough agreement within 40 % with results from simulated molecular hydrogen spectra with *Yacora* H_2 [Wün04, WF15] created on basis of the plasma parameters. The simulated values are obtained by integrating the synthetic spectra in the corresponding wavelength interval of the respective filter combination. In the case of photon energies above

11.0 eV, it should be noted that the simulation is restricted to molecular emission while the measured values also include atomic radiation from the Lyman series in this energy range. Regarding the driver, the simulation of the Werner band overestimates the measurement by a factor of 1.7 which slightly exceeds the uncertainty range of the diode system. In contrast, the results of the Lyman band agree well within $\pm 7\%$. A comparison of the results in front of the plasma grid shows a good agreement within the error bars of the measurement for the Werner band. However, the simulation of the Lyman band leads to an underestimation with counting 39 % of the measured emissivity.

The absolute emissivities given in figure 8.8 lead to photon fluxes onto the inner side of the driver vessel and the expansion chamber, respectively. With these results, the total photon flux onto the grid area Γ_{PG} can be quantified. Γ_{PG} includes contributions from the expansions chamber as well as from the driver plasma and is given by the ratio

$$\Gamma_{\mathrm{PG}} = \frac{\dot{N}_{\mathrm{PG}}}{A_{\mathrm{PG}}}. \tag{8.1}$$

$\dot{N}_{\mathrm{PG}}$ denotes the photon rate in units of $1/\mathrm{s}$ that reaches the plasma grid with an area of $A_{\mathrm{PG}} = 0.4\,\mathrm{m}^2$.

Photons leaving the driver with the flux Γ_{Driver} are emitted into the half-sphere, i.e. into a solid angle of 2π with a spatial divergence into the expansion chamber. As a consequence, the corresponding solid angle of the plasma grid is required for the calculation of the respective contribution from the driver. The situation is illustrated in figure 8.9 with the area A_{D} of the driver exit, its radius $R = 12.25\,\mathrm{cm}$ and $z_0 = 29.0\,\mathrm{cm}$ being its distance to the plasma grid. The solid angle of the plasma grid area with respect to an arbitrary position $\mathbf{r} = (r, \varphi, z = 0)$ on A_{D} is denoted as $\Omega_{\mathrm{PG}}(r, \varphi, z = 0)$ with

$$\Omega_{\mathrm{PG}}(r, \varphi, z = 0) = \frac{A_{\mathrm{PG}} \cos(\theta)}{r^2 + z_0^2} = A_{\mathrm{PG}} z_0 \left[r^2 + z_0^2\right]^{-\frac{3}{2}}. \tag{8.2}$$

θ describes the angle enclosed by the vector $\mathbf{r}$ and the normal of the plasma grid area. With equation (8.2), the rate of the photons from the driver reaching the plasma grid is given by

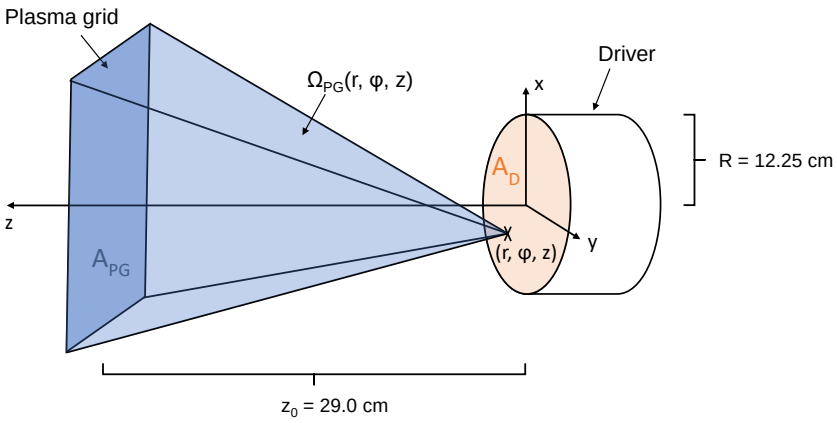

Figure 8.9: Illumination of the solid angle $\Omega_{\mathrm{PG}}(r, \varphi, z = 0)$ of the plasma grid with respect to one position in the driver exit area. It is required for the calculation of the photon flux onto the plasma grid arising from the driver plasma.

$$\begin{aligned}
\dot{N}_{\mathrm{PG,Driver}} &= \Gamma_{\mathrm{Driver}} \int_0^{2\pi} \int_0^{R} \frac{\Omega_{\mathrm{PG}}(r, \varphi, z = 0)}{2\pi} r \mathrm{d}\varphi \mathrm{d}r \\
&= \Gamma_{\mathrm{Driver}} \cdot \underbrace{A_{\mathrm{PG}} z_0 \left[- \left(R^2 + z_0^2 \right)^{-\frac{1}{2}} + \frac{1}{z_0} \right]}_{:=f} \\
&= \Gamma_{\mathrm{Driver}} \cdot f. \qquad (8.3)
\end{aligned}$$

The factor f is determined by the geometry of the setup and is calculated to $f \approx 0.03\,\mathrm{m}^2$. Dividing the expression (8.3) by the plasma grid area A_{PG} leads to the photon flux onto the plasma grid produced by the driver plasma $\Gamma_{\mathrm{PG,Driver}}$. This value has to be understood as an upper limit since reabsorption of photons from the Lyman series travelling from the driver to the plasma grid might occur. The sum of the photon fluxes measured in the expansion chamber directly in front of the plasma grid and $\Gamma_{\mathrm{PG,Driver}}$ gives the total photon flux Γ_{PG} onto the plasma grid.

The figures in the following section will present the resulting photon fluxes onto the plasma grid in the investigated energy ranges for three different operating conditions: the standard pulse, pulses with increased pressure ($p = 0.6\,\mathrm{Pa}$) and pulses without magnetic filter field ($I_{\mathrm{PG}} = 0\,\mathrm{kA}$). Blank bars refer to the photon flux from the driver while ruled bars give the results of the measurements directly in front of the plasma grid. Moreover, the sum of the measured photon fluxes is

indicated.

Additionally, the positive ion and atomic hydrogen fluxes onto the plasma grid are shown. The calculation is based on the assumption that the dominant contribution to the particle fluxes arises from the plasma in the expansion chamber close to the plasma grid. The positive ion fluxes are calculated from averaged values of the electron temperature and the positive ion density which were obtained from Langmuir probe measurements in front of the plasma grid [SWF18]. An averaged positive ion mass of 1.8 u is applied corresponding to the assumed ion constitution of 40 % H^+, 40 % H_2^+ and 20 % H_3^+ [SWF18]. The atomic hydrogen fluxes are calculated from the gas temperature and the atomic hydrogen density which were determined close to the plasma grid with optical emission spectroscopy. For the sake of clarity the uncertainty ranges are neglected.

Detailed values of T_e, n_e and T_{gas} for pulses with increased pressure or without current through the plasma grid obtained from OES measurements are summarized in table 8.1 in comparison to the standard pulse [Bri19]. The atomic hydrogen density n_H in front of the plasma grid as well as the results from the Langmuir probe measurements can be found in the corresponding figures 8.10, 8.11 and 8.12.

Figure 8.10 summarizes the obtained fluxes during the standard pulse. With a flux of $7.3 \cdot 10^{21}\,m^{-2}s^{-1}$, atomic hydrogen produces the dominant flux onto the plasma grid. The positive ion flux accounts to $3.7 \cdot 10^{21}\,m^{-2}s^{-1}$ and is comparable to the total measured VUV photon flux of $2.1 \cdot 10^{20}\,m^{-2}s^{-1}$ which can include photon energies up to 15 eV. The main contribution of roughly 90 % arises from the driver plasma. Regarding the spectral distribution, 44 % of the total VUV photon flux is assigned to the energy range above 11 eV (Werner band together with Lyman lines L_β, L_γ, ...), 22 % is produced by the atomic L_α line at 10.2 eV and 34 % arises from the Lyman band in the range 8.4 - 6.6 eV.

Increasing the operating pressure to 0.6 Pa leads to a slight decrease of the electron temperature in the driver and an increase of the electron density as well as the gas temperature. The same effects are imposed on the plasma in the expansion chamber.

Resulting fluxes at an increased pressure of 0.6 Pa are shown in figure 8.11. Doubling the operating pressure and a slightly increased gas temperature lead to an almost doubled atomic density in the expansion chamber. As a consequence, the atomic hydrogen flux is doubled to a value of $1.4 \cdot 10^{22}\,m^{-2}s^{-1}$. The total VUV photon flux is increased by 60 % to a value of $3.4 \cdot 10^{20}\,m^{-2}s^{-1}$ without significant

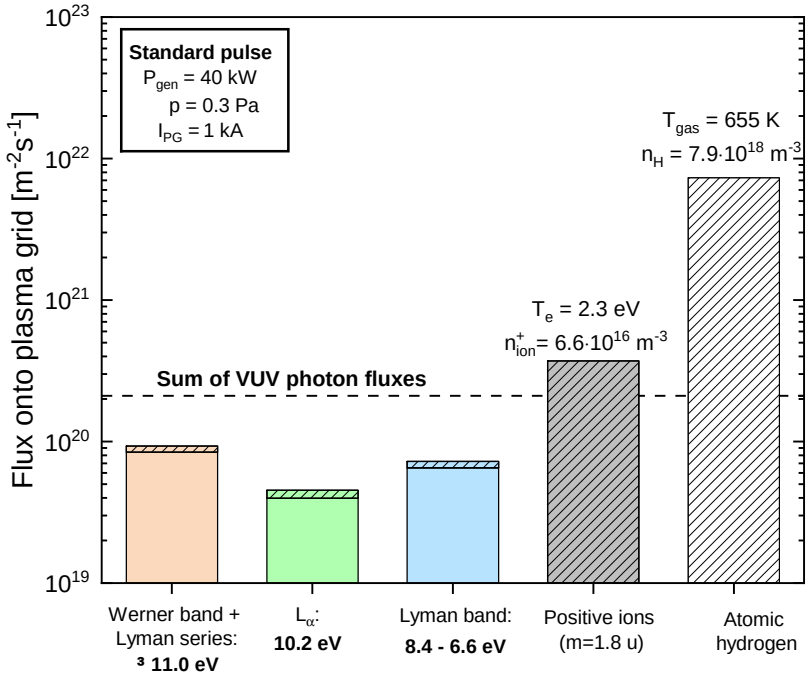

Figure 8.10: Photon and particle fluxes onto the plasma grid for standard pulses in *Batman Upgrade* ($P_{\mathrm{gen}} = 40\,\mathrm{kW}$, $p = 0.3\,\mathrm{Pa}$, $I_{\mathrm{PG}} = 1\,\mathrm{kA}$). Blank bars refer to photon fluxes arising from the driver plasma while the ruled bars indicates the contribution from the plasma in front of the plasma grid. The corresponding electron temperature and positive ion density are obtained from Langmuir probe measurements in front of the plasma grid [SWF18]. The atomic hydrogen flux is determined with the gas temperature and atomic hydrogen density from OES measurements in the expansion chamber [Bri19]. These results have been published in [WBFF21].

Operating parameter			Driver			Expansion chamber		
P_{gen} [kW]	p [Pa]	I_{PG} [kA]	T_{e} [eV]	n_{e} [$10^{17}\,\mathrm{m}^{-3}$]	T_{gas} [K]	T_{e} [eV]	n_{e} [$10^{17}\,\mathrm{m}^{-3}$]	T_{gas} [K]
40	0.3	1	9.8	5.0	643	2.9	0.47	655
40	0.6	1	9.2	10	790	2.3	0.88	772
40	0.3	0	10.2	5.7	639	6.5	0.65	648

Table 8.1: Plasma parameters measured in the driver and the expansion chamber by optical emission spectroscopy [Bri19]. Please note that T_{e} in the expansion chamber might deviate from the results obtained from Langmuir probe measurements [SWF18].

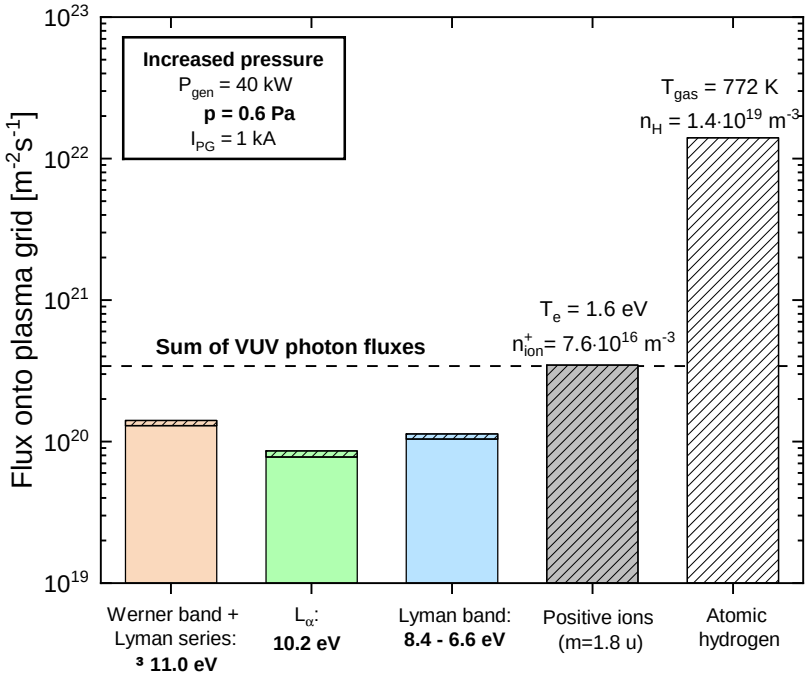

Figure 8.11: Photon and particle fluxes onto plasma grid for increased pressure of 0.6 Pa. Details can be found in the caption of figure 8.10.

influence on the spectral composition. Moreover, the portions arising from the driver and the plasma in front of the plasma grid stay roughly constant with 91 % and 9 %, respectively. The positive ion flux is almost unaffected by the increased pressure and accounts to $3.5 \cdot 10^{20}\,\mathrm{m^{-2}s^{-1}}$. The total VUV photon flux equals the positive ion flux.

Turning off the magnetic filter field (i.e. $I_{\mathrm{PG}} = 0\,\mathrm{kA}$) drastically increases the electron temperature in the expansion chamber by more than a factor of 2, measured both with optical emission spectroscopy (see table 8.1) and Langmuir probe measurements (see figure 8.12). Moreover, the atomic density is reduced by a factor of 2. The electron density rises by about 40 % and the gas temperature is unchanged in the expansion region. However, no significant effect on the plasma parameters regarding the driver plasma can be observed.

Figure 8.12 exhibits the photon and particle fluxes measured without plasma grid current. The results are discussed with respect to the standard pulse. The atomic hydrogen flux of $3.8 \cdot 10^{21}\,\mathrm{m^{-2}s^{-1}}$ is lower. This result roughly equals half

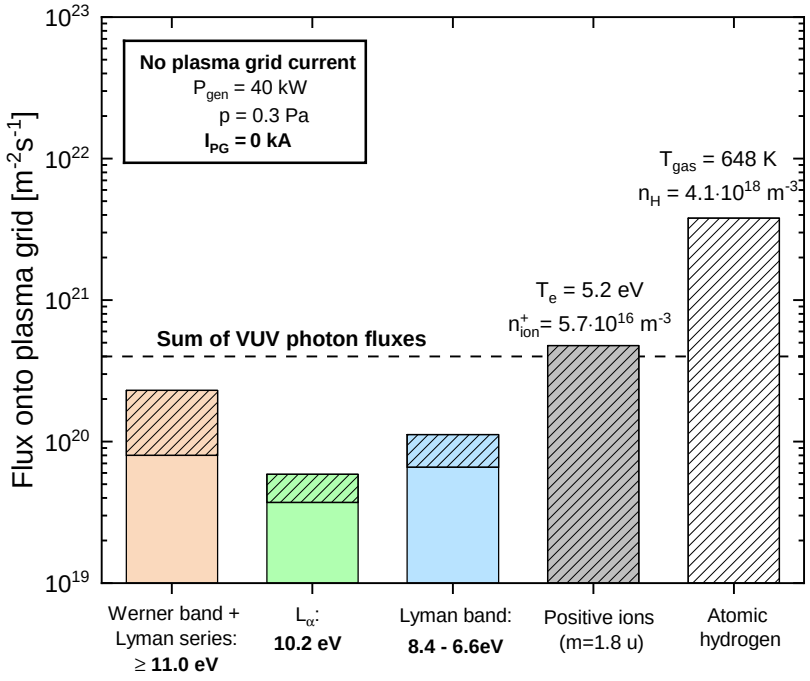

Figure 8.12: Photon and particle fluxes onto the plasma grid for pulses without magnetic filter field ($I_{\mathrm{PG}} = 0\,\mathrm{kA}$). Details can be found in the caption of figure 8.10.

of the value obtained during standard pulses which is directly connected to the reduced atomic hydrogen density. The flux of the positive ions is determined to be $4.8 \cdot 10^{20}\,\mathrm{m^{-2}s^{-1}}$ which refers to an increase of 30 % with respect to standard conditions.

The total measured VUV photon flux is roughly doubled up to $4.0 \cdot 10^{20}\,\mathrm{m^{-2}s^{-1}}$ which is comparable to the positive ion flux and, hence, is highly significant. The increase can be traced back primarily to the higher electron temperature in the expansion region in combination with the increased electron density.

While for the standard pulse the VUV photon flux is dominated by the driver plasma, the distribution without magnetic filter field shifts to 44 % assigned to the driver plasma and 56 % resulting from the plasma in front of the plasma grid[1]. The absolute photon flux from the driver plasma is nearly unaffected with $1.9 \cdot 10^{20}\,\mathrm{m^{-2}s^{-1}}$ during the standard pulse and $1.8 \cdot 10^{20}\,\mathrm{m^{-2}s^{-1}}$ without any current through the plasma grid.

[1]It should be noted that the vertical axis in the figures 8.10, 8.11 and 8.12 are each plotted in a logarithmic scale.

The spectral distribution of the VUV photon fluxes is slightly shifted towards higher energies. The Werner band in combination with the Lyman series L_β, $L_\gamma, \ldots$ gives the main contribution of 57 % while the atomic L_α line and the Lyman band produce 15 % and 28 %, respectively.
The diode system enabled the very first measurements of absolute photon fluxes at the ion source of *Batman Upgrade* and allowed a comparison with particle fluxes onto the plasma grid. The results are in good agreement with the expected influence of the corresponding plasma parameters on the emission. At the investigated operating parameters, the diode system showed that the investigated photon flux onto the plasma grid is in the range of the positive ion flux and impressively demonstrated the influence of the magnetic filter field. At standard conditions, it could reveal that the main contribution of the VUV photon flux onto the plasma grid arises from the driver plasma.

9 Summary

Due to the high energy, VUV photons occuring during plasma treatment processes potentially have a significant influence onto material. The impact depends both on the energy range and on the absolute photon flux reaching the surface. Low pressure plasmas can provide significant VUV photon fluxes from resonant ionic and atomic transitions. Prominent examples are the resonant atomic argon lines at 104.8 nm and 106.7 nm corresponding to photon energies of 11.6 eV and 11.8 eV, respectively.

For optimizing the performance of a specific setup, an absolute and energy resolved quantification of photon fluxes down to the VUV range is of crucial importance. The application of necessary VUV spectrometers is limited due to high technical requirements such as high vacuum conditions and the challenges regarding an absolute intensity calibration. In order to overcome these difficulties, this work aimed at the development of a portable and flexible diagnostic tool which allows the absolute quantification of VUV photon fluxes. The device is based on a VUV silicon diode and a set of bandpass or edge filters to achieve some energy resolution. Its unique feature compared to other VUV detectors is based on its direct absolute calibration against an absolutely calibrated VUV spectrometer which has been performed specifically for each filter and gas.

Applying an absolutely intensity calibrated optical spectrometer (*Acton SP2750*) and a VUV spectrometer (*Model 225* by *McPherson*), absolute photon fluxes in the range from 46 nm up to 933 nm were accessible at the laboratory experiment *PlanICE*. The latter spectrometer can be equipped either with a solar-blind photomultiplier tube (PMT) or a windowless channel electron multiplier (CEM). Due to the cut-on wavelength of the LiF_2 window, the PMT cannot be used below 104.5 nm and the spectrometer is equipped with the CEM in this wavelength range and below.

In this work, an in-house absolute intensity calibration of the VUV spectrometer was performed in order to circumvent a calibration with synchrotron radiation. The calibration extends the standard procedure which is restricted to a lower

wavelength limit of 116 nm. A combination of secondary standard sources and methods was applied: the relative calibration was performed with two deuterium arc lamps, branching ratios of nitrogen plasma emission and a high current hollow cathode. Using overlap regions between the standards, a continuous relative calibration curve in the range 46 - 300 nm was achieved. An absolute scaling factor was obtained by simultaneous measurements with the VUV spectrometer and the absolutely intensity calibrated optical emission spectrometer at a helium discharge in *PlanICE*.

The resulting over-all inverse sensitivity of the VUV spectrometer obtained by the combination of PMT and CEM covers roughly three orders of magnitude. The calibration curves for both detectors peak around 120 nm with a peak value of $2 \cdot 10^{25}\,(\mathrm{sm^2nmV})^{-1}$ which could be assigned to a contamination of the applied diffraction grating.

The spectroscopic system at *PlanICE* allowed to identify gas specific wavelength ranges with relevant photon flux emission in order to select gas-specific filters sets for the diode system. The pure gases argon, hydrogen, nitrogen and oxygen as well as nitrogen/hydrogen (50:50), hydrogen/oxygen (85:15) and nitrogen/oxygen (80:20) mixtures were investigated. The relevance of the emission ranges regarding the fluxes was estimated with respect to the corresponding photon energy and the photon-to-ion flux ratio, respectively. Exemplarily, the photon flux from the resonant atomic lines at 104.8 nm and 106.7 nm in pure argon discharges below 3.5 Pa was identified as highly relevant due to its high energy around 12 eV and a photon-to-ion-flux ratio up to 0.72 at 1 Pa. This value corresponds to an absolute photon flux in the range of $(2-3) \cdot 10^{20}\,\mathrm{m^{-2}s^{-1}}$.

Based on these results, detailed lookup tables were provided which give an overview of relevant emission features in the investigated gases and mixtures and indicate appropriate filters and filter combinations with the corresponding filter intervals.

A crucial aspect regarding the diode concerns its performance behaviour and possible degradation effects due to VUV radiation. They were extensively characterized and a measurement procedure with a 30 second measurement interval was developed in which the diode system's output signal is averaged in the second 15 seconds. The reproducibility of the diode system was confirmed with measurements at a reference hydrogen discharge. No significant degradation was observed during the investigation period of roughly two years.

The diode system's direct absolute calibration against the VUV spectrometer represents an unique feature in which the diode system differs from other VUV

in-situ diagnostic tools. The calibration was achieved by simultaneous measurements together with the VUV spectrometer and/or the high resolution optical emission spectrometer. Calibration factors were obtained individually for each filter combination and each pure gas. The values comprise roughly three order of magnitude and are in the range of $(0.1 - 160) \cdot 10^{22}\,\mathrm{m^{-3}s^{-1}V^{-1}}$. For gas mixtures, linear combinations according to the gas composition were used. In the case of additional emission ranges (e.g. OH band), a specific calibration of the corresponding filter combination was carried out.

At *PlanICE*, extensive power and pressure scans were performed with the diode system in argon, hydrogen, nitrogen and oxygen as well as mixtures thereof. Due to the geometry of the setup, the plasmas show a cylindrical symmetry. However, pressure dependent vertical emission profiles were observed in molecular discharges. Depending on the gas (mixture), the operating pressure was in the range of 0.3 - 10 Pa with a generator power being varied from 200 W (in argon) to 1100 W in hydrogen. A electron temperature of several eV were measured. The electron density was in the order of $(10^{16} - 10^{17})\,\mathrm{m^{-3}}$ in molecular discharges and reached values of several $10^{18}\,\mathrm{m^{-3}}$ in argon. During the benchmark measurements, the VUV and/or optical emission spectrometer at rotation-symmetric lines of sight were applied as a reference. The diagnostics' viewing cones or cylinders differ with regarding their spatial expansion across the plasma vessel.

The benchmark measurements showed a good overall agreement between the results from the diode system and the reference spectrometer. The maximum deviation of +237 % was detected for the Second positive system in pure nitrogen which could be assigned to the the pressure dependent influence of spatial inhomogeneities in *PlanICE*. Further possible effects on the diode measurement could be identified which might also occur in various degrees at the diode system's plasma setup in use.

The transfer to three different setups demonstrated impressively the flexible and reliable applicability of the diode system. The inhouse ICP laboratory experiment *ACCesS* investigates the influence of hydrogen plasmas on caesiated surfaces. At an operating pressure of 10 Pa and an input power of 450 W, *ACCesS* produces emissivities around $2 \cdot 10^{21}\,\mathrm{m^{-3}s^{-1}}$ both in the energy range of the Lyman band and of the Werner band including the Lyman series. The emissivity of the L_α was determined to a value of $1.4 \cdot 10^{21}\,\mathrm{m^{-3}s^{-1}}$. It could be shown that a comparison with results at *PlanICE* at 10 Pa and 700 W is in good agreement with the plasma parameters obtained by optical emission spectroscopy together with collisional

radiative models.
The diode system's applicability was further demonstrated at the double ICP experiment *PlasmaDecon* at the Institute for Electrical Engineering and Plasma Technology at RUB. It is used for investigations on sterilizing properties of different plasmas. The photon fluxes in the VUV range corresponding to the wavelength range lower or equal to 153 nm arising in argon plasmas with a nitrogen admixture (100:5), an oxygen admixture (100:5) and a hydrogen/oxygen admixture (100:4:2), respectively, were determined to be in the range of $10^{20}\,\mathrm{m^{-2}s^{-1}}$. The maximum value could be observed in the argon/hydrogen/oxygen plasma due to the atomic hydrogen Lyman series and the molecular hydrogen Werner and Lyman bands. The measurements showed a minor pressure dependency in the investigated range of 3 - 10 Pa for each gas. This was confirmed by another portable VUV detector based on the consersion of VUV radiation by a sodium salicylate layer.
Finally, the diode system was successfully applied at the ion source of the *Batman Upgrade* test stand at the Max-Planck-Institut für Plasmaphysik (IPP, Garching) in order to determine ocurring VUV photon fluxes for the very first time. Studies at *Batman Upgrade* concern the impact of VUV photon fluxes onto the cesiated surface of the plasma grid and on the production of photoelectrons. Emissivities of the plasmas in the driver and in front of the plasma grid were derived for standard conditions (0.3 Pa, 40 kW, plasma grid current $I_{\mathrm{PG}} = 1\,\mathrm{kA}$). For the driver plasma, the energy intervals assigned to the Werner band including the Lyman series, the L_α line and the Lyman band, respectively, produce emissivities around $10^{22}\,\mathrm{m^{-3}s^{-1}}$ each. In comparison, the emissivities in front of the plasma grid are reduced by a factor of 55 - 71. The total VUV photon flux onto the plasma grid in the energy range above 6.6 eV amounts to $2.1 \cdot 10^{20}\mathrm{m^{-2}s^{-1}}$ with a 90 % contribution from the driver plasma. Rising the pressure to 0.6 Pa in the ion source led to an increase of the VUV photon flux by 60 %. The ratio arising from the driver plasma stayed unchanged. Without magnetic filter field ($I_{\mathrm{PG}} = 0\,\mathrm{A}$), the total VUV photon flux roughly doubled with respect to the standard pulse. The contribution by the driver plasma was significantly reduced to 44 %. During the parameter variation, the total absolute VUV photon fluxes onto the plasma grid were comparable to the corresponding positive ion fluxes.

Appendix

A Energy diagrams of atomic nitrogen and oxygen

In the following, energy diagrams of atomic nitrogen and oxygen which were mentioned in section 2.2.1 are presented. They indicate the wavelength of several emission lines in Angström, e.g. the atomic oxygen line at 844.6 nm or the atomic nitrogen line at 174.3 nm. Measured emissivities of these lines were used to determine the atomic ground state density by a corona model described in section 5.1.3. One hat to note that the states' spectroscopic notation in the following energy schemes may differ from equation (2.16) and is given by ${}^{2S+1}Z$ while the electrons' configuration nl^N is given additionally. N refers the number of electrons in the atomic orbital corresponding to the quantum numbers n and l.

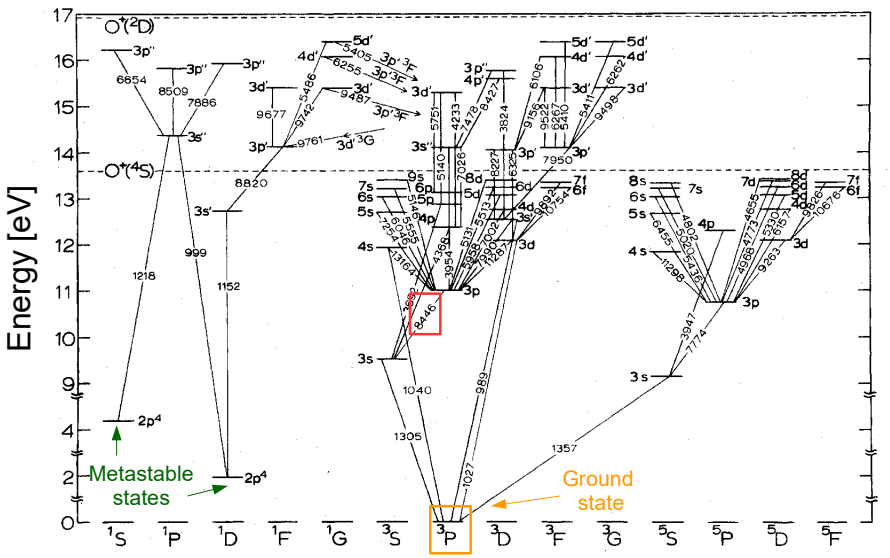

Figure A.1: Energy levels of atomic oxygen [SSC+85]. The wavelengths of several emission lines are given in Angström. The emissivity of the line at 844.6 nm (red box) is obtained by optical emission spectroscopy and it is used for the determination of the atomic ground state density described in section 5.1.3.

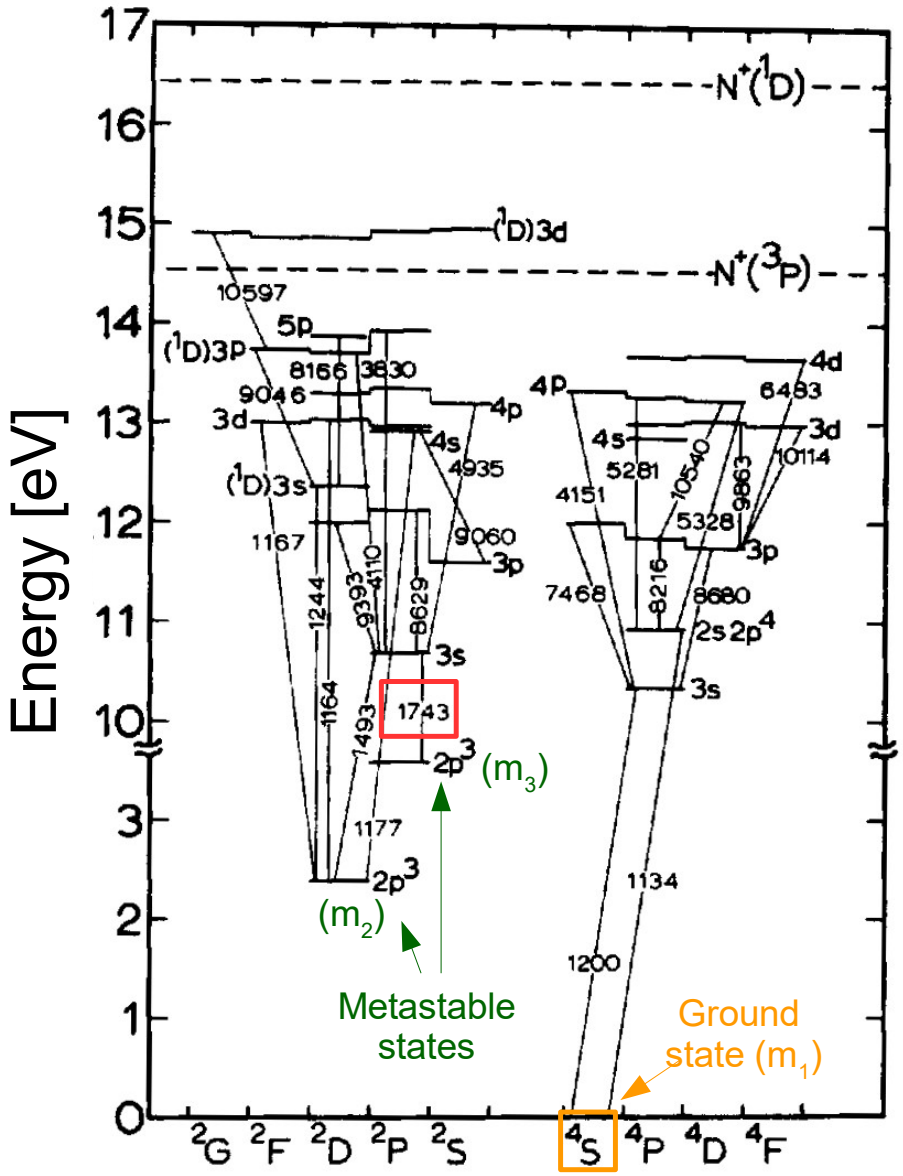

Figure A.2: Energy levels of atomic nitrogen [FSLM82]. The wavelengths of several emission lines are given in Angström. The emissivity of the line at 174.3 nm (red box) is obtained by optical emission spectroscopy and it is used for the determination of the atomic ground state density described in section 5.1.3.

B Potential energy curves of molecular nitrogen and oxygen

In the following, potential energy curves of neutral molecular nitrogen and oxygen as well as their corresponding singly charged ions which were mentioned on section 2.2.2 are given. The diagrams are taken from [Gil65].

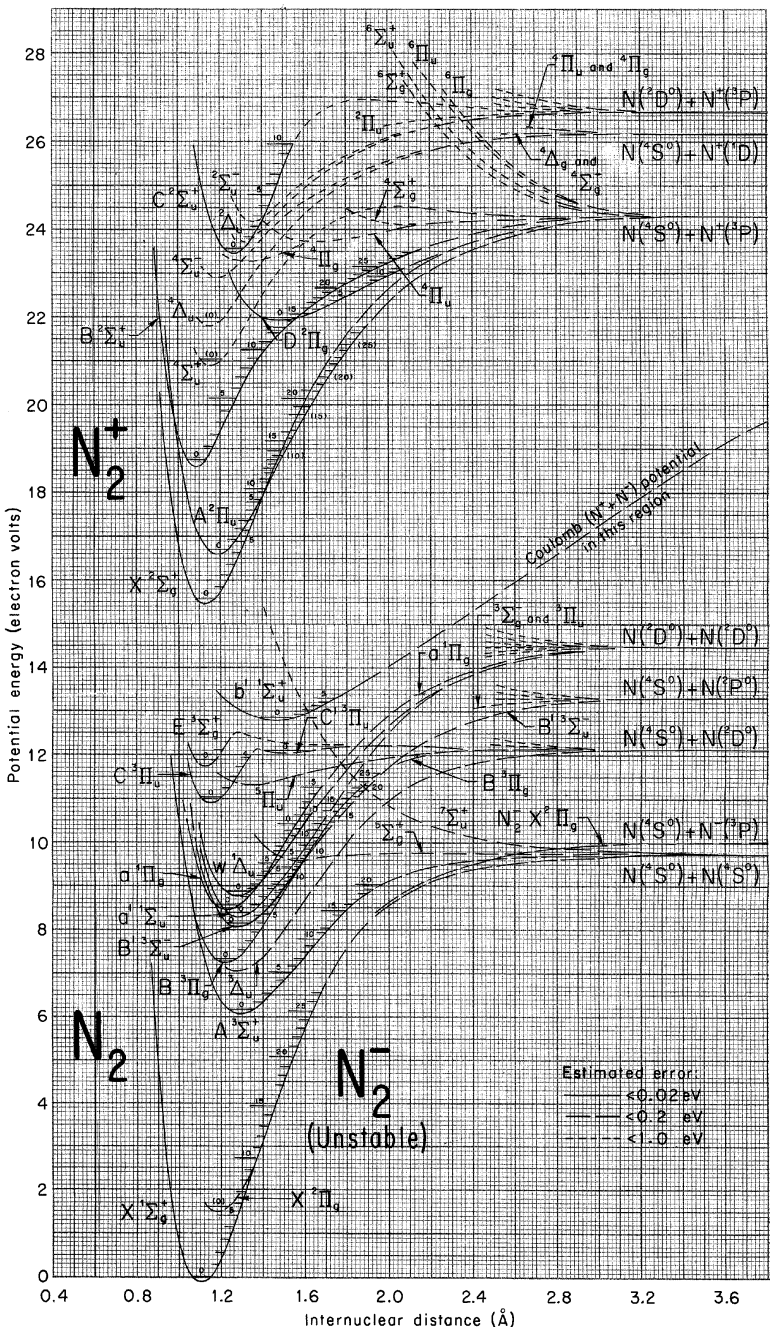

Figure B.1: Potential curves of molecular nitrogen and its ions [Gil65].

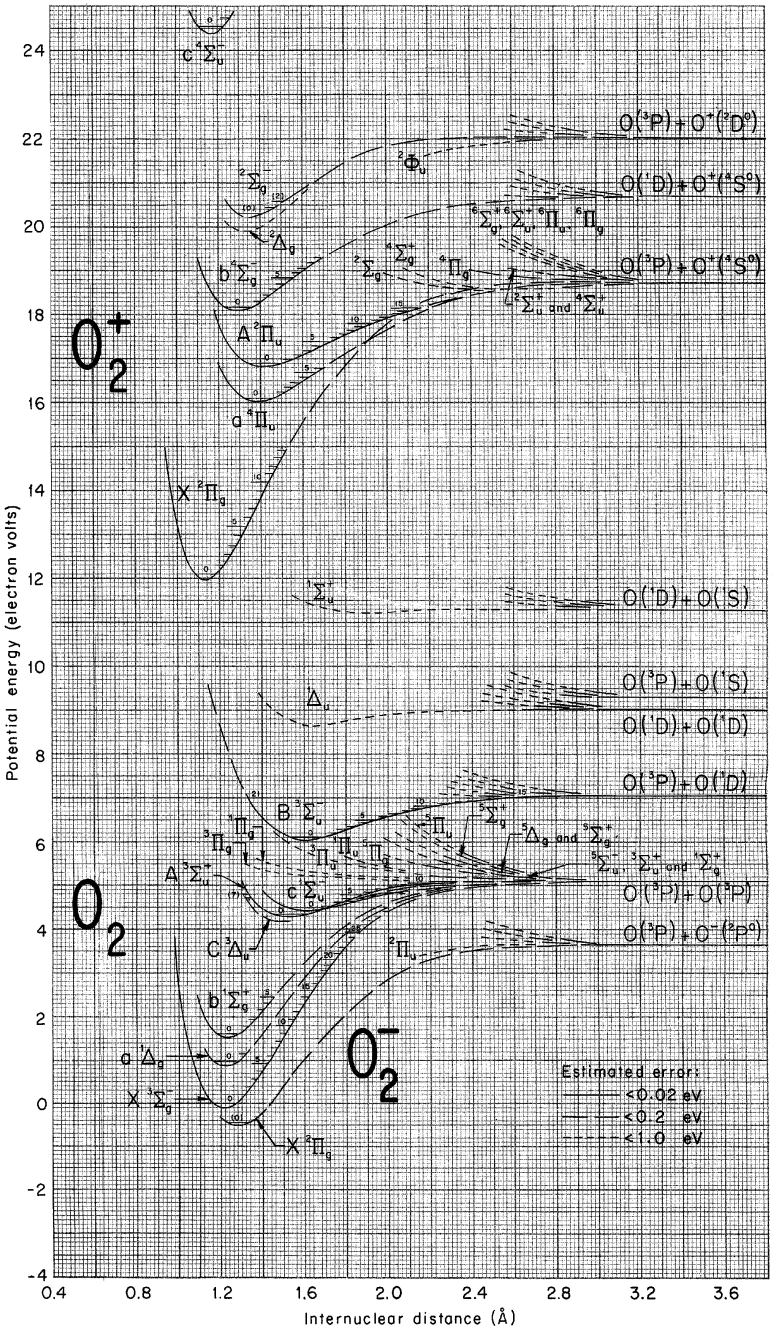

Figure B.2: Potential curves of molecular oxygen and its ions [Gil65].

C Details on the calibration procedure of VUV spectrometer

The following section gives further details on the absolute calibration procedure of the VUV spectrometer which was described in section 4.1.2. The presented tables have been already published in [FBFBF21].

C.1 Overview of the applied standard sources and techniques

The tables C.1 and C.2 present the calibration standards applied for the calibration of the VUV spectrometer equipped with the PMT and the CEM, respectively. Moreover, it includes the accessible wavelength region given by the standard source or method including overlap ranges and the range eventually feeding the calibration curve.

C.2 Overview of the relative uncertainty of the intensity calibration

The following tables C.3 and C.4 have been published in [FBFBF21] where also a detailed discussion can be found. The tables summarize the total wavelength-dependent relative uncertainties of the VUV spectrometer's relative and absolute intensity calibration with the PMT and the CEM, respectively. The values are calculated based on a Gaussian error propagation. No additional contribution arising from the fit functions is assumed.

Standard source	Accessible wavelength range	Considered wavelength range	Figure 4.1 (a)
High current hollow cathode (HCHC)	104.8 - 123.6 nm	104.8 - 106.7 nm	orange squares
Xe, N_2 and O_2 discharges	107.4 - 120.1 nm	107.4 - 116.5 nm	blue squares
Deuterium arc lamp II	116.0 - 400.0 nm	116.5 - 169.5 nm	black squares
Branching ratios in nitrogen	116.4 - 210.0 nm	169.5 - 198.2 nm	green squares
Deuterium arc lamp I	190.0 - 400.0 nm	198.2 - 300.0 nm	grey line
		200.0 - 300.0 nm (with quartz filter)	black line
He discharge	269.6 - 294.5 nm		black/gray stars

Table C.1: Standard sources applied during the intensity calibration of the VUV spectrometer equipped with the PMT. They include two deuterium arc lamps and branching ratios of a nitrogen discharge leading to a relative calibration. The simultaneous observation of the helium lines with the VUV and optical spectrometer allows an absolute scaling. Provided that the CEM is absolutely intensity calibrated below 116.5 nm, the investigations at the high current hollow cathode (HCHC) and xenon, nitrogen and oxygen discharges performed with both detects result in absolute calibration factors. The table has been published in [FBFBF21].

Standard source	Accessible wavelength range	Considered wavelength range	Figure 4.1 (b)
High current hollow cathode (HCHC)	46.1 - 123.6 nm	46.1 - 116.5 nm	orange squares
Deuterium arc lamp II	116.0 - 400.0 nm	116.5 - 160.0 nm	black squares

Table C.2: Standard sources applied during the intensity calibration of the VUV spectrometer equipped with the CEM. Furthermore, the absolute calibration procedure is based on the PMT's absolute calibration above 140 nm. The table has been published in [FBFBF21].

Wavelength range (PMT)	Quartz filter	Relative uncertainty of relative calibration	Relative uncertainty of absolute calibration
104.8 - 107.4 nm	w/o	20 %	63 %
107.4 - 116.5 nm	w/o	18 %	63 %
116.5 - 120.4 nm	w/o	7 %	17 %
120.4 - 122.8 nm	w/o	18 %	24 %
122.8 - 169.5 nm	w/o	7 %	17 %
169.5 - 198.4 nm	w/o	20 %	25 %
198.4 - 200.0 nm	w/o	14 %	21 %
200.0 - 240.0 nm	w/	14 %	22 %
240.0 - 300.0 nm	w/	13 %	22 %

Table C.3: Wavelength-dependent relative uncertainty regarding the relative and absolute intensity calibration of VUV spectrometer equipped with the PMT (without and with quartz filter in line of sight). The table has been published in [FBFBF21].

Wavelength range (CEM)	Relative uncertainty of relative calibration	Relative uncertainty of absolute calibration
< 116.5 nm	20 %	60 %
116.5 - 120.4 nm	7 %	27 %
120.4 - 122.8 nm	18 %	31 %
122.8 - 160.0 nm	7 %	27 %

Table C.4: Wavelength-dependent relative uncertainty regarding the relative and absolute intensity calibration of VUV spectrometer equipped with CEM (without quartz filter in line of sight). The table has been published in [FBFBF21].

D Applied filter set

D.1 Transmission curves

In this section, the measured wavelength dependent transmission curves of the diode system's filter set (see section 4.2.1) are presented. The applied radiation source for the transmission measurement is stated. The filter interval which is defined by a transmission of greater or equal to 5 % is indicated with the corresponding threshold wavelength. For the 337BP, this definition could not be applied since the peak transmission is below 5 %. In this case, the filter interval was defined by the zero crossing of the transmission curve.
Figure D.1 contains the band pass filters and gives the corresponding peak transmission and full width half maximum (FWHM). Regarding the 122BP filter, the figure shows the manufacturer's data since the transmission could not be measured due to the lack of an appropriate radiation source. However, the filter's peak transmission of 6.3 % could be determined using a hydrogen discharge at *Plan-ICE*. Therefore, figure D.1 additionally displays the manufacturer's data scaled to this measured value.
The long pass filters are summarized in figure D.2 together with the cut-on wavelength.

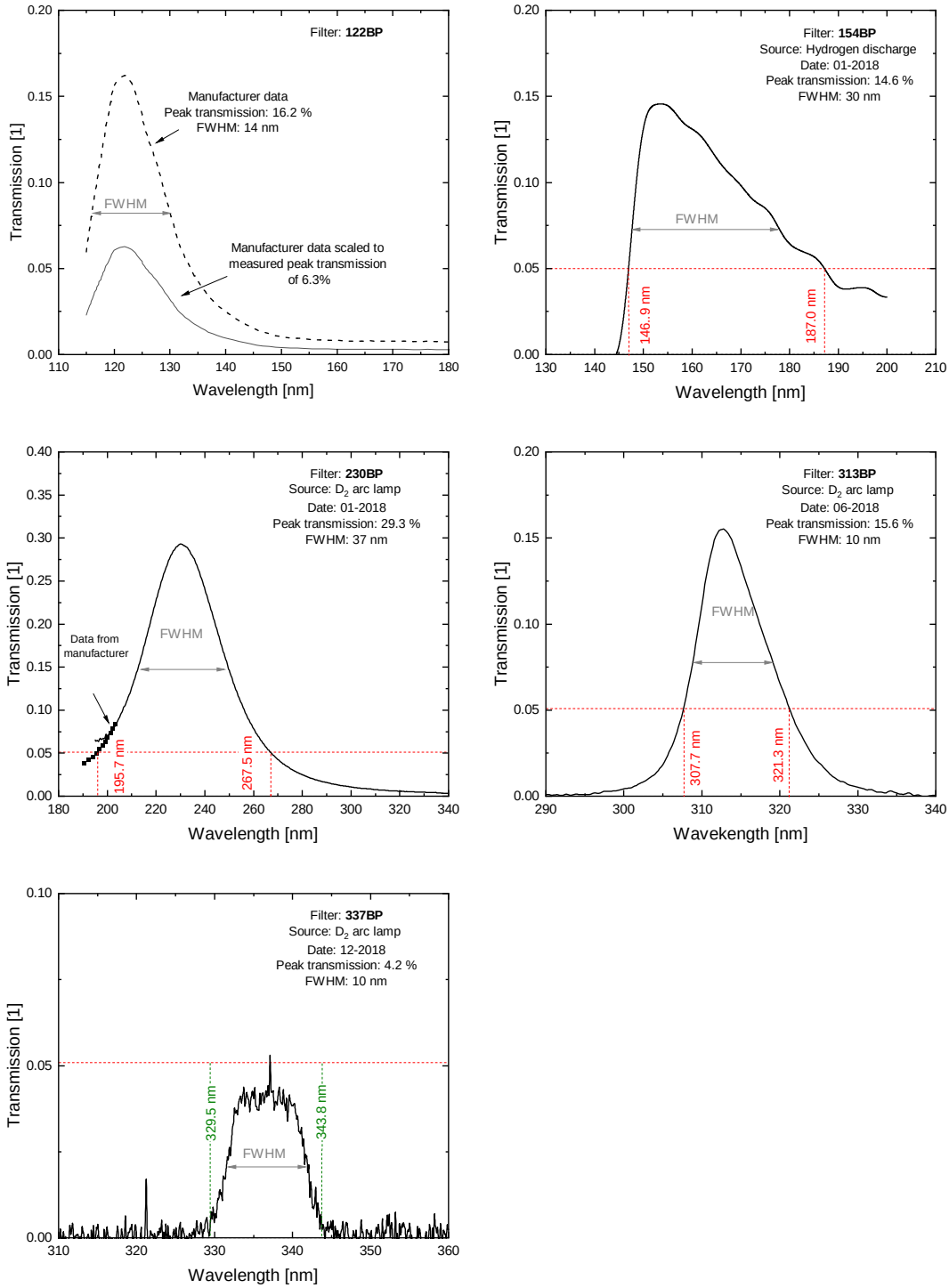

Figure D.1: Wavelength dependent transmission curves of the band pass filters of the diode system. The threshold wavelengths of the corresponding filter intervals with a transmission of greater or equal to 5 % are given in red. For 122BP filter, the manufacturer's data and scaled values of them are shown. For the 337BP, the filter interval is defined by the zero crossing of the transmission curve (green values).

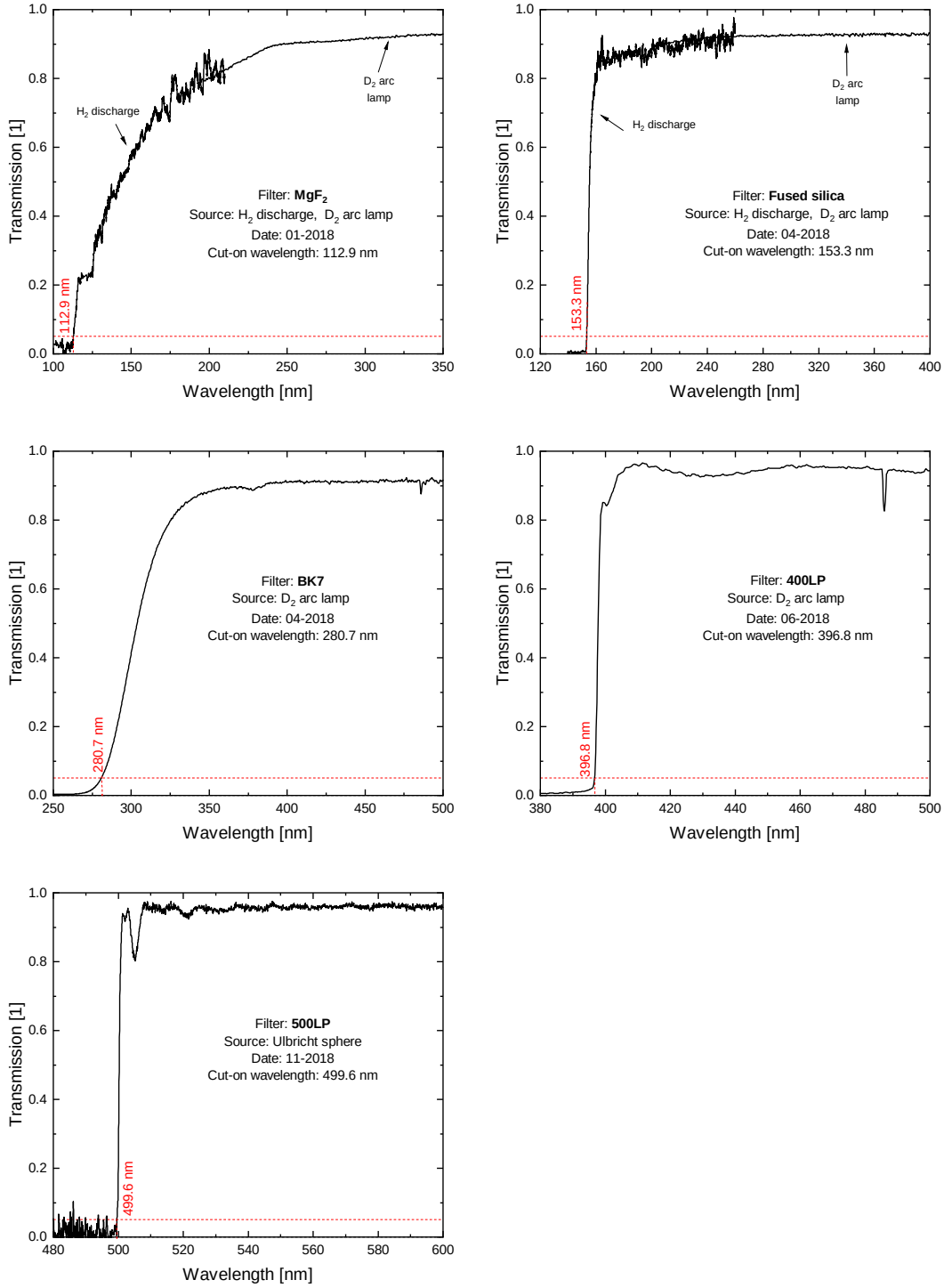

Figure D.2: Wavelength dependent ransmission curves of the long pass filters of the diode system. The cut-on wavelength of the filter interval (i.e. a transmission of greater or equal to 5 %) is given in red.

D.2 Pictures of the 122BP and 154BP filter

The following pictures indicate slight surface modifications within the illuminated area which were observed during investigations regarding a possible degradation (see section 4.2.5).

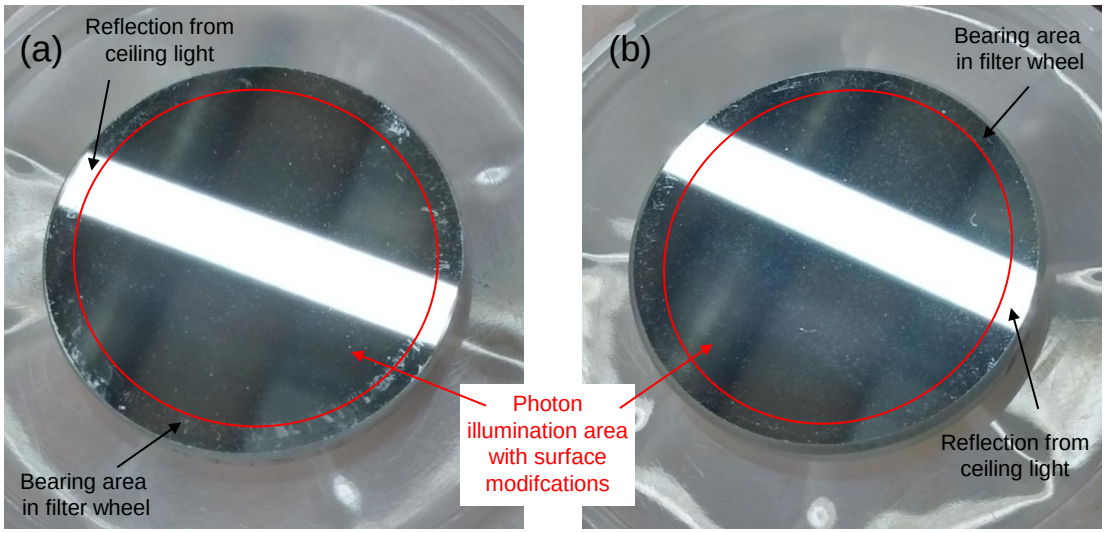

Figure D.3: Pictures of the 122BP filter (a) and the 154BP filter (b). The white stripes results from reflections of the ceiling light and are not related to degradation effects. The area of photon illumination is indicated in red. Both indicate similar material modifications (e.g. opaque haze, scattered dim, dust beneath the surface) as the 230BP filter after 6000 seconds total illumination which is discussed in section 4.2.5.

E Vertical emission profiles at PlanICE

The presented vertical emission profiles were taken with the optical survey spectrometer in order to check for the vertical emission homogeneity of hydrogen and argon plasmas. Homogeneous plasma emission is crucial for the calibration of the diode system (see section 4.2.4) and deviations from the homogeneity at high pressures might influence benchmark measurements (see section 7).

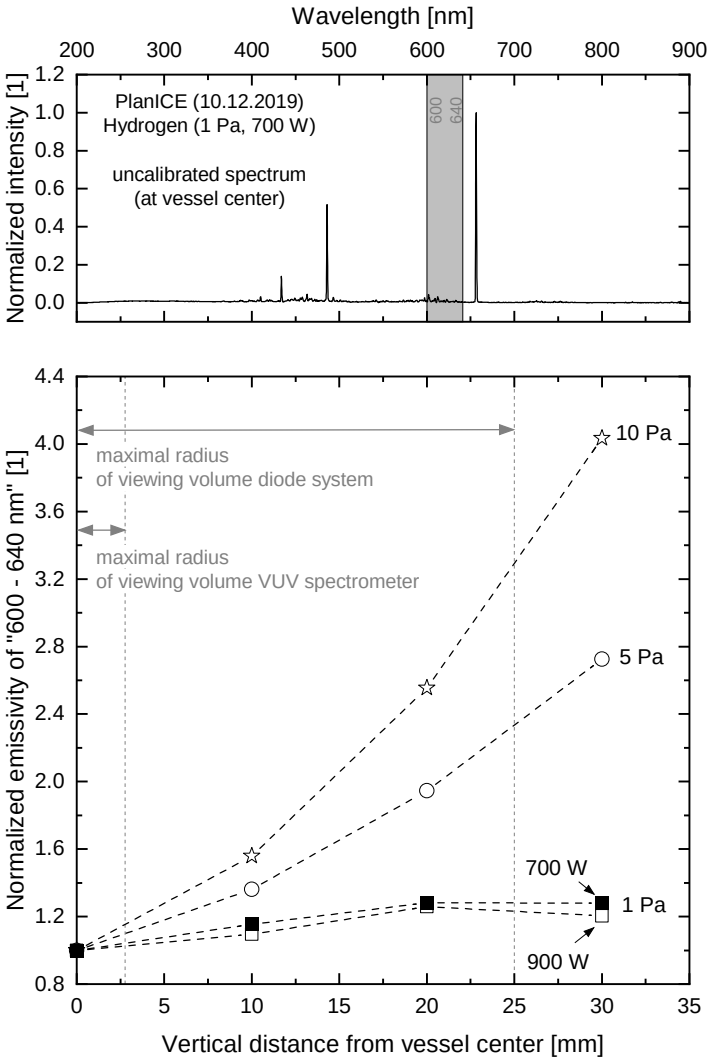

Figure E.1: Pressure dependent vertical emission profile in hydrogen at a generator power of 700 W. The upper part shows a spectrum at 1 Pa taken with the optical survey spectrometer. The wavelength range 600 - 640 nm is indicated corresponding to the emission range of the Fulcher transition. The integrated emissivities are displayed in the lower part with a normalization at the vessel center. In addition a power variation to 900 W is shown.

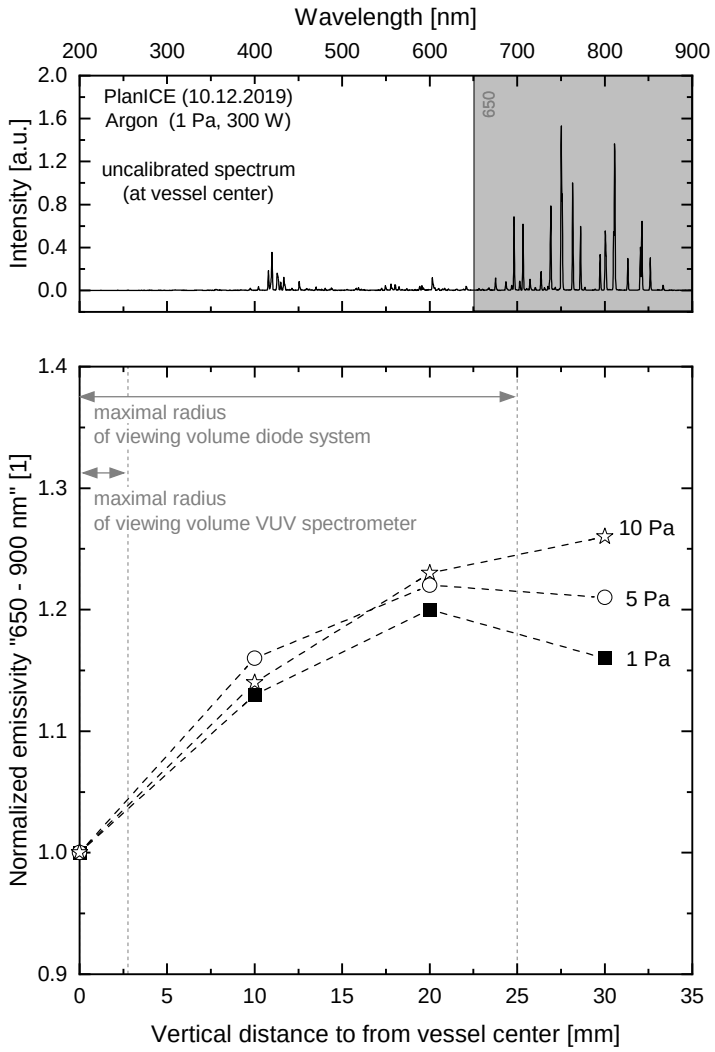

Figure E.2: Pressure dependent vertical emission profile in argon at a generator power of 300 W. The upper part shows a spectrum at 1 Pa taken with the optical survey spectrometer. The exemplar wavelength range 650 - 900 nm is indicated whose integrated emissivities are displayed in the lower part with a normalization at the vessel center.

F *PlanICE*: Plasma parameters, photon and particle fluxes

In the following, the plasma parameters electron temperature, the electron density, the gas temperature as well as the ion species distribution in the investigated discharges are compiled for the power and pressure scans. For each gas, they are shown in the first figure with T_{gas} in the upper part. If not otherwise stated, error bars of $\pm 50\,\mathrm{K}$ are not indicated. T_{e} (red) as well as n_{e} (open, black) are given in the lower part. The two latter parameters were derived in the vessel center. For calculating the ion distribution which is shown as vertical bars, the average over the radial profile of the electron density was used.
Based on these results, the corresponding particle fluxes are calculated which can be also found in this section for the power scan. Additionally, the photon fluxes from the most prominent emission ranges are depicted. In section 6, the corresponding results for pressure scans are presented.

F.1 Argon

In argon, the ion distribution has not been measured with the mass spectrometer. The natural istopic distribution is applied. With the diagnostic setup available at the experiment *PlanICE*, the gas temperature cannot be assessed. Therefore, a value of 700 K has been used for the calculation of the neutral particle flux. The uncertainty of $\pm 300\,\mathrm{K}$ is not shown.

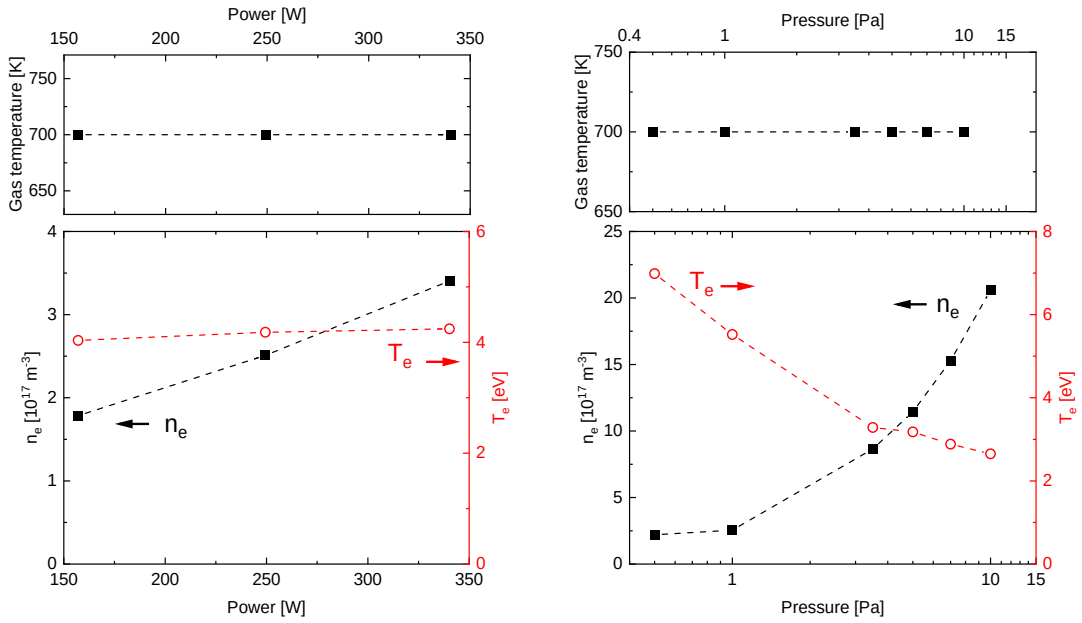

Figure F.1: Plasma parameters determined in argon. The gas temperature could not be measured with the diagnostic system and is assumed to be 700 K. The natural isotopic ratio is assumed for the dominant ion species and is not additionally shown.

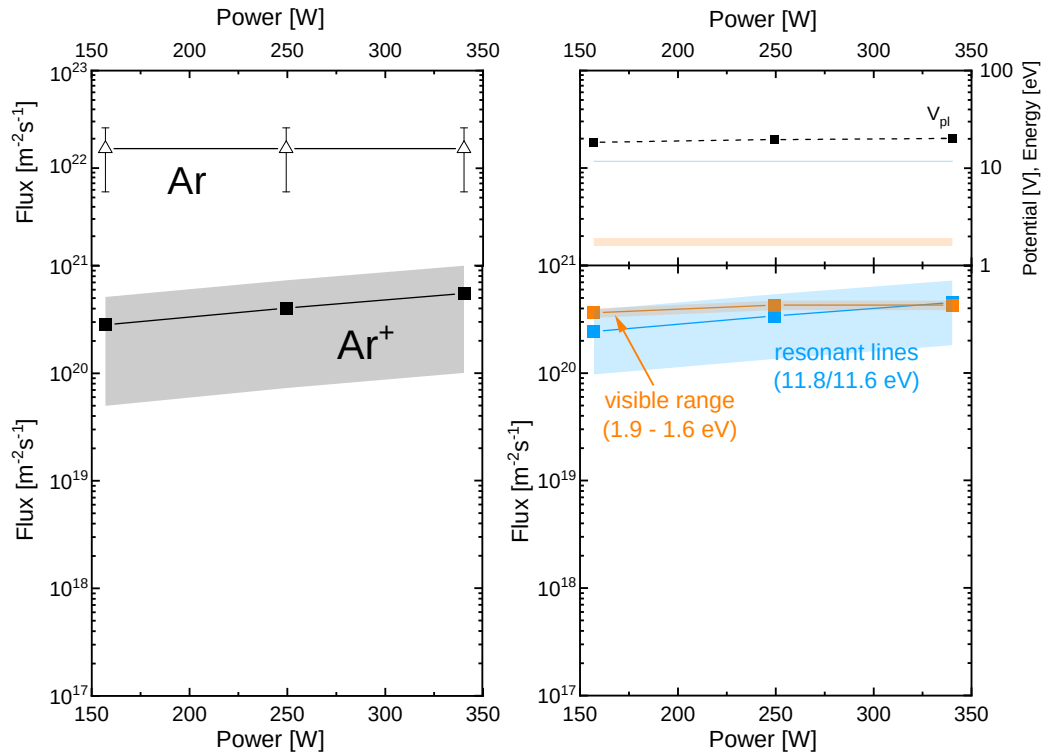

Figure F.2: Particle and photon fluxes determined in argon during the power scan at 1 Pa.

F.2 Hydrogen

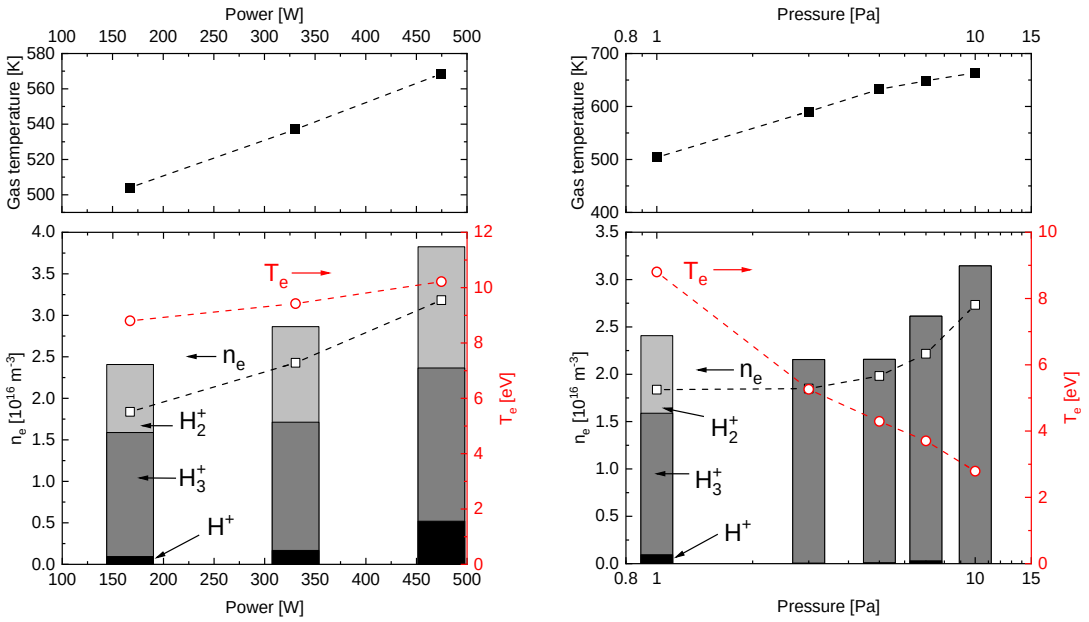

Figure F.3: Plasma parameters and dominant ion species determined in hydrogen.

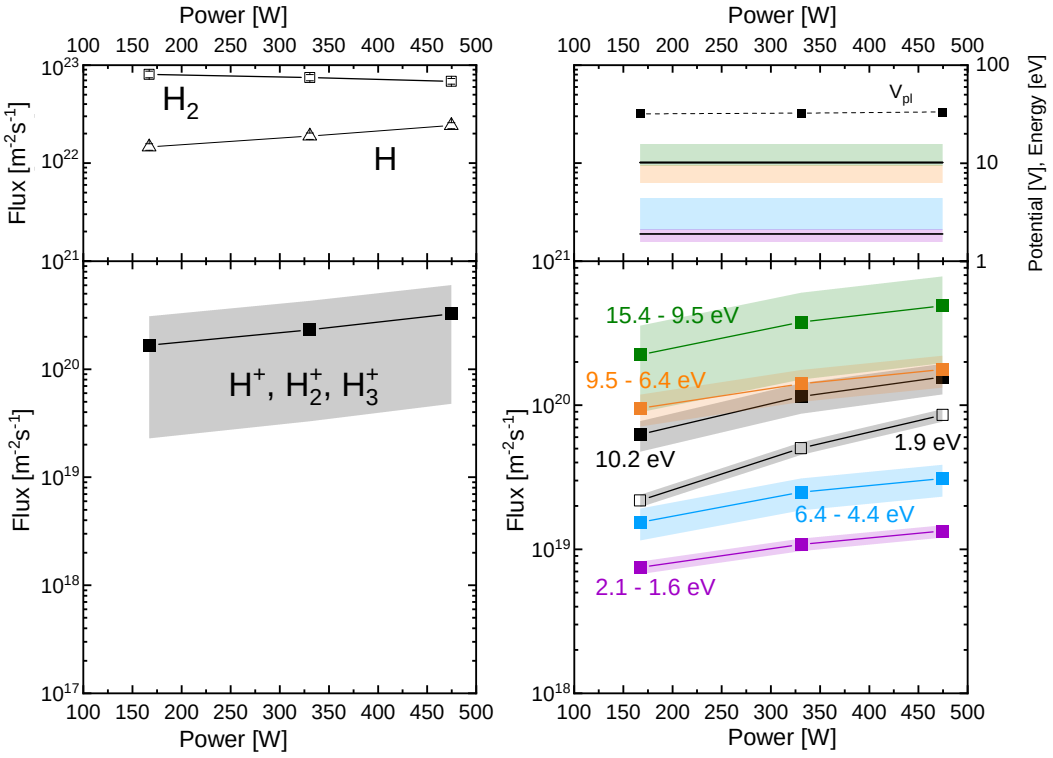

Figure F.4: Particle and photon fluxes determined in hydrogen in power scan at 1 Pa.

F.3 Nitrogen

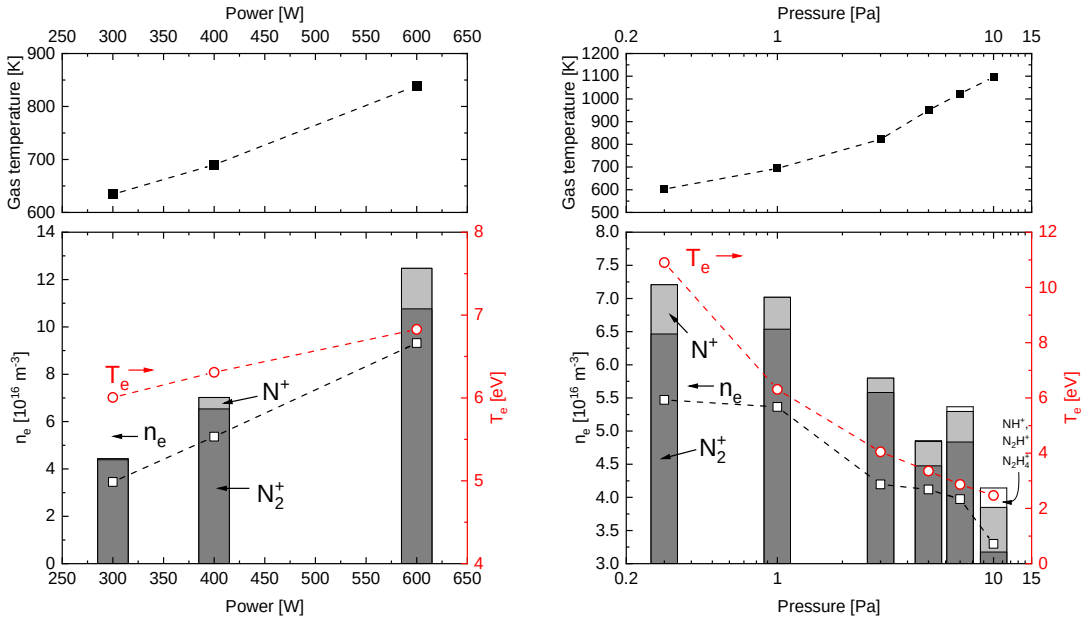

Figure F.5: Plasma parameters and dominant ion species determined in nitrogen.

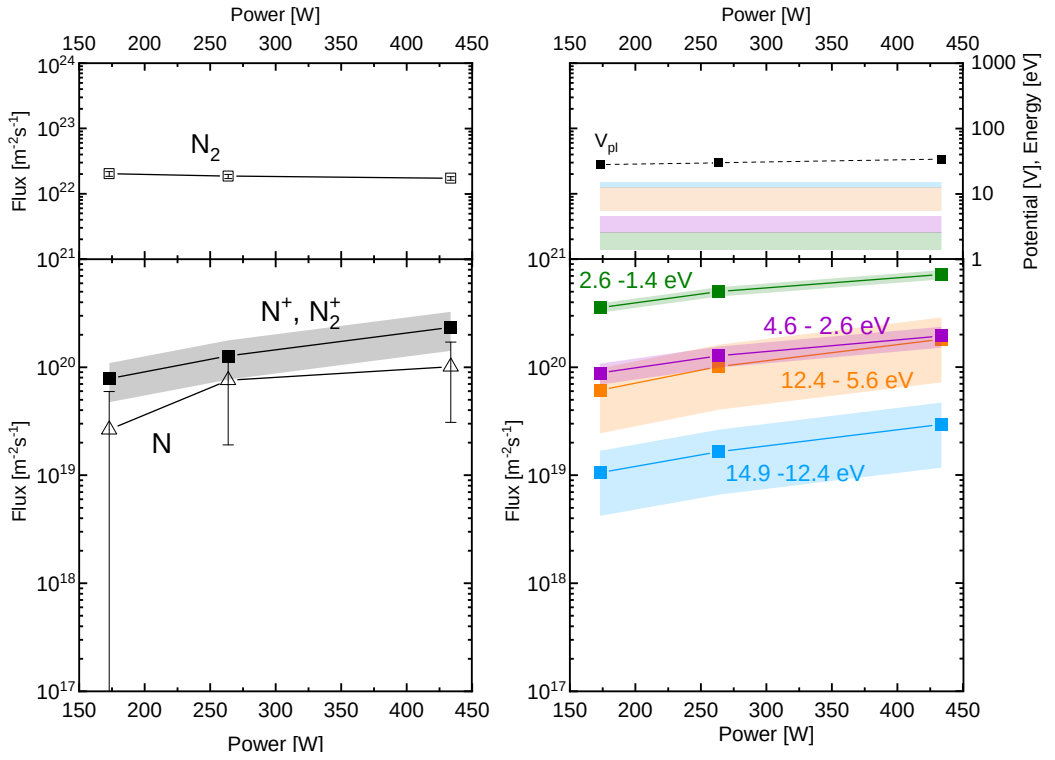

Figure F.6: Particle and photon fluxes determined in nitrogen in the power scan at 1 Pa.

F.4 Oxygen

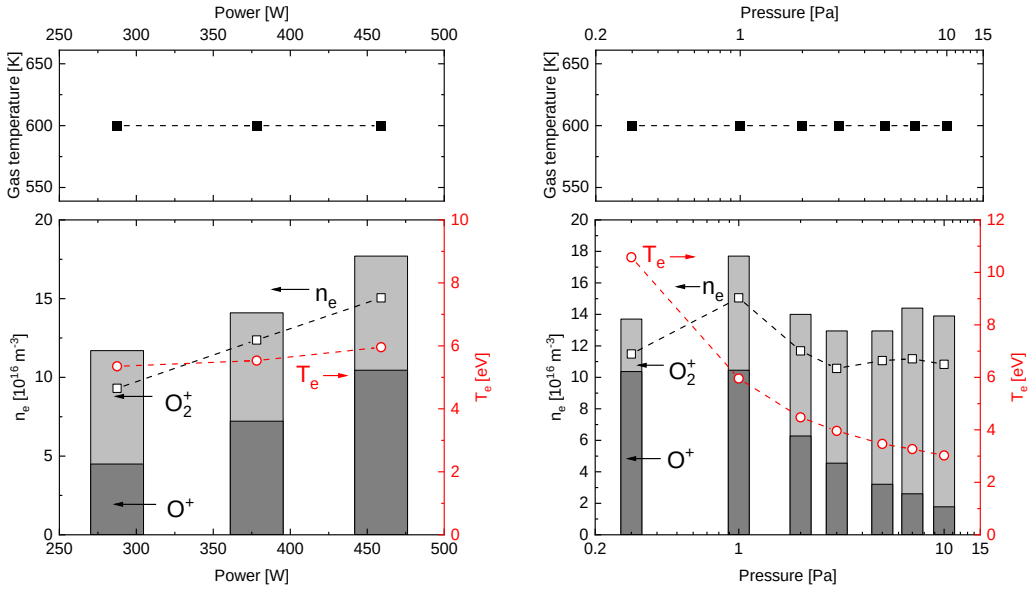

Figure F.7: Plasma parameters and dominant ion species determined in oxygen. The gas temperature could not be measured with the diagnostic system and is assumed to be 600 K.

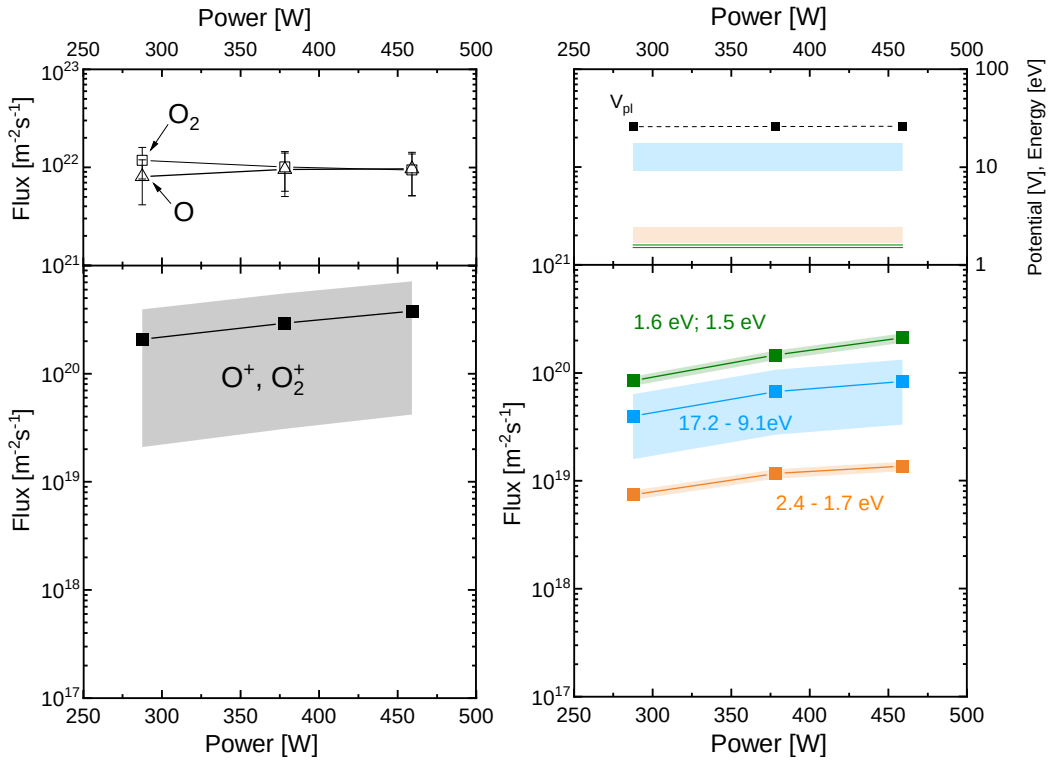

Figure F.8: Photon and particle fluxes determined in oxygen in the power scan at 1 Pa.

F.5 Nitrogen/hydrogen (50:50)

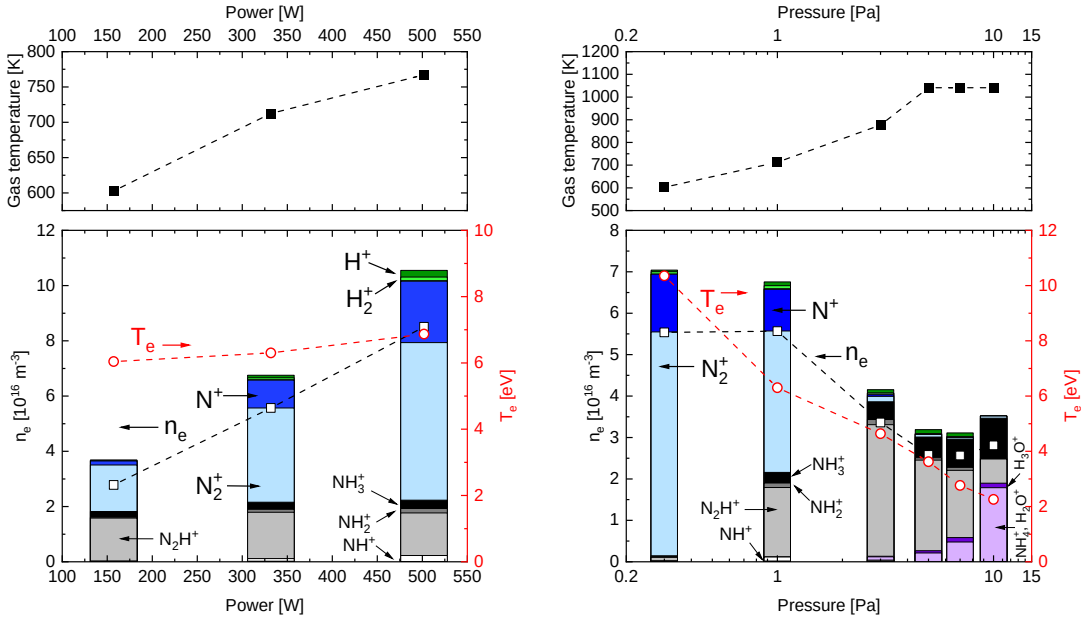

Figure F.9: Plasma parameters and dominant ion species determined in the nitrogen/hydrogen mixture (50:50).

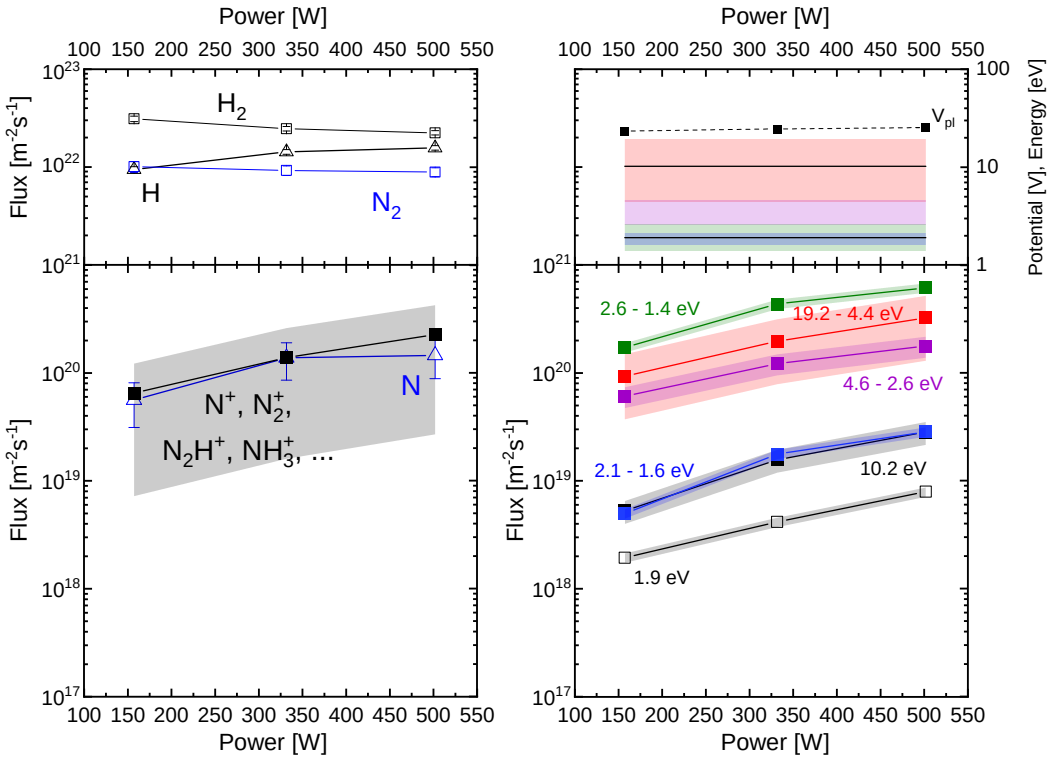

Figure F.10: Particle and photon fluxes determined in the nitrogen/hydrogen mixture (50:50) in the power scan at 1 Pa.

F.6 Hydrogen/oxygen (85:15)

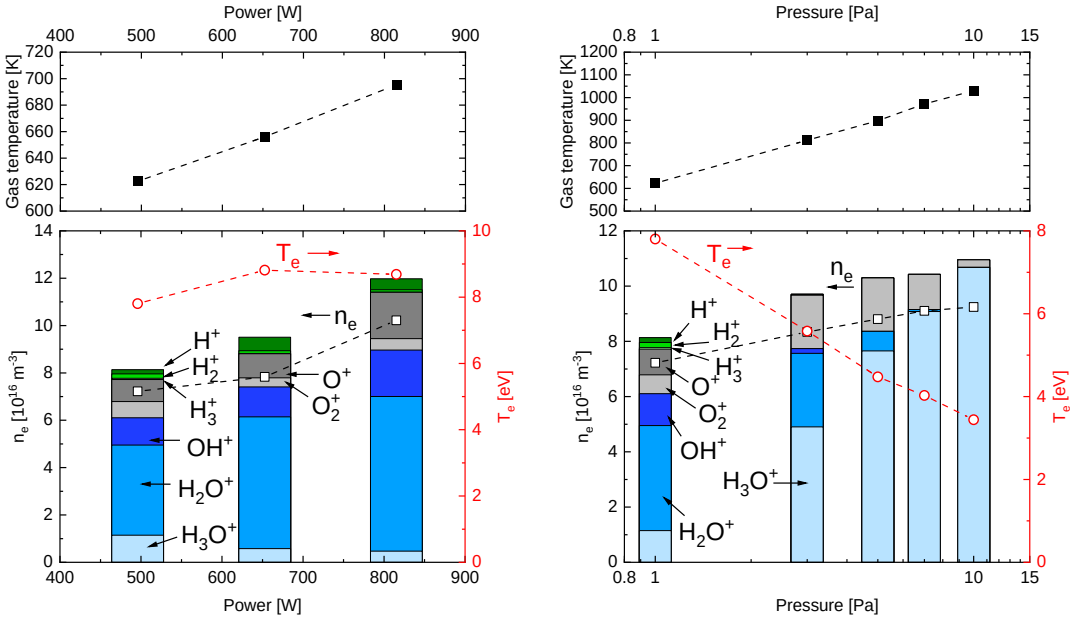

Figure F.11: Plasma parameters and dominant ion species determined in the hydrogen/oxygen mixture (85:15).

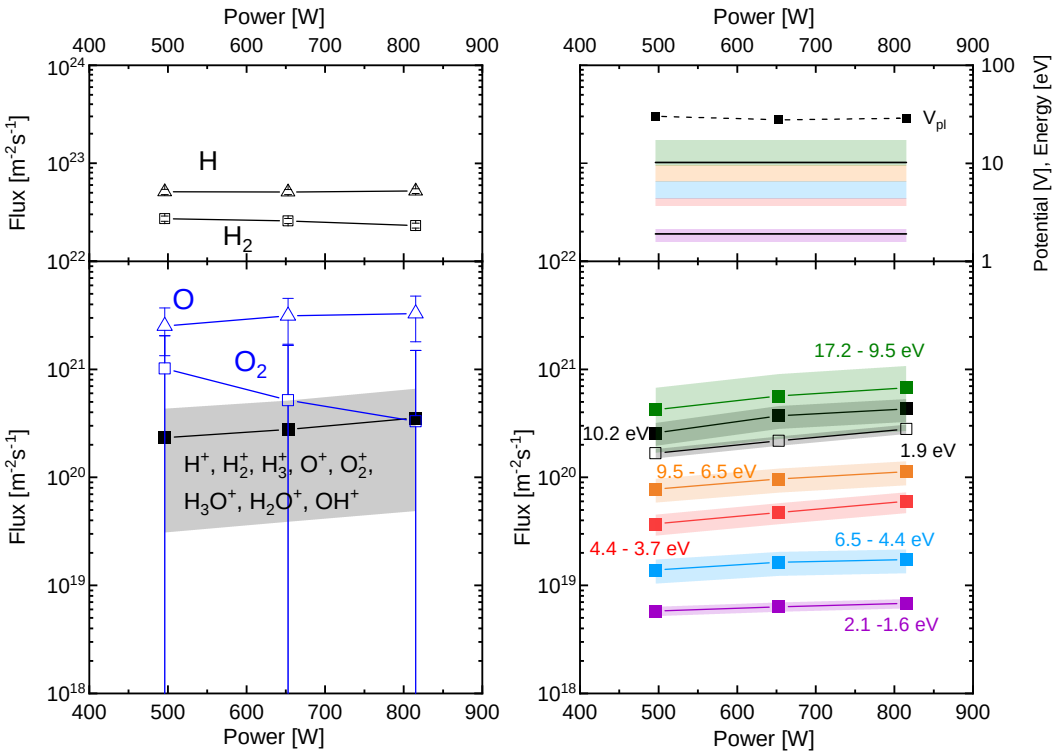

Figure F.12: Particle and photon fluxes determined in the hydrogen/oxygen mixture (85:15) in the power scan at 1 Pa.

F.7 Nitrogen/oxygen

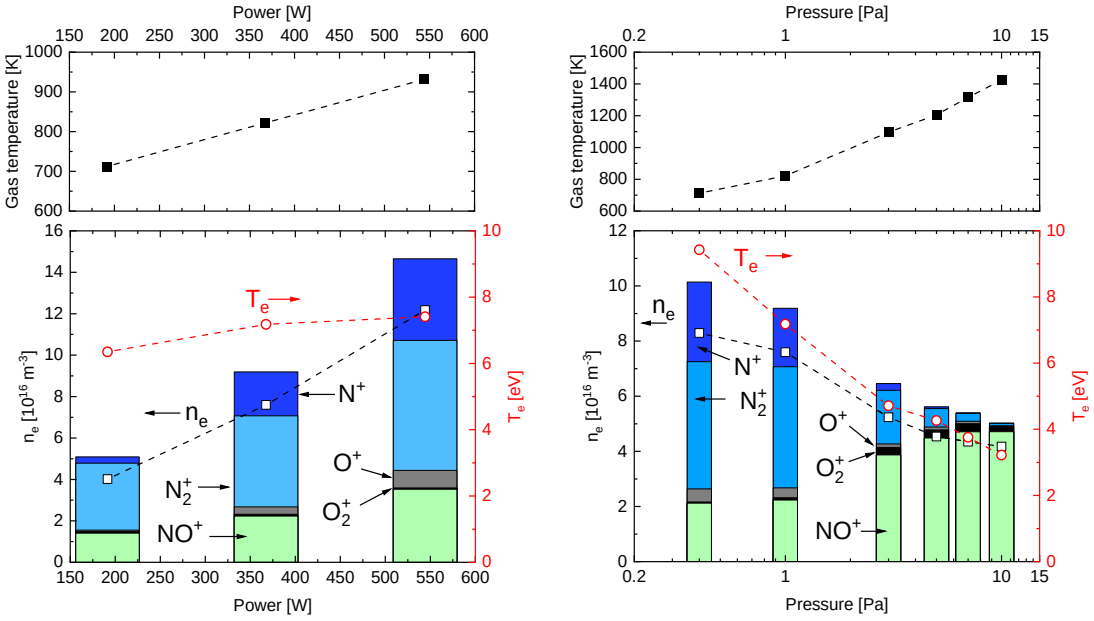

Figure F.13: Plasma parameters and dominant ion species determined in the nitrogen/oxygen mixture (80:20).

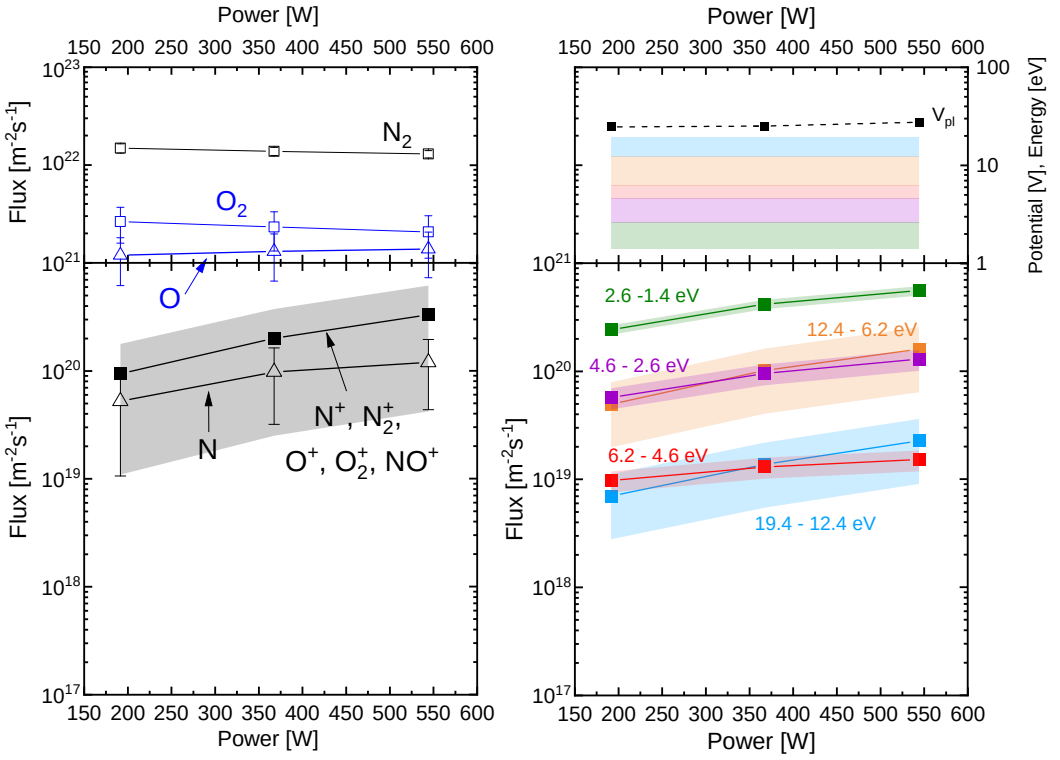

Figure F.14: Particle and photon fluxes determined in the nitrogen/oxygen mixture (80:20) in the power scan at 1 Pa.

G Cross sections for the 844.6 nm atomic oxygen line

The presented cross sections were used to calculate corresponding emission rate coefficients for the atomic oxygen line at 844.6 nm. As described in section 5.1.3, they were applied in a corona model in order to derive the neutral atomic oxygen density from optical emission spectroscopy.

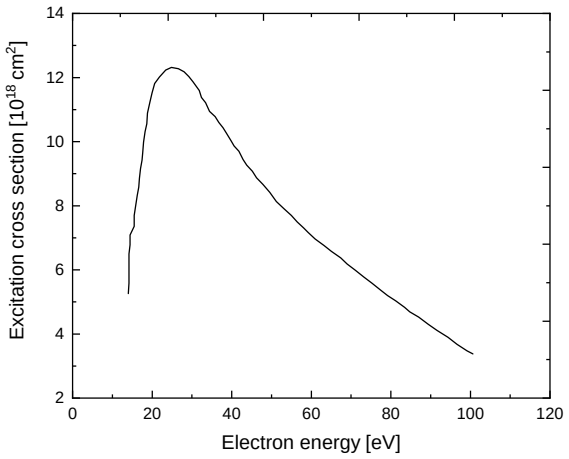

Figure G.1: Excitation cross section of the $3p\ ^3P$ state in atomic oxygen. This state serves as upper level of the emission line at 844.6 nm. The presented values are calculated by [TH88] and are digitized from [II90].

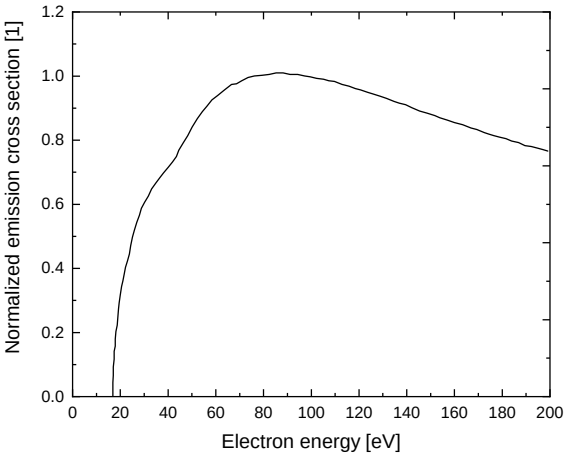

Figure G.2: Emission cross sections of the 844.6 nm line digitized from [SSC+85].

H Benchmark of diode system in pure gases

In this section, the results of the benchmark of the diode system which is described in chapter 7 are presented for pure gases. A selection of the results obtained in argon and hydrogen will be published in [FFBF22]. Corresponding calibration factors for the diode system are taken from table 4.9. For each gas and filter combination, the absolute emissivities measured during the power and pressure scans with the diode system and the reference are displayed. The latter is represented either by the VUV spectrometer, by the high resolution optical spectrometer or a combination of both spectrometer depending on the particular emission range. Throughout the entire section, the formatting of the results is as follows: Full symbols indicate the diode system while open symbols correspond to the reference. A tube assigning ± 25 % around the reference is added to give an impression about the agreement of the diode system with the reference. Moreover, comments on the benchmark are given in tabular form including effects that are identified to be considered for the comparison between the diagnostics. The letters in the first column refer to the corresponding part of the figure and the emission range stated there.

H.1 Argon

In argon, the calibration of the diode system was performed at 1 Pa with 300 W and 400 W generator power, respectively.

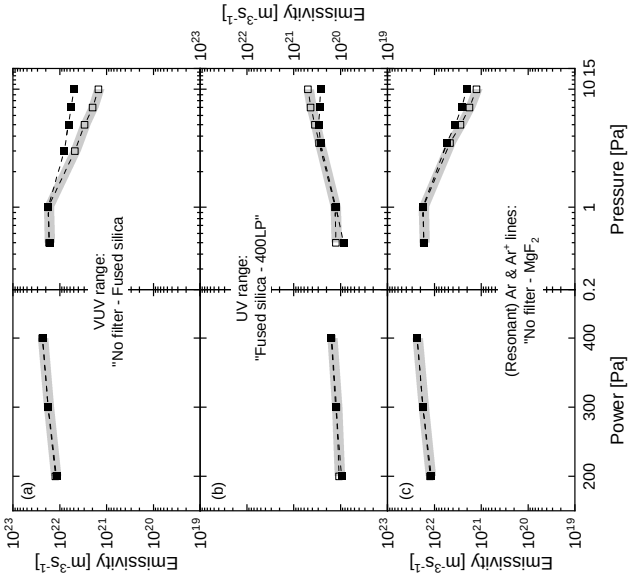

Figure H.1: Benchmark of the diode system in argon at *PlanICE* (power scan: 1 Pa, pressure scan: 300 W).

Table H.1: Comments on the benchmark of the diode system in argon for (a) the VUV range, (b) the UV range, (c) atomic and ionic lines.

#	Power scan (@1 Pa)	Pressure scan (@300 W)
(a)	Absolute agreement within ±5 %	For ≤1 Pa absolute agreement within ±1 %, for >1 Pa increasing deviation with pressure up to 234 % at 10 Pa Effect: Pressure dependent emission from carbon multiplet in transmission edge of fused silica filter
(b)	Absolute agreement within ±12 %	Absolute agreement within 6 % for 1 Pa and 3 Pa; for 0.5 Pa and pressure above 3 Pa deviation up to 46 % with increasing pressure whereas diode system below VUV spectrometer Effect: Variation of intensity distribution in transmission edge of fused silica filter due to pressure dependent impurities (e.g. carbon multiplet, nitrogen bands)
(c)	Absolute agreement within ±6 %	Absolute agreement within ±18 % for ≤3 Pa, increasing deviation with pressure above 3 Pa up to 64 % Effect: Broad transmission edge of MgF_2 in combination with pressure dependent emission from carbon multiplet and nitrogen bands

H.2 Hydrogen

The calibration of the diode system in pure hydrogen was performed at 1 Pa with 900 W and 1100 W generator power, respectively.

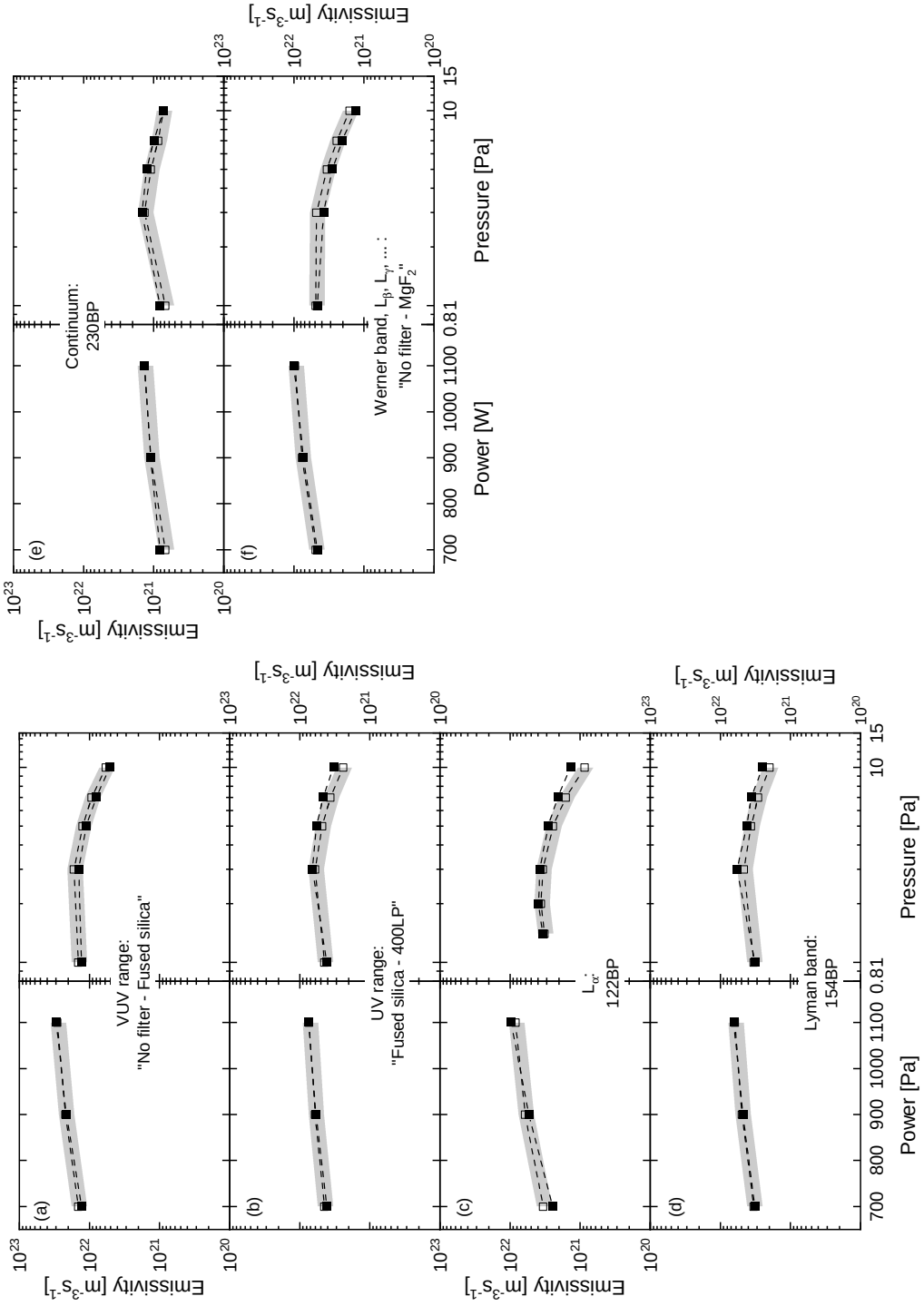

Figure H.2: Benchmark of the diode system in hydrogen at *PlanICE* (power scan: 1 Pa, pressure scan: 700 W).

Table H.2: Comments on the benchmark of the diode system in hydrogen for (a) the VUV range, (b) the UV range, (c) L_α, (d) Lyman band, (e) Continuum, (f) Werner band with L_β, L_γ, ...

#	Power scan (@1 Pa)	Pressure scan (@700 W)
(a)	Absolute agreement within ±10 %	Absolute agreement within ±14 %; no influence of vertial emission profile observed
(b)	Absolute agreement within ±8 %	For ≤5 Pa absolute agreement within ±21 %, increasing deviation with pressure up to 37 % at 10 Pa Effect: Vertical emission profile
(c)	Absolute agreement within ±27 %	For ≤5 Pa absolute agreement within ±18 %, increasing deviation with pressureup to 59 % at 10Pa Effect: Pressure dependent intensity distribution of L_α and molecular hydrogen band within FWHM of filter transmission (taken from manufacturer), additionally vertical emission profile
(d)	Absolute agreement within ±4 %	Absolute agreement within ±26 %
(e)	Absolute agreement within ±19 %	Absolute agreement within ±19 %
(f)	Absolute agreement within ±5 %	Absolute agreement within ±20 %

H.3 Nitrogen

The calibration in pure nitrogen was performed at 1 Pa with 400 W and 600 W generator power, respectively.

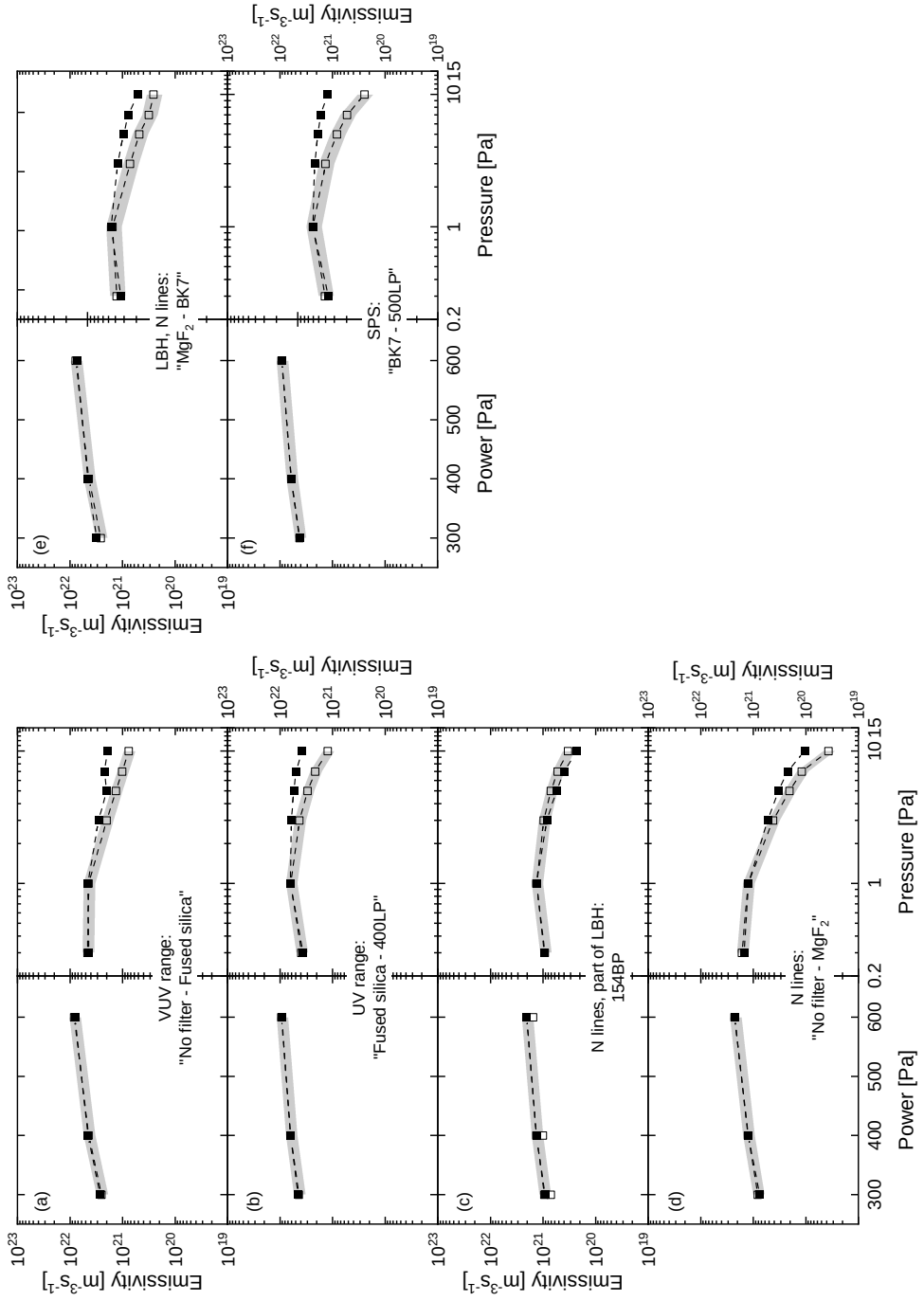

Figure H.3: Benchmark of the diode system with power and pressure scans in pure nitrogen at *PlanICE* (power scan: 1 Pa, pressure scan: 400 W). "LBH" corresponds to the Lyman-Birge-Hopfield system of N_2 and "SPS" refers to the Second positive system of N_2.

Table H.3: Comments on the benchmark of the diode system in pure nitrogen for (a) the VUV range, (b) the UV range, (c) N lines, part of Lyman-Birge-Hopfield system of N_2, (d) N lines, (e) Lyman-Birge-Hopfield system of N_2, (f) Second positive system of N_2.

#	Power scan (@1 Pa)	Pressure scan (@400 W)
(a)	Absolute agreement within ±6 %	For ≤1 Pa absolute agreement within ±4 %, increasing deviation with pressure up to 155 % at 10 Pa Effect: Vertical emission profile
(b)	Absolute agreement within ±3 %	For ≤1 Pa absolute agreement within ±7 %, increasing deviation with pressure up to 214 % at 10 Pa Effect: Vertical emission profile
(c)	Absolute agreement within ±2 %	Absolute agreement within ±30 % whereas deviation is increasing with pressure Effect: Vertical emission profile
(d)	Absolute agreement within ±2 %	For ≤1 Pa absolute agreement within ±10 %, increasing deviation with pressure up to 185 % at 10 Pa Effect: Vertical emission profile, additional pressure dependent spectral emission ranges above 113 nm due to broad transmission edge of MgF_2
(e)	Absolute agreement within ±20 %	For ≤1 Pa absolute agreement within ±12 %, increasing deviation with pressure with maximum of 96 % at 7 Pa Effect: Vertical emission profile, possibly concurring influence of transmission edges of the applied filters
(f)	Absolute agreement within ±1 %	For ≤1 Pa absolute agreement within ±10 %, increasing deviation with pressure up to 237 % at 10 Pa Effect: Vertical emission profile

H.4 Oxygen

The calibration of the diode system in oxygen was performed at 1 Pa with 500 W and 600 W generator power, respectively.

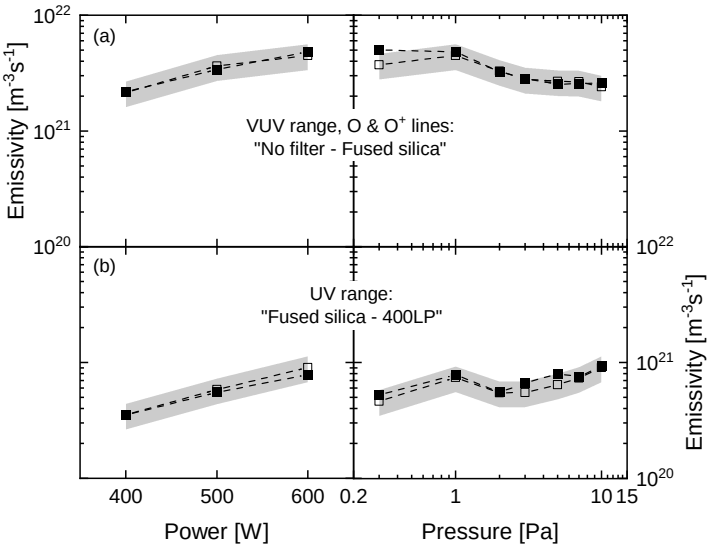

Figure H.4: Benchmark of the diode system at *PlanICE* (power scan: 1 Pa, pressure scans: 600 W)

Table H.4: Comments on the benchmark of the diode system in pure oxygen for (a) the VUV range, O & O^+ lines (b) the UV range.

#	Power scan (@1 Pa)	Pressure scan (@600 W)
(a)	Absolute agreement within ±7 %	For ≥1 Pa absolute agreement within ±8 %, at 0.3 Pa deviation of 30 % Effect: Possible occurence of ionic oxygen lines below 46 nm and limited sensitivity of VUV spectrometer in this range
(b)	Absolute agreement within ±6 %	Absolute agreement within ±25 %

I Benchmark of diode system in gas mixtures

In the following, the results obtained from the benchmark of the diode system which is discussed in chapter 7 in gas mixtures are presented. A selection of the results obtained in nitrogen/oxygen (80:20) will be published in [FFBF22]. In addition to the pure gases, also emission ranges of composed molecules are investigated with corresponding filter combinations. The formatting of the figures and tables is adopted from the previous section. For the calibration factors in pure gases, it is referred to table 4.9. Calibration factors for the NH band, the OH band and the NO band are taken from table 4.10.

I.1 Nitrogen/hydrogen (50:50)

The NH band (with the 337BP) was directly calibrated at the nitrogen/hydrogen mixture at 1 Pa with 500 W and 700 W, respectively.

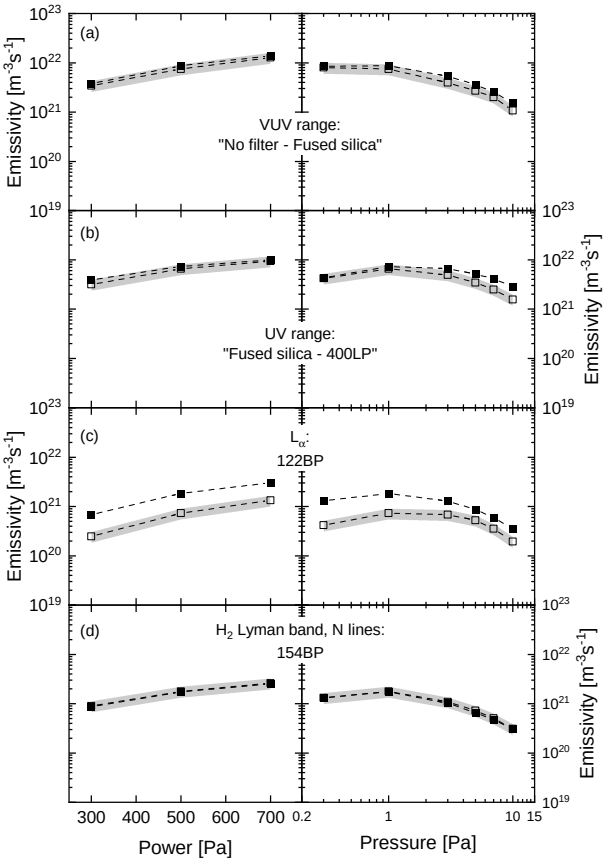

Figure I.1: Benchmark of the diode system in nitrogen/hydrogen mixture (50:50) at *PlanICE* (power scan: 1 Pa, pressure scan: 500 W). "LBH" refers to the Lyman-Birge-Hopfield system of N_2.

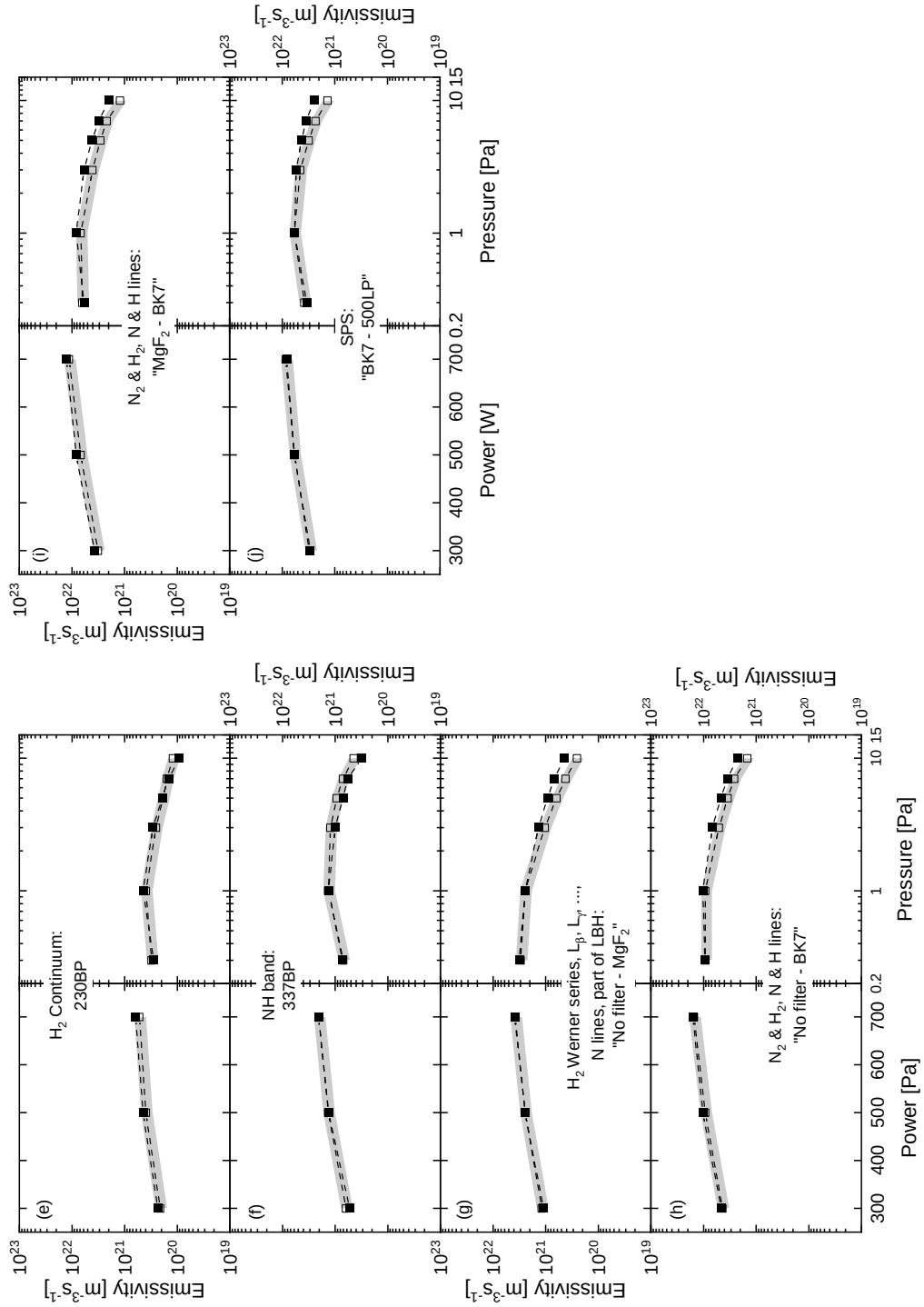

Figure I.2: Benchmark of the diode system in nitrogen/hydrogen mixture (50:50) at *PlanICE* (power scan: 1 Pa, pressure scan: 500 W). "LBH" refers to the Lyman-Birge-Hopfield system of N_2, "SPS" corresponds to the Second positive system of N_2.

Table I.1: Comments on the benchmark of the diode system in nitrogen/hydrogen (50:50) for (a) the VUV range, O & O^+ lines (b) the UV range, (c) L_α, (d) H_2 Lyman band, (e) H_2 Continuum, (f) NH band, (g) H_2 Werner series, L_β, L_γ, ..., part of Lyman-Birge-Hopfield system, N lines (h) N_2, H_2, N & H lines.

#	Power scan (@1 Pa)	Pressure scan (@500 W)
(a)	Absolute agreement within ±17 %	For ≤1 Pa absolute agreement within ±17 %, increasing deviation with pressure up to 42 % at 10 Pa Effect: Vertical emission profile
(b)	Absolute agreement within ±24 %	For ≤1 Pa absolute agreement within ±11 %, increasing deviation with pressure up to 84 % at 10 Pa Effect: Vertical emission profile
(c)	Absolute deviation between +128 % and +178 %	Deviation between 64 % at 5 Pa and 212 % at 0.3 Pa
	Effect: Deviating intensity distribution within FWHM of filter transmission (taken from manufacturer) regarding L_α, the molecular Werner band and additional atomic nitrogen triplet at 120.0 nm compared to calibration in hydrogen	
(d)	Absolute agreement within ±4 %	Absolute agreement within ±8 %
(e)	Absolute agreement within ±17 %	For ≤1 Pa absolute agreement within ±17 %, for >1 Pa deviation up to 42 %
(f)	Absolute agreement within ±15 %	Absolute agreement within ±30 %
(g)	Absolute agreement within ±7 %	For ≤1 Pa absolute agreement within ±8 %, increasing deviation with pressure up to 74 % at 10 Pa Effect: Vertical emission profile, additional pressure dependent emission above 113 nm due to broad transmission edge of MgF_2
(h)	Absolute agreement within ±12 %	For ≤1 Pa absolute agreement within ±12 %, increasing deviation with pressure up to 53 % at 10 Pa Effect: Vertical emission profile

Table I.2: Comments on the benchmark of the diode system in nitrogen/hydrogen (50:50) for (i) N_2, H_2, N & H lines (above 113 nm), (j) Second positive system.

#	Power scan (@1 Pa)	Pressure scan (@500 W)
(i)	Absolute agreement within ±23 %	For ≤1 Pa absolute agreement within ±23 %, increasing deviation with pressure up to 63 % at 10 Pa Effect: Vertical emission profile
(j)	Absolute agreement within ±4 %	For ≤3 Pa absolute agreement within ±19 %, increasing deviation with pressure up to 81 % at 10 Pa Effect: Vertical emission profile

I.2 Hydrogen/oxygen (85:15)

The calbration of the OH band (with the 313BP filter) was directly calibrated at the hydrogen/oxygen mixture at 1 Pa with 900 W and 1100 W, respectively.

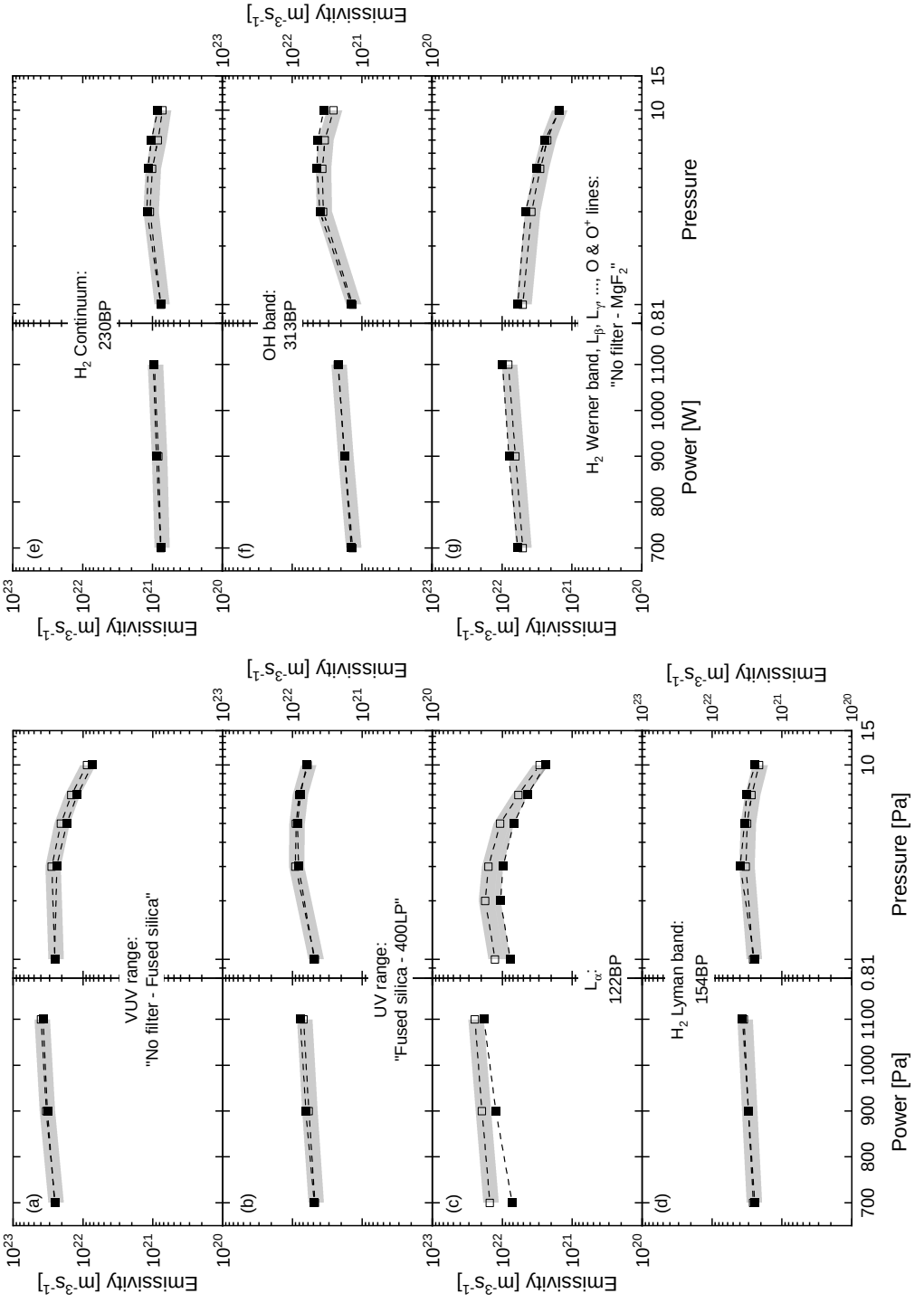

Figure I.3: Benchmark of the diode system in hydrogen/oxygen mixture (85:15) at *PlanICE* (power scan: 1 Pa, pressure scan: 700 W).

Table I.3: Comments on the benchmark of the diode system in hydrogen/oxygen (85:15) for (a) the VUV range, O & O^+ lines (b) the UV range, (c) L_α, (d) H_2 Lyman band, (e) H_2 Continuum, (f) OH band, (g) H_2 Werner series, L_β, L_γ, ..., O & O^+ lines.

#	Power scan (@1 Pa)	Pressure scan (@700 W)
(a)	Absolute agreement within ±7 %	Absolute agreement within ±18 %
(b)	Absolute agreement within ±11 %	Absolute agreement within ±11 %
(c)	Absolute deviation between -26 % and -52 %	Absolute agreement within -40 % whereas deviation is decreasing with increasing pressure Effect: Vertical emission profile
	Effect: Deviating intensity distribution within FWHM of filter transmission (taken from manufacturer) regarding L_α, the molecular Werner band and the atomic oxygen line at 115.2 nm compared to calibration in hydrogen	
(d)	Absolute agreement within ±5 %	Absolute agreement within ±21 %
(e)	Absolute agreement within ±7 %	Absolute agreement within ±24 %
(f)	Absolute agreement within ±4 %	For ≤5 Pa absolute agreement within ±19 %, increasing deviation with pressure up to 37 % at 10 Pa due to vertical emission profile Effect: Vertical emission profile
(g)	Absolute agreement within ±23 %	Absolute agreement within ±23 %

I.3 Nitrogen/oxygen (80:20)

The NO band (with the 230BP filter) was directly calibrated at the nitrogen/oxygen mixture at 1 Pa with 500 W and 700 W, respectively.

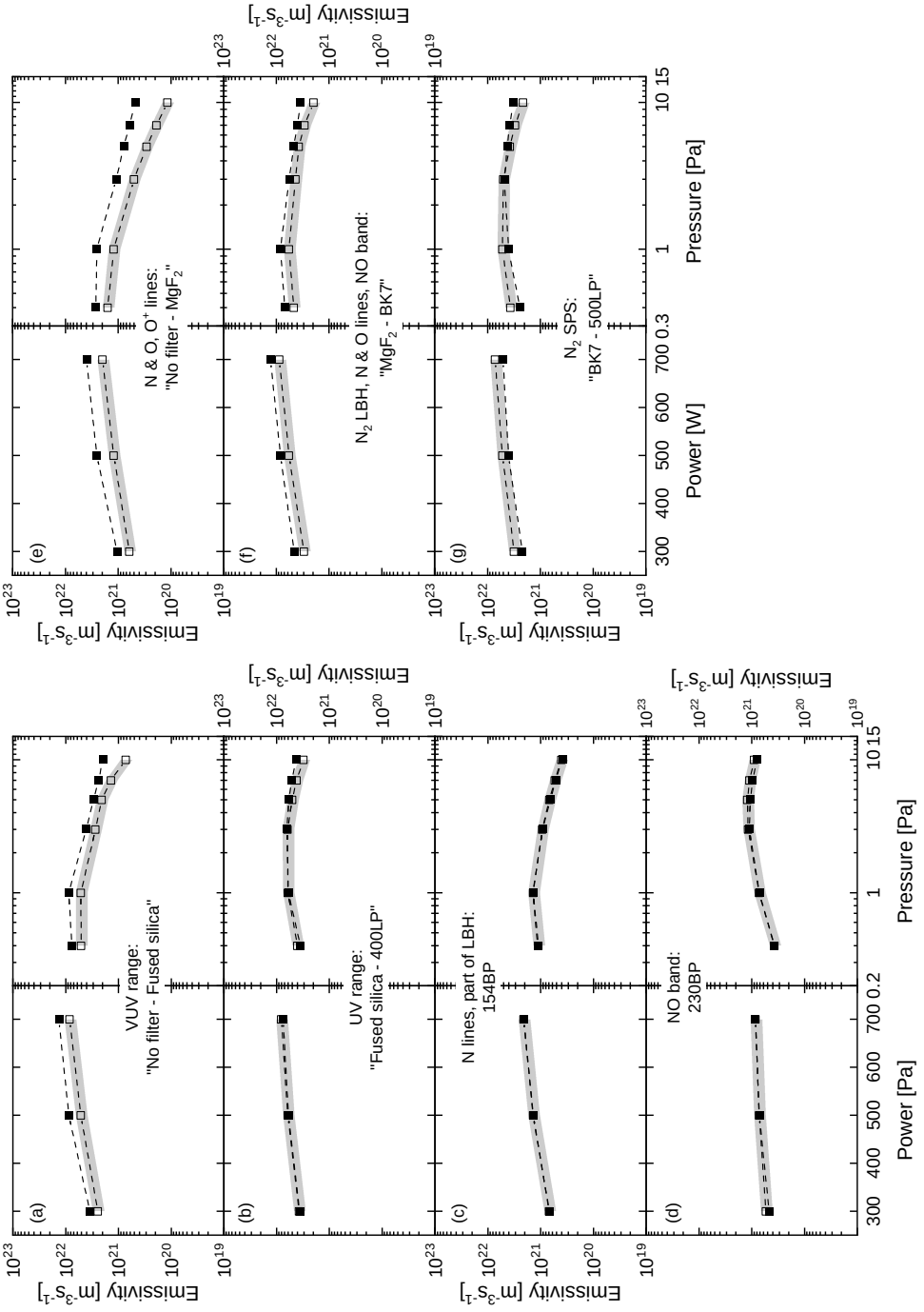

Figure I.4: Benchmark of the diode system in nitrogen/oxygen mixture (80:20) at *PlanICE* (power scan: 1 Pa, pressure scan: 500 W). "LBH" refers to the Lyman-Birge-Hopfield system of N_2, "SPS" corresponds to the Second positive system of N_2.

Table I.4: Comments on the benchmark of the diode system in nitrogen/oxygen (80:20) for (a) the VUV range (b) the UV range, (c) N lines, part of Lyman-Birge-Hopfield system of N_2, (d) NO band, (e) N, O & O^+ lines.

#	Power scan (@1 Pa)	Pressure scan (@500 W)
(a)	Relative agreement within ±17 %, absolute deviation between +40 % and +68 % Effect: ??	For ≤7 Pa relative agreement within ±15 %, at 10 Pa relative deviation +62 %, absolute deviation between +44 % and +172 %
(b)	Absolute agreement within ±8 %	For ≤7 Pa absolute agreement within ±24 %, increasing deviation with pressure up to 39 % at 10 Pa Effect: Vertical emission profile together with different viewing volumes of diagnostics
(c)	Absolute agreement within ±4 %	Absolute agreement within ±6 %
(d)	Absolute agreement within ±13 %	Absolute agreement within ±13 %
(e)	Relative agreement within ±18 %, absolute deviation between +68 % and +103 % Effect: ??	For ≤3 Pa relative agreement within ±19 %, absolute deviation between +65 % and +301 %, relative and absolute deviation increasing with pressure Effect: Vertical emission profile together with different viewing volumes, additional pressure dependent emission above 113 nm due to broad transmission edge of MgF_2

Table I.5: Comments on the benchmark of the diode system in nitrogen/oxygen (80:20) for (f) Lyman-Birge-Hopfield system of N_2, N & O lines, NO band, (g) Second positive system of N_2.

#	Power scan (@1 Pa)	Pressure scan (@500 W)
(f)	Relative agreement within ±6 %, absolute deviation between +44 % and 52 % Effect: ??	Relative agreement within ±23 %, absolute deviation between +25 % and +77 % without obvious pressure dependence
(g)	Relative agreement within ±10 %, absolute deviation between +24 % and +30 % Effect: ??	For ≤3 Pa relative agreement within ±26 increasing with pressure up to +102 %, absolute deviation between +4 % and +54 % without obvious pressure dependence Effect: Vertical emission profile together with different viewing volumes of diagnostics

Bibliography

[ABR57] J. E. Allen, R. L. F. Boyd, and P. Reynolds. The Collection of Positive Ions by a Probe Immersed in a Plasma. *Proceedings of the Physical Society. Section B*, 70:297–304, 1957.

[All92] J. E. Allen. Probe theory - the orbital motion approach. *Physica Scripta*, 45:497–503, 1992.

[Bal] *Plasma Prozess Monitor PPM421.* 9496 Balzers, Liechtenstein. BG 800 411 BD/1 (9409), publication date not given.

[Beh91] K. Behringer. Diagnostics and modelling of ECRH microwave discharges. *Plasma Physics and Controlled Fusion*, 33:997–1028, 1991.

[Beh98] K. Behringer. Escape Factors for Line Emission and Population Calculations. *IPP-Report 10/11, Max-Planck-Institut für Plasmaphysik, Garching*, 1998.

[Ber02] P. F. Bernath. *Handbook of Molecular Physics and Quantum Chemistry, Volume 3: Molecules in the Physicochemical Environment: Spectroscopy, Dynamics and Bulk Properties.* John Wiley & Sons, Ltd, 2002.

[BHAW07] N. Bibinov, H. Halfmann, P. Awakowicz, and K. Wiesemann. Relative and absolute intensity calibrations of a modern broadband echelle spectrometer. *Measurement Science and Technology*, 18:1327–1337, 2007.

[BHH+83] K. Boller, R.-P. Haelbich, H. Hogrefe, W. Jark, and C. Kunz. Investigation of carbon contamination of mirror surfaces exposed to synchrotron radiation. *Nuclear Instruments and Methods in Physics Research*, 208:273 – 279, 1983.

[BLC+14] J. B. Boffard, C. C. Lin, C. Culver, S. Wang, A. E. Wendt, S. Radovanov, and H. Persing. Comparison of surface vacuum ultraviolet emissions with resonance level number densities. I. Argon plasmas. *Journal of Vacuum Science & Technology A*, 32:021304, 2014.

[BRF17] S. Briefi, D. Rauner, and U. Fantz. Determination of the rotational population of H_2 and D_2 including high-N states in low temperature plasmas via the Fulcher-α transition. *Journal of Quantitative Spectroscopy and Radiative Transfer*, 187:135 – 144, 2017.

[Bri11] S. Briefi. *Spectroscopic Investigation of Indium Halides as Substitutes of Mercury in Low Pressure Discharges for Lighting Applications*. PhD thesis, University of Augsburg, 2011.

[Bri19] S. Briefi. Max-Planck-Institut für Plasmaphysik, Garching, Germany. *Personal communication*, 2019.

[Bri20] S. Briefi. Max-Planck-Institut für Plasmaphysik, Garching, Germany. *Personal communication*, 2020.

[BSS+81] A. L. Broadfoot, B. R. Sandel, D. E. Shemansky, J. B. Holberg, G. R. Smith, D. F. Strobel, J. C. McConnell, S. Kumar, D. M. Hunten, S. K. Atreya, T. M. Donahue, H. W. Moos, J. L. Bertaux, J. E. Blamont, R. B. Pomphrey, and S. Linick. Extreme Ultraviolet Observations from Voyager 1 Encounter with Saturn. *Science*, 212:206–211, 1981.

[BSSL14] P. J. Bruggeman, N. Sadeghi, D. C. Schram, and V. Linss. Gas temperature determination from rotational lines in non-equilibrium plasmas: a review. *Plasma Sources Science and Technology*, 23:023001, 2014.

[CB11] P. Chabert and N. Braithwaite. *Physics of Radio-Frequency Plasmas*. Cambridge University Press, Cambridge, 2011.

[CC03] F. F. Chen and J. P. Chang. *Lecture notes of PRINCIPLES OF PLASMA PROCESSING*. Kluwer Academic/Plenum Publishers, New York, 2003.

[CCC16] Y. J. Cho, H. Cha, and H. S. Chang. Plasma nitridation of atomic layer deposition (ALD) Al_2O_3 by NH_3 in plasma-enhanced chemical vapor deposition (PECVD) for silicon solar cell. *Surface and Coatings Technology*, 307:1096–1099, 2016. The 10th Asian-European International Conference on Plasma Surface Engineering.

[CFF20a] S. Cristofaro, R. Friedl, and U. Fantz. Correlation of Cs flux and work function of a converter surface during long plasma exposure for negative ion sources in view of ITER. *Plasma Research Express*, 2:035009, 2020.

[CFF20b] S. Cristofaro, R. Friedl, and U. Fantz. Effect of a low pressure low temperature hydrogen plasma on the work function of europium. *Journal of Vacuum Science & Technology A*, 38:063002, 2020.

[Cha87] P. J. Chantry. A simple formula for diffusion calculations involving wall reflection and low density. *Journal of Applied Physics*, 62:1141–1148, 1987.

[CP20] J. E. Caplinger and G. P. Perram. The importance of cascade emission and metastable excitation in modeling strong atomic oxygen lines in laboratory plasmas. *Plasma Sources Science and Technology*, 29:015011, 2020.

[DC62] G. H. Dieke and H. M. Crosswhite. The ultraviolet bands of OH Fundamental data. *Journal of Quantitative Spectroscopy and Radiative Transfer*, 2:97 – 199, 1962.

[Dem16] W. Demtröder. *Experimentalphysik 3: Atome, Moleküle und Festkörper*. Springer Verlag Berlin Heidelberg, 2016.

[DGF+88] K. Danzmann, M. Günther, J. Fischer, M. Kock, and M. Kühne. High current hollow cathode as a radiometric transfer standard source for the extreme vacuum ultraviolet. *Appl. Opt.*, 27:4947–4951, 1988.

[DH66] R. D. Craig and E. H. Harden. The interpretation of mass spectra in vacuum measurement. *Vacuum*, 16:67–73, 1966.

[DK13] V. M. Donnelly and A. Kornblit. Plasma etching: Yesterday, today, and tomorrow. *Journal of Vacuum Science & Technology A*, 31:050825, 2013.

[DKK] *Operating Manual, High Current Hollow Cathode, DKK 042.* Institut für Atom- und Molekülphysik, Abteilung Plasmaphysik der Universität Hannover, Hannover, Germany. Publication date not given.

[Dru30] M. J. Druyvesteyn. Der Niedervoltbogen. *Zeitschrift für Physik*, 64:781—798, 1930.

[DV57] G. J. Dienes and G. H. Vineyard. *Radiation effects in solids*, volume II of *Monographs in physics and astronomy*. Interscience Publishers Inc., New York, 1957.

[Eck19] M. Eckerskorn. Max-Planck-Institut für Plasmaphysik, Garching, Germany. *Personal communication*, 2019.

[F18] F. Chen F. *Introduction to Plasma Physics and Controlled Fusion*. Springer International Publishing Switzerland, 2016, corrected publication 2018.

[Fan04] U. Fantz. Emission Spectroscopy of Molecular Low Pressure Plasmas. *Contributions to Plasma Physics*, 44:508–515, 2004.

[Fan06] U. Fantz. Basics of plasma spectroscopy. *Plasma Sources Science and Technology*, 15:S137–S147, 2006.

[FASB98] R. M. Frost, P. Awakowicz, H. P. Summers, and N. R. Badnell. Calculated cross sections and measured rate coefficients for electron-impact excitation of neutral and singly ionized nitrogen. *Journal of Applied Physics*, 84:2989–3003, 1998.

[FBA20] M. Fiebrandt, N. Bibinov, and P. Awakowicz. Determination of atomic oxygen state densities in a double inductively coupled plasma using optical emission and absorption spectroscopy and probe measurements. *Plasma Sources Science and Technology*, 29:045018, 2020.

[FBFBF21] C. Fröhler-Bachus, R. Friedl, S. Briefi, and U. Fantz. Absolute radiometric calibration of a VUV spectrometer in the wavelength range 46-300 nm. *Journal of Quantitative Spectroscopy and Radiative Transfer*, 259:107427, 2021.

[FCF18] R. Friedl, S. Cristofaro, and U. Fantz. Work function of Cs-free materials for enhanced H^- surface production. *AIP Conference Proceedings*, 2011:050009, 2018.

[FF17] R. Friedl and U. Fantz. Influence of H_2 and D_2 plasmas on the work function of caesiated materials. *Journal of Applied Physics*, 122:083304, 2017.

[FFBF22] R. Friedl, C. Fröhler-Bachus, and U. Fantz. A flexible diagnostic system for the quantification of VUV fluxes emitted from plasmas. *submited to: Meas. Sci. Techn.*, 2022.

[FHL+18] M. Fiebrandt, B. Hillebrand, J.-W. Lackmann, M. Raguse, R. Moeller, P. Awakowicz, and K. Stapelmann. Inactivation of B. subtilis spores by low pressure plasma—influence of optical filters and photon/particle fluxes on the inactivation efficiency. *Journal of Physics D: Applied Physics*, 51:045401, 2018.

[FK11] A. Fridman and L. A. Kennedy. *Plasma Physics and Engineering*. CRC Press, Taylor & Francis Group, Boca Raton, USA, 2011.

[FOA17] M. Fiebrandt, M. Oberberg, and P. Awakowicz. Comparison of Langmuir probe and multipole resonance probe measurements in argon, hydrogen, nitrogen, and oxygen mixtures in a double ICP discharge. *Journal of Applied Physics*, 122:013302, 2017.

[FRHK01] H. O. Funsten, S. M. Ritzau, R. W. Harper, and R. Korde. Response of 100% internal carrier collection efficiency silicon photodiodes to low-energy ions. *IEEE Transactions on Nuclear Science*, 48(6):1785–1789, 2001.

[Fri13] R. Friedl. *Experimental investigations on the caesium dynamics in H_2/D_2 low temperature plasmas*. PhD thesis, University of Augsburg, Augsburg, 2013.

[FSLM82] A. R. Filippelli, F. A. Sharpton, C. C. Lin, and R. E. Murphy. Production of atomic nitrogen emission by electron-impact dissociative excitation of nitrogen molecules. *The Journal of Chemical Physics*, 76:3597–3606, 1982.

[FSM+73] G. B. Fisher, W. E. Spicer, P. C. McKernan, V. F. Pereskok, and S. J. Wanner. A Standard for Ultraviolet Radiation. *Applied Optics*, 12:799–804, 1973.

[FSRK97] H. O. Funsten, D. M. Suszcynsky, S. M. Ritzau, and R. Korde. Response of 100% internal quantum efficiency silicon photodiodes to 200 eV-40 keV electrons. *IEEE Transactions on Nuclear Science*, 44:2561–2565, 1997.

[Fuj04] T. Fujimoto. *Plasma Spectroscopy*. Clarendon Press, Oxford, 2004.

[FW06] U. Fantz and D. Wünderlich. Franck-Condon factors, transition probabilities, and radiative lifetimes for hydrogen molecules and their isotopomeres. *Atomic Data and Nuclear Data Tables*, 92:853 – 973, 2006.

[GBMB08] A. Greiche, W. Biel, O. Marchuk, and R. Burhenn. Absolute intensity calibration of the Wendelstein 7-X high efficiency extreme ultraviolet overview spectrometer system. *Review of Scientific Instruments*, 79:093504, 2008.

[GD11] V. A. Godyak and V. I. Demidov. Probe measurements of electron-energy distributions in plasmas: what can we measure and how can we achieve reliable results? *Journal of Physics D: Applied Physics*, 44:233001, 2011.

[Gil65] F. R. Gilmore. Potential energy curves for N_2, NO, O_2 and corresponding ions. *Journal of Quantitative Spectroscopy and Radiative Transfer*, 5:369 – IN3, 1965.

[GLTM99] M. Galand, J. Lilensten, D. Toublanc, and S. Maurice. The Ionosphere of Titan: Ideal Diurnal and Nocturnal Cases. *Icarus*, 140:92–105, 1999.

[GMK+99] P. T. Gallagher, M. Mathioudakis, F. P. Keenan, K. J. H. Phillips, and K. Tsinganos. The radial and angular variation of the electron

density in the solar corona. *The Astrophysical Journal*, 524(2):L133–L137, 1999.

[GPA92] V. A. Godyak, R. B. Piejak, and B. M. Alexandrovich. Measurement of electron energy distribution in low-pressure RF discharges. *Plasma Sources Science and Technology*, 1(1):36–58, mar 1992.

[GPA93] V. A. Godyak, R. B. Piejak, and B. M. Alexandrovich. Probe diagnostics of non-Maxwellian plasmas. *Journal of Applied Physics*, 73:3657–3663, 1993.

[GSE08] O. Gabriel, D. C. Schram, and R. Engeln. Formation and relaxation of rovibrationally excited h_2 molecules due to plasma-surface interaction. *Phys. Rev. E*, 78:016407, 2008.

[Hei18] A. Heiler. Messung der Elektronenenergieverteilung eines induktiv gekoppelten Niederdruckplasmas mittels AC-Sondendiagnostik. Master's thesis, University of Augsburg, Augsburg, 2018.

[HFF+15] B. Heinemann, M. Fröschle, H.-D. Falter, U. Fantz, P. Franzen, W. Kraus, R. Nocentini, R. Riedl, and B. Ruf. Upgrade of the BATMAN test facility for H^- source development. *AIP Conference Proceedings*, 1655:060003, 2015.

[HFF+21] A. Heiler, R. Friedl, U. Fantz, R. Nocentini, and M. Sasao. Work function behavior of a biased C12A7 electride in low temperature hydrogen plasmas. *AIP Conference Proceedings*, 2373:020004, 2021.

[HFK+17] B. Heinemann, U. Fantz, W. Kraus, L. Schiesko, C. Wimmer, D. Wünderlich, F. Bonomo, M. Fröschle, R. Nocentini, and R. Riedl. Towards large and powerful radio frequency driven negative ion sources for fusion. 19:015001, 2017.

[HH18] K. P. Huber and G. H. Herzberg. Constants of Diatomic Molecules. In P. J. Linstrom and W. G. Mallard, editors, *NIST Chemistry WebBook, NIST Standard Reference Database Number 69*. National Institute of Standards and Technology, Gaithersburg MD, 20899, 2018. data prepared by Jean W. Gallagher and Russell D. Johnson, III; Retrieve Date: 28.05.2020.

[HKHW02] J. Hollandt, M. Kühne, M. C. E. Huber, and B. Wende. Source Standards for the Radiometric Calibration of Astronomical Instruments in the VUV Spectral Range Traceable to the Primary Standard BESSY. In A. Pauluhn, M.C.E. Huber, and R. von Steiger, editors, *The Radiometric Calibration of SOHO, ESA SR-002*, pages 51 –68. International Space Science Institute Bern, (2002).

[HKSS08] R. Hippler, H. Kersten, M. Schmidt, and K. H. Schoenbach, editors. *Low temperature plasmas*, volume 2: Fundamentals, Technologies, and Techniques. WILEY-VCH Verlag GmbH & Co. KGaA, Weinheim, 2008.

[HKW94] J. Hollandt, M. Kühne, and B. Wende. High-current hollow-cathode source as a radiant intensity standard in the 40–125-nm wavelength range. *Applied Optics*, 33:68–74, 1994.

[HL65] R. H. Huddlestone and S. L. Leonard. *Plasma diagnostic techniques*. Academic Press, New York, London, 1965.

[Hoh05] *Operation Instructions - Hollow cathode discharge system (Version 01-07-2005)*. Institut für Plasmaphysik, Forschungszentrum Jülich GmbH, Jülich, Germany, 2005.

[Hol51] T. Holstein. Imprisonment of Resonance Radiation in Gases. II. *Physical Review*, 83:1159–1168, 1951.

[Hop94] J. Hopwood. Planar RF induction plasma coupling efficiency. *Plasma Sources Science and Technology*, 3:460–464, 1994.

[Hor83] C. M. Horwitz. Radio frequency sputtering — the significance of power input. *Journal of Vacuum Science & Technology A*, 1:1795–1800, 1983.

[Hur19] A. Hurlbatt. Max-Planck-Institut für Plasmaphysik, Garching, Germany. *Personal communication*, 2019.

[Hur20] A. Hurlbatt. Unintuitive behaviour of fibre coupled collimating optics used for plasma emission observations. *Journal of Physics D: Applied Physics*, 53:125204, 2020.

[Igl19] E. Iglesias. Institute for electrical engineering and plasma technology (aept, ruhr-universität bochum). *Personal communication*, 2019.

[IHM+19] E. J. Iglesias, A. Hecimovic, F. Mitschker, M. Fiebrandt, N. Bibinov, and P. Awakowicz. Ultraviolet/vacuum-ultraviolet emission from a high power magnetron sputtering plasma with an aluminum target. *Journal of Physics D: Applied Physics*, 53:055202, 2019.

[II90] Y. Itikawa and A. Ichimura. Cross Sections for Collisions of Electrons and Photons with Atomic Oxygen. *Journal of Physical and Chemical Reference Data*, 19:637–651, 1990.

[IMF+17] E. J. Iglesias, F. Mitschker, M. Fiebrandt, N. Bibinov, and P. Awakowicz. In situ measurement of VUV/UV radiation from low-pressure microwave-produced plasma in Ar/O_2 gas mixtures. *Measurement Science and Technology*, 28:085501, 2017.

[Int91] International Union of Pure and Applied Chemistry (IUPAC). Isotopic composition of the elements 1989. *Pure and Applied Chemistry*, 63, 1991.

[Iro79] F. E. Irons. The escape factor in plasma spectroscopy-I. the escape factor defined and evaluated. *Journal of Quantitative Spectroscopy and Radiative Transfer*, 22:1 – 20, 1979.

[KBF+00] S. Kumar, M. J. Baldwin, M. P. Fewell, S. C. Haydon, K. T. Short, G. A. Collins, and J. Tendys. The effect of hydrogen on the growth of the nitrided layer in r.f.-plasma-nitrided austenitic stainless steel AISI 316. *Surface and Coatings Technology*, 123:29–35, 2000.

[KCF+18] M. Kubkowska, A. Czarnecka, T. Fornal, M. Gruca, S. Jabłoński, N. Krawczyk, L. Ryć, R. Burhenn, B. Buttenschön, B. Geiger, O. Grulke, A. Langenberg, O. Marchuk, K. J. McCarthy, U. Neuner, D. Nicolai, N. Pablant, B. Schweer, H. Thomsen, Th. Wegner, P. Drews, K.-P. Hollfeld, C. Killer, Th. Krings, G. Offermanns, G. Satheeswaran, and F. Kunkel. Plasma impurities observed by a pulse height analysis diagnostic during the divertor campaign of the Wendelstein 7-X stellarator. *Review of Scientific Instruments*, 89:10F111, 2018.

[KD80] K. Katsonis and H. W. Drawin. Transition probabilities for argon(I). *Journal of Quantitative Spectroscopy and Radiative Transfer*, 23:1 – 55, 1980.

[Kov69] I. Kovács. *ROTATIONAL STRUCTURE IN THE SPECTRA OF DIATOMIC MOLECULES*. Adam Hilger Ltd, London, 1969.

[KPC+03] R. Korde, C. Prince, D. Cunningham, R. E. Vest, and E. Gullikson. Present status of radiometric quality silicon photodiodes. *Metrologia*, 40:S145–S149, 2003.

[KRR+98] P. Kuschnerus, H. Rabus, M. Richter, F. Scholze, L. Werner, and G. Ulm. Characterization of photodiodes as transfer detector standards in the 120 nm to 600 nm spectral range. *Metrologia*, 35:355–362, 1998.

[Kru72] P. H. Krupenie. The Spectrum of Molecular Oxygen. *Journal of Physical and Chemical Reference Data*, 1:423–534, 1972.

[KTK+15] J. Komppula, O. Tarvainen, T. Kalvas, H. Koivisto, R. Kronholm, J. Laulainen, and P. Myllyperkiö. VUV irradiance measurement of a 2.45 GHz microwave-driven hydrogen discharge. *Journal of Physics D: Applied Physics*, 48:365201, 2015.

[Kun09] H.-J. Kunze. *Introduction to Plasma Spectroscopy*. Springer-Verlag Berlin Heidelberg, 2009.

[KYRa19a] A. Kramida, Y. Ralchenko, J. Reader, and and NIST ASD Team. NIST Atomic Spectra Database (ver. 5.7.1), [Online]. Available: https://physics.nist.gov/asd [2020, July 13]. National Institute of Standards and Technology, Gaithersburg, MD., 2019.

[KYRa19b] A. Kramida, Y. Ralchenko, J. Reader, and and NIST ASD Team. NIST Atomic Spectra Database (ver. 5.7.1), [Online]. Available: https://physics.nist.gov/asd [2020, June 5]. National Institute of Standards and Technology, Gaithersburg, MD., 2019.

[KYRa19c] A. Kramida, Y. Ralchenko, J. Reader, and and NIST ASD Team. NIST Atomic Spectra Database (ver. 5.7.1), [Online]. Available: https://physics.nist.gov/asd [2020, May 28]. National Institute of Standards and Technology, Gaithersburg, MD., 2019.

[KYRa19d] A. Kramida, Y. Ralchenko, J. Reader, and and NIST ASD Team. NIST Atomic Spectra Database (ver. 5.7.1), [Online]. Available: https://physics.nist.gov/asd [2020, August 14]. National Institute of Standards and Technology, Gaithersburg, MD., 2019.

[KYRa19e] A. Kramida, Yu. Ralchenko, J. Reader, and and NIST ASD Team. NIST Atomic Spectra Database (ver. 5.7.1), [Online]. Available: https://physics.nist.gov/asd [2020, August 5]. National Institute of Standards and Technology, Gaithersburg, MD., 2019.

[LK77] A. Lofthus and P. H. Krupenie. The spectrum of molecular nitrogen. *Journal of Physical and Chemical Reference Data*, 6:113–307, 1977.

[LL05] M. A. Lieberman and A. J. Lichtenberg. *Principles of Plasma Discharges and Materials Processing*. John Wiley and Sons, Inc., Hoboken, New Jersey, 2005.

[LOU79] B. P. Lavrov, V. N. Ostrovskii, and V. I. Ustimov. Rotational transitions in the excitation of electronic states of molecules by electron impact. *Journal of Experimental and Theoretical Physics*, 49:772–776, 1979. Russian original published in Zh. Eksp. Teor. Fiz., Vol. 76, No. 5, p. 1521-1529, 1979.

[LRR+17] D. V. Lopaev, T. V. Rakhimova, A. T. Rakhimov, A. I. Zotovich, S. M. Zyryanov, and M. R. Baklanov. Silicon dioxide and low-k material sputtering in dual frequency inductive discharge by argon ions with energies from 16 to 200 eV. *Journal of Physics D: Applied Physics*, 51:02LT02, 2017.

[LWY01] S. Lerouge, M. R. Wertheimer, and L'H. Yahia. Plasma Sterilization: A Review of Parameters, Mechanisms, and Limitations. *Plasmas and Polymers*, 6:S175–S188, 2001.

[Mar96] M. Marr. Messung der spektralen Bestrahlungsstärke an einer D_2-Lampe. Technical report, Heraeus Noblelight GmbH, 1996.

[MBC+02] M. Moisan, J. Barbeau, M.-C. Crevier, J. Pelletier, N. Philip, and B. Saoudi. Plasma sterilization. Methods and mechanisms. *Pure and Applied Chemistry*, 74:349–358, 2002.

[MBVR07] B. Moine, G. Bizarri, B. Varrel, and J.-Y. Rivoire. VUV-extended measurements of quantum efficiency of sodium salicylate and of some NBS standard phosphors. *Optical Materials*, 29:1148–1152, 2007.

[McP86] *Instruction Manual, Model 225, 1-meter scanning monochromator*. McPherson Instrument, Acton, Massachusetts, USA, 1986. year from personal communication.

[MDCK+08] P. McNeely, S. V. Dudin, S. Christ-Koch, U. Fantz, and the NNBI Team. A Langmuir probe system for high power RF-driven negative ion sources on high potential. *Plasma Sources Science and Technology*, 18:014011, 2008.

[Mei00] S. Meir. Spektroskopische Diagnostik im VUV/UV und sichtbaren Spektralbereich . Master's thesis, University of Augsburg, Augsburg, 2000.

[Min73] L. Minnhagen. Spectrum and the energy levels of neutral argon, Ar I. *Journal of the Optical Society of America*, 63:1185–1198, 1973.

[MMS12] L. Maaloul, S. Morel, and L. Stafford. Populations of metastable and resonant argon atoms in radio frequency magnetron plasmas used for deposition of indium-zinc-oxide films. *Journal of Vacuum Science & Technology A*, 30(2):021301, 2012.

[Möl93] W. Möller. Plasma and surface modeling of the deposition of hydrogenated carbon films from low-pressure methane plasmas. *Applied Physics A*, 56:527 – 546, 1993.

[MSL26] H. M. Mott-Smith and I. Langmuir. The Theory of Collectors in Gaseous Discharges. *Physical Review*, 28:727–763, 1926.

[MTG72] W. T. Miles, R. Thompson, and A. E. S. Green. Electron-Impact Cross Sections and Energy Deposition in Molecular Hydrogen. *Journal of Applied Physics*, 43:678–686, 1972.

[Mül90] R. Müller. *Rauschen*, volume 15 of *Halbleiter-Elektronik*. Springer-Verlag Berlin, Heidelberg, 2nd edition, 1970, 1990.

[Mum72] M. J. Mumma. Molecular Branching-Ratio Method for Intensity Calibration of Optical Systems in the Vacuum Ultraviolet. *Journal of the Optical Society of America*, 62:1459–1466, 1972.

[MW02] W.C. Martin and W.L. Wiese. Atomic, Molecular, and Optical Physics Handbook (version 2.2), [Online]. Available: https://www.nist.gov/pml/atomic-spectroscopy-compendium-basic-ideas-notation-data-and-formulas [2021, March 31]. National Institute of Standards and Technology, Gaithersburg, MD, 2002.

[MZ71] M. J. Mumma and E. C. Zipf. Dissociative Excitation of Vacuum-Ultraviolet Emission Features by Electron Impact on Molecular Gases. II. N_2. *The Journal of Chemical Physics*, 55:5582–5588, 1971.

[NZ94] E. E. Nikitin and R. N. Zare. Correlation diagrams for Hund's coupling cases in diatomic molecules with high rotational angular momentum. *Molecular Physics*, 82:85–100, 1994.

[Opt19] *Data sheet of AXUV100G*. Opto Diode, 1260 Calle Suerte, Camarillo, CA 93012 USA, 2019. www.optodiode.com (07.05.2020).

[Pen22] C. Penniman. Pelham Research Optical LLC. *Personal communication*, 2022.

[Pfe] *Plasma Prozess Monitor PPM422*. Pfeiffer Vacuum GmbH, Asslar. BG 805 813 BD (0306), publication date not given.

[Pfe13] Pfeiffer Vacuum GmbH. The Vacuum Technology Book Volume II. Berliner Strasse 43, 35614 Asslar, Germany, 2013.

[PG76] R. W. B. Pearse and A. G. Gaydon. *The identification of molecular spectra*. Chapman and Hall Ltd., London; John Wiley & Sons, Inc., New York, 4th edition, 1976.

[PRZ58] W. Paul, H. P. Reinhard, and U. von Zahn. Das elektrische Massenfilter als Massenspektrometer und Isotopentrenner. *Zeitschrift für Physik*, 152, 1958.

[Rac42] G. Racah. On a New Type of Vector Coupling in Complex Spectra. *Physical Review*, 61:537–537, 1942.

[Rau18] D. Rauner. *Efficiency of RF plasma generation for fusion relevant sources*. PhD thesis, University of Augsburg, Augsburg, 2018.

[RBF17] D. Rauner, S. Briefi, and U. Fantz. RF power transfer efficiency of inductively coupled low pressure H_2 and D_2 discharges. *Plasma Sources Science and Technology*, 26:095004, 2017.

[Ric97] A Ricard. The production of active plasma species for surface treatments. *Journal of Physics D: Applied Physics*, 30:2261–2269, 1997.

[RRM+02] T. Roschek, T. Repmann, J. Müller, B. Rech, and H. Wagner. Comprehensive study of microcrystalline silicon solar cells deposited at high rate using 13.56 MHz plasma-enhanced chemical vapor deposition. *Journal of Vacuum Science & Technology A*, 20:492–498, 2002.

[RRM+13] T. V. Rakhimova, A. T. Rakhimov, Yu. A. Mankelevich, D. V. Lopaev, A. S. Kovalev, A. N. Vasil'eva, S. M. Zyryanov, K. Kurchikov, O. V. Proshina, D. G. Voloshin, N. N. Novikova, M. B. Krishtab, and M. R. Baklanov. Low-k films modification under EUV and VUV radiation. *Journal of Physics D: Applied Physics*, 47:025102, dec 2013.

[Sam67] J. A. R. Samson. *Techniques of Vacuum Ultraviolet Spectroscopy*. John Wiley and Sons, Inc., New York, 1967.

[SC94] I. D. Sudit and F. F. Chen. RF compensated probes for high-density discharges. *Plasma Sources Science and Technology*, 3:162–168, 1994.

[Sch40] E. G. Schneider. An Estimate of the Absorption of Air in the Extreme Ultraviolet. *Journal of the Optical Society of America*, 30:128–132, 1940.

[Se67] H. Z. Sar-el. Cylindrical Capacitor as an Analyzer I. Nonrelativistic Part. *Review of Scientific Instruments*, 38:1210–1216, 1967.

[SE00] J. A. Samson and D. Ederer. *VACUUM ULTRAVIOLET SPECTROSCOPY I*. Academic Press, San Diego, 2000.

[Sei46] F. Seitz. Color Centers in Alkali Halide Crystals. *Reviews of Modern Physics*, 18:384–408, 1946.

[Sei54] F. Seitz. Color Centers in Alkali Halide Crystals. II. *Reviews of Modern Physics*, 26:7–94, 1954.

[SFAP01] P. Scheubert, U. Fantz, P. Awakowicz, and H. Paulin. Experimental and theoretical characterization of an inductively coupled plasma source. *Journal of Applied Physics*, 90:587–598, 2001.

[SFF+06] E. Speth, H. D. Falter, P. Franzen, U. Fantz, M. Bandyopadhyay, S. Christ, A. Encheva, M. Fröschle, D. Holtum, B. Heinemann, W. Kraus, A. Lorenz, C. Martens, P. McNeely, S. Obermayer, R. Riedl, R. Süss, A. Tanga, R. Wilhelm, and D. Wünderlich. Overview of the RF source development programme at IPP Garching. *Nuclear Fusion*, 46(6):S220–S238, 2006.

[Sha70] T. E. Sharp. Potential-energy curves for molecular hydrogen and its ions. *Atomic Data and Nuclear Data Tables*, 2:116–169, 1970.

[Sha71] T. E. Sharp. Erratum. *Atomic Data and Nuclear Data Tables*, 3:299, 1971.

[Sie15] M. Siebenhütter. Simulation von Stickstoff Molekülspektren zur Plasmadiagnostik. Master's thesis, University of Augsburg, Augsburg, 2015.

[SRN+12] H. Sinha, H. Ren, M. T. Nichols, J. L. Lauer, M. Tomoyasu, N. M. Russell, G. Jiang, G. A. Antonelli, N. C. Fuller, S. U. Engelmann, Q. Lin, V. Ryan, Y. Nishi, and J. L. Shohet. The effects of vacuum ultraviolet radiation on low-k dielectric films. *Journal of Applied Physics*, 112:111101, 2012.

[SRP+14] K. C. Sabat, P. Rajput, R. K Paramguru, B. Bhoi, and B. K. Mishra. Reduction of Oxide Minerals by Hydrogen Plasma: An Overview. *Plasma Chemistry and Plasma Processing*, 34:1–23, 2014.

[SS70] J. D. Swift and M. J. R. Schwar. *Electrical Probes for Plasma Diagnostics*. ILIFFE BOOKS LTD., London, 1970.

[SSC+85] M. B. Schulman, F. A. Sharpton, S. Chung, C. C. Lin, and L. W. Anderson. Emission from oxygen atoms produced by electron-impact dissociative excitation of oxygen molecules. *Physical Review A*, 32:2100–2116, 1985.

[Sum04] H. P. Summers. The ADAS User Manual, version 2.6. Technical report, University of Strathclyde, 2004. http://www.adas.ac.uk.

[SWF18] L. Schiesko, C. Wimmer, and U. Fantz. Langmuir probe investigations of different magnetic filter field configurations at BATMAN upgrade. *AIP Conference Proceedings*, 2052:040006, 2018.

[SZDE12] H. Shin, W. Zhu, V. M. Donnelly, and D. J. Economou. Surprising importance of photo-assisted etching of silicon in chlorine-containing plasmas. *Journal of Vacuum Science & Technology A*, 30:021306, 2012.

[TGYH11] M. J. Titus, D. B. Graves, Y. Yamaguchi, and E. A. Hudson. Effects of vacuum ultraviolet photons, ion energy and substrate temperature on line width roughness and RMS surface roughness of patterned 193 nm photoresist. *Journal of Physics D: Applied Physics*, 44:085204, 2011.

[TH88] S. S. Tayal and R. J. W. Henry. Electron-impact excitation of atomic oxygen. *Physical Review A*, 38:5945–5948, 1988.

[Tho15] R. Thornagel. Kalibrierschein Deuterium-Lampe L9841/SN HY2739 Gesch.-Zeichen 7.1-1.1-15-03. Technical report, Physikalisch-Technische Bundesanstalt Braunschweig und Berlin, 2015.

[TL29] L. Tonks and I. Langmuir. A General Theory of the Plasma of an Arc. *Physical Review*, 34:876–922, 1929.

[TLJ99] A. P. Thorne, U. Litzén, and S. Johansson. *Spectrophysics - Principles and Applications*. Springer-Verlag, Berlin, Heidelberg, 1999.

[VHU99] I. Velchev, W. Hogervorst, and W. Ubachs. Precision VUV spectroscopy of Ar I at 105 nm. *Journal of Physics B: Atomic, Molecular and Optical Physics*, 32:L511–L516, 1999.

[vRVG+07] G. J. van Rooij, V. P. Veremiyenko, W. J. Goedheer, B. de Groot, A. W. Kleyn, P. H. M. Smeets, T. W. Versloot, D. G. Whyte, R. Engeln, D. C. Schram, and N. J. Lopes Cardozo. Extreme hydrogen plasma densities achieved in a linear plasma generator. *Applied Physics Letters*, 90:121501, 2007.

[VSE04] P. Vankan, D. C. Schram, and R. Engeln. High rotational excitation of molecular hydrogen in plasmas. *Chemical Physics Letters*, 400(1):196 – 200, 2004.

[WBFF21] D. Wünderlich, S. Briefi, R. Friedl, and U. Fantz. Emission spectroscopy of negative hydrogen ion sources: From VUV to IR. *Review of Scientific Instruments*, 92:123510, 2021.

[WBHF87] R. C. Wetzel, F. A. Baiocchi, T. R. Hayes, and R. S. Freund. Absolute cross sections for electron-impact ionization of the rare-gas atoms by the fast-neutral-beam method. *Physical Review A*, 35:559–577, 1987.

[WF15] D. Wünderlich and U. Fantz. Emission of photoelectrons and their impact on the plasma sheath in hydrogen plasmas. *XXXII International Conference on Phenomena in Ionized Gases (ICPIG)*, 2015. Iasi, Romania.

[WF16] D. Wünderlich and U. Fantz. Evaluation of State-Resolved Reaction Probabilities and Their Application in Population Models for He, H, and H_2. *Atoms*, 4, 2016.

[WRA+01] J. R. Woodworth, M. E. Riley, V. A. Amatucci, T. W. Hamilton, and B. P. Aragon. Absolute intensities of the vacuum ultraviolet spectra in oxide etch plasma processing discharges. *Journal of Vacuum Science & Technology A*, 19:45–55, 2001.

[Wün04] D. Wünderlich. *Berechnung von Teilchendichten für die Diagnostik an Niedertemperaturplasmen.* PhD thesis, University of Augsburg, Augsburg, 2004.

[YS08] Y. Yin and H. H. Sawin. Surface roughening of silicon, thermal silicon dioxide, and low-k dielectric coral films in argon plasma. *Journal of Vacuum Science & Technology A*, 26:151–160, 2008.

[ZKL+11] S. M. Zyryanov, A. S. Kovalev, D. V. Lopaev, E. M. Malykhin, A. T. Rakhimov, T. V. Rakhimova, K. N. Koshelev, and V. M. Krivtsun. Loss of Hydrogen Atoms in H_2 Plasma on the Surfaces of Materials Used in EUV lithography. *Plasma Physics Reports*, 37:881–889, 2011.

Acknowledgements

Zum Abschluss möchte ich mich bei allen bedanken, die zum Entstehen dieser Arbeit beigetragen und mich auf diesem langen Weg begleitet haben. Dabei warteten Höhen und Tiefen auf mich, ich wurde aus meiner Komfortzone herausgelockt und die ein oder andere Träne ist geflossen. Trotzdem oder deswegen werde ich immer gerne an diese Zeit zurückdenken.

Mein besonderer Dank gilt **Prof. Dr.-Ing. Ursel Fantz**, die mir die Möglichkeit für diese Arbeit in der *AG Experimentelle Plasmaphysik* gegeben hat, und mir jederzeit eine hervorragende Betreuung zukommen hat lassen. Besonders möchte ich mich für ihr Verständnis und ihre Geduld bedanken, die mir stets entgegen gebracht wurden, als ich die Fertigstellung der Arbeit während meines zweijährigen Referendariats unterbrechen musste.

Ich möchte mich ebenfalls bei **Prof. Dr. Wolfgang Brütting** für die Übernahme des Zweitgutachtens bedanken.

Herausragenden Dank möchte ich an dieser Stelle **Dr. Roland Friedl** aussprechen, dessen Unterstützung und Ratschläge für mich während der ganzen Zeit von unschätzbarem Wert waren. Er hatte immer Zeit für eine Diskussion und bei Schwierigkeiten immer ein offenes Ohr.

Bedanken möchte ich mich bei **Dr. Stefan Briefi** für alle wertvollen Tipps und experimentellen Tricks an *PlanICE*.

Mein Dank gilt auch **Dr. Christian Wimmer** für seine Unterstützung bei den Messungen mit dem Diodensystem an *Batman*, die ein besonderes Highlight für mich waren. Ebenso möchte ich mich bei **Dr. Dirk Wünderlich** bedanken für die Bereitsstellung des Stoß-Strahlungsmodells *Yacora* H_2 und die wertvollen Tipps dazu.

Bedanken möchte ich mich bei **Dr. Marcel Fiebrandt** für seine Unterstützung beim Einsatz des Diodensystems an der Ruhr-Universität Bochum. In diesem Zusammenhang gilt mein Dank auch **Prof. Dr. Enrique Iglesias** für seine Messergebnisse mit dem NaSal-Detektor und die fruchtbaren wissenschaftlichen Diskussionen.

Großer Dank gilt **Dr. Birger Buttenschön** für die Möglichkeit die "Kock-Lampe" nach Augsburg auszuleihen. Ohne seine Hilfe bei der Installation an *PlanICE* und die Einweisung in den Betrieb der Lampe wäre die Kalibrierung des VUV-Spektrometers in der vorgestellten Weise nicht möglich gewesen.
Ich möchte mich bei **Dr. David Rauner**, **Adrian Heiler**, **Frederik Merk** und **Dr. Sofia Cristofaro** (Mi mancano le nostre cene dopo il lavoro!) sowie allen weiteren EPP-lerinnen und EPP-lern für die Zusammenarbeit und das angenehme Arbeitsklima bedanken. Vielen Dank an **Adrian Heiler**, der mich mit seinen Messungen an *ACCesS* beim ersten Ausflug des Diodensystems unterstützt hat.

Auch möchte ich meinen beiden treuen Wegbegleitern – dem *Diodensystem* und dem "*McPherson*" – danken, ohne die es diese Arbeit nicht gäbe. Wir haben viele schöne Momente zusammen im Labor erlebt!

Außerdem bedanke ich mich bei einem namentlich unbekannten Teilnehmer der 24^{th} ISPC in Neapel 2019, der mit folgenden Worten die Dringlichkeit eines *portable diagnostic tools* für den VUV-Bereich verdeutlicht hat: *"VUV is important, but we don't do it."*

Abschließend gilt mein Dank meinen Eltern, meinen Brüdern und Schwägerinnen und natürlich meinem Ehemann Sebastian, die in jeder Lebenslage an meiner Seite stehen und mir in schwierigen Situationen während der Doktorarbeit immer wieder vor Augen geführt haben, dass Plasma zwar 99.9 % der sichtbaren Materie im Universum ausmacht, aber doch nicht alles ist.